

University of Warwick institutional repository: <http://go.warwick.ac.uk/wrap>

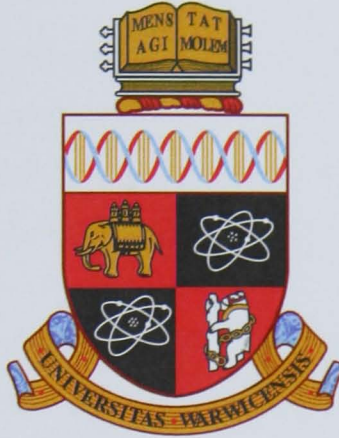
A Thesis Submitted for the Degree of PhD at the University of Warwick

<http://go.warwick.ac.uk/wrap/50195>

This thesis is made available online and is protected by original copyright.

Please scroll down to view the document itself.

Please refer to the repository record for this item for information to help you to cite it. Our policy information is available from the repository home page.



**Development and characterisation of traceable force
measurement for nanotechnology**

by

Christopher Weir Jones MSci (Hons) ARCS

Thesis

Submitted to the University of Warwick

in partial fulfilment of the requirements

for admission to the degree of

Doctor of Philosophy

School of Engineering

July 2012

THE UNIVERSITY OF
WARWICK

Contents

List of Tables	v
List of Figures	vii
Acknowledgments	xviii
Declarations	xix
Abstract	xx
Abbreviations	xxi
List of publications by the author	xxii
Chapter 1 Introduction and context of low force metrology	1
1.1 Overview and motivation	1
1.2 Objectives	2
1.3 Outline of thesis	3
Chapter 2 Background	5
2.1 Context and motivation for a low force facility	5
2.2 A brief history of low force measurement at the National Physical Laboratory .	7
2.3 A direction for traceable low force metrology at NPL	17
2.4 Precedent for the NPL low force facility	19
2.5 Conclusions	38

Chapter 3 The NPL Low Force Balance	39
3.1 The design of the Low Force Balance	40
3.2 AC modulation of the LFB drive signal to mitigate surface charging effects . . .	44
3.3 Development of a fringe counter for the z interferometer	47
3.4 Vibration isolation of LFB	50
3.5 Capacitance gradient determination	53
3.6 Voltage measurement approach	55
3.7 Indentation mode LFB operation	56
3.8 LFB platen and effective LFB stiffness	58
3.9 Performance verification by comparison with mass standards	60
3.10 Performance verification by international comparison with low force standards at other NMIs	64
3.11 Summary of development	81
 Chapter 4 Requirements for a successful low force transfer artefact	 84
4.1 Calibration of artefacts on LFB	85
4.2 Calibration of stiff target instruments using a compliant transfer artefact	86
4.3 Calibration of compliant target instruments using a compliant transfer artefact	88
4.4 Calibration of stiff artefacts on LFB	90
4.5 Other general constraints	91
4.6 Summary	95
 Chapter 5 Review of the state-of-the-art in transfer artefact design	 96
5.1 Flexure design	97
5.2 Force (or strain) detection and actuation mechanisms	106
5.3 Summary of useful artefact fabrication techniques	125
5.4 Conclusions	127

Chapter 6	Optimisation of transfer artefact flexure design by modelling	131
6.1	Overview of chapter	131
6.2	Development of models for the triskelion	133
6.3	Prototype artefact development	144
6.4	Prototype artefact evaluation	171
6.5	Conclusions	182
Chapter 7	Optimisation of instrumentation and control for the artefacts	185
7.1	Overview of chapter	185
7.2	Background theory	186
7.3	Sensor circuit development	189
7.4	Verification experiments	214
7.5	Conclusions	221
Chapter 8	Conclusions	223
8.1	Achievement of objectives	223
8.2	Overall conclusions	227
8.3	Recommendations	228
Chapter 9	Recommendations for a future working low force transfer artefact	229
9.1	Overview of recommended design	229
9.2	Flexure fabrication	229
9.3	Flexure dimensions and related performance	230
9.4	Piezoresistive sensors and control electronics	232
9.5	Interpretation of signals	232
9.6	Packaging	233
9.7	External motion stage requirements	234
9.8	Uncertainty in operation	235
9.9	Summary	237

Appendix A Summary of surface interaction forces	238
Appendix B Analytical model of triskelion flexure mechanics: MATLAB code	240
Bibliography	247
Vita	268

List of Tables

3.1	Summary of drive signals for the LFB under AC operation.	45
3.2	Material properties required for Hertzian compression model of LFB-artefact contact.	60
3.3	Manufacturer specification for the FMT-400 sensor. (*) Calculated with assumptive deflection of 10 % and the lowest force constant. (†) Dependent on the bias voltage (V_{bridge}) that is applied to the series resistance of sensor and reference.	67
3.4	Combined uncertainty in measurements of z_K . The uncertainty in z_{nano} is dominated by the closed loop repeatability.	73
3.5	Combined uncertainty in estimate of k_K	78
3.6	Combined uncertainty in estimate of s_K	81
3.7	Summary of results and uncertainties in the NPL estimates of the stiffness and force sensitivity of the Kleindiek cantilever artefact #3.	82
5.1	Summary of methods for determining a cantilever spring constant: dimensional methods (adapted from [1, 2])	99
5.2	Summary of methods for determining a cantilever spring constant: static experimental methods (adapted from [1, 2])	100
5.3	Summary of methods for determining a cantilever spring constant: dynamic experimental methods (adapted from [1, 2])	101
5.4	Summary of findings of review.	127
6.1	List of proposed test artefacts and their parameter variation from the original microprobe prototype.	150

6.2	Summary of result of application of the previously described finite element and analytical models to the parameter sets in table 6.1. Note that the analytical model would produce meaningless values for model "I" identical to those for model "A", due to the identical beam geometry. As the arms are no longer rigid for this structure, the analytical model would clearly break down.	156
6.3	Comparative analysis of vertical stiffnesses from the two models, and corresponding relative dimensional values as multiples of Artefact A's A , L and T values (s_A , s_L and s_T respectively).	157
6.4	Comparative analysis of lateral stiffness derived from FE and analytical modelling techniques.	165
6.5	Summary of defects to artefacts considered in chapter 6	173
6.6	Difference in thickness between specified and actually fabricated devices. . .	174
6.7	Exemplary calculation of uncertainty in measurement of artefact spring constant, for artefact B.	180
6.8	Summary of spring constant estimates for all mechanically-tested artefacts .	181
6.9	Comparison of modelled and experimentally obtained spring constant estimates for three artefacts. Ratios are defined to simplify comparison.	182
7.1	The spread of maximum resonance amplitudes achieved for the set of sensors and actuators. Since all use the same flexure, the results indicate the quality of each sensor and actuator.	192
7.2	Overview of initial experiments undertaken on artefact D to evaluate the stability of the displacement sensitivity.	216
7.3	Summary of experiments to determine the dependence of artefact sensitivity upon rate of vertical deflection.	220
A.1	Summary of surface interaction force equations. In these equations F is a force component, U the work function difference between the materials, D the sphere-flat separation, γ the free surface energies at state boundaries, and H the Hamaker constant. In the capillary force the step function $u(\cdot)$ describes the breaking separation; e is the liquid layer thickness and r the radius of meniscus curvature in the gap. θ , the contact angle of in-interface liquid on the opposing solid surfaces, is assumed to be approximately zero (wet).	238

List of Figures

2.1	Two key types of instrumented indenter suitable for traceable low force calibration: (a) electromagnetically actuated, capacitively-monitored macroscopic precision flexure design; and (b) modified atomic force microscope.	12
2.2	Various AFM techniques [3].	14
2.3	Schema of NPL microprobe and an image of a fully assembled device (from [4])	17
2.4	Traceability of the newton to fundamental constants of nature, in terms of practical realisations in which base units may be dependent on derived units.	21
2.5	Schematic diagram of the NIST EFB, from [5]. Labelled components are as follows: Schematic of balance components: (1) parallelogram balance, (2) differential plane mirror interferometer, (3) main inner electrode (cross-section), (4) main outer electrode (cross-section), (5) vacuum chamber, (6) optical table, (7) granite foundation block, (8) heterodyne laser light source, (9) mass lift and (10) counterweight.	23
2.6	Comparator mass balance schematic diagram (from [6])	25
2.7	Schematic overview of the mass comparator primary force balance concept. .	26
2.8	Computer model of the NPL electrical nanobalance device. The area shown is $980\ \mu\text{m} \times 560\ \mu\text{m}$. Dimensions perpendicular to the plane have been expanded by a factor of twenty for clarity. Taken from [7].	30
2.9	NPL LEN for lateral force calibration, from [8]. Inset in the expanded view is a side-on view of the $10\ \mu\text{m}$ thick structure of the device.	31
2.10	Force extension curves obtained by stretching titin proteins show periodic features that are consistent with their modular construction (from [9]). The extension curve in the spacer region preceding the saw-tooth is not well defined and would likely hinder traceability.	34

2.11	Four consecutive extension-force curves on a single titin molecule using a 'small' (length $\sim 10 \mu\text{m}$) cantilever. All extension curves were acquired at a pulling rate of 30 mm s^{-1} to 39 mm s^{-1} , which is an order of magnitude faster than previously performed with conventional cantilevers. System was left at rest for thirty seconds between pulls to allow protein to refold (from [10]). . . .	35
3.1	The force balance principle.	40
3.2	Schematic diagram of the LFB.	42
3.3	Photograph of the LFB in situ. Note that the outer cylinder hull is about 20 cm in height and diameter. The LFB mechanism is within and above the tray marked with the TU/e logo.	43
3.4	Sign convention used in the work with phase-locked AC signals	45
3.5	Schematic diagram of capacitor plate numbering system.	45
3.6	Block diagram of the physical elements of the AC LFB controller.	46
3.7	Block diagram of the software behind the LFB controller under AC operation.	46
3.8	Control diagram of the LFB controller under AC operation.	47
3.9	Constructing the lissajous figure for the LFB: 'sine' and 'cosine' photodiode sensor analogue voltages (top left) form a virtual lissajous figure (top right); the analogue voltages are pre-amplified, normalised using an intensity reference, offset and read using ADCs. The software signals are offset to recentre the final ellipse. The deviation from circular, resulting from interferometer sensor misalignment, produces a periodic error in the final displacement signal. . . .	49
3.10	Qualitative comparison of raw data for different vibration isolation unit (AI) and acoustic chamber (AC) state under the 'quiet background' (QB) condition. The QB reference assumes constant noise amplitudes from noise sources in the laboratory, primarily the environmental handling system. Interferometer noise is given in terms of lissajous figure phase, where 0.1 rad is approximately 2.5 nm balance displacement.	51
3.11	A modified arrangement of the LFB system components to mitigate heating within the acoustic enclosure.	52
3.12	Non-linearities in C'_{34} after simple linear fit. The vertical axis is in attofarads; the horizontal axis in micrometres, in software engineering notation.	55
3.13	Example data from the estimate of the balance stiffness by electrostatic force deflection.	57

3.14	Details of the platen used for the comparison: (a) ruby sphere attached to brass collar - note the slight asymmetric setting due to the W-section centre ring; (b) a size comparison between the Kleindiek cantilever (approximated) and various sphere sizes; and (c) an early concept of the sphere platen, with V-section and dimensions not optimised for fabrication and handling. Also shown to approximate scale in (c) is a sketch of the mass platen used in section 3.9.	59
3.15	Results of experiments to determine the weight of a 2.91 mg mass artefact using the LFB: (top) absolute forces readings on the $\pm 36 \mu\text{N}$ LFB force scale, with setpoint changes, and (bottom) the measured weight over time, ignoring off-scale outliers.. . . .	65
3.16	Comparison of artefact weight estimates via mass/gravity and electrostatic force (LFB) routes. The uncertainty in the mass estimate is too small to show clearly on this scale.	66
3.17	The Kleindiek FMT-400 Sensor, a commercial cantilever-format piezoresistive force sensor. (from [11])	67
3.18	Schema of mechanical arrangement for calibration of the Kleindiek cantilever.	69
3.19	Overview of information flow in mass-traceable calibration of the Kleindiek cantilever.	70
3.20	Residuals to linear fit of LFB interferometer fit to Nanocube target position over a range of target positions.	72
3.21	Raw Kleindiek calibration data: LFB force output versus Nanocube target position.	74
3.22	Raw Kleindiek calibration data: cantilever output signal versus Nanocube target position.	75
3.23	Raw Kleindiek calibration data: cantilever output signal versus LFB force output.	75
3.24	Force drift as zeroth order term in linear fit of LFB force to nanocube position.	76
3.25	Cantilever stiffness estimates as first order term in linear fit of LFB force to nanocube position.	77
3.26	Residuals in linear fit of LFB force to (change in) nanocube position.	77
3.27	Collated plot of cantilever sensor output versus applied force, for all 15 runs.	79
3.28	Residuals in linear fit of artefact sensor output signal to LFB force, for all runs.	80

3.29	Cantilever force sensitivity estimates as first order term in linear fit of artefact sensor output signal to LFB force.	80
4.1	Schema of calibration of compliant artefact on LFB.	86
4.2	Cartoon of measurement loop deflection	87
4.3	Schematic diagram of use of transfer artefact to calibrate a stiff target instrument.	87
4.4	Schema of calibration of a compliant target with a passive transfer artefact of similar stiffness.	89
4.5	Schema of calibration of a compliant target with an active (pushing) transfer artefact of similar stiffness.	89
4.6	Schematic of stiff artefact calibration on LFB using secondary flexure	91
5.1	Experimental prototype reference cantilever array - plan view (from [12])	103
5.2	Commercially available AFM 'calibration' cantilevers from Bruker, formerly Veeco Probes: photograph of the three cantilevers, with quoted nominal spring constants of 0.157 Nm^{-1} , 1.3 Nm^{-1} and 10.4 Nm^{-1} (left) and a side view of one cantilever (right) (from [13]).	103
5.3	The NPL triskelion form, with nomenclature used in this and related documents. The hub and arms are nominally non-compliant (achieved through extra thickness on these portions) concentrating deflection in the outer beams.	105
5.4	A MARS. Above the spiral spring is the more massive poly-crystalline silicon platform, suitable for AFM contact. A scale bar of $100 \mu\text{m}$ has been overlaid on this optical micrograph (from [7]).	107
5.5	General form of the Wheatstone bridge.	108
5.6	Tortonese et al.'s early piezoresistive AFM cantilever: schematic diagram of piezoresistive detection scheme (top); SEM photograph (centre) and plane view drawing (bottom). Images from [14].	109
5.7	Images of the NPL C-MARS device, with detail of its fiducial markings; the $10 \mu\text{m}$ oxide squares form a binary numbering system along the axis of symmetry (adapted from [15]).	111
5.8	Types of piezoresistive silicon sensors developed at PTB: (a) two-leg cantilever with a glass sphere as probing tip; (b) single cantilever with integrated silicon tip (from [16]).	112

5.9	The NIST piezoresistive cantilever (from [17]; see also [18]).	113
5.10	SEM micrograph of integrated cantilevers and CMOS circuits in an intermolecular force detection device developed at CNM-IMB, Spain (from [19]).	114
5.11	The 'blocking force' concept: Piezoelectric element free end displacement as a function of applied force and voltage.	115
5.12	A commercially available stacked piezoelectric force actuator [20].	116
5.13	The capacitor comb for linear sensing and actuation.	118
5.14	Capacitive force sensor and the study of fruit flies: (top) schematic diagram of probe showing axial force direction; (centre) block diagram of associated control circuitry; and (c) the sensor in action. From electronic version of [21].	120
5.15	A commercially available capacitor-based force sensor (from [22]). The device is accompanied by a controller unit, the cable from which connects to the green pin headers shown.	121
5.16	(left) schematic diagram of a resonance string sensor; (right) example of actual experimental set-up showing shear piezo for tension adjustment and magnet for actuation of Lorentz oscillations (from [23])	122
5.17	Schematic diagram of a double-ended tuning fork resonance force sensor (from [24]).	123
5.18	Illustration of resonance force sensing AFM tip presented by Harley <i>et al.</i> (from [25])	125
6.1	The NPL triskelion form, with nomenclature used in this and related documents. The hub and arms are nominally non-compliant, that is, much stiffer than the beams. This stiffness difference is achieved through extra thickness on the arms and hub, and results in concentration of deflection in the outer beams.	132
6.2	Schematic of general model, showing the five key geometry variables for the artefact concept. The shape of the inner arm and hub section is fairly flexible to suit fabrication constraints; the key is that it be much stiffer than the outer beams. Dashed lines show the effective radius of each beam end from the hub centre. The beams are rotated 120° from these lines.	133
6.3	Microprobe geometry used in this discussion	135
6.4	Dimensions of the rectangular outer beams	135

6.5	Effect of a small rotation about x on the vertical position of the arm ends . . .	137
6.6	Schema of FEA model corresponding to simplest analytical model. This has been chosen as the basis for the shape of the prototype transfer artefact set. Shown are the in-plane geometry variables with their working values at the time this figure was created. The 'chain' and 'sum' signs indicate links to constant and derived parameters respectively. The quantity $w-2$ is a derived parameter equal to $w/2$. The measured gap $D1$ is shown at its smallest value of $17\ \mu\text{m}$, corresponding to the smallest value of A in the artefact set, $0.6\ \text{mm}$	142
6.7	A comparison of the alignment sensitivity of a cantilever and a triskelion: (a) the physical comparison; and (b) a simple model of the triskelion flexure. . . .	143
6.8	Representative results for comparative alignment sensitivity of triskelion and simple cantilever, with common nominal spring constant of $20\ \text{Nm}^{-1}$. Modelled triskelion arm length: $1\ \text{mm}$. Modelled cantilever nominal axial contact point: $5\ \text{mm}$	144
6.9	Wafer layout options: (a) existing layout with twelve $13\ \text{mm} \times 13\ \text{mm}$ chips, as used successfully in microprobe project; (b) proposed higher density layout using $12\ \text{mm} \times 12\ \text{mm}$ chips to maximise prototype population. Half-die, shown within the red dotted squares, were not present on the microprobe wafers but are to be added to further increase functionality; see 'partial chip' discussion below.	146
6.10	Schematic diagrams of the proposed sensor/actuator design adapted from previous drawings by Cranfield, not to scale: (a) top-down (from substrate side) view of sensor/actuator electrode layout over PZT and nickel layers; (b) expected cross-section of proposed beam showing PZT layer somewhat wider than the nickel flexure.	148
6.11	Simple cantilevers C1 to C3 equivalent to portions of beams on full artefacts A and D; these cantilevers allow investigation of sensor dimensional requirements in a simplified system. The cantilevers have common thickness nickel thickness $5\ \mu\text{m}$ (circa $9.5\ \mu\text{m}$ with PZT) equal to the beam thicknesses on full artefacts A, D.	152
6.12	Multiple-legged cantilever variants with a less critical stiffness dependence on length. The cantilevers C4 to C6 are identical except for base leg width. These are based on a previous concept developed at NIST [18].	154

6.13 Schema highlighting the possibility for reuse of at least four, if not eight of the full chip solder contact pads on the partial chips. Note that the current ground pad position also remains viable. The pink square and red quadrilateral indicate the expected edge locations of the proposed full and partial chips respectively; the blue dotted square indicates the previous 13 mm chip edge. Adapted from mask drawings from Cranfield University.	155
6.14 Placement of proposed chips on the wafer such that duplicate chips are spatially separated. The numbers refer to the chip ID ('#') column in table 6.1. Letters refer to the partial chips; A, B are the simple cantilever; C, D are the two-legged cantilevers.	156
6.15 Total displacement (left) and strain (right) plots of artefact A under a ten micronewton vertical (z) load at the hub centre. View is in the $-z$ direction. Other views clarify that the total displacement is effectively entirely vertical in the hub centre.	159
6.16 Total displacement (left) and strain (right) plots of artefact I under a ten micronewton vertical (z) load at the hub centre. View is in the $-z$ direction.	160
6.17 Total displacement (left) and strain (right) plots of artefact F under a ten micronewton vertical (z) load at the hub centre. View is in the $-z$ direction.	161
6.18 Total deflection of chip A under lateral ($+x$) force: (top) view along $+x$ -axis; (bottom) view along $-z$ -axis with $+x$ direction towards this caption. Deflection at the hub centre is entirely along the $+x$ -axis. The deflections in each axis are to scale but greatly magnified. Lateral deflections dominate.	162
6.19 Comparative analysis of results from FEA and Analytical models of the eight comparable artefact types. The stiffness ratio $k_{x,FEA}/k_{x,Anal}$ maps to the right-hand secondary axis; the other raw and descaled FE stiffness plots map to the left-hand axis.	166
6.20 The apparent linear relationship between the relative geometry factor and the analytical lateral stiffness results. The trend line is a linear least-squares fit to the data. The horizontally groups points share common L and T values but different A values.	167
6.21 A 'simple' cantilever from partial chips A, B (a) and its displacement (b) and stress (c) distributions under a $5 \mu\text{N}$ vertical load. The cantilever shown is C1.	168
6.22 A 'modified' cantilever from partial chips C, D (a) and its displacement (b) and stress (c) distributions under a $5 \mu\text{N}$ vertical load. The cantilever shown is C4.	169

6.23 Fabrication defects on artefact A, obtained using a digital optical microscope.	172
6.24 The workaround two-step prototype artefact spring constant measurement process.	176
6.25 Parallel-flexure reference cantilever employed to measure prototype artefact spring constants: (top) schematic diagram; (bottom) actual implementation.	177
6.26 Raw data from the measurement of the reference cantilever spring constant.	179
6.27 Processed data from the measurement of the reference cantilever spring constant.	179
6.28 Per-cycle approach and retract stiffness estimates from least-squares linear fits.	180
6.29 Displacement-displacement curve for the use of the reference cantilever to measure the spring constant of artefact B.	181
7.1 The piezoelectric effect in quartz: (A) unstressed unit cell; (B) unit cell under compression produces a dipole; (C) under tension, the sign of the dipole is reversed (from [26]).	186
7.2 An electronic model of the sensor, charge amplifier system (from [27])	188
7.3 An unsuccessful early interaction experiment that produced a fictitious sensor signal, due to electric fields from the PI Nanocube nanopositioner system: (top) the physical arrangement; (bottom) example results.	190
7.4 A typical frequency response characteristic for the triskelion obtained from a laser Doppler vibrometer using a software tool developed by others at NPL. This plot was obtained from energising actuator '3Am' on artefact D. The first mode corresponds to the vertical oscillation mode; the higher pair of peaks show the two plane-tilt modes and if fabricated perfectly would overlap. The small low-frequency notches are assumed to correspond to resonant modes of the metrology frame.	191
7.5 The tuning fork actuator system. The fork is placed across the centre of this image and secured with bolts through the handle out of shot. The coil is glued to the fork, and the magnet to the square-section rigid aluminium bar along the top of the image. On the opposite fork, approximately coaxial to the coil, a wire stylus is attached to contact the artefact. The system was rigidly mounted to a 5 mm high-resolution motion stage of the kind used elsewhere in this work.	193
7.6 Summary of physical interactions, noise sources and data flow in the tuning fork experiment.	194

7.7	Sensor reponse to abrupt coil power connection state changes.	195
7.8	Sensor reponse to abrupt coil removal of driving signal from function generator.	196
7.9	Sensor response using charge amplifier with high-pass filter of 2.3 kHz. Time and frequency are in units of seconds and hertz respectively.	198
7.10	Circuit diagram for noise reduction through subtraction of a nearby noise reference.	199
7.11	Sensor circuit output voltage using noise subtraction circuit, using the LF412CN amplifier. Time and frequency are in units of seconds and hertz respectively.	200
7.12	Sensor circuit output voltage using the noise subtraction circuit based on the LMC6082 amplifier. Time and frequency are in units of seconds and hertz respectively.	201
7.13	Observed reduction in noise in the sensor circuit output due to optimisation of feedback resistor. Time and frequency are in units of seconds and hertz respectively.	202
7.14	The manual mechanical oscillator system: (a) detail of artefact interaction; (b) schematic overview of physical arrangement of cam oscillator; (c) overview photograph showing noise enclosure and pull-cord system bottom-right.	205
7.15	Sensor circuit output response to repeated bursts of excitation at around 5 Hz using the cam oscillator system.	206
7.16	Sensor circuit output response for a steady manual oscillation input in the range 0.5 1Hz. Time and frequency axes have units of seconds and hertz respectively.	207
7.17	The nanopositioner actuation system.	208
7.18	Sensor response using section 7.3.6 circuit under square wave input. One volt supplied to the nanopositioner will command a ten micrometre move in closed-loop operation.	209
7.19	Sensor response using section 7.3.6 circuit under stepped input.	209
7.20	Response of initial circuit to square (left) and triangle (right) wave input displacements.	209
7.21	Sensor-charge amplifier response to a sinusoidal mechanical input, showing effect of use of the feedback capacitor reset button. The top plot shows detail of the lower plot.	210

7.22	Evaluation of the long-term behaviour of the charge amplifier circuit. One day equates to about 82 ks. The simplicity of the lower plot, taken from the upper plot, emphasises the danger of assumptions about long-term behaviour. . . .	211
7.23	Driving signal and sensor response signals in response to 1 Hz motion commands with intended amplitudes 500 nm, 300 nm, 200 nm and 100 nm respectively from left to right.	212
7.24	Results of initial experiments undertaken on artefact D to evaluate the stability of the displacement sensitivity. The input movement is the commanded nanopositioner displacement step calculated from the change in command voltage; it was not independently verified.	215
7.25	Displacement-sensor voltage plot for collection of initial experiments.	216
7.26	Example gradient linear fit data for 5 μm amplitude, 10 $\mu\text{m s}^{-1}$ artefact deflection experiment, artefact D.	218
7.27	Summary of calculated sensitivity as a function of artefact displacement amplitude. Error bars are the standard error in the mean of all gradient estimates for the direction of motion for a given amplitude.	219
7.28	Summary of experiment series S1, S2 and S3 to determine the dependence of displacement sensitivity upon rate of artefact deflection. Data for increasing and decreasing artefact deflection are shown separately. Series are connected for readability and not necessarily to infer a trend.	220
7.29	Summary of experiment series S4 to determine the dependence of displacement sensitivity upon rate of artefact G deflection. Data for increasing and decreasing artefact deflection are shown separately. Series are connected for readability and not necessarily to infer a trend.	221
9.1	A rapid-prototyped artefact demonstrator designed by the author and produced by the University of Nottingham showing a likely packaging format for the low force artefact. The dimensions are 10 mm \times 7 mm \times 1 mm.	233
9.2	A concept sketch for a better traceable low force artefact: (a) overview of artefact system including artefact module and external positioning stage; (b) top view of artefact chip showing location of electronic contacts and artefact; (c) side view of the same; and (d) cross-sectional end view through the hub centre with suggested instrument contact modes. The labelled items are explained in the text.	236

A.1 Comparative plot of described surface interaction forces, based on the following values: $R = 2 \mu\text{m}$; $U = 0.5 \text{ V}$; $\gamma = 72 \text{ mJ m}^{-2}$; $H = 10^{-18} \text{ J}$; $e = r = 100 \text{ nm}$. Physical constants take their standard values: $\epsilon_0 = 8.854 \times 10^{-12} \text{ C}^2 \text{ N}^{-1} \text{ m}^{-1}$; $\hbar = 1.055 \times 10^{-34} \text{ m}^2 \text{ kg s}^{-1}$ and $c = 3 \times 10^8 \text{ m s}^{-1}$ 239

Acknowledgments

A thesis is a metaphor for academic endeavour as a whole, being something novel crafted from the groundwork laid by others. There are a number of people I must thank for their 'groundwork' to my education, my career and this thesis.

First of all, many thanks to my supervisors Derek Chetwynd and Richard Leach for their patient guidance and support over the past years, not least for detailed comments and sage advice at the eleventh hour.

My thanks to my examiners and thesis committee for taking time to consider my progress and final manuscript; to NPL, for funding¹ and operational support; to my colleagues in the mass and dimensional area at NPL, too many to fairly name, but the ready help of whom is greatly appreciated; to my various student assistants; to the international low/small force NMI community for lively discussions, especially to Dr Jon Pratt at NIST for his insight and the opportunity to second to Gaithersburg; and to Chris Shaw et al. at Cranfield University for artefact production.

To those who have supported and encouraged me throughout my education and career: I extend hearty thanks; to those who tried to hold me back: a raspberry to you!

I dedicate this thesis to my family. To Mum and Dad, thank you for setting me on the right path and tirelessly supporting me and encouraging me along it. To my wife, Winnie, thank you for being an unending source of patience, and for finding sense in the muddle for ten years!

To the future! I wonder what's next?

¹The described work was funded by the NMO Engineering Measurement programmes 2005 to 2008 and 2008 to 2011.

Declarations

The majority of the work presented in this thesis is the work of the author alone. The contributions of others to the reported work are noted here.

This thesis concerns critical contributions for the continuing long-term development of the traceable low force facility at NPL. As such, it inevitably both builds on the earlier contributions of several colleagues and benefits from their present work in related areas. The thesis presented is the work solely of the author except where explicitly stated otherwise and cited in the main text.

Significant contributions of others are as follows. The triskelion artefact holder (see figure 7.17) was developed with James Claverley, who also provided the laser Doppler vibrometer testing procedure described in section 7.3.2. The fabrication of the prototype artefacts (section 6.3) was formulated and undertaken by Cranfield University to meet specifications provided by the author.

Detailed testing, minor design and some artwork were undertaken by masters students under the direct supervision of the author. Specifically, Jewan Singh [28] contributed to section 6.4; Hassan Mashini [29] contributed to section 7.3; and Laurent Lestage [30] contributed to sections 7.3 and 7.4. Some artwork was produced with the assistance of the NPL Graphics team, to the author's specifications, during the course of the project.

Abstract

Traceable low force metrology should be an essential tool for nanotechnology. Traceable measurement of micro- and nanonewton forces would allow independent measurement and comparison on material properties, MEMS behaviour and nanodimensional measurement uncertainties. Yet the current traceability infrastructure in the UK is incomplete. This thesis describes the incremental development of the low force facility at the National Physical Laboratory (NPL).

The novel contribution of this thesis has three components. First, specific modifications to the NPL Low Force Balance were undertaken. This involved developing novel or highly modified solutions to address key issues, as well as undertaking detailed comparisons with external and internal traceability references. Second, a triskelion force sensor flexure was proposed and mathematically modelled using both analytical and finite element techniques, and compared to experimentally measured spring constant estimates. The models compared satisfactorily, though fabrication defects in developed prototype artefacts limited the experimental confirmation of the models. Third, a piezoelectric sensor approach for quasi-static force measurement was proposed, experimentally evaluated and rejected. Finally, an improved design for a low force transfer artefact system is presented, harnessing the findings of the reported investigations. The proposed design combines proven strain-sensing technology with the advantageous triskelion flexure, incorporating an external stage and packaging aspects to achieve the requirements for a traceable low force transfer artefact.

Abbreviations

- ADC analogue-to-digital convertor, an electronic component
- BIPM International Bureau of Weights and Measures, after the French name
- CIPM International Committee for Weights and Measures, after the French name
- CMS-ITRI Centre for Measurement Standards (Industrial Technology Research Institute), the Taiwanese NMI
- DAC digital-to-analogue convertor, an electronic component
- GUM Guide to the Uncertainty in Measurement
- KRISS Korea Research Institute of Standards and Science, the South Korean NMI
- LFB Low Force Balance, the primary traceable nanonewton balance at NPL
- LNE Laboratoire national de métrologie et d'essais, the French NMI
- MEMS micro-electromechanical system
- MPE maximum permissible error
- NIST National Institute of Standards and Technology, the American NMI
- NMI national metrology institute
- NMO National Measurement Office
- NPL National Physical Laboratory, the British NMI
- PTB Physikalisch Technische Bundesanstalt, the German NMI
- SME small- to medium-sized enterprise

List of publications by the author

The following publications were authored or co-authored by the present author during the period of registration and relate to low force metrology.

Review of low force transfer artefact technologies Published [31] as an NPL Report in 2008 (primary author), this review report contributed to chapters 2 through 5 of this thesis.

Adding a dynamic aspect to amplitude–wavelength space Published [32] in Measurement Science and Technology in 2012 (primary author), this paper relates to the need for low force metrology for stylus surface topography instruments (see chapter 2).

Comparison of NIST SI force scale to NPL SI mass scale Published [33] in the Proceedings of 2008 ASPE Annual Meeting, Portland, Oregon, (primary author) to accompany an oral presentation by the author, this paper relates to section 3.9.

Report on the first international comparison of small force facilities: A pilot study at the micronewton level Published [34] in Metrologia in 2012 (co-author), the author contributed details of NPL's participation (see section 3.10).

Concept and modelling of a novel active triskelion low force transfer artefact Presented [35] at the 11th Int. Conf. of the Euspen, Como, Italy (primary author), this poster relates to the work described in section 6.4.

Advances in engineering nanometrology at the National Physical Laboratory Published [36] in Measurement Science and Technology in 2012 (co-author), the author contributed a review of progress in low force metrology at NPL.

Chapter 1

Introduction and context of low force metrology

1.1 Overview and motivation

Progress in UK nanometrology and in other areas of nanotechnology has been constrained by an incomplete traceability chain for micro- to nanonewton force measurement. The general aim of the work described in this thesis was to complete a facility at the National Physical Laboratory (NPL) to disseminate traceability for such low forces.

A lack of suitable traceable transfer artefacts has kept the primary realisation of the nanonewton unavailable to industry and academia, and hence to dependent applications. Traceability is an essential prerequisite for the quantitative comparison of independent processes and for meaningful estimates of forces acting on real micro- and nanotechnology applications.

This thesis describes key development steps towards the completion of the NPL Low Force Facility, intended to provide the source of traceable micro- to nanonewton force measurement in the UK. The described work has three key strands.

1. Upgrades, commissioning and verification of the NPL Low Force Balance (LFB), realising traceable force measurement in the 10 nN to 30 μ N range.
2. Development of an improved transfer artefact flexure design based on the triskelion concept.
3. Evaluation of the suitability of the piezoelectric effect for traceably calibratable quasi-static force sensors for a low force transfer artefact.

1.2 Objectives

The specific objectives of the work reported in this thesis can be listed as follows. The list incorporates objectives defined at the outset of the project and additional objectives set or redefined during the course of the project.

Objective 1.1 Establish a new LFB controller to mitigate surface charging effects in the mechanism whilst respecting the electrostatic force balance principle.

Objective 1.2 Develop full continuous fringe-counting operation on the LFB z interferometer.

Objective 1.3 Establish effective vibration isolation for the LFB.

Objective 1.4 Establish techniques or procedures for measurement of capacitance gradient and plate voltages.

Objective 1.5 Verify LFB performance via comparison with small calibrated masses.

Objective 1.6 Verify LFB performance via international comparison with low force standards at other National Metrology Institutes.

Objective 2.1 Review the state-of-the-art in flexure design and fabrication techniques, as relevant for transfer artefact design.

Objective 2.2 Establish a concept for the flexure design for a novel transfer artefact for low force traceability.

Objective 2.3 Develop an analytical model of the flexure sufficient to allow the behaviour of a prototype implementing the concept to be predicted.

Objective 2.4 Develop a finite element model to complement and improve confidence in the analytical model.

Objective 2.5 Design, and have fabricated, a suite of prototype artefacts suitable for experimental confirmation of the developed models.

Objective 2.6 Experimentally evaluate the performance of the fabricated artefacts and compare with model-predicted behaviour.

Objective 3.1 Review the state-of-the-art in on-board strain sensing in microfabricated flexures, as relevant for transfer artefact design.

Objective 3.2 Develop a sensor circuit capable of detecting the electronic response of a piezoelectric sensor to quasistatic deflection.

Objective 3.3 Experimentally evaluate the suitability of the piezoelectric effect for strain generation and strain sensing on a traceable low force transfer artefact, given the associated requirements.

Objective 3.4 Establish recommendations for the future use of the piezoelectric effect in the traceable low force measurement context.

1.3 Outline of thesis

This thesis is arranged in a manner that reflects the undertaking of the project, and can be summarised as follows. Chapter two elaborates on the background to the project, the motivation, and the context for the work in terms of activity at NPL and at equivalent institutes worldwide. The status of the NPL Low Force facility at the outset of the reported work is also clarified.

Chapter three describes the function and operation of the LFB and reports on the first strand of the project, that is, efforts to meet objectives 1.1 through 1.6 to make the LFB ready for use with artefacts. This strand of the project expanded in scope throughout the project as challenges and opportunities arose.

Chapter four initiates the second and third strands of the project, defining the requirements for a successful low force transfer artefact for use with the LFB based on the author's metrology experience and discussions with leading low force experts. The calibration of the transfer artefacts and their use to calibrate both stiff and compliant targets is discussed. The requirements in this chapter inform the direction and discussion of the subsequent chapters.

Chapter five contains a review of the state-of-the-art in low force transfer artefact technology, considering both flexure design and fabrication and relevant strain sensing technologies (objectives 2.1 and 3.1). The development, optimisation and evaluation of models to understand and predict the electromechanical behaviour of the basic concept are considered. Based on consideration of the requirements set down by users and the specifications demanded from the artefacts, a suite of test artefacts was fabricated as a realisation of the concept and to verify the models developed. Stiffness measurements were undertaken using the prototype artefacts to consider the suitability of the developed mathematical models, as will be discussed.

Chapter six describes the bulk of the effort to complete the second strand of the project, addressing objectives 2.2 through 2.6. Chapter seven describes the completion of the third strand of the project, addressing objectives 3.2 through 3.4. A sensing circuit and metrology fixture was developed in order to interface with, characterise and evaluate the

performance of the transfer artefact prototypes. The best-case observed artefact sensor performance for quasistatic force measurement is presented and the viability of the approach evaluated. This development included significant prototyping work undertaken using the test artefacts.

Chapter eight contains the final conclusions and key recommendations to the project and thesis, and informs chapter nine, the recommendations for a future working low force transfer artefact. Chapter nine considers a best-case design for the transfer artefact based on the knowledge accumulated over the body of the work. Sources of uncertainty in the operation of an artefact of the recommended design are considered.

Chapter 2

Background

It is clear that the ability to measure nanonewton-scale forces has wide appeal across all fields of research and application of micro- and nanotechnology. However, the prior and on-going experience of the National Physical Laboratory, in addition to the precedent set by others, has influenced the formation of a low force facility for the UK.

This chapter sets out the context for the development of the low force facility, considering prior experience and local applications at NPL, as well as equivalent and potential facilities at other institutions. Also presented are the starting point and direction of development from the point of view of this thesis.

2.1 Context and motivation for a low force facility

The past twenty years have seen an increasing move towards quantitative understanding, fabrication and manipulation of processes and objects, for which behaviour on the micro- and nano-scale is key to function. Function on this sub-micro scale is typically governed by forces on the micro- to nanonewton scale. As such nanometrology applications mature and there is greater and greater need for integration and independent quantitative comparison of those sub-micro processes, traceability to the definition of the newton for small forces is becoming essential.

Traceability of force measurement directly affects surface topography measuring instruments and material property testing instruments. Traceability is indirectly of high importance for real-world problems as diverse as timely deployment of vehicle accident management systems and accurate dosage in oral (nebuliser) drug delivery.

The mature measurement capabilities that exist to characterise and predict the performance of function of objects on the macro-scale must be miniaturised to produce analogous measurement capabilities on the micro- to nanoscale. In some cases this is 'merely' a question of more precise manufacturing capabilities to reduce the size of some mechanical gauge whose function remains effectively the same.

However, typically this reduction in working scale necessitates a complete reformulation of measurement strategy to avoid increasingly overwhelming measurement uncertainties. Force measurement is a good example of measurement uncertainty barrier.

Traceably calibrated deadweights, derived from the first standardised merchant scales from antiquity, have been, and continue to be used extensively to provide traceable force, mass and torque measurements from tens of meganewtons down to a millinewton. For smaller forces the measurement uncertainties encountered render the calibrated deadweight impractical, and a replacement force calibration artefact and traceability route is required.

As might be expected, developments in industries concerned with micro- and nanoscale processes have led to methods of 'calibrating' force measurement to meet the requirements of those industries. However, those low force measurement standards are typically comparative in nature, relying on repeatability and assumed linearity of instrument scale; the standards are typically highly industry specific and often proprietary intellectual property, and lack the rigorousness of design and the open, verified traceability of standards developed at the world's national metrology institutes (NMIs).

The National Physical Laboratory (NPL) is one such NMI that has undertaken to develop a facility for low force measurement¹. This development was undertaken within the 2008 to 2011 National Measurement Office (NMO) Engineering Measurement programme, funded the UK taxpayer, and supports a more general strategy within the European metrology community [37].

The NPL facility complements comparable small force facilities developed at other major global NMIs including NIST, KRISS, PTB and CMS-ITRI, which will be reviewed in this thesis. The facility aims to provide a route to traceability in the most technically challenging part of the force range with immediate application and relevance for UK industry, namely the 10 μN down to 1 nN regime.

A facility representing a primary traceability route such as in this case is typically made up of two components: primary instrument or realisation; and transfer artefacts.

The primary instrument traceably realises the basic quantity, embodying some base underlying principle. This primary instrument is optimised for best possible (lowest) uncer-

¹The author has been a full-time employee of NPL for the duration of this project

tainty in the primary instrument and is typically unsuitable for direct, efficient interaction with instruments or processes to be calibrated.

The link between the primary instrument and those instrument or processes is made using specialised transfer artefacts – typically suites thereof – that are optimised for the requirements and rigours of transfer of calibration. For example, a calibrated metre rule is a transfer artefact for the primary, optical realisation of the metre; similarly a commercially available kilogram artefact is a transfer artefact for the international prototype kilogram, \mathcal{K} [38].

In addition to the requirement to make a traceable low force facility available to UK industry, as discussed above, there are several local projects at NPL that would directly benefit from the development of such a facility. A traceable low force measurement capability directly supports the quantitative understanding and modelling of surfaces and surface texture, which are often critical to function and yet poorly defined on the micro-to nanoscale. In micro-coordinate metrology, for example, a consistent and traceable definition of the threshold of force interaction defining contact is essential for measurement standards. Such a low force capability would also help to make traceable the extensive body of work undertaken in the materials sector through the calibration of nanoindenters and atomic force microscopes.

At the commencement of this project, previous NMO funded work had resulted in the development, and very early-stage testing, of the NPL Low Force Balance, as the primary instrument in the NPL low force measurement facility. The appropriate next step, therefore, was to develop a transfer artefact concept to transfer low force calibrations from the LFB to users in industry.

2.2 A brief history of low force measurement at the National Physical Laboratory

2.2.1 The National Physical Laboratory

The National Physical Laboratory (NPL) is, amongst other roles, the UK's National Measurement Institute (NMI). As such, NPL receives up to 60 % of its total funding from the National Measurement Office (NMO) to develop and disseminate world-leading capability to support UK industry. The NMO is an agency of the UK government and so NPL's NMI activity is funded directly by the UK taxpayer.

Specific responsibilities include the maintenance and development of the UK's primary definitions of the base units (metre, kilogram, etc.), as well as maintaining equivalence of those units to other countries' definitions under the stewardship of the International Bureau of Weights and Measures (BIPM).

NPL also has a responsibility to ensure that its measurement capability is available to all sectors and members of UK industry, in some case subsidising access to calibrations and advice for small- to medium sized enterprises (SMEs).

This dual responsibility to develop world leading metrology capabilities and to ensure that traceable measurement is accessible to industry can lead to conflicting requirements that must be overcome for each area of measurement. Specifically, the instrument or technique developed as the primary realisation of the relevant unit is usually much too expensive or impractical to be directly used by an end-user. This is certainly the case for low force measurement, as will be discussed. The solution is to maintain a complete dissemination chain ranging from primary standards and definitions to physical calibration artefacts and good practice guides for direct use on the factory floor. Some of this dissemination responsibility may be delegated officially or unofficially to appropriate intermediate bodies such as calibration laboratories and instrument manufacturers.

The work described in this thesis was funded by the NMO Engineering Measurement Programme 2008 – 2011 and its preceding equivalents. NPL's low force capability develops upon established local capability for force, displacement and electrical measurements.

2.2.2 Traceability

When measurements are made in the world around us, the measurement scale or instrument used, whether a metre rule, mass balance or thermometer, is often assumed to be infallible by the user. If the measurement is not 'faulty', then its readout is 'accurate', at least to the resolution provided.

This assumption is naïve, and usually wrong. The relationship between the measured and actual value of the quantity under observation is complicated and often varies with time. Changes in environment such as temperature, pressure or external forces may change the quantity being measured, and distort the reference scale.

If the measurand and instrument are understood, the different uncertainty sources affecting the measurement can often be isolated and estimated. The uncertainties are then combined using a set of procedures to obtain an overall estimate for the measurement uncertainty.

Many of these uncertainties may be provided in some form by the instrument manufacturer, and originated (we hope) from calibrations at the factory, which had their own associated uncertainties. If everyone has done their job, there should be an unbroken chain of calibrations, and uncertainty estimates, back to one or more primary standards or length, mass and so on, maintained by national metrology institutes (NMIs) such as NPL. This is the principle of traceability. Traceability is formally defined [39] as follows:

Traceability is “the property of a measurement or the value of a standard whereby it can be related to stated references, usually national or international standards, through an unbroken chain of comparisons all having stated uncertainties”.

Thus it is the implicit chain of uncertainty, if it exists, that makes a measurement traceable. If a traceable measurement of mass is found to be $25.3 \text{ kg} \pm 0.6 \text{ kg}$ ($k = 2$) then one can be 95 % certain that the actual mass value falls within 0.6 kg of 25.3 times the mass of the international prototype kilogram.

The concept of traceability and propagation of uncertainty is discussed in the Guide to the Uncertainty in Measurement (GUM), originally published in 1995 [40] and later amended and supplemented [41, 42]. The GUM introduces methods to estimate the uncertainty in a measurement and hence continue the chain of traceability. A familiarity with the GUM is highly recommended and will aid the understanding of discussions presented later in this thesis.

2.2.3 Macro- to mesoscale force calibration

Standard ‘weights’ (reference masses) and comparator balance techniques stretch back into antiquity due to their value in commerce, and the kilogram (or rather, the gram) was an essential component from the outset of the metric system and its successor, the International System of Units (SI) [43].

In line with other NMIs globally, the development of the NPL low force facility has been influenced in part by many decades of traceable measurement of larger masses and forces. Precision balances to compare masses on the order of a kilogram were part of the original NPL capability in 1910. NPL was fortunate to inherit into its regular facilities the famous balance used by Poynting to ‘weigh the Earth’ [44, 45]. NPL developed one of many precision balances in 1930, as described by Lewis and Havard [46]. Today, NPL routinely calibrates up to 1.2 MN by directly applying deadweight forces, yielding relative uncertainties

of 0.001 % [47]. Forces up to 30 MN are accessible via a hydraulic secondary standard, with increased uncertainties.

Since force traceability is derived from comparison with the weight of the kilogram, the lowest relative uncertainties in traceable force measurement can be found at around 10 N [48]. The kilogram has a relatively low surface-area to volume ratio, reducing the effects of contamination; it is of practical size to be manipulated, and yet small enough to be easily enclosed within an environmentally-stabilised chamber. Calibrated masses in the gram to kilogram range are routinely used in research and industry, and the OIML specifies multiple grades of standardised masses for this purpose [49].

The limit of usefulness of this technique is reached when uncertainties and practical considerations due to contamination and handling grow too great and too problematic for cost-effective use. It is at this level where a transition to the force measurement techniques considered in this thesis become preferable. At the lower end of the practical deadweight scale, small masses are nevertheless used at NMIs to produce force, torque and density standards, to calibrate mass balances, and so on. Since the challenges in small mass calibration are dominated by contamination and the time penalty of appropriate handling, but otherwise produce highly repeatable results, they remain in use at NMIs, in which the clean operating environment and tolerance of time-consuming procedures in place are conducive to their use.

2.2.4 Direct force measurement applications

For 'real' applications of force measurement in industry and academia, what is needed is a calibrated force sensor capable of measuring a force from an arbitrary direction, and with an arbitrary (and variable) magnitude on a continuous force scale, amongst other requirements. These requirements, and others, which are described in more detail in chapter 4, necessitate a force measuring solution other than deadweights.

NPL developed a micronewton thrust balance for ESA for the calibration of ion thrusters ultimately intended for satellites such as GOCE [50, 51, 52]. This macroscopic-sized device balanced an input thrust with an electromagnetic force to maintain an interferometrically-determined deflection at a constant position. This system incorporated a relatively large inertial mass for high-frequency stability, and an ultra-low friction pivot arrangement. The thrust balance was capable of balancing 220 μN with an expanded uncertainty of 3.3 μN .

2.2.5 Material property research

In the advanced materials team at NPL, complementary capabilities incorporating force measurement have been developed to assist directly with the characterisation of material properties.

Aside from atomic force microscopy, covered in the next section, the area of interest of most significance for the development of sub-newton force metrology is instrumented indentation, for which NPL has a long-established capability [53, 54].

Much can be learnt about a material by producing an indent in a sample through the application of a known force with a tip of known shape [55]. Traditionally, the tip was removed, and the indent dimensions measured optically. Instrumented indenters differ somewhat from this traditional approach, in that the vertical position of the tip is continuously measured as a calibrated force actuator pushes the tip into the surface.

This approach offers clear advantages in terms of continuous measurement, higher resolution and repeatability, to the general benefit of advanced materials understanding.

The range of force and motion supported by each type instrumented indenter varies, and these ranges are somewhat arbitrarily demarcated into indenters, microindenters and nanoindenters. Typical commercial suppliers of nanoindenters include Agilent Technologies, Asylum Research, Bruker AXS, Hysitron and MTS Systems [56, 57, 58, 59, 60]. In addition, the mechanism by which the indenter force is produced and the displacement measured varies, in accordance with the expected operating range. One option (see figure 2.1) is to use a large flexure guide, electromagnetic coil force drive and capacitive displacement sensor; an alternative employs a modified AFM arrangement to achieve the indentation.

Regardless of the technique employed in the indenter, the result is a system aiming to apply a known force through a tip of known vertical displacement. To do this, the indenter must be calibrated. One option is to indent samples of well-characterised materials, and back-calculate the applied force from the observed indent, having previously calibrated the displacement scale with a step-height standard. Such an approach is not very repeatable and leads to a necessarily 'discrete' calibration curve. It would be better if the force could be calibrated directly using a calibrated reference sensor, such as a low force artefact. The vertical spring constant of each indenter mechanism is chosen for compatibility with the force and displacement ranges of the instrument itself, which are in turn optimised for the expected surface contact stiffness values to be encountered. Commercially available indenters provide exemplary values for spring constant in the range 1 kNm^{-1} to 10 kNm^{-1} . Whilst the lower end of this range is most applicable to the low force regime, indenters nevertheless represent the stiffest typical target of traceable low force calibration. The range of force covered by

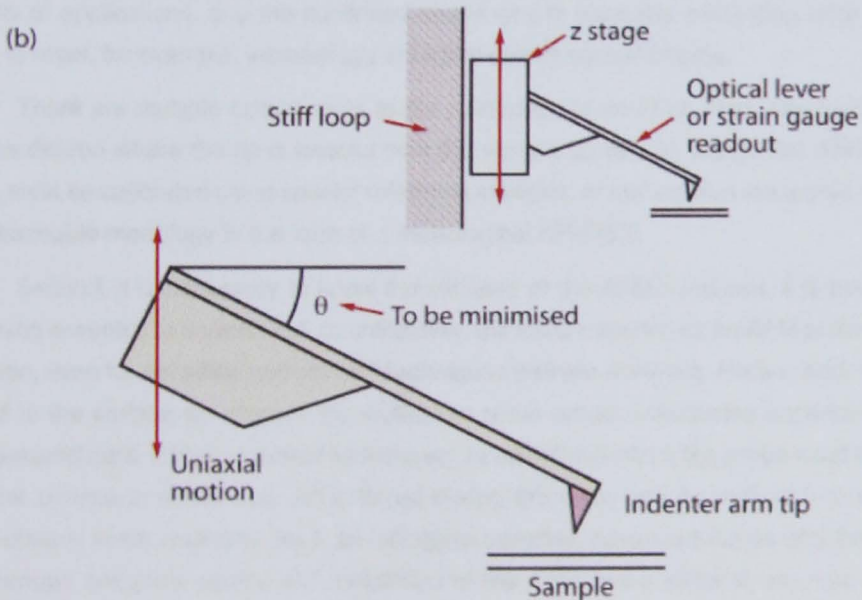
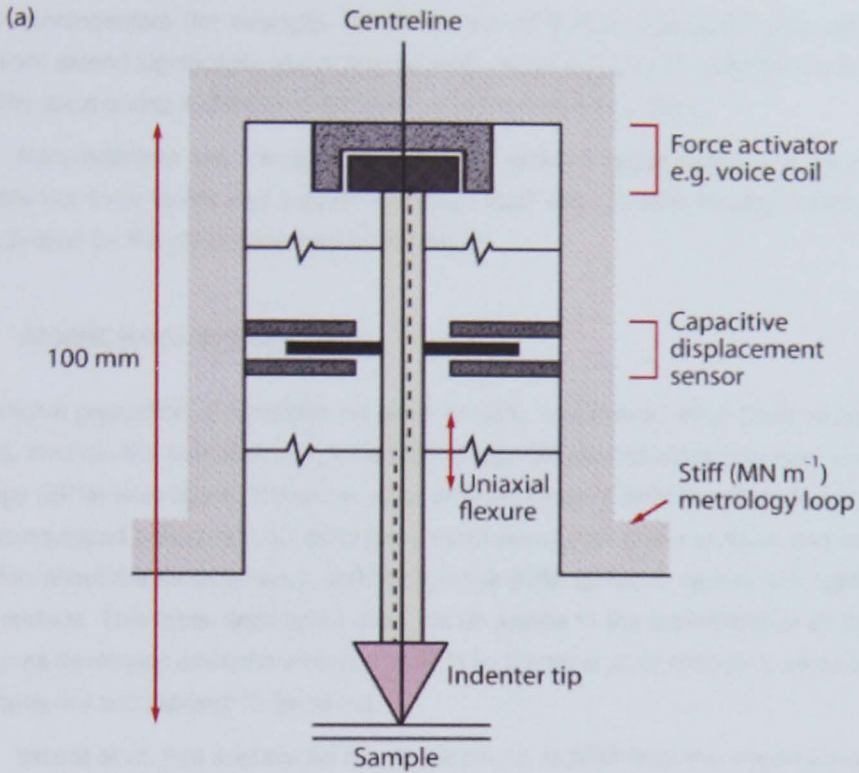


Figure 2.1: Two key types of instrumented indenter suitable for traceable low force calibration: (a) electromagnetically actuated, capacitively-monitored macroscopic precision flexure design; and (b) modified atomic force microscope.

typical nanoindenters (for example, 10 mN for the MTS NanoindenterXP [60], with 1 nN resolution) extend significantly above the low force range, but one could imagine a low force capability augmenting a cheaper millinewton-scale calibration system.

Nanoindenters are therefore an extremely relevant target instrument sector for a traceable low force facility and support of related local effort at NPL directly contributed to the motivation for the effort described in this report.

2.2.6 Atomic force microscopy

A significant proportion of Materials research at NPL, and indeed other fields at NPL and beyond, involves the use of atomic force microscopy (AFM) and other scanning probe microscopy (SPM) techniques. There are many different types of SPM but all involve scanning a stylus-equipped spring (almost exclusively cantilevers) over a test surface, and using information about the instantaneous deflection of the AFM spring to deduce the topography of the surface. This facile description does not do justice to the sophistication of the AFM techniques developed since the invention of AFM by Binnig *et al.* in 1986 [61]; some of these techniques are summarised in figure 2.2.

Yacoot *et al.* [62] summarise the development of AFM from the dimensional nanometrology perspective. The authors note both the widespread appreciation of SPM for a diversity of applications, and the continued challenges in traceably calibrating such instruments to meet, for example, increasingly stringent quality control criteria.

There are multiple components to the calibration of an AFM. First, one must know to some degree where the tip is located over the sample surface in $\{xyz\}$. The AFM stage scales must be calibrated using special reference samples, or the location measured directly using traceable metrology in the form of a metrological AFM [62].

Second, it is necessary to know the stiffness of the AFM cantilever. It is becoming increasingly essential to understand, quantitatively, the force imparted by an AFM probe under operation, even for so-called non-contact techniques that are nominally force-nulled. A force applied to the surface will change the surface to some extent, introducing uncertainties to the measured data. For non-contact techniques, to track the surface the probe must interact with that surface in some way. Peak forces during the cycle can be sufficient to permanently deform softer materials such as biological samples, advanced foams and aerogels. Only through adequate choice and calibration of the AFM probe stiffness can this risk be appropriately mitigated.

Thirdly, the metrology for the deflection of the probe tip must be calibrated or characterised. In the case of deflection-nulled techniques, including phase-locking techniques, it

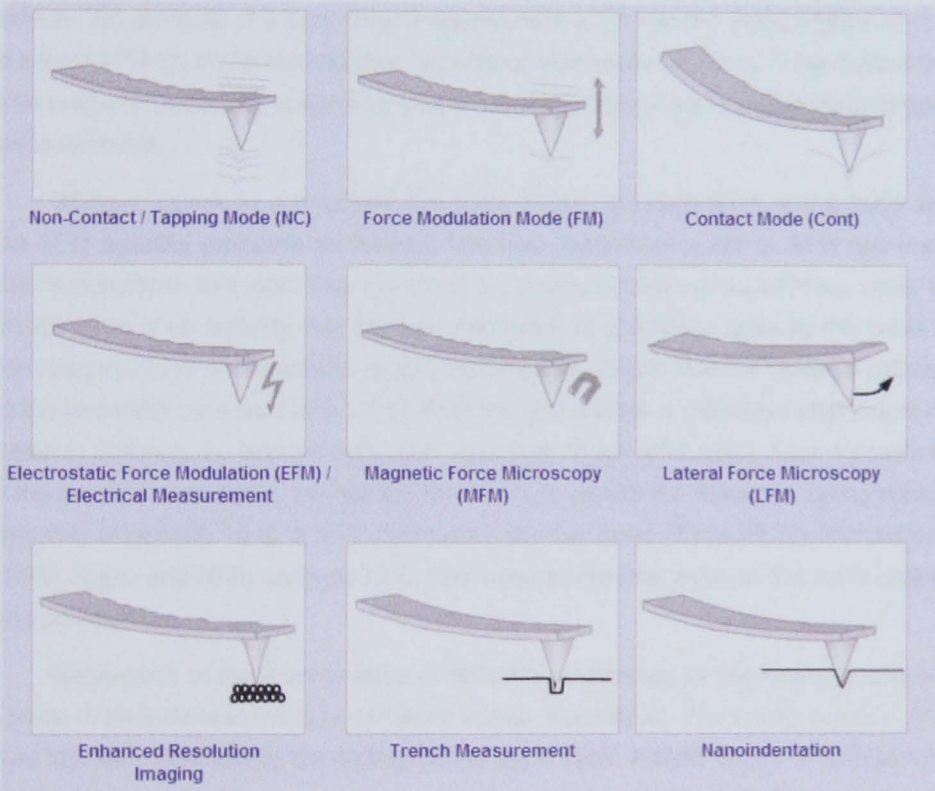


Figure 2.2: Various AFM techniques [3].

may be sufficient to verify the long-term stability of the deflection analogue, perhaps as part of a wider characterisation of the instrument's mechanical stability. For contact-mode AFM, the deflection output would need to be fully calibrated against some traceable reference. Common deflection sensors include optical levers and piezoresistive strain gauges.

To use an AFM as a force sensor, or otherwise to understand the force being applied to a scanned surface, one can either combine the calibration of the deflection metrology with that of the cantilever spring constant, or calibrate the deflection analogue directly in terms of applied force rather than induced deflection: force sensitivity, in place of displacement sensitivity. An example of a pure force measurement would be the manipulation of CNTs with a fixed AFM tip, or the manipulation of proteins (see section 2.4.1.5). If the applied force can be measured traceably, a significant barrier to traceability of measured material property value is removed.

Without access to a traceable low force facility, the calibration of the force scale of an AFM typically proceeds as follows. The user purchases a set of AFM tips from a probe manufacturer to install. The tips carry a manufacturer-specified stiffness value with some measure of uncertainty over the expected range of operation. Typically this value has some obscure claim of traceability, or the manufacturer states that the value is estimated from the geometry (see section 5.1.2.1). With the tip installed, a calibrated step height may be used to calibrate the internal deflection metrology of the AFM head. From Hooke's law, and the displacement signal, the applied force can be calculated. Since the spring constant uncertainty of typically 10 % to 20 % dominates, the key focus of traceability improvements for SPM users, and NMIs such as NPL, has been to develop ways to traceably calibrate spring constants.

Regardless of the internal force or deflection metrology, or the mode of operation, the probe of an SPM is essentially a uniaxial flexure, a cantilever. The spring constant of this flexure can vary significantly depending on the application. A brief review of commercially-available AFM cantilevers, for example, reveals a spring constant range from 0.1 Nm^{-1} to 100 Nm^{-1} for standard applications.

It is not the intention of this thesis to belittle the impact of the great body of SPM research published to date, nor that of instrumented indentation, despite the lack of SI force traceability. The demonstrated resolution and repeatability of such systems is sufficient to allow informative comparative material property measurements and the refinement of theoretical descriptions. Increasingly however, the function (and hence quality control) of micro- and nanofabricated devices rely on the traceability of such material property measurements. Hence, both areas are key targets for low force traceability and motivated the described work.

2.2.7 Dimensional measurement

The measurement of force is also extremely important for the development of traceable, low uncertainty dimensional measurement on the 100 μm range, 1 nm resolution scale. The NPL low force facility explicitly supports advances in surface metrology and micro-coordinate metrology within engineering nanometrology.

Significant uncertainties associated with the operation of high-end stylus surface texture measuring instruments, such as NPL's Nanosurf 4 (the primary profile measuring instrument) [63] and the Areal instrument (the primary areal surface topography measuring instrument) [64] originate in the continuous nature of the various interaction force fields that define, on the nanoscale, surfaces that appear discrete on the macroscale. See appendix A for a discussion of these forces. These force fields provide the mechanism of ideal operation of non-contact measuring techniques, in which proximity of the probe to the surface induces a detectable change in, typically, the resonant characteristic of the probe.

NPL has developed [4] a micro-coordinate metrology probe based on a patented non-contact vibrating sensor, to augment the resolution and application of micrometre-scale coordinate measuring machines such as the Zeiss F25 [65]. The F25 uses a touch probe equipped with a 300 μm diameter sapphire sphere to measure the dimensions of small components to 250 nm MPE within a volume of 100 mm \times 100 mm \times 100 mm. This versatile instrument nevertheless applies significant forces (up to 300 μN) to the sample and damage is sustained in many samples. NPL's probe is, in contrast, designed to impart negligible probing forces under vibrating non-contact operation. The NPL Low Force Facility will be used to verify this quantitatively. The non-contact operation will also assist in the avoidance of 'snap-in' adhesion by the approaching probe, an effect that not only affects obtained measurement data but can, in some circumstances, prove catastrophic for the probe tip or sample on the subsequent 'snap-out' transition.

Non-contact operation of this probe implies some sort of finite, fixed standoff maintained over the course of the measurement by feedback control. Both the effective tip radius created by this non-contact operation, combined with the definition and stability of the surface arrival threshold involved, imply the need for accurate, traceable force metrology.

The NPL microprobe uses a piezoelectrically instrumented nickel 'triskelion' flexure as shown in figure 2.3. The triskelion is equipped with a rigid tungsten stylus with monolithic tip, forming the surface interaction point. $\{xyz\}$ motion of the tip maps to $\{\theta_x, \theta_y, z\}$ motion of the triskelion centre, and vice versa. Motion is generated at the outer edges of the triskelion and induced perturbation to that motion, in proximity to the sample, is sensed on adjacent elements.

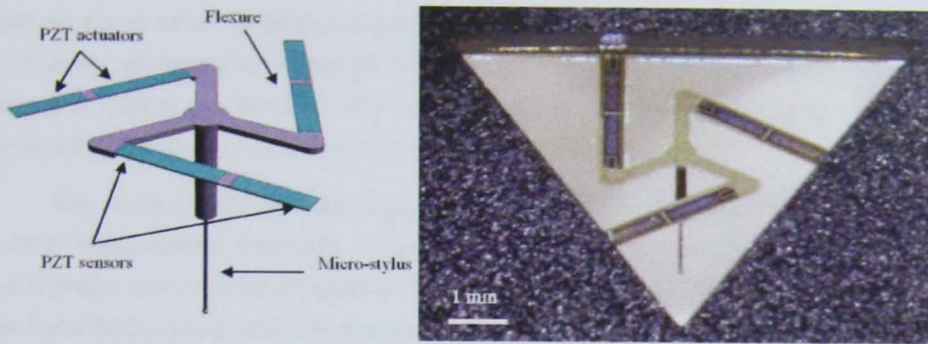


Figure 2.3: Schema of NPL microprobe and an image of a fully assembled device (from [4])

Based on the weight of local applications alone, as summarised above, the motivation for the development of a traceable low-force measurement capability was clear. The initial development of this capability, prior to the direct involvement of this author, will be discussed in the following section.

2.3 A direction for traceable low force metrology at NPL

When developing a primary standard with the lowest possible uncertainties, the key to success is usually simplicity. A simple operating principle implies a simple propagation of uncertainties – and a limited set of sources in the first instance – and a more well-defined (and hence lower) total uncertainty in the realisation of the unit associated with the instrument's purpose.

The simplest realisation of a unit of force, at least on the macroscale, is the weight of a known mass. Since local gravitational acceleration may be determined very accurately (see section 2.4.1.3), a constant mass can produce a very constant reference force in the form of weight. For very small forces however, below $10\ \mu\text{N}$, contamination causes the assumption of constant mass in a mass artefact to break down significantly. Furthermore, the weight of small masses is tied to the orientation of gravity and such artefacts offer no advantages over other more sophisticated microscale force sensors in terms of ease of handling. Indeed, the need to completely disengage from a mass artefact to realise its calibrated weight, as well as to calibrate that weight, necessitates many repeat measurements and statistical analysis to minimise the effects of force spikes that occur during on-off contact transitions. Finally, small mass artefacts necessarily produce a set of discrete, fixed force values, limiting their application in continuous force sensing applications.

Therefore, NMIs seek to realise their definition of the newton in the low force regime

based on some other continuous principle. Practical considerations have resulted in the use of either electrostatics (bespoke instrument) or electromagnetism (commercial mass balance) to generate a force to balance the input test force. A control system is used to maintain dynamic force equilibrium and enable traceable comparison.

The range of force, range of application and range of user requirements for traceable low force measurement are broad. In general, higher instrument or sensor performance has an associated cost in terms of practical usage of that instrument. NPL undertook to produce a low force facility with performance and uncertainties approaching that of the NIST vacuum-operated facility (as will be discussed in section 2.4.1), but with the more rugged nature and accessibility of the then-fledgling PTB facility. In this way NPL would be best placed to meet the requirements of internal users and wider UK industry.

The proposed strategy was therefore to develop an air-operated electrostatic force balance, after the NIST precedent, operating down to one nanonewton, and further to produce practical, high-performance, affordable artefacts to transfer traceability to users. Further, NPL would design its artefacts in order to overcome key uncertainties associated with precedent artefacts, and ultimately offer a step-change in performance for the same level of useability. The implementation of this strategy will become clear in the remainder of this thesis.

2.3.1 Status of the NPL low force facility at the outset of this project

At this juncture it is appropriate to define the start-point for this thesis in terms of development of the low force facility. Broadly speaking, the NPL low force facility has two intended components: the LFB, and a collection of transfer artefacts to facilitate the link between the LFB and potential users of a calibrated low force facility.

At the outset of this project, the mechanism of the LFB had been designed and produced, in collaboration with a key industry partner, and initial characterisation work undertaken. Initial consideration of vibration isolation was underway but no formal steps had been undertaken other than to site the LFB in an environment with low mechanical and acoustic noise, and to install an acrylic draught shield around the LFB.

A simple FPGA-based PID controller had been written to provide null-position feedback based on a single-fringe intensity lock interferometer operation. A full fringe-counting interferometer had not been implemented. A basic procedure had been developed to measure the capacitance gradients of the balance, but full characterisation of linearity and stability had not been undertaken. Initial results had been obtained based on small mass artefacts

[66], but subsequent work undertaken by this author casts doubt on the uncertainties associated with the results. In chapter 3, key improvements to the LFB made by this author will be discussed in more detail.

At the outset of the project, no work had yet been undertaken towards a candidate low force transfer artefact. The development of low force transfer artefacts at NPL by the author is described in this thesis in detail.

2.4 Precedent for the NPL low force facility

The development of the NPL low force facility has continued against a backdrop of complementary small force facilities at other NMIs worldwide. Significant capabilities developed at NIST, PTB, KRISS and, latterly, at CMS-ITRI, will be introduced below.

Kim and Pratt [17] thoroughly reviewed these capabilities; however, for the purposes of this narrative the most pertinent details of international efforts to date will be summarised in this section.

Each NMI's endeavours represent a response to the same motivation, domestically and internationally. Political aspects aside, it may appear unnecessary to duplicate the same capability at different NMIs. The metrological argument for duplication is subtle but important. Each facility functions as the primary realisation of a measurement, based on first principles. With an uncertainty budget developed, the instrument should stand alone at the top of the traceability tree for that unit. It is naïve to assume that all uncertainty sources can be properly identified and quantified, and it is equally naïve to assume that the physical principle used to define the unit can be implemented without flaw.

Parallel, complementary, primary facilities are therefore essential for confidence in the traceability infrastructure. A key activity of NMIs is to carry out suitable intercomparisons of facilities, with formal instances registered on the BIPM key comparison database (KCDB). A by-product of this undertaking is that facilities from different countries (NMIs) can be considered equivalent subject to individual uncertainty budgets, supporting the principle of the mutual recognition arrangement (MRA). Two such examples to which this author has contributed are: a comparison of the NPL mass traceability route to the NIST electrostatic force traceability route for low forces [33]; and an international comparison of low force balances using a commercial piezoresistive cantilever [34].

2.4.1 Primary balances

Two distinct bases for a primary force balance have emerged. Bespoke electrostatic force balances, produced by NPL and NIST, and latterly at PTB, are considered first. Primary force balances traceable through mass and derived from commercial precision mass comparators at PTB and KRISS are also considered. Finally, alternative force balances of varying degrees of suitability are considered.

2.4.1.1 Electrostatic force balances

Overview The last century's advances in electromagnetic theory and electronic engineering have permitted highly attractive alternatives to dead-weight force production. Electronically generated forces are continuous, range tuneable, and may be pre-conditioned to minimise the effect of noise sources and systematic effects, resulting in excellent signal to noise ratios and repeatability. In fact, almost all modern active mass balances are realised as mass-calibrated electronic force producers, as will be discussed later.

But with careful design, an electronic force producer may be made intrinsically traceable. Given suitably defined geometry, the electrostatic force in a capacitor or the electromagnetic force in a voice coil may be calculated extremely accurately, in terms of the volt, farad or ampere. These units are in turn traceable to fundamental constants of nature, as shown in figure 2.4. This means that, in principle, uncertainties can be decreased arbitrarily, and traceability is not reliant on a changeable kilogram. The technical approach and more philosophical motivation for an electronic newton relate to the Watt balance [67, 68, 69] and the redefinition of the kilogram, the volt balance [70], and the general trend to redefine the SI units and their hierarchy in terms of fundamental constants of nature [71].

Directly traceable force production was therefore a good candidate for incorporation into a primary low force balance design. The removal of the need for mass calibration (though admittedly usefully retained as a method of intercomparison) allows an arbitrary force axis vector and removes the need to align the balance mechanism to the direction of gravity.

For a force balance for force measurement, an arbitrary electronic force is generated to establish force equilibrium, monitored by deflection against a traceable fixed displacement scale, and the input electrical driving signals (voltage, current) are measured using instruments traceable to quantum standards. Values for additional quantities in the force generation equation, such as capacitance or displacement, are similarly measured. As shown in figure 2.4, the LFB is ultimately traceable in terms of the speed of light c , Planck's constant h , the electronic charge e , and repeatable behaviour of the caesium atom. The generated

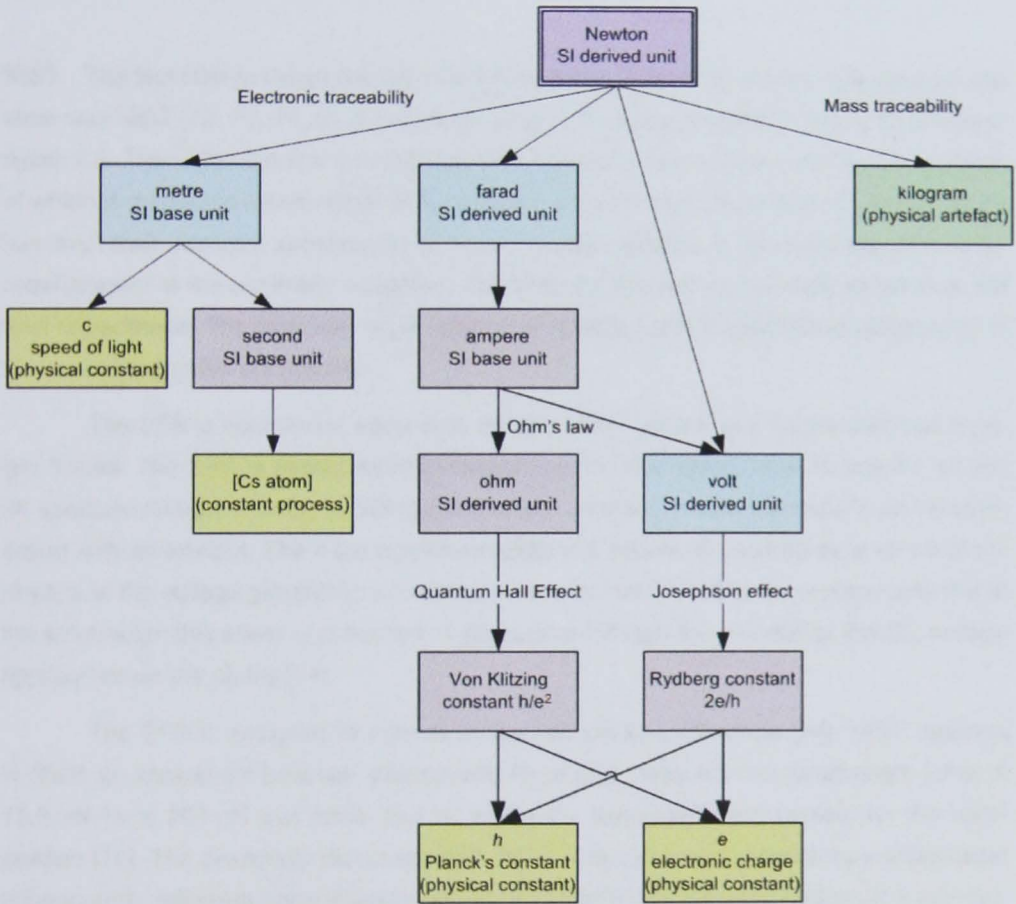


Figure 2.4: Traceability of the newton to fundamental constants of nature, in terms of practical realisations in which base units may be dependent on derived units.

force is calculable *via* a form of the equation

$$F_{el} = \frac{1}{2} \frac{dC}{dx} V^2 \quad (2.1)$$

which gives the force F_{el} along x between two capacitor plates with mutual capacitance C under an applied voltage V . See chapter 3 section 3.1 for a more detailed explanation of this equation for the LFB.

NIST The first NMI to report the use of a force balance based on a calculable electrostatic force was NIST [72, 73, 74, 5]. A number of design iterations resulted in the EFB, shown in figure 2.5. The EFB contains a nested cylinder capacitor, the relative coaxial plate position of which is measured interferometrically. Concentric cylindrical plates with separation much less than their diameter approximate to a parallel plate system. It can be shown that radial misalignment of the nominally concentric cylinders contributes a non-linear variation to the total capacitance. The relatively large balance is modular, with the benefit of adaptability at the cost of alignment uncertainty.

The EFB is operated in vacuum to remove water vapour and hence minimise capillary forces. The EFB is almost entirely coated in a metallic (gold) layer to provide an exit for spurious charge, thereby avoiding electrostatic parasitic forces, particularly on an interaction with an artefact. The most significant additional source of uncertainty in terms of the physics of the voltage generation and balance mechanism relates to the surface potential at the electrodes; this effect is cancelled by procedure through the reversal of the DC voltage applied across the plates [74].

The EFB is designed to operate in the 200 μN to 1 nN range [74]. NIST reported in 2006 an agreement between electrostatic force and mass-artefact deadweight force of 13.3 nN for a 200 μN test force, that is, within the expanded uncertainties for this comparison [75]. The previously discussed NPL-NIST mass-force comparison was undertaken subsequently following some adjustments at NIST and led to the identification of a key systematic error due to a new artefact manipulation stage (see [33] and section 3.9).

PTB Since the initiation of this thesis PTB have developed a somewhat divergent design of electrostatic force balance using a pendulum, rather than a flexure, as a means of transducing any force inequality into a measureable, nullable displacement error [76, 77, 78, 79]. This balance is designed to facilitate the calibration of quasistatic forces below 1 μN with a resolution of 1 pN, and as a consequence of the resolution target has more stringent environmental specifications associated with it. For example, vacuum operation is mandatory

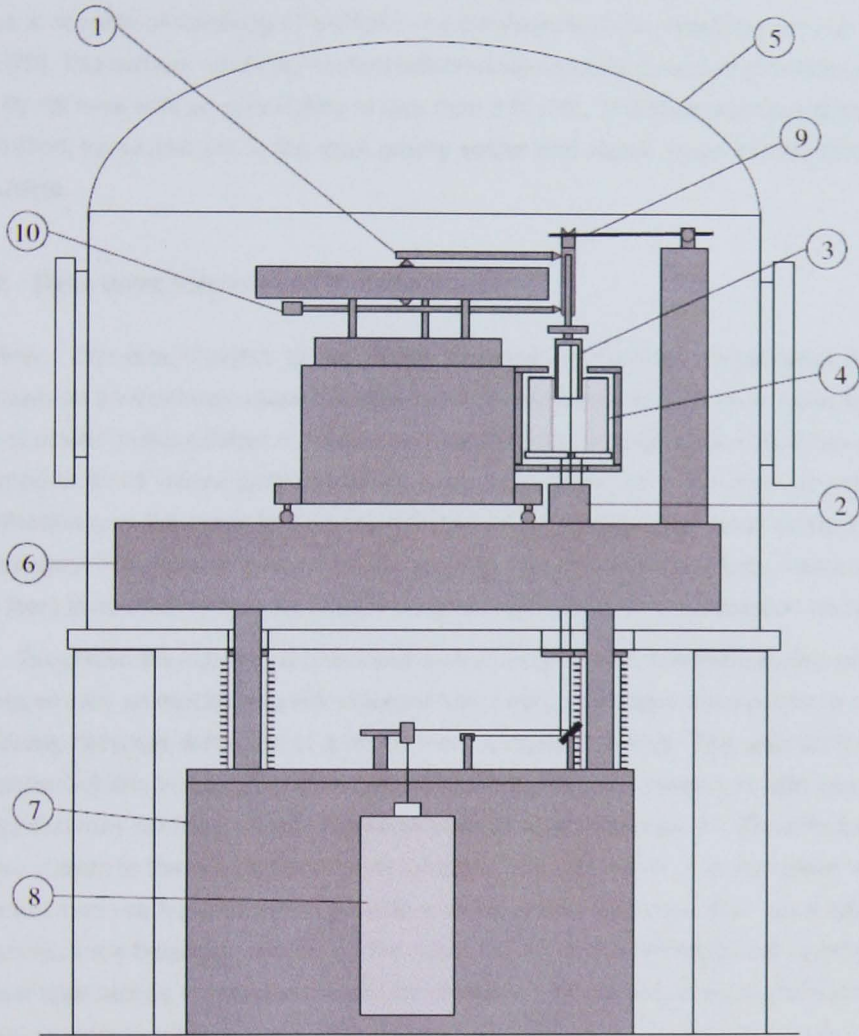


Figure 2.5: Schematic diagram of the NIST EFB, from [5]. Labelled components are as follows: Schematic of balance components: (1) parallelogram balance, (2) differential plane mirror interferometer, (3) main inner electrode (cross-section), (4) main outer electrode (cross-section), (5) vacuum chamber, (6) optical table, (7) granite foundation block, (8) heterodyne laser light source, (9) mass lift and (10) counterweight.

for this instrument, but merely recommended for the NIST balance. The PTB balance does incorporate features such as a secondary pendulum for tidal and seismic input reference, as well as a novel method for effective balance stiffness reduction through prescribed driving of the internal electrodes. Both features increase the force resolution of the balance. The balance is capable of resolving 47 pN forces as demonstrated via radiation pressure experiments [78]. The authors report agreement between electrostatic force and gravitational force at the 80 nN level with an uncertainty of less than 3 % [79]. The force interface direction is, by definition, perpendicular to the local gravity vector and hence mass intercomparison is not possible.

2.4.1.2 Mass comparator-based force balances

Overview The dissemination of traceability for mass measurement is facilitated by a device known as an electronic mass comparator, more commonly known as a 'mass balance' or 'set of scales' in the context of home use. Low to medium performance balances are implemented as a stiff flexure deflected by the load to be measured. A strain gauge measures the deflection and the mass is calculated based on pre-determined linear scaling factors and displayed. This approach must also be used for precision dynamic force measurement, where there is insufficient time for lengthy mass compensation and stabilisation routines.

To achieve the highest precision and lowest uncertainties, commercial ultra-precision balances employ an electromagnetic drive (or 'voice coil') to balance the input force and null the optically-detected deflection of a much more compliant flexure. This approach is illustrated schematically in figure 2.6. The deflection of the flexure is measured using an optical indicator that may not have a linear response outside a narrow range. A PID controller alters the drive current to the actuator coil so as to cancel any deflection. The gain parameters of the control loop are typically set to provide a much slower response than associated with electrostatic force balances, relying on the static nature of the intended load (a mass) and statistical approaches to mitigate the effects of noise. The coil would be equipped with temperature sensors to track, and possibly counter, a temperature rise due to actuation of the coil.

It follows that such comparators may be used as force balances, for the calibration of cantilevers and similar. Figure 2.7 gives a schematic overview of example balances from PTB, KRIS and CMS-ITRI. The artefact to be calibrated is pressed, using a secondary vertical stage, onto a special point or sphere platen on the balance pan. The recorded 'mass' and artefact sensor output may be used to determine the force sensitivity. Since this type of balance actively maintains a fixed platen position, if the vertical position of the artefact substrate (and hence the artefact's deflection) is also known, an artefact spring constant may

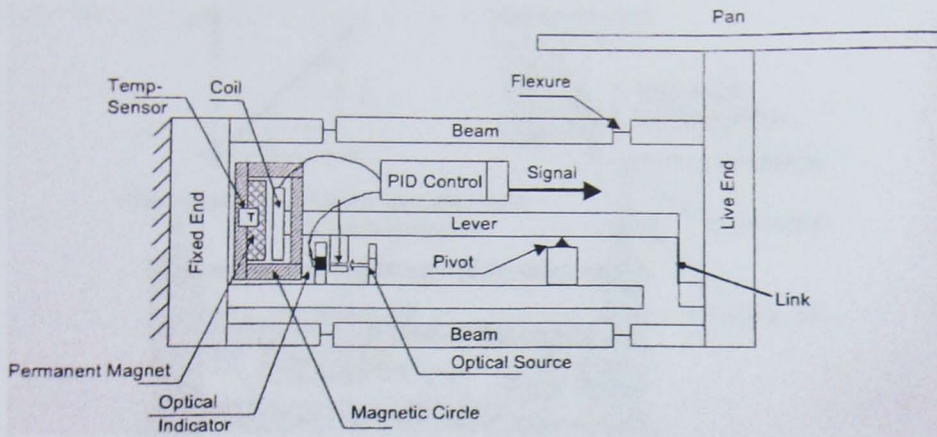


Figure 2.6: Comparator mass balance schematic diagram (from [6])

be derived. Alternatively, an additional compliant component may be inserted into the force chain, forming a 'displacement divider' such that the force step associated with the resolution of the secondary stage is much smaller. Note that, of course, such a divider system would be applicable to any balance. Comparator balances typically achieve displacement (and hence force) equilibrium after one to ten seconds, and therefore whilst relatively insensitive to high-frequency oscillations are slow to operate.

Nevertheless given a pre-existing suitable operating environment, such balances are straightforward to commission and exploit the development effort of the relevant commercial supplier. This is important for metrology institutes for whom scientific ideal must be tempered by a relative lack of development resource. The caveat is, of course, the need for reliance on proprietary IP and the associated quality systems.

PTB PTB has developed a number of mass-comparator force balances for the calibration of force sensors, though all but one operate in the force regime above that considered in this thesis. The PTB 12 N and 2 N balances are intended to facilitate the calibration of force transducers to ISO 376 [80, 81, 82]. ISO 376 was developed for macro-scale force transducers but could in principle be applied to the smallest force sensors. The incorporated feedback control of the balances is able to stabilise force down to $\pm 1 \mu\text{N}$.

The PTB Micro-force Measuring Device has an operating range of 50 μN to 400 mN, employing a 41 g capacity Mettler SAG245 mass comparator with 0.2 μN equivalent resolution [83, 84]. The PTB Nanoforce Measuring Device has an operating range of 10 nN to 20 mN, employing a Sartorius SC2 mass comparator with 1 nN equivalent resolution [84]. A 100 μm PIFOC precision stage is used in each to deflect the sensor under calibration. These

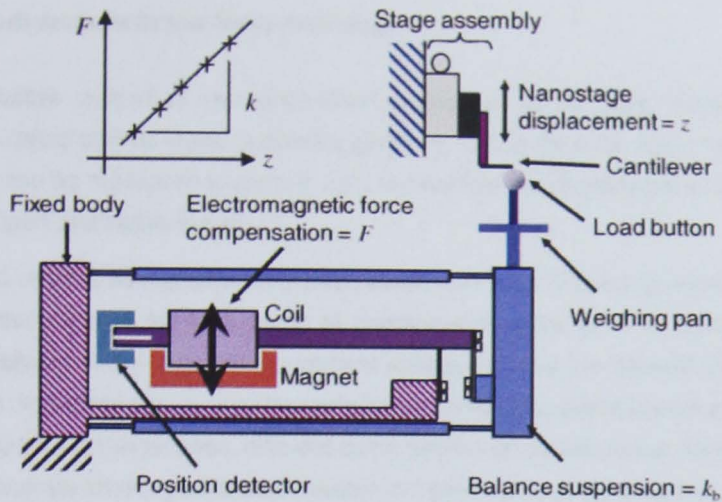


Figure 2.7: Schematic overview of the mass comparator primary force balance concept.

systems have been used for the determination of spring constant and force sensitivity of a commercial piezoresistive AFM cantilever, a vibration sensor [83], V-shaped cantilevers [85] and a PTB cantilever-type force sensor [16].

KRISS The KRISS small force facility targets the force range from 500 nN to 100 μN , that is, within the scope of this thesis. The facility is based around the 'nano-force calibrator' (NFC), derived from a 5 g mass comparator (Mettler-Toledo UMX-5) with an equivalent resolution of 1 nN. The NFC is intended to facilitate traceable calibration of the spring constant, and force sensitivity where applicable, of AFM cantilevers and force sensors in the range 0.01 N m^{-1} to 100 N m^{-1} . Demonstrative calibrations have been reported [86, 87], with associated relative standard uncertainties of better than 1 %. The NFC contributed to a local comparison of methods to calibrate the spring constant of AFM cantilevers [88].

CMS-ITRI In recent years, the Taiwanese NMI has developed a broad sub-newton facility with an emphasis on practical application of established techniques [89, 90, 91, 92]. The facility includes the Nano Universal Testing Machine, a tensile force instrument operating below 500 mN; a nanoindentation system calibrator based on a Mettler-Toledo UMT5 balance; and, most recently, a promising prototype electrostatic force balance [91]. The group have developed a torsion pendulum balance for the measurement of horizontal gravitational forces below 50 nN with a target resolution of a few piconewtons. The balance incorporates active damping based on radiation pressure from a 1.3 W Nd:YAG laser with interferometric displacement monitoring [92].

2.4.1.3 Small masses in low force metrology

The most intuitive method of force production makes use of the Earth's gravitational field acting on an object of finite mass: a deadweight force. Since the local value for gravitational acceleration can be measured to parts in 10^9 , in principle the deadweight would produce a very well-defined and stable force².

Dead weights have traditionally been used, and are still used routinely, for maintaining force traceability in the millinewton to meganewton range [64]. Traceable calibration below the kilogram of any mass measurement device, such as the derived force measurement devices discussed above, must be undertaken using the process known as 'subdivision from the kilogram'. In this process, different combinations of calibrated sub-kilogram masses are used to generate arbitrary calibrated masses in a process analogous to the use of coins in transactions. The process accumulates uncertainty with each division, limiting the extension of the scale, and ultimately limiting the usefulness of mass artefacts intended to generate small forces. The trend is for the relative uncertainty to increase in inverse proportion to the decrease in mass [48], with maximum uncertainty over the LFB working range reached at 1 nN deadweight force. For the calibration of a mass comparator intended to be used to measure a 1 μ N force with a resolution of 10 nN, a traceable mass artefact of 1 μ N weight would be required to preserve SI traceability of force via the mass route. Below 10 μ N, handling difficulties and contamination lead to high relative uncertainties in weight measurement. For example, a 2 μ g mass, equivalent to a weight of approximately 20 μ N, can most practically be formed from a length of fine gauge wire of length around 10 mm [33].

In this force range, small mass artefacts are no more robust or immune to contamination than equivalent MEMS devices. Moreover, such mass artefacts lack the mechanical tether to a larger substrate of a MEMS artefact and consequently are troublesome to manipulate. Aside from practical issues of designing automated lifters that will not 'drop' the artefacts despite disruptive adhesion forces, it is typically extremely difficult to smoothly and repeatably land a mass artefact as required for calibration. In this author's experience, demonstrative experiments to calibrate a cantilever with a similarly-dimensioned mass artefact resulted in repeatabilities of around 20 %, and the technique was not used further.

Mass artefacts have further disadvantages when considered as low force transfer

²High specification absolute gravimeters available have quoted accuracies on the order of $2 \times 10^{-8} \text{ ms}^{-2}$ (see for example [93]). The average local value for gravitational acceleration is highly dependent on latitude, altitude and proximity to massive objects, in order of significance, but has been modelled to below the accuracy of available gravimeters [94]. Local gravitational acceleration varies predictably at the part in 10^7 level due to solar and lunar tidal effects. Calculations undertaken for shipping applications [95] suggest a lunar tidal variation amplitude in g of 1.1×10^{-7} and a solar tidal variation amplitude in g of 0.52×10^{-7} ; the latter component varies itself by about 3 % annually due to the elliptical nature of the earth's orbit.

artefacts. Their associated weight is tied to the local vector of gravitational acceleration. The forces produced are discrete, rather than continuous, and the adjustment of the applied force requires significant disturbance of the measurement vicinity, including transient force spikes. They do not have a well-defined point of application, no single tip. Finally, and more philosophically, mass artefacts perpetuate the reliance on lumps of matter to define mass, despite the current push toward the redefinition of the kilogram.

Where time allows, however, and given sufficiently clean and tolerant operating conditions, small mass artefacts may be used to ensure traceability via mass, or to compare traceability routes. Ad-hoc manual production of masses has been attempted by investigators at various NMIs over the years, with formal instances reported more recently. KRISS describe a calibrated set of mass artefacts of mass 0.05 mg (0.5 μ N), 0.1 mg (1 μ N), 0.2 mg (2 μ N) and 0.5 mg (5 μ N) for use in the calibration of compliant cantilevers. The relative standard uncertainty of the smallest artefact contributed, at 0.4 %, the largest component of uncertainty in the cantilever calibration [86].

NPL and NIST devised a method to use calibrated mass artefacts to compare the established NPL SI mass scale to the new NIST SI electrostatic force scale [33], and as a result identified and removed a key systematic uncertainty in the NIST EFB (see section 3.9.2). A similar internal mass-force comparison was subsequently undertaken at NPL, as will be described in more detail in section 3.9. It is possible to transfer electronic force traceability via a small mass, by directly measuring its weight using a traceable electronic low force balance. This process, partially demonstrated also by Pratt *et al.* [75], avoids the deterioration in uncertainty associated with sub-division from the kilogram.

LNE produced a calibrated set of artefacts in the range 0.1 mg to 0.9 mg to calibrate the sensitivity, or smallest detectable mass, (rather than the scale) of mass comparators [96]. The reported standard uncertainty of the smallest mass standard of 0.1 mg was 0.06 μ g based on correct usage and storage.

As a consequence of the above mentioned and related work in the metrology community, OIML has produced a specification for commercially-produced calibrated masses intended for clean, high-performance users such as metrology organisations or pharmaceutical companies [49]. The E_1 mass scale in this specification extends down to 1 mg (approximately equivalent to 10 μ N) with an MPE of 3 μ g (approximately equivalent to 30 nN). This MPE sets a lower limit on the uncertainty in the use of such small masses, which is dramatically increased by additional uncertainties as a result of any attempt to actually use the masses.

It is clear then that the use of small masses as deadweight force producers is unsuitable for a practical low force transfer artefact system, and is a non-ideal uncertainty-limiting

necessity in the calibration of mass comparators and in specialist NMI operations.

2.4.1.4 MEMS-based primary force sensors

Whilst the developments reported above show there is still scope for improvement and optimisation of balance topology and performance, macro-scale primary balances are essentially a mature concept. Innovation is focussed on the development of novel transfer artefacts, exemplified by this thesis. The focus of future development of primary balances is now to provide traceable measurement for forces down to the attonewton level to better understand quantum-based forces such as the Casimir force or to characterise devices that manipulate objects with light. A force probe accessible to such experiments would have to be of millimetre size or smaller.

Of course, one could conceive of using a MEMS sensor previously calibrated on a macro balance to measure such tiny forces. However, the uncertainties associated with such a calibration, involving extrapolation through several orders of magnitude of force, would be unacceptably high. Clearly, an inherently traceable device would be preferable. In general, MEMS devices are surprisingly robust because their moving elements have very small masses; the low inertia leads to resilience to mechanical shock, whilst the weight becomes small in comparison with the working forces.

Note that it is already possible to *resolve* forces on the attonewton scale (see for example [97]). However, traceability is only possible at the piconewton levels discussed in this section, and force units associated with reported values below this level must be treated as arbitrary.

Miniaturisation of current macro balances is understood to be restricted by at least two practical aspects [98] that limit the determination of the applied force. The first is an extension of the surface potential challenge observed in the NIST EFB; the second is due to the increasing difficulty of capacitance gradient determination with miniaturisation. NIST demonstrated calculable electrostatic forces nominally from 5 nN to 100 nN with uncertainties at the level of a few percent under the direct calibration of a colloidal AFM probe at the low end of the viable force range [99].

Cumpson *et al.* at NPL previously developed novel comb-drive devices for the calibration of AFM cantilever spring constants. One example, the 'Electrical Nanobalance' device [7], is shown in figure 2.8. A vertical asymmetry in the fields generated in a pair of comb drives levitates a landing stage against an internal elastic element. Measurements of the driving electrical signal and resultant deflection lead to a spring constant value potentially traceable to the SI. At end-use, the device becomes a passive, calibrated, elastic

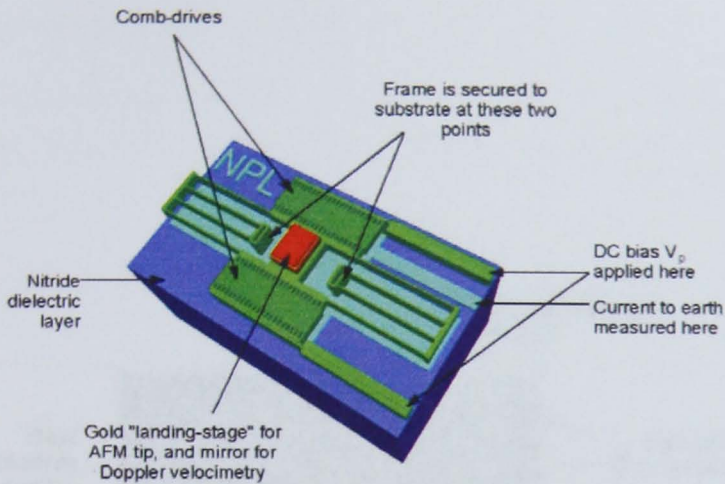


Figure 2.8: Computer model of the NPL electrical nanobalance device. The area shown is $980 \mu\text{m} \times 560 \mu\text{m}$. Dimensions perpendicular to the plane have been expanded by a factor of twenty for clarity. Taken from [7].

device requiring no electrical connections and producing no interacting fields. To convert the Nanobalance to an active device it may be possible to recalculate displacement from the capacitance across the comb-drive. The device is susceptible to stiction in the drives and to the well-known MEMS ‘snap-on’ effect wherein the moving stage catastrophically adheres to the base plate on contact due to van der Waals forces. The authors report a landing stage centre-point spring constant of $0.195 \text{ Nm}^{-1} \pm 0.010 \text{ Nm}^{-1}$ and suitability for calibration of AFM cantilevers in the range 0.03 Nm^{-1} to 1 Nm^{-1} . The device, calibrated dynamically, must be operated in vacuum to avoid dust contamination of the key working elements. A similar technique is used in the same group’s Lateral Electrical Nanobalance (LEN) designed to measure lateral forces such as friction in AFM [8], shown in figure 2.9.

It may be possible, with developments in onboard signal processing, to develop a fully functioning null-servo electrostatic force balance in a MEMS package. Difficulties in altering servo parameters in a chip-implemented servo loop would suggest a limited range of operation. Furthermore, a metrologically stable uni-axial flexure would be required to allow the MEMS and full size balances to each reach their set-points, adding further complexity to such a design. Two interacting servo loops would require appropriate bandwidth matching for successful operation, and that of a MEMS device would not be trivial to tune.

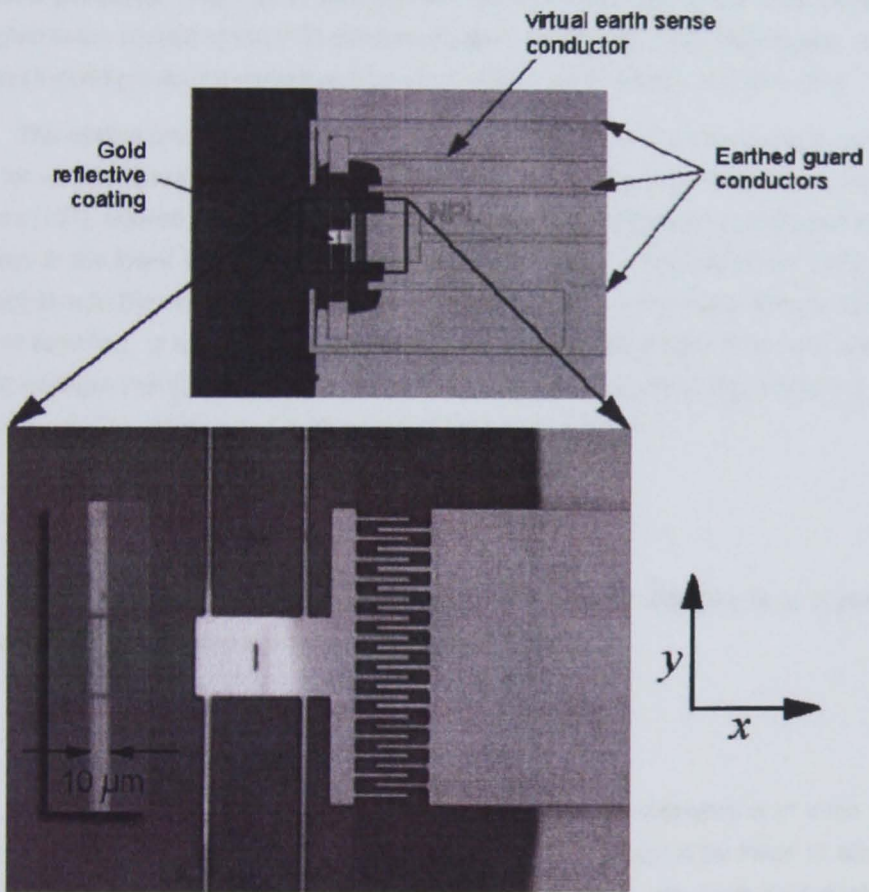


Figure 2.9: NPL LEM for lateral force calibration, from [8]. Inset in the expanded view is a side-on view of the $10\ \mu\text{m}$ thick structure of the device.

2.4.1.5 Alternative calculable force generation techniques

Alternative calculable force generation techniques become practical at very small forces, and in some cases are preferable to macro-scale techniques. Such techniques are considered in this section.

Radiation pressure The use of radiation pressure for calculable small force production was noted in the context of the PTB pendulum balance [100] and CMS-ITRI torsion balance [92], and indeed previously considered by other NMIs including NIST and NPL [31].

The optical pressure exerted by a focussed laser beam is currently under consideration for verification of the lower end of the LFB's force range, adapting similar examples (such as [101], applied in vacuum). This technique could be adapted for calibration transfer purposes at the lower end of the LFB operating force range. A medium power laser would be directed onto the end of the balance platen, to which a very high reflectivity (> 99.99 %) mirror is attached, of suitable size to intercept most of the laser light. From any standard text (for example [102]) the radiation pressure p_{rad} on a surface, reflecting fraction α of the incoming radiation of intensity I , with speed of light c , is given by

$$p_{\text{rad}} = \frac{(1 + \alpha)I}{c}. \quad (2.2)$$

In the ideal case, the force F_{rad} generated on a perfectly reflective ($\alpha = 1$) platen by a perpendicularly impinging laser beam of power W is given by

$$F_{\text{rad}} = \frac{2W}{c}. \quad (2.3)$$

This simple model indicates that, in the best case, a nanonewton of force would be generated by 150 mW of input optical power. Care would need to be taken to eliminate spurious radiometer effects, which would need to be traded off with lower heat dissipation when deciding on the use of a vacuum for operation. Some noise will originate from the effect of particles boiling off the mirror. The design of the NPL LFB combined with operation in position-nulled mode is such that thermal expansion in the vicinity of the platen would have a negligible effect on the measured force. Furthermore, with a high-reflectivity mirror in place the transmitted power would be of the order of a milliwatt or less, acceptable provided exposure times are kept short. Radiation pressure has also been used to manipulate, cool and characterise microcantilevers [103, 104].

SQUIDs: quantised magnetic force Quantum phenomena are now routinely used to define the SI electrical units, so that each unit is defined in terms of fundamental constants of nature.

Other quantum effects may be employed to create an analogous fundamental reference for force. Researchers at KRISS have investigated the use the quantisation of flux through a cantilever-mounted SQUID to produce fixed, well-defined force steps [105, 106]. The deflection of the extremely compliant 0.1 mNm^{-1} cantilever is monitored interferometrically as the applied force changes in device-dependent steps of 184 fN. The minimum force step F_Q is given by the expression

$$F_Q = m_Q \frac{dB}{dz}$$

where $\frac{dB}{dz}$ is the calibrated external magnetic field gradient and $m_Q = \frac{h}{2e}$ is the flux quantum. The system has an estimated capacity of 40 pN. The ability to define the newton on this scale, perhaps facilitated by a precisely (atom by atom) built cantilever and the traceable external magnetic field, would be attractive. Many secondary force sensors or processes to be calibrated could be compatible with the cooled vacuum required for operation. However, it is suggested that a magnetic field strong enough to establish the required uniform 10 T m^{-1} field gradient would be incompatible with many devices to be calibrated. Alternatively, the device could function as both balance and artefact, with the quantum effect used to calibrate the cantilever spring constant and then disabled, relying on the interferometry to monitor the spring deflection under onward calibration.

Protein-based intrinsic force standards At first inspection, the stepped force trace produced when unfolding protein structures such as DNA provide a elegant and readily available source of transfer artefacts for the high-piconewton to low nanonewton range. A single protein is attached at each end to a piezoelectric translator and the force probe of the LFB or target; the former stretches the protein whilst the latter records the tension in the protein.

In principle, once the force step associated with a given protein is 'calibrated' on a low force facility, then any party can produce their own calibrated artefact by following a defined synthesis procedure. It is likely that well-defined, probably artificial protein designs will be specified from the standard biochemistry toolbox, thus creating a range of samples with fixed force steps. Any artificial protein constructs would likely be protected by patent and not remain freely available for use.

Force stepping in biological molecules have been extensively studied by various groups, for example [107, 108, 109]. Apart from artificial constructs, the usual choice of working protein is titin, probably the longest common protein at around $1 \mu\text{m}$ in length [110].

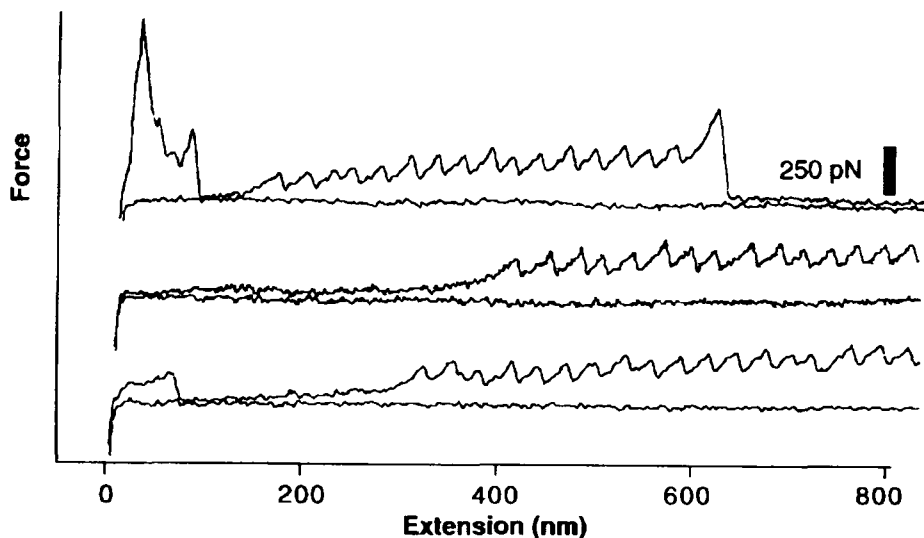


Figure 2.10: Force extension curves obtained by stretching titin proteins show periodic features that are consistent with their modular construction (from [9]). The extension curve in the spacer region preceding the saw-tooth is not well defined and would likely hinder traceability.

Well-defined force steps in the 100 pN to 300 pN range, as protein structures are unfolded in sequence, have been reported (see for example [9]) (see figure 2.10). To demonstrate the measurement bandwidth performance of so-called 'small' cantilevers (length of order 10 μm), Viani *et al.* [10] repeatedly stretched a titin molecule, obtaining extension-force curves as shown in figure 2.11.

From a metrological perspective there are significant problems associated with using protein unfolding in a transfer artefact. The mechanisms for folding and unfolding are not sufficiently understood to put confidence on the repeatability of the behaviour of a protein based 'spring'. A discussion of comparative times of refolding and spontaneous unfolding is presented in [111]. Hysteresis and hence irreversibility is common for large proteins, although not universal [112]. Clearly, one would not be able to isolate one characterised protein molecule and reuse it for each step of a calibration transfer between the LFB and a target; it would be 'lost' between disassembling the LFB-artefact interaction and assembling for the artefact-target interaction. The assumption must be made that all molecules behave alike; this is unsatisfactory for application in a high-accuracy transfer artefact.

The inconvenience of specialist laboratory conditions, equipment and skills required for protein handling, along with the not insignificant challenge of 'installing' a protein onto the LFB platen, would add significantly to the cost and risks for this method.

An alternative, perhaps for future consideration, is the artificial creation of simplified biochemical 'binding-site' structures on two interacting surfaces, with calculable interaction

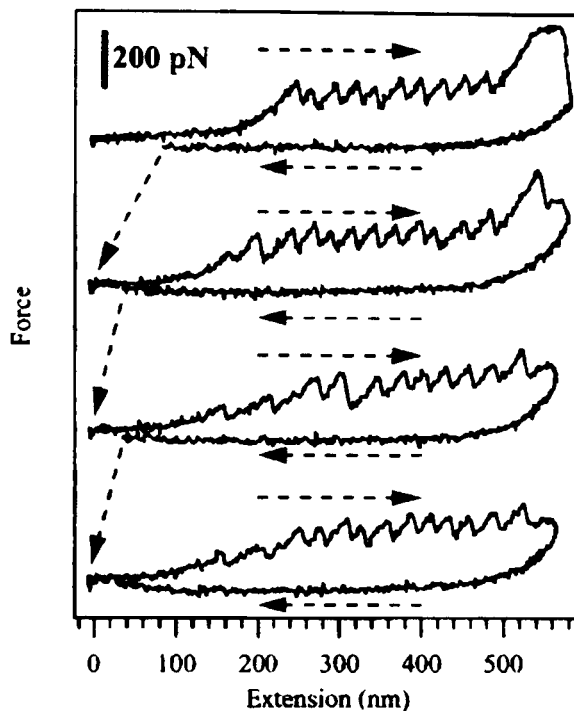


Figure 2.11: Four consecutive extension-force curves on a single titin molecule using a 'small' (length $\sim 10 \mu\text{m}$) cantilever. All extension curves were acquired at a pulling rate of 30 mm s^{-1} to 39 mm s^{-1} , which is an order of magnitude faster than previously performed with conventional cantilevers. System was left at rest for thirty seconds between pulls to allow protein to refold (from [10]).

energies and hence force-separation curves. At the most basic level charge writing [113] could be used, though reliant on expensive bottom-up fabrication techniques; developing further, whole artificial binding molecules could be configured on a surface, preferably in arrays for comparison.

2.4.1.6 Unsuitable force generation techniques

There are a number of force production methods that, superficially, might be considered suitable for a quantised or repeatable low force generation system or balance. Such techniques are considered and discarded in this section. In general the underlying processes are either not fully characterisable, too dependent on environment, or not possible to control sufficiently to follow a prescribed procedure. The techniques might also be considered, for similar reasons, for use in a low force transfer artefact (see chapter 5), but similarly rejected.

Quantum surface forces In this section, methods to utilise forces on the very short range will be briefly considered. These forces, the product of processes explained by quantum mechanics, are typically considered as unwanted additional interaction forces bringing uncertainty to the use of larger forces. See appendix A for a reference of interaction length for each force.

A manifestation of quantum effects within individual atoms, the van der Waals force has been demonstrated in the nanonewton regime using MEMS-scale technology [114, 115]. This range compatibility and the force's ubiquitous nature would suggest the use of the van der Waals force in a force transfer artefact. However, the force only has a useful magnitude under very small separations that are experimentally very difficult to maintain. Interacting surfaces must be very well characterised; clean, uncharged and nonmagnetic, to remove other force production mechanisms; and the operating environmental conditions must be carefully controlled. Usually operation in vacuum is required to avoid effects from particles between surfaces. Specialist equipment would also be required to measure the surface separation, and the traceability of such measurements would likely be very poor. Furthermore, traceable application of the van der Waals interaction requires the determination of the Hamaker constant [116], which varies depending on the interacting materials, to a level of accuracy not currently available.

Considered a macroscopic equivalent of the van der Waals force, the Casimir effect is becoming increasingly important in the development of the ever-smaller, miniaturised components of emerging microtechnologies and nanotechnologies and has been investigated by various groups [117, 118, 119]. The Casimir effect is an outcome of quantum field theory. Applying boundary conditions to the quantum electromagnetic field around interacting bodies reveals a vacuum energy mismatch that manifests as a very small force. The size and direction of the Casimir force depends on interface geometry. As an example of operating range, the attractive Casimir force between two mirrors, each of area 100 mm^2 , placed $1 \text{ }\mu\text{m}$ apart, is approximately 100 nN . The net Casimir effect between a sphere and plate is a repulsive force. Practical experiments using the Casimir effect suffer the same requirements as van der Waals interaction experiments [120] and both would appear impractical and insufficiently understood for a transfer artefact solution compared to the more straightforward alternatives discussed elsewhere in this chapter.

The accurate measurement of these forces implies a mastery of control over the larger forces (that is, capillary and electrostatic) and may be an ideal demonstration experiment for a low force facility. There appears to be little practical use for these effects for transfer artefacts on the proposed scale, however.

Fluid flow and capillary forces Nanonewton forces may be generated by directing a suitable flow of a fluid at a target that deflects that fluid. Force is generated from the change in fluid momentum. To generate sufficiently small forces for use here, the fluid would either need to be very low in density (and hence a gas) or flowing at an extremely low rate. Actuation of an AFM cantilever in a fluid by an acoustic transducer at radio frequencies has been more successfully demonstrated [121] but as a dynamic method is not suitable for this application. Force production by fluid flow is likely to be very noisy, extremely hard to set up, and will produce poor repeatability. It is difficult to see how any platen or working surface could be coupled to the flow of fluid, whilst preventing any interaction with the remainder of the calibration system.

Surface tension in liquids can produce forces in the low force regime (see for example [122]). Indeed the capillary forces generated from condensate forming between a probe tip and sample surface in atmosphere are a common nuisance for the experimenter. Even a monolayer of water molecules can cause significant capillary attraction between hydrophilic surfaces [114]. The sudden and significant 'snap-in' effect as the water layers on two micro-scale surfaces adhere can destroy smaller SPM probes and introduces a significant source of uncertainty in the operation of a precision balance. In the latter case, in this author's experience, the steep force gradient overcomes balance displacement control gain parameters, which are de-tuned to avoid force spikes under normal operation. The result is a significant displacement error excursion, with a force drift cost due to flexure hysteresis. The relative size of these forces might suggest good candidacy for use in a low force balance or artefact. However, the difficulties in establishing the contact surface geometries and separation and hence the liquid surface shape, combined with fluid property changes due to humidity and local surface chemistry, makes force prediction and traceability extremely difficult. These methods are, therefore, completely unsuitable for use in a low force facility. Fortunately provided capillary force issues during contact cycling can be overcome, for example by suitable servo loop dynamic tuning, capillary forces do not contribute significantly to the mechanics of two hard interacting surfaces once contact is made.

2.4.2 Transfer artefacts

The second component of the low force facility is the low force transfer artefact, the device that facilitates the dissemination of the newton to target instruments and processes in research and industry. The current precedent for low force transfer artefacts will be discussed in the context of the review of candidate technologies in chapter 5.

2.5 Conclusions

This chapter has established the context for the development of the traceable low force facility at NPL, considering in particular prior related experience, the chosen direction of development, and the status of complementary activities at other NMIs worldwide. At the time of writing, there are still only a handful of NMIs with any capability to measure small forces traceably, though their collective experience is growing, partly as a result of international collaboration for the benefit of micro- and nanotechnology as a whole.

In the following chapters, modifications to the NPL LFB will be described, as well as a review of low force transfer artefacts and related technologies.

Chapter 3

The NPL Low Force Balance

This chapter introduces in greater detail the NPL Low Force Balance (LFB), the primary realisation of traceable low force in the UK. The design and function of the LFB directly influence and constrain the function of the transfer artefacts that are the focus of this thesis.

The working body of the LFB had been designed and constructed, and a rudimentary control system developed at the commencement of this project. This chapter summarises the development, by this author, of several key components of the LFB to support this project. These included

- the addition of an AC modulation to the basic balance principle to remove previously unanticipated dielectric surface charging effects;
- the development of a full fringe-counting displacement metrology system, adding functionality to the LFB by replacing the existing fringe-locking design;
- the addition of vibration isolation to the LFB and caveats to its use;
- an optimised procedure for the determination of the capacitance gradients in the LFB;
- an unsuccessful attempt to operate the LFB with a reduced number of expensive calibrated DVMS, and an evaluation of this attempt;
- an evaluation of the suitability of the LFB to operate in indentation mode to facilitate the calibration of a wider range of artefacts; and
- the development of prototype platens to allow interaction with the LFB, and the estimation of the resultant effective LFB stiffness.

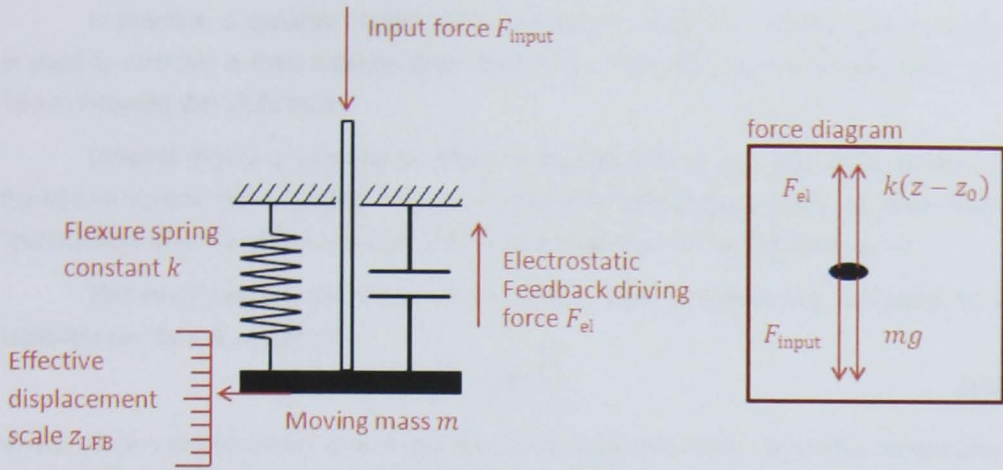


Figure 3.1: The force balance principle.

This chapter also presents efforts to verify the performance of the LFB by comparison with the NPL traceable mass scale, and by international comparison with low force facilities at other NMIs.

3.1 The design of the Low Force Balance

It is prudent to explain the LFB operating principle in more detail at this juncture, since some inherent subtleties contribute significant sources of uncertainty to the operation of the primary instrument. Consider the simple, uniaxial balance system shown in figure 3.1.

Newton's laws require that a system at equilibrium has no net force acting: the forces in figure 3.1 sum to zero. At equilibrium we have

$$F_{\text{input}} - F_{\text{el}} + mg - k(z - z_0) = 0 \quad (3.1)$$

Assuming the weight (third) and elastic (fourth) restoring terms are unknown, which is typically the case, it is not possible to equate F_{el} to F_{input} in order to measure F_{input} . However, it is possible to equate the forces when changes in force are instead considered. Neglecting tidal effects, discussed later, mg can be considered constant. The term $k(z - z_0)$ can be considered constant if z is accurately measured and found to be constant at all times. Then it is a simple matter of subtracting two instances of (3.1) above for two values of F_{input} to obtain the differential force equation

$$\Delta F_{\text{input}} - \Delta F_{\text{el}} = 0 \quad (3.2)$$

In practice, a dynamic equilibrium is maintained, in which a closed loop controller is used to maintain a fixed balance displacement (z), ensuring zero net acceleration, and hence ensuring that (3.2) holds.

Uniaxial motion is achieved or approximated by limiting the degrees of freedom of the flexure system. NPL's primary instrument, the Low Force Balance, uses an electrostatic implementation of the above concept, known as the electrostatic balance principle.

The electrostatic force active on an arbitrary axis x between the two plates of a capacitor can be calculated as

$$F_x = \frac{1}{2}V^2 \frac{dC}{dx} \quad (3.3)$$

where x is the displacement of a component of the capacitor with associated capacitance gradient $\frac{dC}{dx}$. In the case of the simple parallel plate capacitor,

$$C = \frac{\epsilon_r \epsilon_0 A}{d} \quad (3.4)$$

and a force will be generated along any vector that will change the value of any parameter in (3.4).

That generated force will be proportional to the square of the voltage applied across the capacitor, and to the capacitance gradient.

There is a distinct advantage to having a fixed relationship between the generated force F_x and the applied voltage regardless of the displacement along x . In particular it largely removes the need to determine the absolute value of x . A fixed relationship requires a constant dC/dx and hence a system design such that either A or ϵ_r in (3.4) is proportional to x .

The LFB varies ϵ_r ; its precedent at NIST varies A (see chapter 2 section 2.4.1 for a description of the latter).

For feedback control purposes, a force proportional to V^2 is still not ideal; a linear relationship greatly simplifies the transfer function of the system. It is possible to use a combination of capacitors to sum linear terms, cancel quadratic terms and achieve this linear force, voltage relationship.

A schematic diagram of the realisation of the above abstract principle in the LFB is shown in figure 3.2. A polysilicon dielectric vane is suspended on a flexure between four capacitor plates (implemented as coated Zerodur for thermal stability). The vane is constrained to move vertically between the plates by a monolithic four-bar linkage system incorporating pairs of 20 μm thick flexures at each corner. Additional 10 μm thick flexures added vertically result in extremely well-defined virtual pivot points [123]. The arcuate motion of the flexure

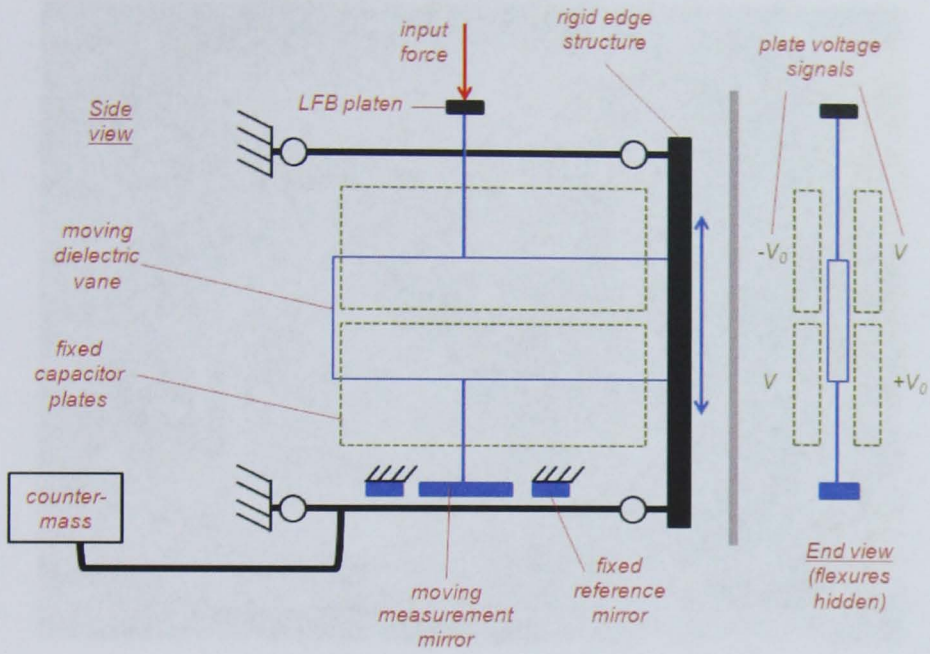


Figure 3.2: Schematic diagram of the LFB.

can be approximated to uniaxial for small deflections. For size reference, a photograph of the LFB is shown in figure 3.3.

The unbalanced mass of the balance system (flexure, vane, pusher) is minimised through the use of a counter-mass, which not only minimises the unladen deflection of the balance (verifiable via known subtle non-linearities in the capacitance gradient, as will be discussed) but also minimises the net effect of tidal oscillation on the measurement uncertainty. The moon varies the local gravitational acceleration g at a level that can be significant to low force measurement (see section 2.4.1.3).

The input force is applied to a silica rod placed at the centre of the silica dielectric vane, laterally, so the net moment on the four-bar linkage is zero. By symmetry, the effective line of action of F_{el} is collinear with F_{input} (see figure 3.2).

Each of the six plate pairs that exist in the four-plate capacitor system of the balance have an associated capacitance and capacitance gradient and contribute a force in the form of (3.3). A matrix equation for the combined force has been derived [124] to give the total force as

$$F_{el} = F_z = \frac{1}{2} \mathbf{V}^T \cdot \frac{d}{dz} \mathbf{C} \cdot \mathbf{V} \quad (3.5)$$

where

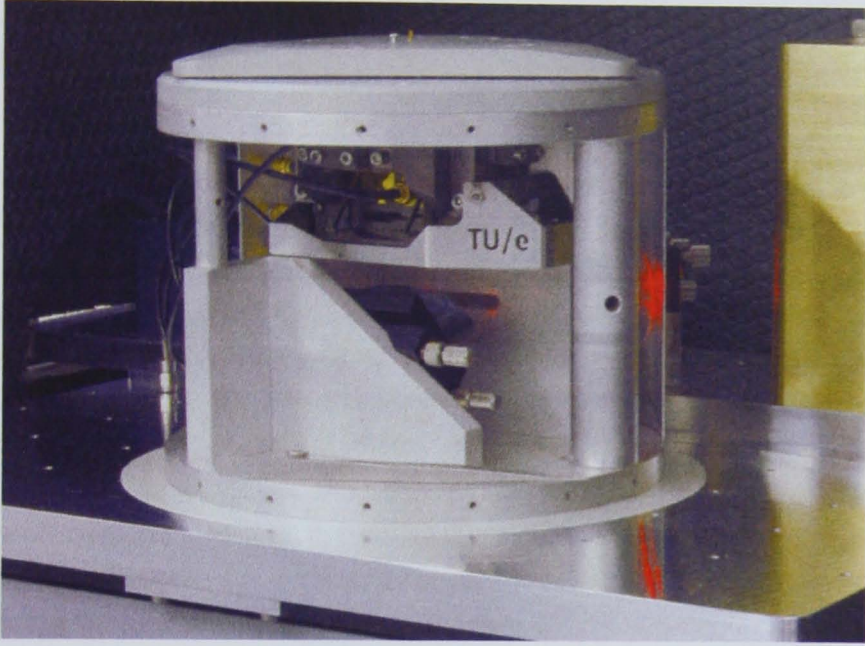


Figure 3.3: Photograph of the LFB in situ. Note that the outer cylinder hull is about 20 cm in height and diameter. The LFB mechanism is within and above the tray marked with the TU/e logo.

$$\mathbf{V} = \begin{pmatrix} V_{14} \\ V_{24} \\ V_{34} \end{pmatrix} = \begin{pmatrix} 0 \\ -V_0 - V \\ V_0 - V \end{pmatrix} \quad (3.6)$$

and

$$\mathbf{C} = \begin{pmatrix} C_{12} + C_{13} + C_{14} & -C_{12} & -C_{13} \\ -C_{12} & C_{12} + C_{23} + C_{24} & -C_{23} \\ -C_{13} & -C_{23} & C_{13} + C_{23} + C_{34} \end{pmatrix}. \quad (3.7)$$

Each capacitance C_{ij} in equation 3.7 above is the capacitance between plates i and j . Note that it can be shown that

$$\frac{d}{dz}\mathbf{C} = \begin{pmatrix} \frac{d}{dz}C_{12} + \frac{d}{dz}C_{13} + \frac{d}{dz}C_{14} & -\frac{d}{dz}C_{12} & -\frac{d}{dz}C_{13} \\ -\frac{d}{dz}C_{12} & \frac{d}{dz}C_{12} + \frac{d}{dz}C_{23} + \frac{d}{dz}C_{24} & -\frac{d}{dz}C_{23} \\ -\frac{d}{dz}C_{13} & -\frac{d}{dz}C_{23} & \frac{d}{dz}C_{13} + \frac{d}{dz}C_{23} + \frac{d}{dz}C_{34} \end{pmatrix} \quad (3.8)$$

allowing $\frac{d}{dz}\mathbf{C}$ to be assembled from individual two-plate capacitance pre-measurements $\frac{d}{dz}C_{ij}$, or C'_{ij} , as will be described later.

Many of the cross terms in equation 3.5 are small, and it can be shown that to first approximation,

$$|F_z| = \left| V V_0 \frac{d}{dz} C_{12} \right| \quad (3.9)$$

That is, the generated force is proportional to the variable applied voltage V (and to V_0 , and to $\frac{d}{dz} C_{12}$ where C_{12} is the capacitance between plates 1 and 2).

The LFB measures force by balancing the unknown input force with a traceably generated electrostatic force so that a dynamic equilibrium is maintained. This equilibrium is ensured by interferometrically monitoring the deflection, of the uniaxial flexure system, induced by a net force. The deflection is monitored interferometrically via a plane mirror differential interferometer of bespoke design.

The LFB was designed and developed at NPL under the NMO Engineering Measurement Programme 2002-2005 in partnership with the Technical University of Eindhoven (TU/e). The development of the underlying electrostatic force generation system is described in [124]. The design of the flexure system is described in [125].

3.2 AC modulation of the LFB drive signal to mitigate surface charging effects

Implicit traceability in a device such as the LFB demands a faithful implementation of the operating principle from which traceability will be inferred. In the LFB this requirement has two components; firstly, the generated force must equal the applied input force to the balance; and secondly, the generated force must be calculable based on equation (3.5).

Early mass comparison experiments on the LFB showed drift and scaling errors in a measured reference weight, on the order of half that weight. Measured forces were time dependent and consisted of an exponential approach to a settled value after any significant change in feedback voltage due to the change in load. In one experiment the calculated weight, derived from two of these settled values, was around 60 % less than its mass-calibrated value.

The apparent explanation for this behaviour was an additional charge accumulation on the surface of the dielectric sheet due to the presence of a finite water layer on the dielectric vane. Such water layers are inevitable in any non-zero humidity environment (superhydrophobic surfaces notwithstanding).

Surface charging effects are a known problem for the NIST EFB [74] and practical experience of this author with the NIST balance suggested that a rapid reversal of drive

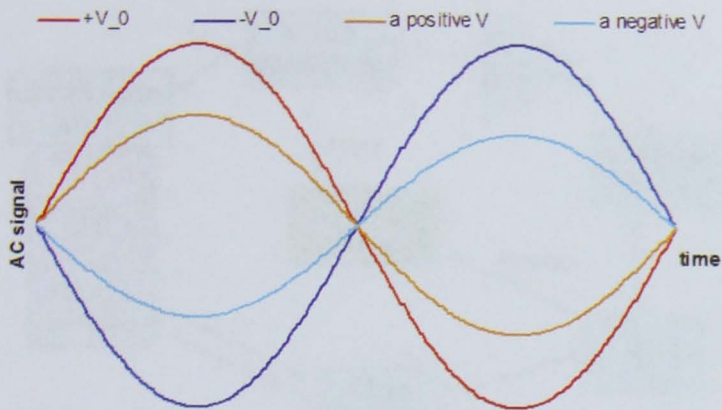


Figure 3.4: Sign convention used in the work with phase-locked AC signals

Table 3.1: Summary of drive signals for the LFB under AC operation.

Plate	Amplitude	Phase
1	V	0
2	V_0	π
3	V_0	0
4	V	0

voltage as a means of preventing significant surface charge from accumulating.

By fixing the relative phase of drive voltages to each plate in the LFB (see figure 3.4) it is possible to achieve DC (rectified) force generation with a per-plate average voltage of zero.

In section 3.1 the DC plate voltages were given as $-V_0$ and $+V_0$ for plates 2 and 3 respectively, and V for plates 1 and 4. Under AC operation, these voltages are modulated with a one kilohertz carrier, as summarised in table 3.1, referencing figure 3.5.

The actual synthesis of this AC generation profile required significant reengineering

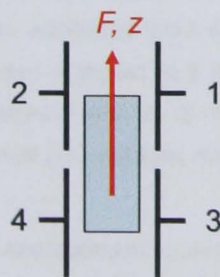


Figure 3.5: Schematic diagram of capacitor plate numbering system.

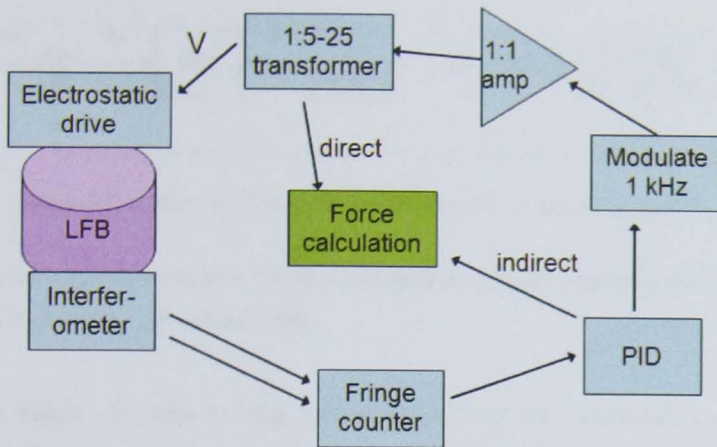


Figure 3.6: Block diagram of the physical elements of the AC LFB controller.

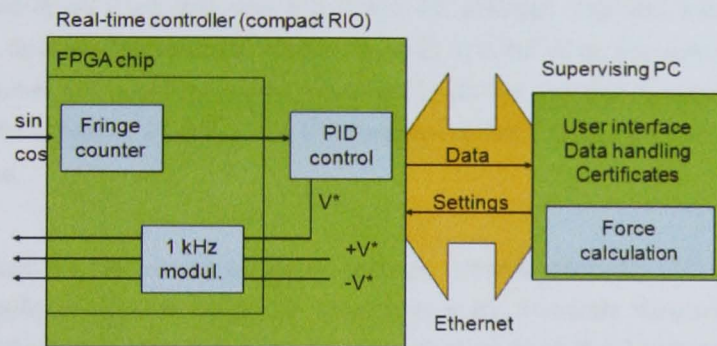


Figure 3.7: Block diagram of the software behind the LFB controller under AC operation.

of the LFB controller.

Physical, software and controller block diagrams of the AC controller are shown in figures 3.6, 3.7 and 3.8. The key components of the AC controller are as follows.

One kilohertz carrier The PID controller outputs an integer digital signal in the range ± 16384 . This variable signal and an additional fixed signal (amplitude ± 16384) are modulated with a one kilohertz sine wave sampled at $8 \mu\text{s}$ (that is, about 125 samples per cycle). The result is two output voltages S and S_0 , of rms amplitude of up to about 7.5 V, representing the feedback (V) and fixed (V_0) voltages respectively.

Amplification stage The digital-to-analogue components of the National Instruments cRIO hardware are capable of high-resolution signal generation but cannot support sufficient current for this application. Unity gain amplifiers are therefore used as a source of additional

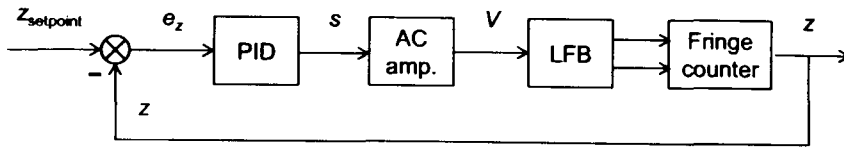


Figure 3.8: Control diagram of the LFB controller under AC operation.

power. Since all amplifiers have a thermal coefficient, a large heatsink with active fan cooling is used to dissipate generated heat.

Transformer stage In order to step from around 7.5 V rms amplitude up to a voltage sufficient for operation, one-kilohertz optimised transformers were used. By centre-tapping the secondary coil of the transformer, it is straightforward to convert one low-voltage AC signal into two equal amplitude, opposite phase, AC voltages. Two 50:1 transformers are used; in one, S_0 is used to generate V_0 and $-V_0$ at 25:1; in the other, S is used to generate V at 25:1 (the other half is not connected). Additional taps are provided to permit transformer ratios between 1:5 and 1:25 in steps of 5, to modify the force range-resolution compromise in the balance.

Consequences for the measurement of voltage Unfortunately the shift to AC voltage also had significant implications for the uncertainty in the traceable measurement of that voltage as will be discussed in section 3.6. The measurement of AC voltage requires the sampling of entire cycles and stable frequency and shape. Typical accuracy values for DVM operation (as quoted by the manufacturer) are around two to three orders of magnitude larger for traceable AC measurement than for DC.

3.3 Development of a fringe counter for the z interferometer

The LFB controller was originally intended to operate in a simple fringe-locking mode, in which the feedback voltage is varied to hold the position of an interferometer fringe minimum at the detector. Some method is used to bring the balance close to a suitable fringe minimum, and PID control is established based on the sensor signal.

It is possible to count fringes to measure larger displacements, such as during capacitance gradient characterisation, with reasonable accuracy. However, any motion greater than a few tens of nanometres must be done under external displacement drive or using non-trivial integral gain tweaks. Under fringe-locking operation the interferometer cannot track LFB deflection across the fringe-fringe transition.

It is initially simpler to implement a fringe locking control system. However, there are disadvantages to this configuration.

In the simple fringe-lock approach, each detector signal is significantly non-linear, and gain parameters optimised for small controller error signals were found to lead to instability and oscillation for transient errors, of significant fraction of a fringe in size, due to load changes. Such abrupt load changes are not ideal but are to be expected due to capillary force snap-in.

Measurement of displacement is effectively quantised in units of a quarter wavelength. This would present a problem for any operation of the LFB in which a continuous displacement scale is important. One example is in indentation mode operation, when displacement-nulled operation is inappropriate (see section 3.7).

One significant benefit of full, fringe-counting operation is that the LFB interferometer can be used to calibrate the z scale of any secondary vertical stage installed above the balance. Such a stage would be used to push an artefact to be calibrated into the platen of the LFB, and scale calibration would be essential for traceable artefact calibration. The spring constant of the LFB is typically some three to four orders of magnitude smaller than that of the secondary stage frame compliance. The LFB operates as a very high accuracy displacement transducer when the balance feedback controller is clamped at a constant output value.

In any case, it is essential that large scale (multiple fringe) displacements be tracked by the LFB interferometer. As will be shown later (section 3.5), significant non-linearities are present in the capacitance gradient of the LFB, and a reasonable estimate of the absolute position is essential.

Based on the balance of the above advantages and disadvantages to fringe-locking operation, it was decided to implement full fringe counting control.

The design of the interferometer permits the development of a full quadrature fringe counter algorithm with subnanometer resolution. Interference fringes at the two detectors are approximately a quarter-cycle out of phase. The resultant 'sine' and cosine' signals are combined into a lissajous figure (see figure 3.9). The instantaneous phase, and hence displacement, is calculated at high speed from this figure using an arctangent look-up table. Any phase change is added to a running phase total as integer-plus-fraction fringe count. This is undertaken on the National Instruments FPGA card with a loop period of about 8 μ s.

The general principle of the FPGA-based fast quadrature fringe counter interferometer for the NPL plane-mirror differential interferometer is derived from established precedent

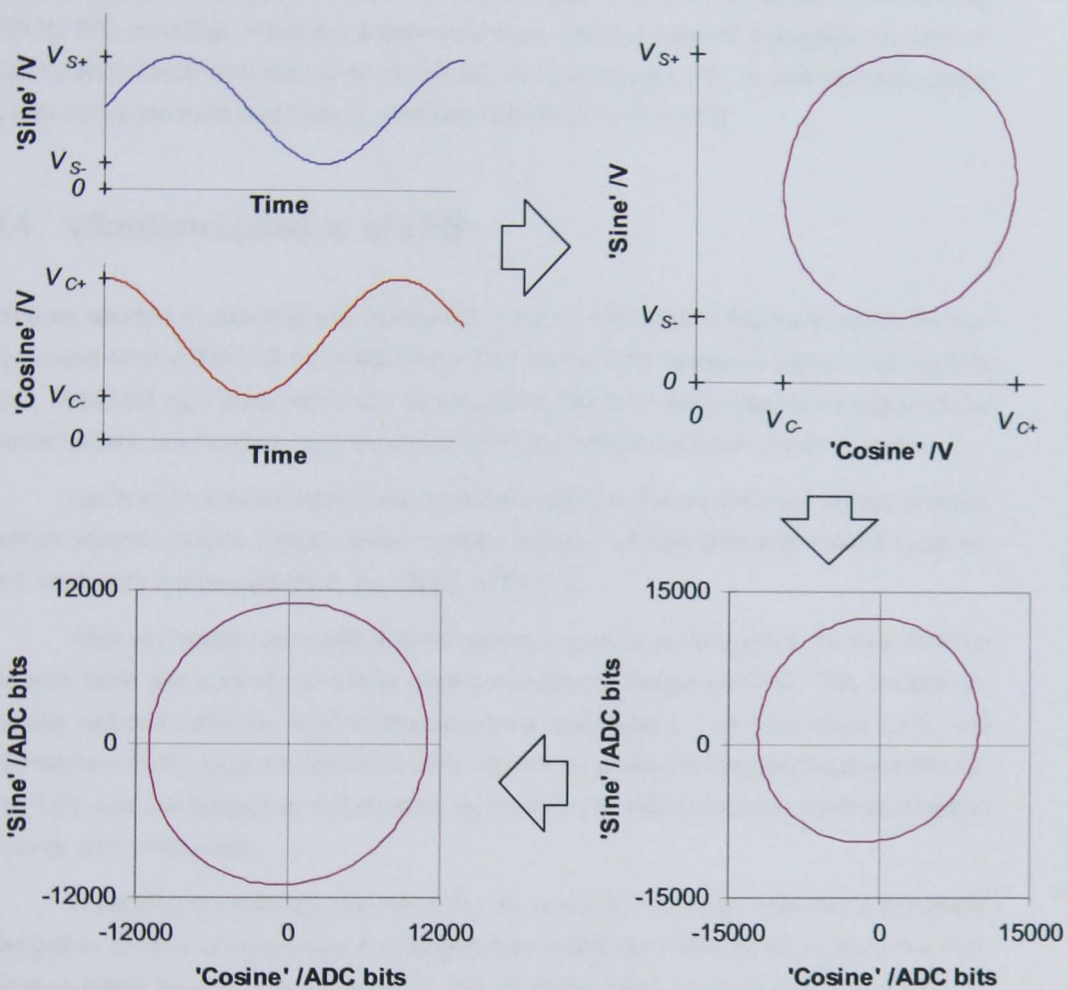


Figure 3.9: Constructing the lissajous figure for the LFB: 'sine' and 'cosine' photodiode sensor analogue voltages (top left) form a virtual lissajous figure (top right); the analogue voltages are pre-amplified, normalised using an intensity reference, offset and read using ADCs. The software signals are offset to recentre the final ellipse. The deviation from circular, resulting from interferometer sensor misalignment, produces a periodic error in the final displacement signal.

at NPL (see for example [126]); the present author undertook a leading role in the implementation of the same using NI hardware.

The FPGA loop also accumulates a one-millisecond buffer of displacement samples and calculates an average to ensure that high-frequency jitter does not influence the circa 800 Hz PID controller. However, subsequent tests showed that the averaging has little influence on the final controller error, in line with the expectation that the one kilohertz carrier is well above the main mechanical oscillation bandwidth of the LFB.

3.4 Vibration isolation of LFB

External sources of acoustic and mechanical input to the balance flexure increase the displacement error in the LFB controller or the jitter on the force feedback signal to cancel that error. Feedback gain parameters can be adjusted to optimise these signals for a given force measurement, but in either case the overall LFB performance will have been reduced.

Yet even in a 'quiet' laboratory, such mechanical noise sources are always present. Typical sources include seismic traffic rumble, vibration of environmental control systems, and necessary human activity in the vicinity of the LFB.

After exploratory tests with a demonstration system, a Halcyonics six-axis vibration isolation table and acoustic chamber were purchased to house the LFB. This system noticeably reduced controller error for frequencies above about 0.1 Hz (see figure 3.10). The effectiveness of the typical vibration isolation system degrades for frequencies below this value [127], and low-frequency drift must be removed using other methods, such as direction reversal and comparison.

A significant challenge presented by the acoustic enclosure was that it prevented dissipation of heat generated by the temperature-stabilised HeNe laser, causing the temperature inside the chamber to rise to an unacceptable level. The only available solution to permit the use of the chamber was to locate the laser outside the chamber. The laser was mounted on a cantilevered beam projecting out through an aperture on the chamber. The cantilevered beam was rigidly connected to the base plate supporting interferometer and LFB. Options in which the laser was mechanically disconnected from the LFB and interferometer were explored. However, the interferometer design has been found to be extremely sensitive to alignment of source laser beam, and in this application the relative motion of laser and interferometer, due to relative expansion and vibration isolation table adjustment, was too great to eliminate unacceptable variation in interferometer signal response.

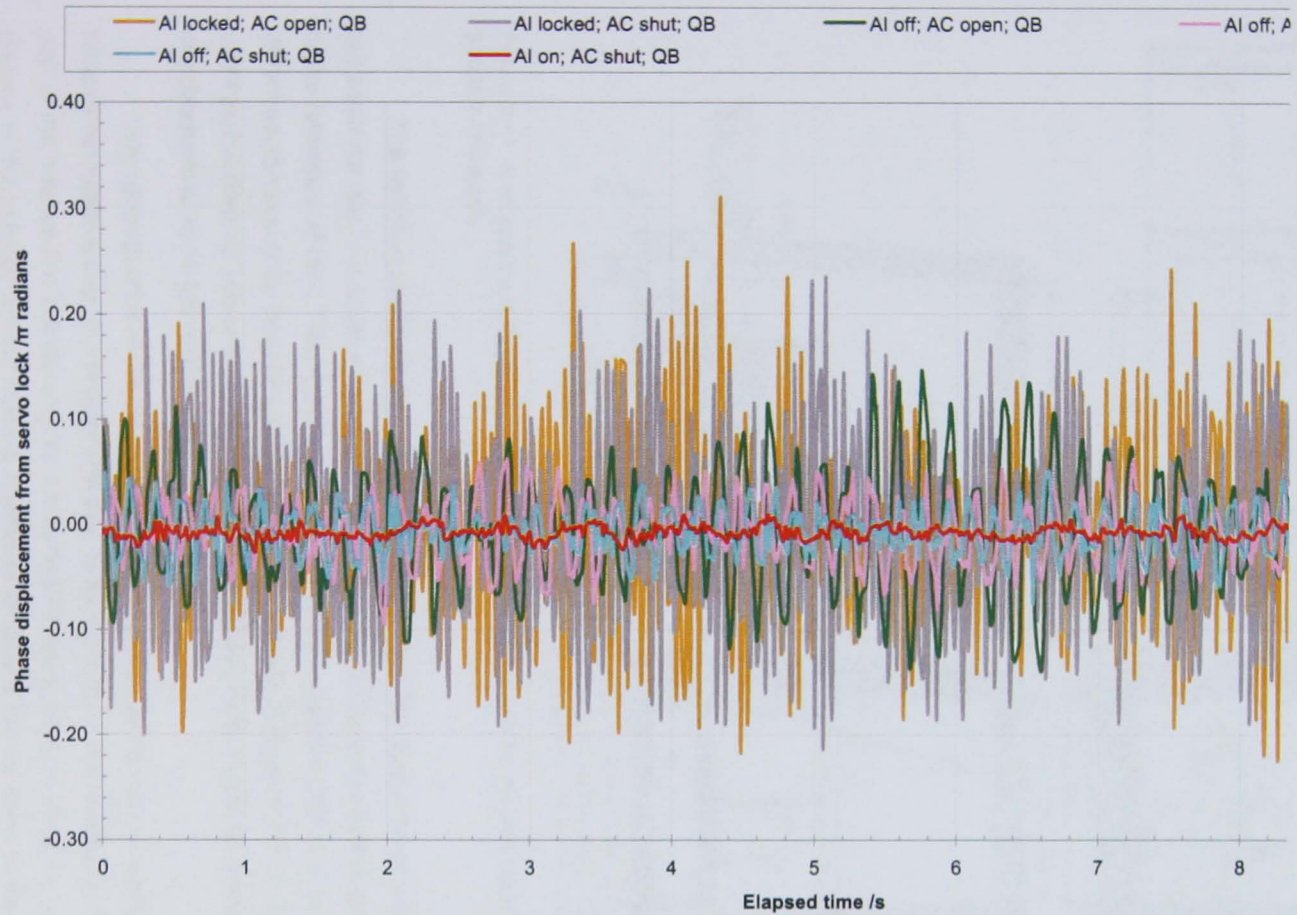


Figure 3.10: Qualitative comparison of raw data for different vibration isolation unit (AI) and acoustic chamber (AC) state under the 'quiet background' (QB) condition. The QB reference assumes constant noise amplitudes from noise sources in the laboratory, primarily the environmental handling system. Interferometer noise is given in terms of lissajous figure phase, where 0.1 rad is approximately 2.5 nm balance displacement.

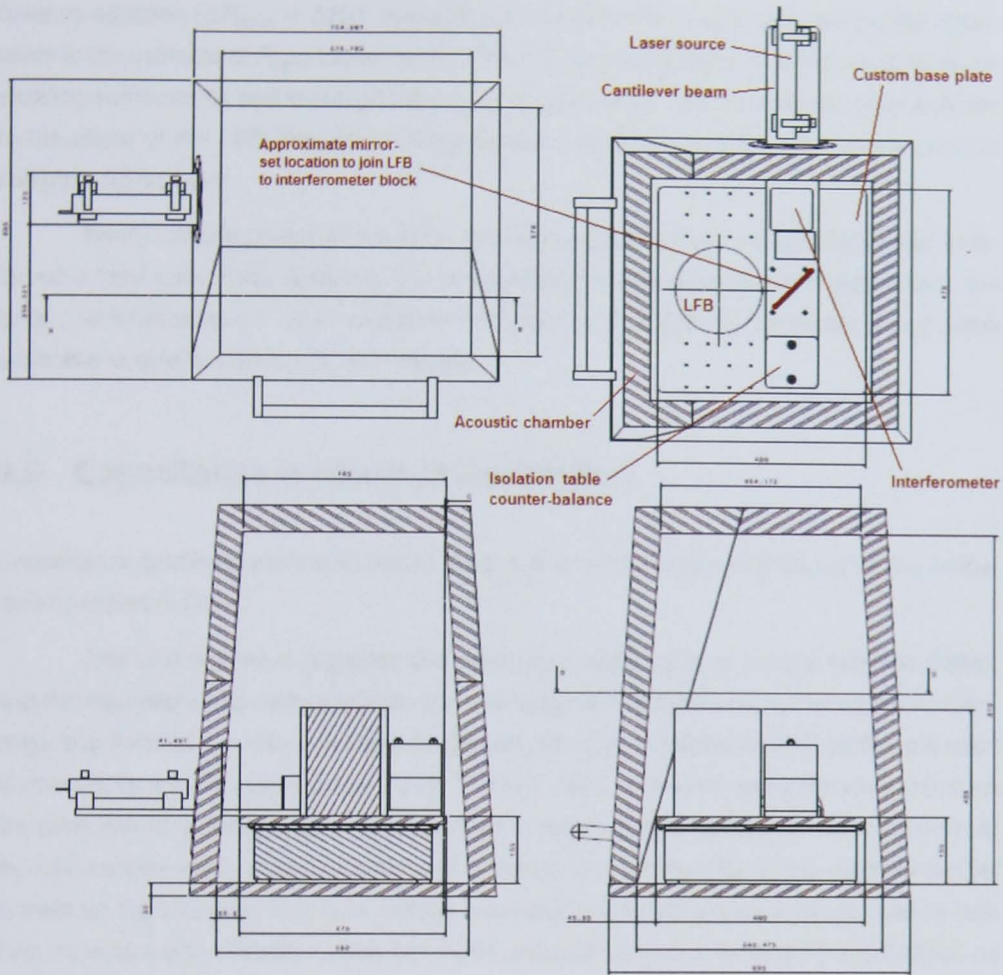


Figure 3.11: A modified arrangement of the LFB system components to mitigate heating within the acoustic enclosure.

The modified arrangement is shown in figure 3.11. The three corner mirrors shown are essential due to a slight angular misalignment of the LFB measurement mirror relative to the reference mirrors. This alignment originates in the assembly of the balance, in which the measurement mirror must be glued in place. As an aside, this misalignment introduces a slight path difference between measurement and reference beams and an additional effective deadpath of up to two millimetres.

One consequence of the cantilevered laser arrangement is that the system is vulnerable to moments acting on the laser unit due to air currents in the laboratory. The moving part of the balance has a finite angular inertia and tilt inputs close to the 2 Hz resonant frequency of the balance will introduce a significant additional inertial force to the differential

balance equation ($\Delta F_{\text{input}} = \Delta F_{\text{ej}}$). Averaging over time is then required to reduce the uncertainty in the estimate of F_{input} based on F_{ej} . It may have been better to introduce further beam steering components and redesign the mounting plate to place the cantilever perpendicular to the plane of the LFB, though coupling between the axes in the system would prevent complete tilt isolation.

Recent development of the NPL differential plane mirror interferometer has introduced a fibre laser feed, removing the requirement for a mechanical connection between laser and interferometer. The incorporation of such in the LFB interferometer would seem advisable should the future opportunity arise.

3.5 Capacitance gradient determination

Capacitance gradients are measured for each pair of plates in the LFB based on the procedure specified in [124].

The LFB flexure is manually deflected by exerting a force on the balance platen, and the capacitance at various points over the range of motion measured using an Andeen-Hagerling AH2500A 1 kHz automatic capacitance bridge. Shielded coaxial cables are used to connect to the two plates under study. The other two plates are connected to ground via the outer shield to remove stray capacitances to those plates. Additional mass is added to the LFB counter-mass to bring the flexure to the top stop, thus allowing the external pusher to traverse the full range of flexure motion. Repeated measurement and comparison of data from each direction of motion allow for identification of various systematic uncertainties, as will be discussed.

The optimised external push system is based on a high-resolution, five millimetre vertical stage driving a compliant pusher into the LFB platen. Using the compliant pusher ($k \sim 10 \text{ Nm}^{-1}$) it is possible to traverse the full flexure range without exceeding the maximum load on the balance platen. Since the generated deflection is measured using the LFB interferometer, it is not necessary to know the pusher spring constant accurately.

To measure a capacitance, the capacitance bridge drives one plate with an AC voltage and monitors the signal at the other electrode. Since the capacitance bridge operates in AC mode, it is not affected by surface charging effects. The observation of relatively drift-free capacitances for a stationary system partially motivated the effort to switch the LFB controller to AC operation (see section 3.2).

Prior experiments, such as those associated with [66], have demonstrated that the capacitance gradients measured for the system follow the expected form. The capacitance

gradient C'_{12} should decrease linearly as the dielectric vane (and balance) is deflected downwards and the fraction of the plate area filled with a higher dielectric constant material decreases. Because of the symmetry of the system, the rate of *increase* in capacitance C_{34} with the downward deflection of the vane should be equal to the rate of decrease of C_{12} . This is confirmed by experiment; C'_{12} and C'_{34} are equal and opposite with magnitude around 400 pF m^{-1} . All other plate pairs in the system have no overlapping area and, according to classical capacitor theory, should have zero capacitance and zero capacitance gradient for all z . Again, experiments confirm that to first approximation the other plate pairs have zero capacitance.

Closer inspection reveals, however, that each capacitance between each two plates is better represented by a quadratic model of the form

$$C = a_0 + a_1z + a_2z^2 + a_3z^3 + \delta \quad (3.10)$$

where a_0 is a capacitance offset subject to drift; a_1 is the nominal capacitance gradient $\frac{dC}{dz}$ of the plate pair, a_2 is a small correction to the gradient proportional to z , and a_3 and δ represent residual non-linearities and noise respectively. The full capacitance gradient is therefore given by

$$C' = \frac{dC}{dz} = a_1 + 2a_2z + 3a_3z^2 + \frac{d\delta}{dz} . \quad (3.11)$$

The propagating uncertainties proportional to z contribute random fluctuations to the values of each of the coefficients $a_{0..3}$ for a given gradient characterisation experiment. This variation can be used to estimate an uncertainty in the determination of $a_{0..3}$. The total contribution of absolute uncertainties in z to the uncertainties in $a_{0..3}$ tend to drop off according to the $n^{-\frac{1}{2}}$ rule, and so for large datasets may be neglected. In other words, it is appropriate to set $\frac{d\delta}{dz} = 0$.

The aim of capacitance gradient determination experiments for each of the plate pairs was to obtain an estimate for the gradient as $a_1 + 2a_2z$. The uncertainty in such an estimate would be the quadrature sum of the a_3 term, the relative component of and the variation or uncertainty in the estimates of a_1 and a_2 . Presentation of the measured results is beyond the scope of this thesis. However, by way of example, figure 3.12 shows non-linearities in the measurement of the capacitance gradient C'_{34} , for which the nominal value (a_1) was found to be $-407.5996 \text{ pF m}^{-1} \pm 0.0092 \text{ pF m}^{-1}$. Since the residuals are highly position-dependent and have a turning point at zero LFB flexure position, it is possible to minimise the uncertainty contribution by ensuring that the interferometer scale is aligned to the true balance deflection to within around $100 \text{ }\mu\text{m}$.

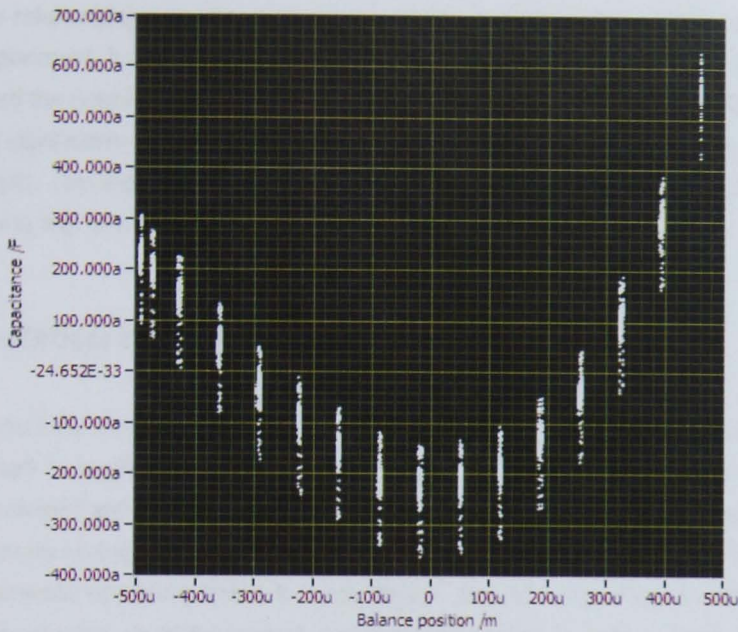


Figure 3.12: Non-linearities in C'_{34} after simple linear fit. The vertical axis is in attofarads; the horizontal axis in micrometres, in software engineering notation.

3.6 Voltage measurement approach

The LFB controller circuitry generates three AC voltages (V_{var} , V_{0+} , V_{0-}). V_{var} is proportional to the digital feedback signal S_{var} , with small additional perturbations; V_{0+} and V_{0-} are nominally constant amplitude and opposite in phase, with small perturbations that are a function of S_{var} . To measure force traceably, all three signals must be measured simultaneously using traceably calibrated digital voltmeters. Since the estimate of the generated electrostatic force is proportional to each voltage, uncertainties in the voltage measurement strongly influence the force measurement uncertainty.

It is more challenging, and consequently more expensive, to measure an AC potential difference to a given level of precision than it is with DC measurement. This is related to the need, in AC measurement, to fit a sinusoid to the incoming signal before estimating the amplitude. The practical consequence of this action was to increase the cost of voltage-measurement instrumentation for the LFB by a factor of at least six.

An alternative is to use a single, loaned digital voltmeter of sufficient performance to 'pre-characterise' the three output voltages as functions of the variable output digital signal. If these characteristic perturbations in each of the output voltages are repeatable, that is, the relationships between S_{var} and V_{var} , V_{0+} and V_{0-} are constant over time, then curves repre-

senting these relationships can be used to imply the output voltages from S_{var} at any given time in an experiment. It was found that the act of removing the voltmeter from the controller circuit changed the output characteristics of the generated voltages, such that the measured force differed significantly from independently traceable reference values, despite remaining extremely stable. This indirect method was used for the comparison work in sections 3.9 and 3.10, confirming that direct voltage measurement must be used.

3.7 Indentation mode LFB operation

In principle, the LFB could be operated in what is known as 'indentation mode'. That is, the LFB is used as a precision instrumented indenter, with platen displacement interferometrically measured and the applied force calculated from a prior traceable measurement of the LFB flexure spring constant. The device under test is then pushed into the balance in order to generate opposing forces in each device. Should circumstances call for it, the electrostatic force drive could be used during experimentation to apply a fixed offset force. However, measurements of the LFB spring constant showed evidence of hysteresis and other effects, suggesting that the LFB must always be used in displacement-nulled mode in order to achieve desired performance levels.

The spring constant of the LFB has been estimated experimentally using the following procedure. The balance set-point was ramped stepwise from zero up to $18 \mu\text{N}$, ramped down through zero to $-18 \mu\text{N}$, and back to zero. At each step of this quasistatic measurement, lasting around four hours, the force required to maintain the setpoint was recorded with the setpoint, using a short average at each step to remove noise from consideration. An example measurement cycle is shown in figure 3.13. Both hysteresis and notching is observable in the curve, both of which are attributed to material effects within the extremely thin flexure elements. The hysteresis is highly repeatable and independent of the time taken to complete the loop.

Based on around 200 cycles of stiffness measurement, and the consideration of the straight sections of the plot (that is, discarding data from the first $5 \mu\text{m}$ of motion following a direction reversal), the balance stiffness was estimated to be $k_{\text{LFB}} = 1.615 \text{ N m}^{-1} \pm 0.009 \text{ N m}^{-1}$. In the region immediately after direction reversal, a better estimate of the stiffness is $k_{\text{LFB}} = 2.5 \text{ N m}^{-1} \pm 0.1 \text{ N m}^{-1}$. This higher value is applicable when considering small deviations such as control loop errors. The knowledge of hysteresis in the LFB flexures has motivated tighter procedures and stiffer control loop gains to ensure that transient excursions from control loop setpoint are minimised.

3.2.1.7.9. Estimation of the balance stiffness by electrostatic force deflection

The stiffness of the balance is estimated by measuring the deflection of the balance arm by the electrostatic force. The electrostatic force is applied to the balance arm by the electrostatic force deflection method. The electrostatic force is applied to the balance arm by the electrostatic force deflection method. The electrostatic force is applied to the balance arm by the electrostatic force deflection method.

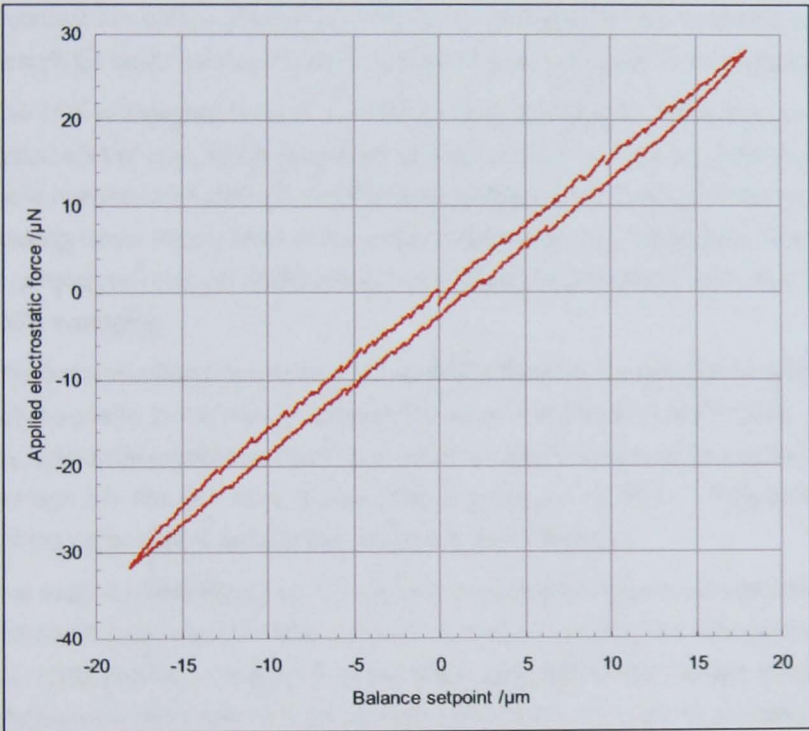


Figure 3.13: Example data from the estimate of the balance stiffness by electrostatic force deflection.

3.8 LFB platen and effective LFB stiffness

To facilitate an appropriate interface between the LFB and test artefact, a bespoke platen was devised for the LFB. The base platen surface of the LFB is a silica rod of radius 1 mm oriented vertically. The interface platen used for this work consisted of a brass collar with a cone-type top surface onto which a ruby sphere was attached with cyanoacrylate adhesive, as shown in figure 3.14. The W-shape centre detail of the brass collar allowed the adhesive to spread sufficiently to allow full contact between collar and sphere. The 0.5 mm diameter sphere was sufficiently small to fit beneath the cantilever substrate whilst allowing the cantilever to contact the sphere top-centre. This latter configuration was achieved by using a manual search for local maximum sphere height using the cantilever force feedback.

The LFB is designed to have an infinite effective stiffness, due to the action of the null deflection control loop, which generates an electrostatic force equal and opposite to an input force to maintain zero deflection of the balance flexure. In practice, the flexure stiffness is finite, having terms proportional to the applied force and a dynamic term. The dynamic term is a consequence of the displacement error signal in the control loop, and is quickly reduced with averaging.

The first proportional term is due to the finite stiffness of the bulk platen and glass rod connecting the platen to the dielectric sheet. Based on the simple model of axial compression of the cylindrical polysilicon platen rod under a uniform end load, the spring constant associated with this first bulk term is estimated to be $k_{PB} = 10 \text{ kNm}^{-1}$. This term is independent of the properties of the artefact contacting the LFB platen.

The second proportional term is due to local Hertzian compression between the ruby sphere of the LFB platen and the artefact or other device contacting the LFB platen. Shi and Polycarpou [128] provide a method for analytically determining the contact stiffness for a smooth Hertzian contact between a sphere and a plane. Based on Hertzian contact theory, Shi and Polycarpou define the following expression (eqn 3.12) for the contact stiffness k_{CH} :

$$k_{CH} = \frac{2}{3} \left(\frac{16RE^{*2}}{9} \right)^{1/3} P^{1/3} \quad (3.12)$$

where R is the radius of the sphere, P is the applied load, and E^* is the equivalent Young's Modulus given by

$$\frac{1}{E^*} = \frac{1 - \nu_1^2}{E_1} + \frac{1 - \nu_2^2}{E_2}$$

in which ν_i and E_i refer to the Poisson's ratio and Young's Modulus of the sphere (subscript 1) and plane (subscript 2) respectively. Shi and Polycarpou also note that for rough contact under light load, a better estimate of the contact stiffness would be $k_{CHR} = \frac{1}{3}k_{CH}$.

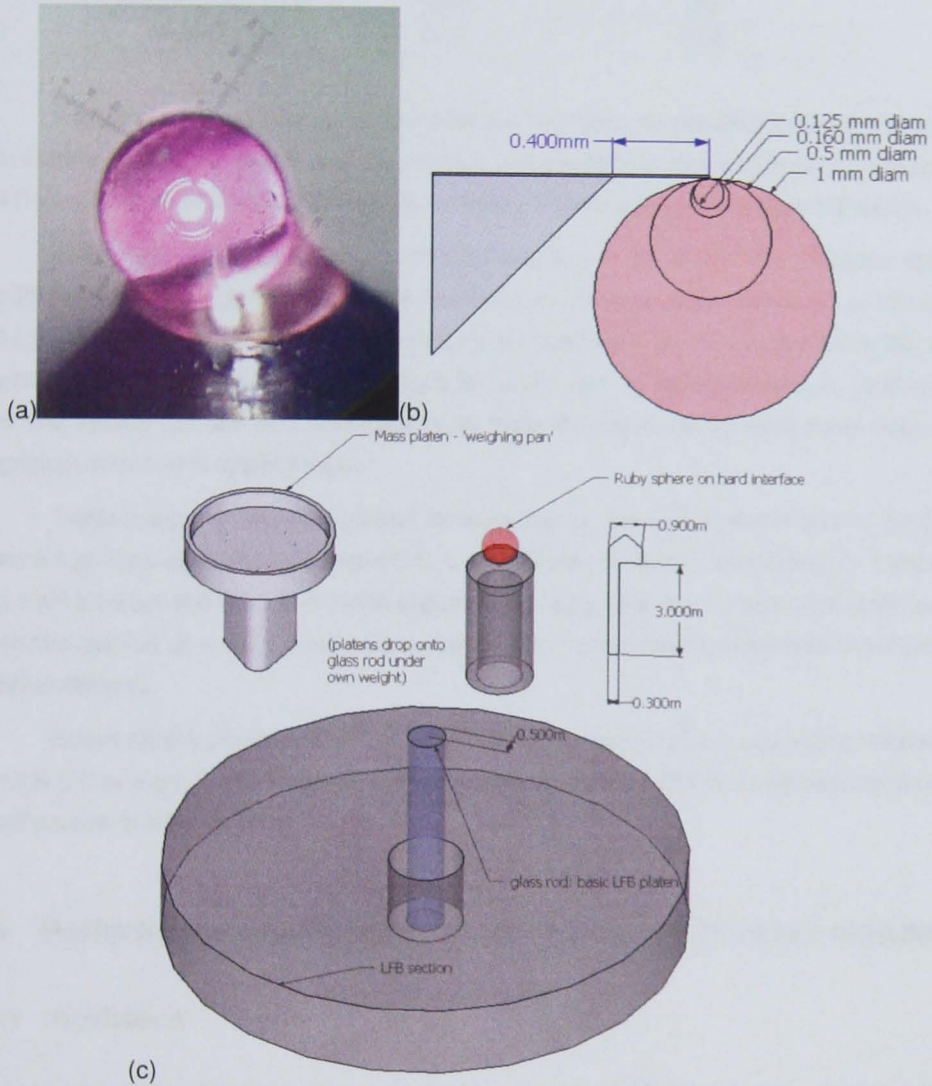


Figure 3.14: Details of the platen used for the comparison: (a) ruby sphere attached to brass collar - note the slight asymmetric setting due to the W-section centre ring; (b) a size comparison between the Kleindiek cantilever (approximated) and various sphere sizes; and (c) an early concept of the sphere platen, with V-section and dimensions not optimised for fabrication and handling. Also shown to approximate scale in (c) is a sketch of the mass platen used in section 3.9.

Table 3.2: Material properties required for Hertzian compression model of LFB-artefact contact.

Material	Poisson's ratio ν	Young's Modulus E/GPa
Synthetic ruby [129]	0.25	380
Silicon [130, 131]	0.27	165
Nickel [132]	0.31	200

Equation 3.12 may be used to estimate the Hertzian compression between the small ruby sphere of the LFB platen and the contact surface of both nickel and silicon artefacts. The Poisson's ratio and Young's Modulus for these materials is given in table 3.2 below.

In the ruby-nickel case, $E^* = 143 \text{ GPa}$ and $k_{\text{CH}} = 31 \text{ kNm}^{-1}$ for a sphere radius of 0.25 mm and an applied load of $1 \mu\text{N}$. Similarly, for the ruby-silicon case, $E^* = 124 \text{ GPa}$ and $k_{\text{CH}} = 29 \text{ kNm}^{-1}$. Taking into account surface roughness, as recommended by Shi and Polycarpou, the contact stiffness k_{CHR} in both cases can be approximated to 10 kNm^{-1} . Note that the contact stiffness increases by an order of magnitude for each three orders of magnitude increase in applied load.

Considering the two proportional terms in series, the effective stiffness of the LFB under a $1 \mu\text{N}$ total applied load is therefore approximately 5 kNm^{-1} , decreasing to 1 kNm^{-1} for a 1 nN total applied load. This result suggests that suggests that nanonewton scale loads should be applied as small variations to a micronewton scale load to maximise the effective balance stiffness.

Based on the above analysis, and assuming contact forces a significant fraction of the LFB force range, the LFB can be approximated as infinitely stiff for compliant cantilevers of stiffness on the order 1 Nm^{-1} .

3.9 Performance verification by comparison with mass standards

3.9.1 Motivation

Concerns about unresolved systematic uncertainties in the LFB force measurement capability, directly traceable via the generated electrostatic force, motivated a comparison with an independent low force traceability route.

The simplest (though certainly not the quickest) method of verifying the performance of the measurement of an input force to the LFB is by weighing small deadweights. Small pieces of wire are lifted repeatedly on and off of the LFB platen and the resultant force cycle compared with the known weight of the wire pieces. If the wire masses and the local gravitational constant are known traceably, such an experiment in effect compares the traceable

mass and electrostatic force scales. If the function of the LFB is known correctly, the two scales should align within their respective uncertainties.

The mass uncertainties and inherent impracticalities associated with the handling of small mass artefacts, coupled with the need for averaging over large numbers of measurements, means that small mass artefacts are unsuitable for use as force transfer artefacts. However, the uncertainties, whilst large, are well understood and hence mass artefacts are appropriate for the comparison work required here.

3.9.2 Precedent activity: NPL mass scale versus NIST force scale

The decision to undertake a performance verification using mass standards was motivated by the success of a similar comparison, also undertaken by the author [33]. In this previous activity, small mass artefacts traceably calibrated using standard traceable mass measurement techniques at NPL were weighed on the NIST EFB, and the weights compared. In this way, the US realisation of the newly emerging electrostatic force traceability route was compared to the NPL realisation of the well-established mass scale, at a level not previously attempted. The use of sub-milligram test masses on the NIST EFB successfully led to the identification of a systematic error of nanonewton size that may now be removed or corrected for. A consistent under-read on the NIST EFB on the order of nanonewtons was later recreated by cycling the EFB mass-loading system without a mass present and diagnosed as an interaction between the lifting stage actuator and the ferromagnetic EFB flexures.

3.9.3 Overview of experiments and data processing

To accomplish the required comparison, pre-calibrated mass artefacts are repeatedly cycled onto and off of a modified LFB platen. The artefact weight is recorded for each transition as the difference between the stable LFB force reading at the on and off positions. The mass artefact is left to settle on the LFB with the lifting stage stationary; subsequently a force estimate is obtained as an average reading over several seconds of stability. The settling time is selected based on prior observation of the post-transition drop in controller error signal noise to a pre-transition level.

The most successful choice of mass artefact is a length of wire of known material. The extended geometry and well-defined cross-section simplify lifting arrangements as well as volume calculations for any buoyancy correction. Raw materials are readily available in the form of multistrand electronics wire. Care must be taken to avoid ferromagnetic materials such as steel, to avoid any parasitic force interaction with either the LFB or the lifting mechanism. A straight length of wire is cut to achieve the desired nominal mass. The ends of

the wire (first and last millimetre of a typically 5 mm to 10 mm length) are turned downwards by about 45° to lower the centre of mass and introduce a resistance to rotation, simplifying artefact containment on the lifting rig. Larger small mass artefacts are often realised are longer, thicker wire bent into a tetrahedral arrangement, but this arrangement increases the risk of the artefact 'walking' out of range of the hook after a number of transitions.

The glass rod forming the base platen of the LFB is equipped with a small turned, rimmed, circular aluminium platform to provide a landing location for the mass artefact. The rim contains notches to accept the artefact. However, experience shows that the experimental data from transitions without the use of these notches contain smaller transient force (and LFB error) spikes and hence lower associated uncertainties.

The lifting mechanism consists of two parallel hooks, as bent metal wire of the same or similar material to the artefacts, glued (cyanoacrylate) to a glass slide, clamped to a vertical stage, specifically a five-millimetre range micropositioner from PI. The clamp incorporates a damping element such as a general-purpose adhesive tack, to reduce stage-to-sample transmission of vibration that would shake off the sample. The introduced hook position drift is not a significant problem for this application. To achieve a mass on-off transition, the lifting hook centres are moved vertically past the desired landing location and the mass transitions between the two locations. The hooks can be manually tweaked to close the distance between the transitions of the two ends of the artefact, to reduce the required hook motions and overall measurement time.

At the mass scale required for this application, the hook-artefact surface forces are on the order of the artefact weight. The LFB controller must act to overcome these transient adhesive forces as the hooks pass the platen; typically a speed-dependent force and error spike results, increasing uncertainties. The dominant component of the adhesion is the capillary force due to the small water layer between hook and artefact. In vacuum, this capillary force is removed, exposing the electrostatic force as the dominant component. In such a situation it would be essential to ensure electrical connection between hook and platen at all times.

The additional milligram-order mass of the artefact does not significantly affect the dynamic behaviour of the LFB, which has a moving mass of around 5 g.

The 28.5 μN weight of the 2.91 mg mass artefact used spanned around half the force range of the LFB, and so the LFB setpoint was varied periodically throughout an extended weighing experiment to observe any systematic changes in measured weight.

3.9.4 Experimental results

3.9.4.1 Artefact weight via the NPL mass scale

The wire mass artefact was measured with a Sartorius C5 microbalance, calibrated via subdivision from the NPL kilogram. The balance used had an associated uncertainty of $0.45\ \mu\text{g}$, incorporating $0.40\ \mu\text{g}$ of calibration uncertainty and $0.18\ \mu\text{g}$ due to subsequent drift. Several mass weighings were taken, correcting for the unladen balance reading. The mean, standard deviation and standard uncertainty in the mass measurements were $2906.09\ \mu\text{g}$, $0.27\ \mu\text{g}$ and $0.10\ \mu\text{g}$ respectively. The estimated artefact mass was therefore established as $2.9061\ \text{mg} \pm 0.0004\ \text{mg}$.

The local gravitational acceleration has been established previously at $9.81182\ \text{m s}^{-2} \pm 0.00001\ \text{m s}^{-2}$. Thus the equivalent weight is calculated as $28.5140\ \mu\text{N} \pm 0.0044\ \mu\text{N}$.

3.9.4.2 Artefact weight via the NPL dimensional and electronic scales

Using the experimental procedure outlined in section 3.9.3, 7355 transitions were completed over six days; of these transitions, 7200 produced meaningful results. Each transition took two minutes, including movement, settling and measurement. The LFB set-point was altered several times during the experiment to highlight related systematic effects. These results are shown as absolute force readings and differentials (weights) in figure 3.15.

There are several points of note in the obtained results. Firstly, there are clear steps in the weight data coinciding with set-point and force endpoint changes. These steps are, however, not proportional to the force endpoint changes. These are particularly pronounced for the adjustments at the two- and three-day marks. Secondly, for large parts of the plot the data is extremely stable, with a standard deviation on the order of the controller noise and with any drift of this size or less. This would suggest that the largest uncertainty contributions are systematic in nature, in line with the previously described derivations. The additional noise in the day-three results is likely to be due to defects in the voltage calibration curves, which could be rectified in future.

The results are centred about $29.27\ \mu\text{N} \pm 0.10\ \mu\text{N}$ and each contributing force reading has an associated uncertainty of about $0.3\ \mu\text{N}$. These results are correlated, but as that correlation is not fully understood it is not appropriate to reduce the uncertainty through statistical or differential arguments. The uncertainty in the final tilt in the vibration isolation table after completion of its internal levelling procedure translates to an alignment uncertainty between the LFB axis and the Earth's gravitational field, and hence a cosine term in the measured weight. The maximum tilt is likely to be considerably better than $2.5\ \text{mrad}$ or

1 mm across the 400 mm width of the table. The cosine error due to such a tilt is 3×10^{-6} , which will be negligible relative to the uncertainty in the raw weight values. The manufacturer specifications suggest a tilt repeatability of 0.4 mrad or a cosine error on the order of 1×10^{-8} .

An estimate for the weight as determined by the LFB is therefore $29.27 \mu\text{N} \pm 0.30 \mu\text{N}$. This is a relative uncertainty of 1.0 %, based on identified sources of uncertainty.

3.9.5 Discussion

The estimates of the artefact's weight from the mass-based and LFB-based routes are shown in figure 3.16. There is a clear discrepancy of about 2.5 % between the two sets of results not explained by the identified uncertainties in either route. The cause of this is unknown but may be due to either a fundamental problem with the LFB operating principle, due to a physical change to the balance post-repair, or even poorer DVM performance than originally estimated.

3.10 Performance verification by international comparison with low force standards at other NMIs

3.10.1 Overview

This section outlines the configuration, undertaking and output of NPL's participation in an international comparison of low force facilities using a Kleindiek force sensor. The NPL Low Force Balance (LFB) is briefly introduced and the Kleindiek cantilever calibration procedure discussed. Due to persisting discrepancies between electrostatic force- and mass-traceable force measurements from the LFB, analysis proceeds using each. The procedure and results for the 'calibration' of the LFB against the NPL mass scale is available in section 3.9 for reference. The calibration of the precision piezo-stage used to lift the Kleindiek cantilever is outlined. Finally the derivation of cantilever stiffness and force sensitivity estimates, and associated uncertainties, is presented. The results are summarised in table form.

3.10.2 Comparison outline

3.10.2.1 Background and motivation

In traceable metrology, primary instruments aim to realise the primary standard for a given measurand within a national metrology system. Such instruments are almost by definition

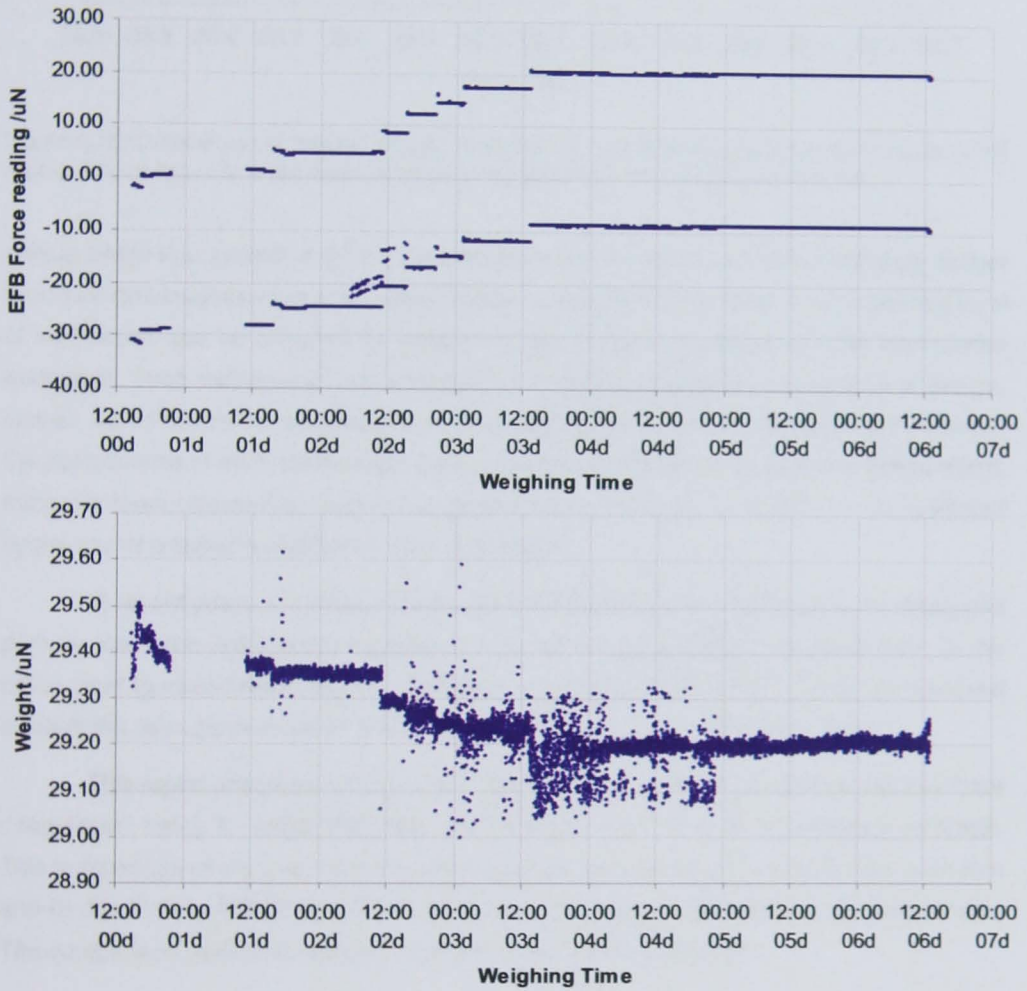


Figure 3.15: Results of experiments to determine the weight of a 2.91 mg mass artefact using the LFB: (top) absolute forces readings on the $\pm 36 \mu\text{N}$ LFB force scale, with setpoint changes, and (bottom) the measured weight over time, ignoring off-scale outliers..

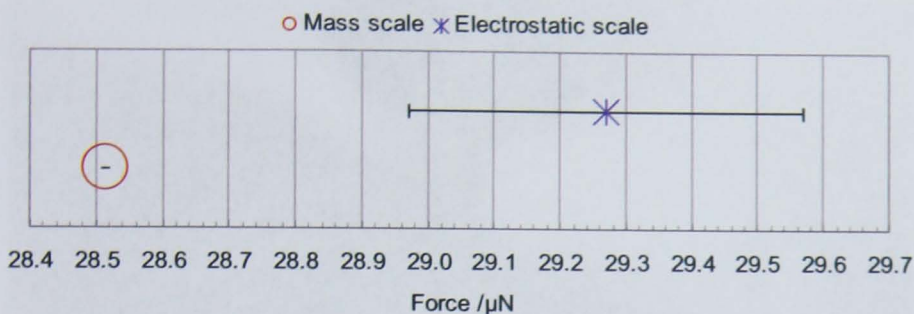


Figure 3.16: Comparison of artefact weight estimates via mass/gravity and electrostatic force (LFB) routes. The uncertainty in the mass estimate is too small to show clearly on this scale.

unique within that system. A primary instrument will have an associated uncertainty budget based on an understanding of how its standard is realised. Nevertheless, an additional level of verification can be provided by comparing equivalent instruments at peer laboratories worldwide. Such instruments are equivalent in function, though not necessarily in design; indeed, agreement between divergent technologies tends to lead to increased confidence in the performance of each technology. Such a comparison provides an effective independent, traceable force comparison scale for a given instrument. Such comparisons are facilitated by the use of a suitable artefact or suite of artefacts.

In recent years a number of national metrology institutes worldwide have developed primary low force instruments capable of realising or measuring a traceable force in the millinewton to nanonewton regime. Comparison between these balances can be achieved through the use of a suitable MEMS transfer artefact, as described in this report.

This report describes NPL's invited participation in an informal international low-force comparison, using Kleindiek FMT-400 and FMT-120 force sensors as reference artefacts. This comparison of low force measurement facilities was administrated by Dr Min-seok Kim and Dr Jon Pratt at KRISS and NIST respectively. PTB also participated in the comparison. The comparison work was recently reported by the participants [34].

3.10.2.2 Basis of the comparison: working artefact

The comparison centred on the calibration of five reference artefacts: four Kleindiek FMT-400 force sensors (see figure 3.17) and one stiffer Kleindiek FMT-120 force sensor. The force sensors take the form of piezoresistive cantilevers and are accompanied by a tunable resistance bridge to create a useful force-to-voltage transducer. For practical reasons, only one FMT-400 was characterised on the LFB, limiting NPL's participation to the comparison.

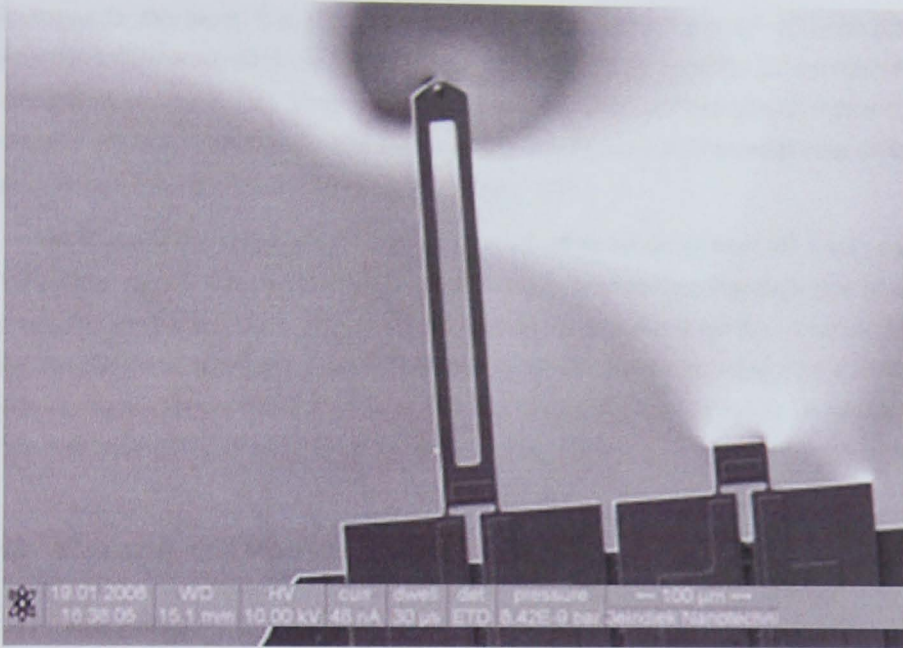


Figure 3.17: The Kleindiek FMT-400 Sensor, a commercial cantilever-format piezoresistive force sensor. (from [11])

Property	Value
Tip force constant (calculation)	2 Nm^{-1} to 4 Nm^{-1}
Maximum tip force *	$80 \mu\text{N}$
Resistance	500Ω to 650Ω
Sensitivity at $V_{\text{bridge}} = 2.5 \text{ V}^\dagger$	$18.8 \times 10^{-3} \text{ mV nm}^{-1}$

Table 3.3: Manufacturer specification for the FMT-400 sensor. (*) Calculated with assumptive deflection of 10 % and the lowest force constant. (†) Dependent on the bias voltage (V_{bridge}) that is applied to the series resistance of sensor and reference.

For reference to the larger comparison effort, note that cantilever #3 was selected. The FMT-400 sensor is shown in figure 3.17 and its specifications listed in table 3.3.

The medium of comparison was the measurement of the stiffness (displacement per unit force) and force sensitivity (signal output change per unit force) of each of the devices.

3.10.2.3 Context of NPL participation in this comparison

Given the value of continual international cooperation in the small force measurement field, NPL was keen to participate in the Kleindiek comparison.

It should be noted, however, that the LFB was operated in a highly non-optimised

configuration for this work. Consequently, uncertainties in raw force readings to be presented from the LFB are significantly higher than understood to be possible for the instrument. The uncertainty increase was primarily due to systematics associated with an indirect measurement of voltage necessitated by a shortage of suitable DMMs. The underlying statistical variation was at the 10 nN level, as shown in section 3.9.

Additionally, the force range-uncertainty tradeoff achieved in the LFB 1 kHz calibrated AC voltage supply transformer ratios could not be optimised for this work due to a lack of associated calibration data. These challenges are logistical rather than metrological in nature. Furthermore, given the uncertainties associated with the handling of the Kleindiek cantilevers, the additional raw force uncertainty increases the total absolute uncertainty values for cantilever stiffness and sensitivity by less than 10 %.

3.10.3 Kleindiek cantilever calibration procedure

3.10.3.1 Procedure

The mechanical arrangement for the comparison experiments is shown in figure 3.18. The Kleindiek cantilever was 'calibrated' by pushing it onto the stationary LFB platen (as described in section 3.8) with a calibrated stage (PI Nanocube nanopositioner) and recording the force, stage displacement and cantilever output signals. The LFB error signal was monitored for significant deviation from controller setpoint. In order to provide traceability to the artefact stiffness, the external displacement scale monitoring the relative position of the artefact body and the LFB platen, that is, the deflection of the cantilever, must be traceably calibrated. This was achieved by deliberately deflecting the LFB with the nanocube and comparing the LFB and nanopositioner displacement scales. The artefact stiffness derives from the relationship between nanopositioner displacement and LFB force reading; the artefact sensitivity derives from the relationship between the artefact sensor output signal and the LFB force reading.

Indenter-mode LFB operation for this cantilever calibration would allow the direct use of the much higher performance LFB interferometer, and might appear to be more appropriate. However, hysteretic effects in the flexure motion increase the uncertainty in the required estimation of the LFB stiffness to an unacceptable level (see section 3.7).

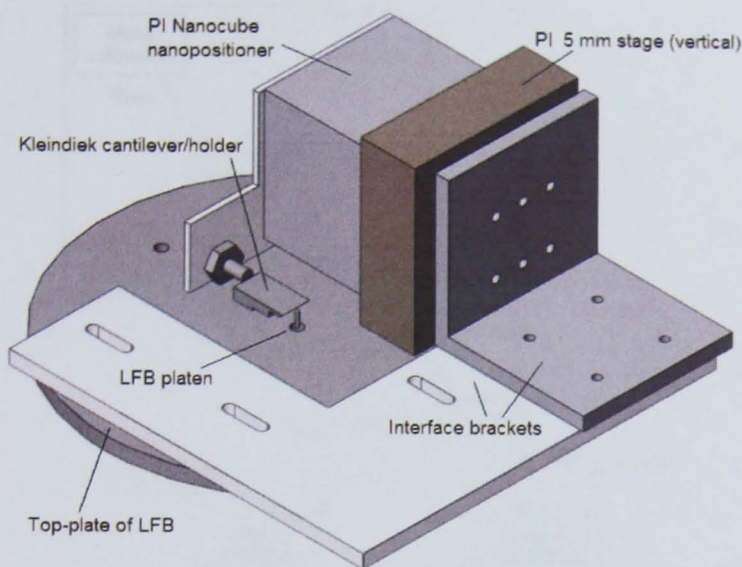


Figure 3.18: Schema of mechanical arrangement for calibration of the Kleindiek cantilever.

3.10.4 Uncertainty propagation

3.10.4.1 Source of traceability for the experiments

Due to preexisting concerns about the systematics shown elsewhere to severely limit the performance of the LFB, a decision was taken to report reports calculated via two routes:

1. Electrostatic force traceability: that is, force values traceable through voltage and capacitance gradient measurements, or
2. Mass traceability: that is, relying only on the proven stability of the LFB force signal, the absolute value of which is 'calibrated' via the comparison described in section 3.9.

Uncertainty and data processing for the two routes will be discussed, with a focus on the latter.

3.10.4.2 Overview of data and uncertainty propagation

An overview of the flow of information, and hence uncertainty, for mass-traceable characterisation of the Kleindiek cantilever is shown in figure 3.19. The mass-comparison experiments summarised in section 3.9 provide a calibration factor to correct the LFB-derived force readings to the mass-traceable force scale. This force scale is used along with the output from

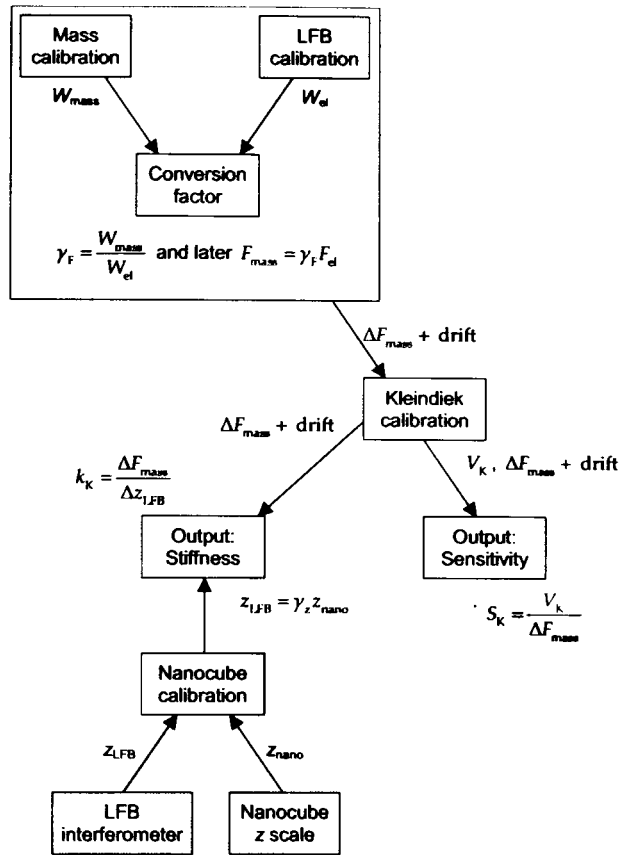


Figure 3.19: Overview of information flow in mass-traceable calibration of the Kleindiek cantilever.

the cantilever controller to calculate a sensitivity value. The vertical axis of the nanopositioner, used to lift the artefact, is calibrated against the LFB interferometer, and an associate conversion factor produced. Corrected nanopositioner positional information is then used along with the force readings to calculate the artefact stiffness.

For the purposes of this discussion, the following consistent shorthand will be used to distinguish between relative and absolute uncertainties:

- u_x is the absolute uncertainty in a representative physical quantity or measurand x , and
- $v_x = \frac{u_x}{x}$ is the relative uncertainty in x , where x is a constant to first approximation.

3.10.5 LFB calibration via mass

The comparison of weight measurements in section 3.9 showed a scale difference between mass-traceable values (W_{mass}) and LFB-derived values (W_{el}). This comparison may be used to 'calibrate' the LFB's electrostatic force scale against the kilogram:

$$W_{\text{mass}} = \gamma_F W_{\text{el}}$$

and subsequently to correct LFB force readings:

$$F_{\text{mass}} = \gamma_F F_{\text{el}} .$$

The uncertainty in γ_F is given by

$$v_{\gamma_F}^2 = v_{W_{\text{mass}}}^2 + v_{W_{\text{el}}}^2 .$$

Based on the results described in section 3.9, the scale factor γ_F is estimated as 0.974 ± 0.010 .

3.10.6 Cantilever stage (PI Nanocube) calibration against LFB

The PI Nanocube nanopositioner vertical stage axis scale was calibrated against the internal LFB displacement scale in a pre-experiment, and a conversion factor γ_z calculated. The base of the cantilever was used to deflect the LFB over the working displacement range. The LFB force output was held at a constant value F_{el} by deliberately saturating the controller digital output. The calculation factor γ_z can be used to calculate the cantilever displacement z_K on the LFB displacement scale z_{LFB} according to

$$\Delta z_K = \gamma_z \Delta z_{\text{nano}} = \gamma_z \left[\frac{1}{\gamma_z} \Delta z_{\text{LFB}} \right] = \Delta z_{\text{LFB}}$$

where $\Delta z_{\text{nano}} = \frac{1}{\gamma_z} \Delta z_{\text{LFB}}$ is implicit from the prior calibration of the nanopositioner.

The use of the base of the Kleindiek cantilever holder in situ on the calibration rig to carry out the nanopositioner calibration means that correlated systematics such as measurement loop compliance, alignment error, abbe error, and so on, are absorbed into the calibration output scale factor.

The uncertainty in the measured displacement z_K of the artefact can be estimated by the quadrature sum of the LFB z scale uncertainty, the experimental variation in γ_z and the manufacturer-specified nanopositioner accuracy according to

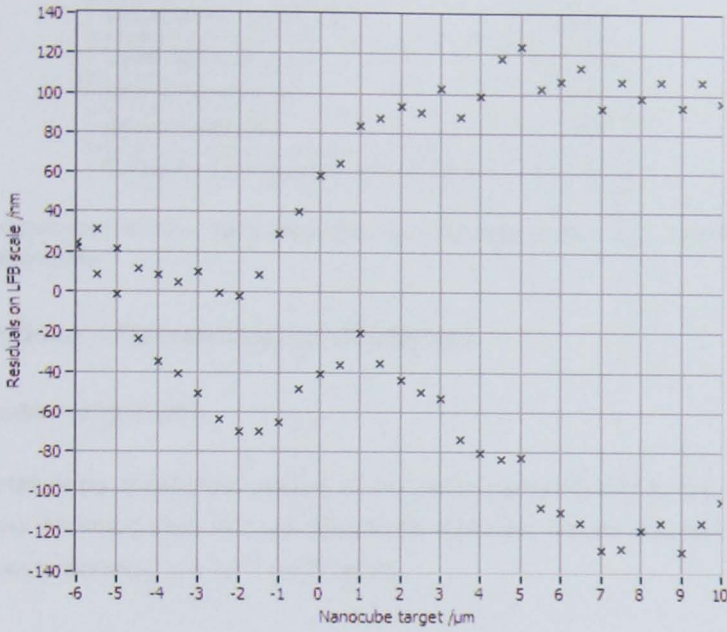


Figure 3.20: Residuals to linear fit of LFB interferometer fit to Nanocube target position over a range of target positions.

$$v_{z_K}^2 = v_{z_{LFB}}^2 + v_{\gamma_z}^2 + v_{z_{nano}}^2 .$$

Due to time constraints, only one nanopositioner calibration experiment could be completed; residuals in the results of this run are shown in figure 3.20. The convergence of the two curves on the left shows the mid-point of the bi-directional experiment. The separation of the curves is due to drift in the nanopositioner. The nominal value of the conversion factor $\gamma_z = \frac{z_{LFB}}{z_{nano}}$ is estimated as the underlying gradient in the whole dataset, that is, that which has been removed from figure 3.20. The underlying gradient is estimated as $1.005 \mu\text{m}\mu\text{m}^{-1}$. The uncertainty in γ_z may be estimated by visual inspection of the residuals; the largest additional gradients are on the order of $\pm 30 \text{ nm}\mu\text{m}^{-1}$ or ± 0.03 . Thus γ_z is estimated to be equal to 1.005 ± 0.030 .

Should repeatable form be evident in the nanopositioner's non-linearities in a future repeat experiment, this uncertainty estimate may be significantly reduced by characterising and correcting for these non-linearities, in a similar approach to that used to recreate the LFB output voltages from prior characterisation.

The combined uncertainty in the measured displacement z_K of the artefact is calculated in table 3.4.

Uncertainty contribution	Value
Uncertainty in z_{LFB}	8.91 nm
Uncertainty in z_{nano}	10 nm
Uncertainty in γ_z	0.03 z
Combined uncertainty at $z = 10 \mu\text{m}$	300 nm

Table 3.4: Combined uncertainty in measurements of z_K . The uncertainty in z_{nano} is dominated by the closed loop repeatability.

3.10.7 Cantilever-LFB interface considerations

3.10.7.1 Interface alignment

Should the artefact be misaligned relative to the plane perpendicular to the LFB axis, a cosine error will be introduced. For typical manual alignment efforts, this misalignment is less than 3° , corresponding to a 10^{-3} uncertainty.

3.10.7.2 Surface friction

Any deflection of a cantilever artefact will inevitably result in parasitic axial deflection. Rotation of the artefact out of horizontal will increase the lateral tip motion with applied force. Due to the likely large difference in horizontal compliance of the LFB platen and artefact, the artefact tip will move across the platen surface. Such motion incurs an uncertainty penalty due to friction forces, which will be hysteretic in nature. Reported experience suggests that uncertainty due to lateral friction will contribute at the 10^{-4} level.

3.10.7.3 Combined impact

The additional combined relative uncertainty in force due to the quality of the interface between the LFB and the artefact is therefore on the order of 10^{-3} , and always reducing. This is around an order of magnitude less than the minimum total relative uncertainty in force measurements with the LFB using the indirect-voltage approach, or 0.01. Thus at present uncertainties due to interface issues will have a negligible additional effect on estimates of artefact stiffness and sensitivity.

3.10.8 Kleindiek artefact stiffness determination

Fifteen force-deflection experiments were completed with the studied artefact. The Nano-cube was used to move the cantilever vertically into contact with the LFB, continue until the

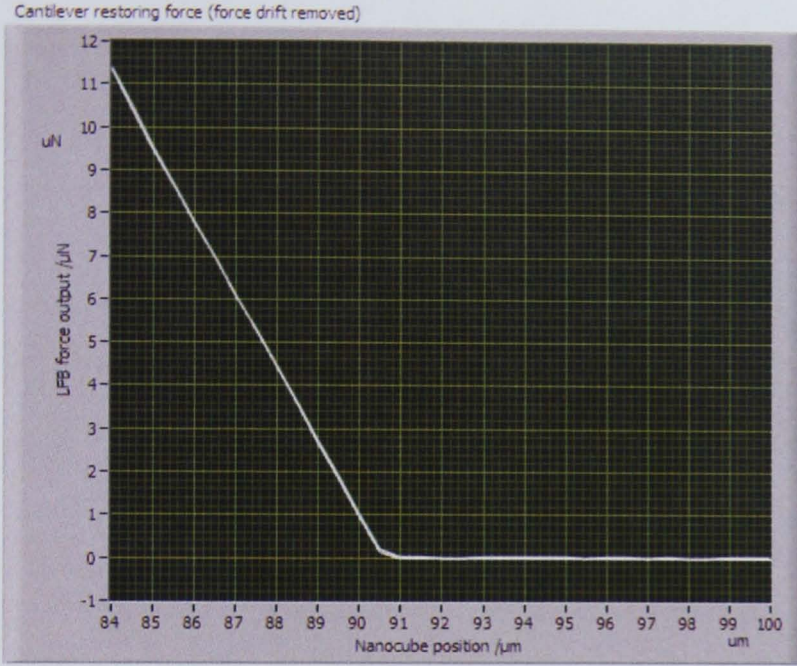


Figure 3.21: Raw Kleindiek calibration data: LFB force output versus Nanocube target position.

cantilever sensor output saturated, and finally to return the cantilever to its original position. The cantilever was held stationary at a number of deflection points whilst stable force, displacement and artefact sensor output values were recorded. Examples of the variation of LFB force output and cantilever signal output with Nanocube position are shown in figures 3.21 and 3.22 respectively. Figure 3.23 shows the general form of the observed relationship between force and cantilever signal output. The three output signals may be combined to derive artefact stiffness and sensitivity.

The cantilever stiffness is given by the gradient of the (corrected) measured LFB force F_{mass} against the cantilever displacement z_K :

$$k_K = \frac{\Delta F_{\text{mass}}}{\Delta z_K} = \frac{\gamma_F \Delta F_{\text{cl}}}{\gamma_z \Delta z_{\text{nano}}}$$

and the uncertainty in k_K by

$$v_{k_K}^2 = v_{F_{\text{mass}}}^2 + v_{z_K}^2 + \text{gradient variation} + \text{residuals}.$$

The stiffness of the artefact is estimated from the gradients of the collection of plots of the form of figure 3.21. A first-order fit was applied to each dataset. The constant (zeroth order) term represents force drift and was removed; its variation is shown in figure 3.24.

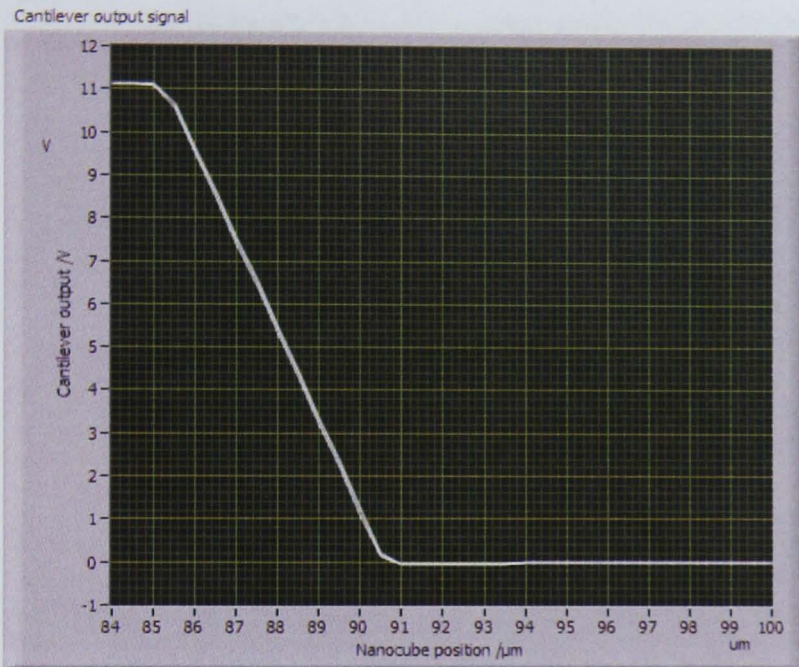


Figure 3.22: Raw Kleindiek calibration data: cantilever output signal versus Nanocube target position.

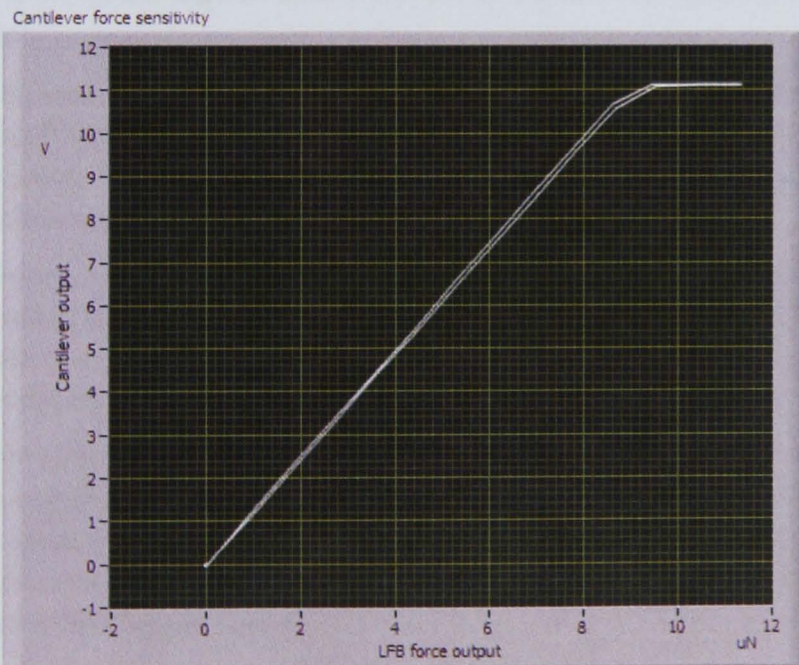


Figure 3.23: Raw Kleindiek calibration data: cantilever output signal versus LFB force output.

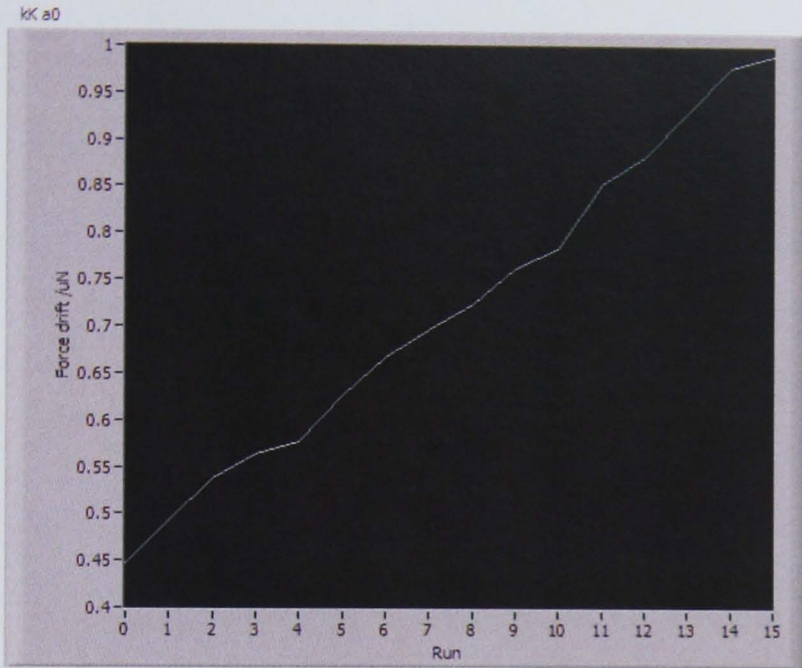


Figure 3.24: Force drift as zeroth order term in linear fit of LFB force to nanocube position.

The drift is particularly large because insufficient settling time was available for suitable reductions.

The linear (first order) coefficient is the nominal stiffness and is shown in figure 3.25 for all runs. The mean and standard error in the first order coefficients are 1.6987 N m^{-1} and 0.0012 N m^{-1} respectively. Applying γ_F and γ_z to this mean gradient gives a nominal artefact stiffness of 1.646 N m^{-1} .

Residuals to the linear fits are shown in figure 3.26. The residuals contribute an additional gradient variation of up to 80 nN in 500 nm , or a standard uncertainty of 0.092 N m^{-1} (rectangular distribution). The apparent repeatability of the non-linearities in the stiffness with deflection suggest a systematic or material property cause.

The estimate of the artefact stiffness based on the electrostatic force traceability route is calculated trivially by setting γ_F equal to unity; in this case the nominal stiffness value increases to 1.690 N m^{-1} . The combined uncertainty in the measured stiffness k_K of the artefact is calculated in table 3.5, in which the uncertainty due to non-linearities in the force-displacement plots dominates.

The stiffness of the studied artefact is therefore estimated to ($k=1$) as

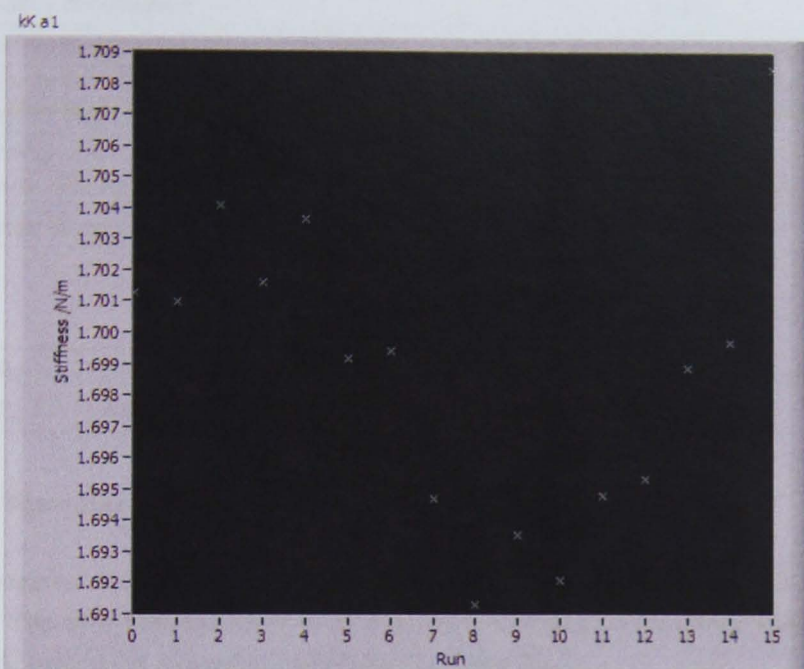


Figure 3.25: Cantilever stiffness estimates as first order term in linear fit of LFB force to nanocube position.

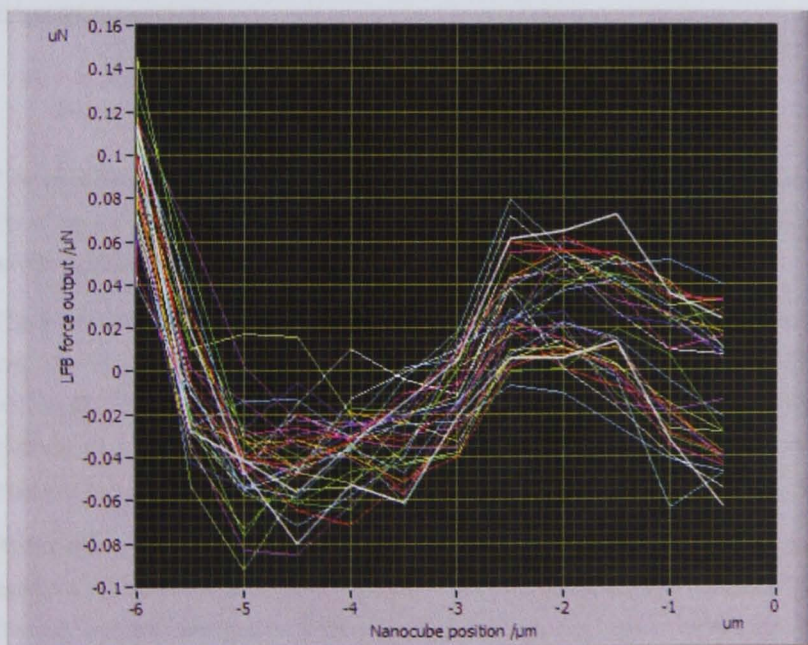


Figure 3.26: Residuals in linear fit of LFB force to (change in) nanocube position.

Uncertainty contribution	Value
Uncertainty due to relative uncertainty in F_{mass}	$0.01 \times 1.690 \text{ Nm}^{-1} = 0.017 \text{ Nm}^{-1}$
Uncertainty due to relative uncertainty in z_K	$0.03 \times 1.690 \text{ Nm}^{-1} = 0.051 \text{ Nm}^{-1}$
Uncertainty due to gradient variation	0.0012 Nm^{-1}
Uncertainty due to non-linearities	0.092 Nm^{-1}
Cantilever misalignment cosine error	$10^{-3} \times 1.690 \text{ Nm}^{-1} = 0.0017 \text{ Nm}^{-1}$
Combined uncertainty	0.106 Nm^{-1}

Table 3.5: Combined uncertainty in estimate of k_K .

$k_K = 1.690 \text{ Nm}^{-1} \pm 0.106 \text{ Nm}^{-1}$ (Electrostatic force traceability route)
$k_K = 1.646 \text{ Nm}^{-1} \pm 0.106 \text{ Nm}^{-1}$ (Mass traceability route)

3.10.9 Kleindiek artefact force sensitivity determination

The estimate for the force sensitivity of the artefact is obtained in a similar manner to the stiffness. The cantilever sensitivity s_K is given by the gradient of cantilever sensor output voltage V_K against the (corrected) measured LFB force F_{mass} :

$$s_K = \frac{\Delta V_K}{\Delta F_{\text{mass}}} = \frac{\Delta V_K}{\gamma_F \Delta F_{\text{mass}}}$$

and the uncertainty in k_K by

$$v_{s_K}^2 = v_{F_{\text{mass}}}^2 + v_{V_K}^2 + \text{gradient variation} + \text{residuals.}$$

The sensitivity of the artefact is estimated from the gradients of the collection of plots of the form of figure 3.23. These raw plots are combined in figure 3.27; residuals to a linear (first order) fit applied to each dataset are shown in figure 3.28.

The linear (first order) coefficient is the nominal sensitivity and is shown in figure 3.29 for all runs. The mean and standard error in the first order coefficients are $1.2343 \text{ V}\mu\text{N}^{-1}$ and $0.0003 \text{ V}\mu\text{N}^{-1}$ respectively. Applying γ_F to this mean gradient gives a nominal artefact force sensitivity of $1.2672 \text{ V}\mu\text{N}^{-1}$. The former value corresponds to the nominal value via the electrostatic force traceability route; the latter to that via the mass traceability route.

Residuals to the linear fits are shown in figure 3.28. The residuals contribute an additional gradient variation of up to 0.08 V in $2 \mu\text{N}$, or a standard uncertainty of $0.023 \text{ V}\mu\text{N}^{-1}$ based on a rectangular distribution of the influence of the residuals. The apparent repeatability of the non-linearities in the stiffness with deflection suggest a systematic or material property cause. The maximum deflection occurs at the right-hand end of this plot; there is a

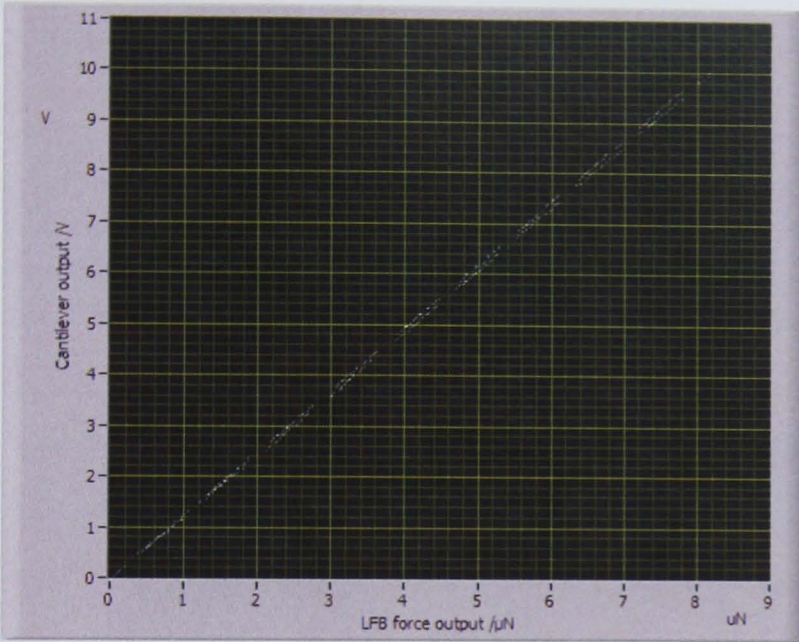


Figure 3.27: Collated plot of cantilever sensor output versus applied force, for all 15 runs.

clear separation in the cantilever sensor output between the 'approach' and 'retract curves'. Note that the curves rejoin at a higher force value, outside the studied region of linear behaviour. The resultant hysteresis loop represents loss in the system.

The artefact sensor output voltage was measured using the same Keithley 2000 DMM used to calibrate the LFB drive voltages. Manufacturer estimates suggest the finite DMM accuracy contributes a relative uncertainty of 5.2×10^{-4} whilst the finite DMM resolution contributes an absolute uncertainty of 0.58 mV. Summing in quadrature for a 10 V working voltage, the uncertainty in the measurement of the artefact sensor output is estimated as 5.2 mV: the accuracy component dominates.

The combined uncertainty in the measured force sensitivity s_K of the artefact is calculated in table 3.6, in which the uncertainty due to non-linearities in the force-displacement plots dominates.

The estimate of the artefact force sensitivity based on the electrostatic force traceability route is calculated trivially by setting γ_F equal to unity; in this case the nominal force sensitivity value increases to $1.234 \text{ V}\mu\text{N}^{-1}$. The force sensitivity of the studied artefact is therefore estimated to ($k=1$) as

$s_K = 1.234 \text{ V}\mu\text{N}^{-1} \pm 0.026 \text{ V}\mu\text{N}^{-1}$	(Electrostatic force traceability route)
$s_K = 1.267 \text{ V}\mu\text{N}^{-1} \pm 0.026 \text{ V}\mu\text{N}^{-1}$	(Mass traceability route)

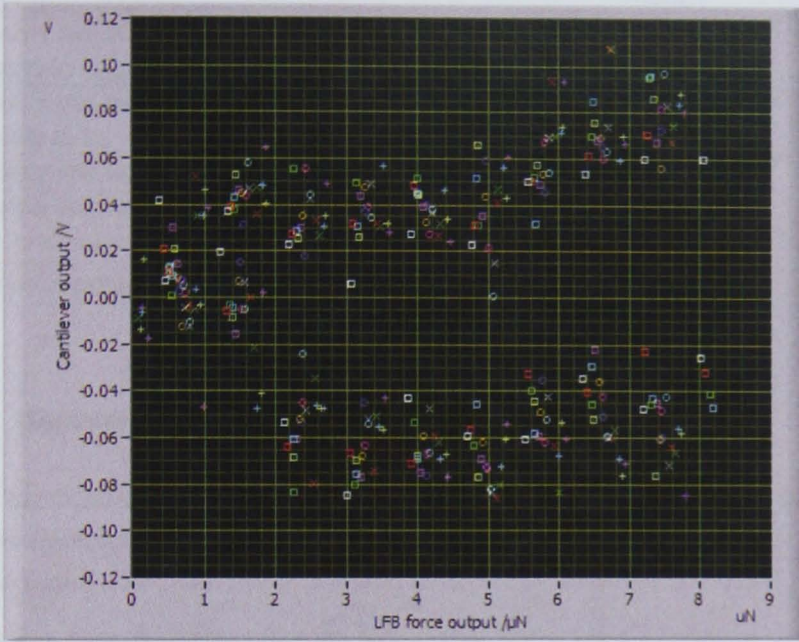


Figure 3.28: Residuals in linear fit of artefact sensor output signal to LFB force, for all runs.

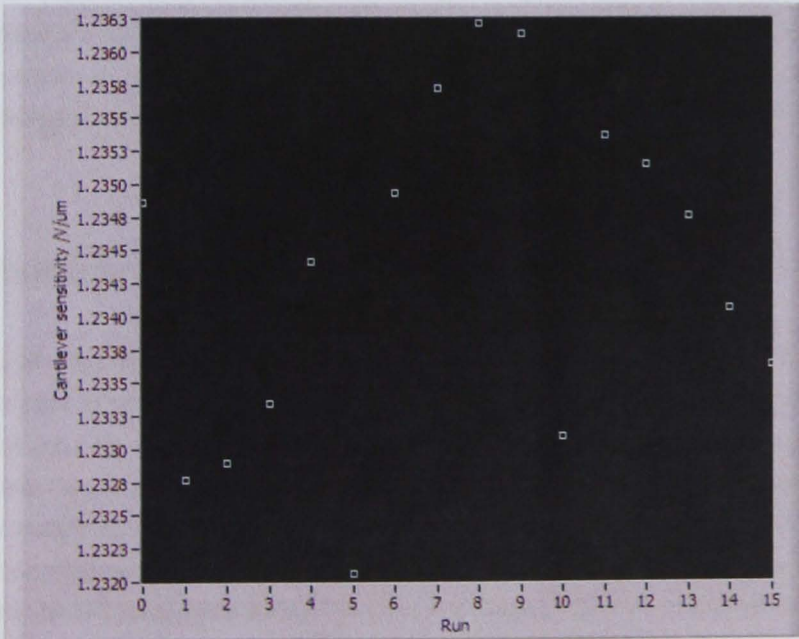


Figure 3.29: Cantilever force sensitivity estimates as first order term in linear fit of artefact sensor output signal to LFB force.

Uncertainty contribution	Value
Uncertainty due to relative uncertainty in F_{mass}	$0.01 \times 1.267 \text{ V}\mu\text{N}^{-1} = 0.013 \text{ V}\mu\text{N}^{-1}$
Uncertainty due to relative uncertainty in V_K	$5.2 \times 10^{-4} \times 1.267 \text{ V}\mu\text{N}^{-1} = 6.6 \times 10^{-4} \text{ V}\mu\text{N}^{-1}$
Uncertainty due to gradient variation	$0.0003 \text{ V}\mu\text{N}^{-1}$
Uncertainty due to non-linearities	$0.023 \text{ V}\mu\text{N}^{-1}$
Cantilever misalignment cosine error	$10^{-3} \times 1.267 \text{ V}\mu\text{N}^{-1} = 0.0012 \text{ V}\mu\text{N}^{-1}$
Combined uncertainty	$0.026 \text{ V}\mu\text{N}^{-1}$

Table 3.6: Combined uncertainty in estimate of s_K .

3.10.10 Summary of results

The LFB has been successfully used to determine values for the stiffness and force sensitivity of the Kleindiek cantilever artefact #3. The results and uncertainty derivation are summarised in table 3.7.

It was later determined that, for either route of traceability (force or mass route), the results reported here agree to the averages of three NMIs' values (NIST, PTB, KRISS) within estimated uncertainties [34]. The average values for the #3 cantilever are, for stiffness, 1.665 N m^{-1} , and for force sensitivity, 1.262 V mN^{-1} . Further investigations would focus on the identification and compensation of systematic uncertainties in the complementary but unique systems at each NMI. Furthermore, future comparisons should be based upon a more universally compatible artefact, such as one developed specifically at a participant NMI.

3.11 Summary of development

This chapter describes the development activities undertaken to bring the LFB to a working state prior to use with transfer artefacts. A fringe-counting interferometer was implemented on the LFB, replacing the existing fringe-locking design to introduce the ability to characterise flexure displacement-dependent systematic effects, such as capacitance gradient non-linearities. The LFB feedback controller output was modulated with an AC signal to mitigate unanticipated surface charging effects, whilst maintaining the instantaneous phase relationship for DC force generation. The LFB was adapted to accommodate vibration isolation hardware, following an investigation into the potential benefits. Improved capacitance gradient and voltage measurement approaches were developed. Also presented are comparisons of the LFB electrostatic force traceability scale with the NPL mass scale, via small

Calibration of Kleindiek comparison artefact #3 on NPL LFB

Calibration information

Artefact description	Kleindiek FMT-400 cantilever		
Identification	#3		
Calibration period	26-Feb-10 to 28-Feb-10		
Operator	Chris Jones		
Average temperature	20 ±	0.05 °C	

Mass comparison (to 'calibrate' LFB against mass scale) - see appendix

Mass artefact calibration (Sartorius C5 mass balance)

Estimated artefact mass	2.9061 ±	0.0004 mg	
Local gravitational acceleration	9.81182 ±	0.00001 m/s ²	
Equivalent weight	28.5140 ±	0.0044 µN	

Mass artefact weighing on LFB

Weight estimate based on 7200 weighings	29.27 ±	0.3 µN	
---	---------	--------	--

LFB 'calibration' scale factor based on comparison

gamma F	0.974 ±	0.010	(k=1)
---------	---------	-------	-------

This is dominated by systematic uncertainties in the force reading, such that the uncertainty in gamma_F is a good estimate for the relative uncertainty in a LFB force reading from either traceability route.

Kleindiek cantilever stage (PI Nanocube) calibration against LFB internal scale

gamma_z for 10µm move	1.005 ±	0.03	(k=1)
-----------------------	---------	------	-------

Kleindiek cantilever stiffness determination k_K based on 15 trials

Nominal cantilever stiffness k_K

Electrostatic force traceability route	1.690	N/m
Mass traceability route	1.646	N/m

Analysis of uncertainty in k_K, both routes

Uncertainty contribution	Value
Relative uncert. in LFB operation = 0.01 k_K	0.017 N/m
Relative uncert. in cantilever stage scale = 0.03 k_K	0.051 N/m
Uncertainty due to gradient variation	0.001 N/m
Uncertainty to to non-linearities	0.092 N/m
Cantilever misalignment cosine error = 0.001 k_K	0.002 N/m
Combined uncertainty	0.106 N/m

Summary

Electrostatic force traceability route	1.690 ±	0.106 N/m	(k=1)
Mass traceability route	1.646 ±	0.106 N/m	(k=1)

Kleindiek cantilever sensitivity determination s_K based on 15 trials

Nominal cantilever force sensitivity s_K

Electrostatic force traceability route	1.234	V/µN
Mass traceability route	1.267	V/µN

Analysis of uncertainty in s_K, both routes

Uncertainty contribution	Value
Relative uncert. in LFB operation = 0.01 s_K	0.013 V/µN
Relative uncert. in cantilever voltage meas. = 0.00052 s_K	0.001 V/µN
Uncertainty due to gradient variation	0.000 V/µN
Uncertainty to to non-linearities	0.023 V/µN
Cantilever misalignment cosine error = 0.001 s_K	0.001 V/µN
Combined uncertainty	0.026 V/µN

Summary

Electrostatic force traceability route	1.234 ±	0.026 V/µN	(k=1)
Mass traceability route	1.267 ±	0.026 V/µN	(k=1)

Electrostatic force traceability route, inverted	0.810 ±	0.017 µN/V	(k=1)
Mass traceability route, inverted	0.789 ±	0.016 µN/V	(k=1)

Table 3.7: Summary of results and uncertainties in the NPL estimates of the stiffness and force sensitivity of the Kleindiek cantilever artefact #3.

mass artefacts, and with primary balances at other NMIs, via a commercial force sensor.

Chapter 4

Requirements for a successful low force transfer artefact

Before considering the technologies available for a low force transfer artefact in chapter 5, it is prudent to clarify the function of the “ideal” low force transfer artefact and the key features that allow it to successfully transfer the traceable realisation of force to a target instrument [31]. By definition, the successful transfer artefact must:

1. be calibrated on the NPL LFB, subject to the constraints imposed by the operation of the LFB;
2. calibrate force acceptors, that is, target systems that deflect mechanically under an external load but do not generate a force other than that associated with elastic restoration;
3. calibrate force producers, that is, systems that generate a force as a function of some control signal, typically generating an insignificant associated deflection; and
4. maintain stable and repeatable behaviour over at least the length of the calibration cycle, that is, calibration on the LFB, then calibration of the target, and finally, verification on the LFB.

Each of these calibration steps imposes a set of strict operating requirements on the function of the ‘ideal’ transfer artefact, requirements which in some cases are in conflict. The details of the requirements for each of these steps are perhaps best illustrated with the help of diagrams.

4.1 Calibration of artefacts on LFB

To interact effectively with the very stiff LFB, an interacting transfer artefact must be relatively compliant (see section 4.4). Experience of the author acquired during, for example, the comparison work described in section 3.10 suggests that the LFB struggles to interact with artefacts with stiffness greater than around 20 N m^{-1} . Note that the stiffness of the transfer artefact is significant in terms of its usage, as will be discussed shortly.

Such a transfer artefact only has value if any metrology required for operation at the target instrument is self-contained within the transfer artefact, or within a supplied controller. It is not sufficient to rely on the end user to provide such metrology, since such metrology equipment would typically not be appropriately calibrated, destroying the traceability of the transfer artefact. Furthermore, in order to obtain the most value from a calibration, it is standard practice to employ a calibrator that is at least a factor of ten more accurate in all respects than the target instrument. As will be later argued, successful force transfer artefacts are typically realised as repeatable springs. According to Hooke's law, for the artefact to measure a force, therefore, the transfer artefact must have onboard displacement metrology. Typically, some integral transducer will convert artefact spring deflection (or more specifically strain) into a useful, conveniently-scaled voltage analogue¹. The transfer function of the transducer would be linear and repeatable, such that if the stiffness of the transfer artefact along the deflected axis were constant over the intended range of deflection, then the output voltage of the transfer artefact strain transducer would be an analogue of the force applied to the transfer artefact.

A more compliant transfer artefact also offers advantages in terms of displacement resolution. Material effects and fundamental noise floors impose limits on the absolute displacement resolution of any onboard strain-sensing metrology. A more compliant artefact would achieve a finer force resolution for a given displacement resolution. For a more compliant artefact, the smallest resolvable displacement would correspond to a smaller change in force.

The ideal transfer artefact would, therefore, be calibrated on the LFB in the following manner, summarised in figure 4.1. A stable external stage would push the transfer artefact into the LFB platen so that the artefact deflects. Traceable measurements of force from the LFB during the quasistatic deflection of the artefact would then be combined with simultaneously acquired voltage analogue data to calculate (and hence calibrate) the force

¹Note that, of course, at some point the data must transfer to the user system and downstream traceability becomes the responsibility of the end user. The aim of this transfer artefact is to make the force value implicit (by actively maintaining a preset deflection, much like in the LFB) or transform it onto a scale measurable by instruments that can be procured and calibrated traceably (e.g. a commercial digital multimeter).

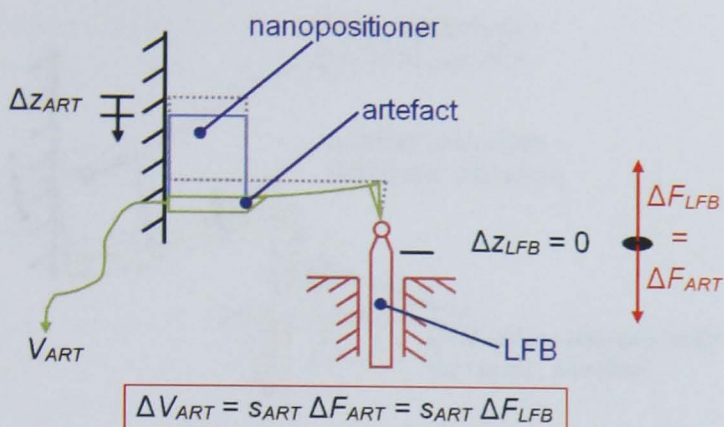


Figure 4.1: Schema of calibration of compliant artefact on LFB.

sensitivity of the transfer artefact. This force sensitivity would have dimensions of force per unit potential difference, typically using practically scaled units of mNV^{-1} or nNmV^{-1} .

If the external stage scale has been traceably calibrated, for example against the internal displacement interferometer of the LFB, then external stage displacement data may be combined with the LFB force data to calibrate the stiffness of the artefact. In this case, attention must be devoted to considering the full displacement metrology loop involved. In particular, the generated displacement of the external artefact stage, from which the stiffness is calculated, will be equal to the deflection of the artefact, plus the deflection of the stage support, plus the compression of the LFB platen (see figure 4.2). Very compliant artefacts would clearly also offer benefits in terms of relative artefact/loop stiffness. The most significant aspects of the characterisation of the external motion stage are its linearity and its stiffness under load. Both would need to be determined to a level appropriate for the artefact under test.

4.2 Calibration of stiff target instruments using a compliant transfer artefact

The ideal operation of the transfer artefacts, in calibrating the diversity of target instruments, is best explained by polarising that range into two distinct scenarios, considered separately.

Interaction with a very stiff target ($k_{\text{target}} \gg k_{\text{artefact}}$), such as an instrumented indenter, would be similar to interaction with the LFB. A precision linear stage, which need not be traceably calibrated, would be used to push the very compliant transfer artefact into the

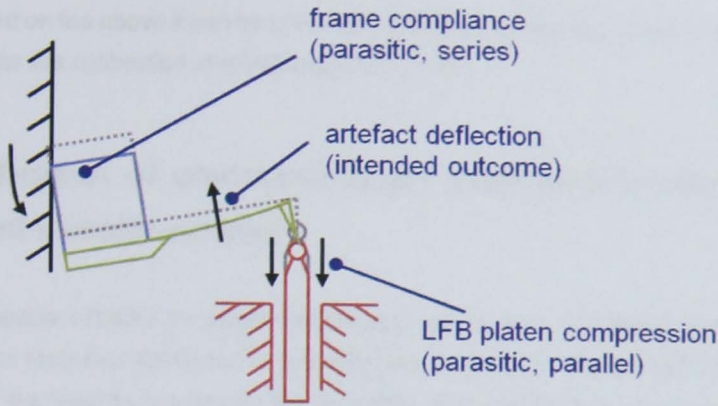


Figure 4.2: Cartoon of measurement loop deflection

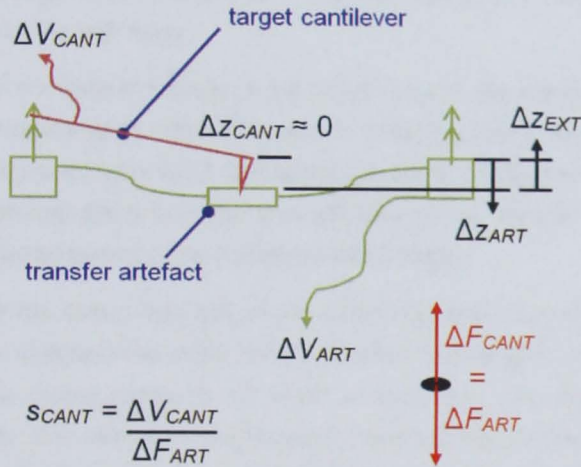


Figure 4.3: Schematic diagram of use of transfer artefact to calibrate a stiff target instrument.

platen of the target instrument, as shown schematically in figure 4.3. After contact, the transfer artefact would deflect significantly; the target instrument would not. The force applied to the target instrument would then be calculated based on the transducer signal and the pre-calibrated artefact force sensitivity. The target instrument would be experiencing a traceably known force, and its internal sensors could be calibrated accordingly.

The uncertainty of the force calibration in this scenario is highly dependent on the ratio of the artefact and target stiffness, and hence the degree to which the target instrument displacement can be considered 'insignificant'. Specifically, the relative uncertainty contribution due to the finite stiffness of the target is on the order of the ratio of those spring constants. Recently reported uncertainty levels of 0.1 % to 1 % correspond to two to three orders of magnitude for this ratio. [133, 15]

Based on the above it can be concluded that a very compliant artefact would be most appropriate for the calibration of a stiff target instrument.

4.3 Calibration of compliant target instruments using a compliant transfer artefact

The ideal transfer artefact for target instruments with a very compliant contact ($k_{\text{target}} \leq k_{\text{artefact}}$) differs from that discussed in the previous sections. In this scenario, the challenge originates in the need to account for the deflection of the target instrument. As the transfer artefact and the target instrument are pushed together, both will deflect (see figure 4.4). The force applied to the target is calculated from the sensor output (as a result of deflection) and force sensitivity as for the stiff target.

To calibrate the force sensitivity of the target - that is, the variation of some internal sensor scale with applied force - the procedure is straightforward. Newton's laws demand that the force experienced by artefact and target are equal, subject to alignment, and the applied force can be calculated, from the pre-calibration of the transfer artefact's own force sensitivity, for any displacement of the transfer artefact holder.

To calibrate the spring constant of the target, the deflection ambiguity presents a challenge. The ratio of deflections of the transfer artefact and target instrument is dependent on the ratio of their spring constants, of which at least one - the target instrument - is not known traceably. The deflection of the transfer artefact may be calculated from a pre-calibration of its displacement sensitivity, though typically with a larger uncertainty than associated with force sensitivity values for practical reasons (see 3.10). Alternatively, the artefact deflection can be reduced to an insignificant level by specifying a high artefact spring constant, in conflict with the requirements for the LFB. Finally the artefact deflection can be artificially reduced to a low level by force feedback, that is, generating a force inside the artefact to null any deflection. This approach would be complex, expensive and not particularly practical (see section 2.4.1.4).

In any case, in order to then calculate the target deflection, the total displacement of the artefact holder must be known traceably. To demand the use of a traceably calibrated displacement stage to displace the artefact holder would either break the requirement for self contained metrology by requiring the user to provide the stage, or demand the inclusion of such a stage with each distributed artefact, driving up the price of each system by perhaps £2 000, at today's prices.

A better approach would be to hold the artefact holder in contact with, and stationary

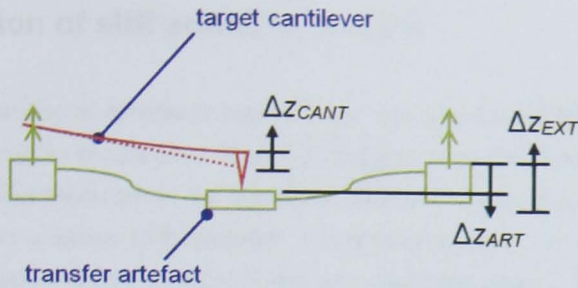


Figure 4.4: Schema of calibration of a compliant target with a passive transfer artefact of similar stiffness.

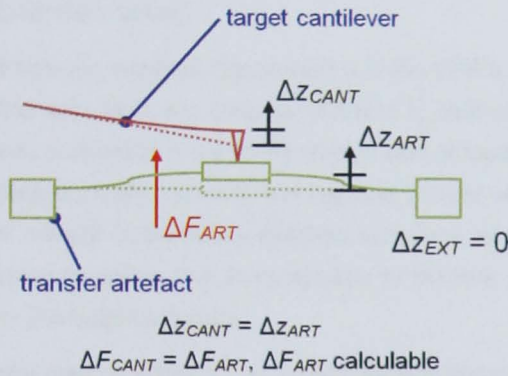


Figure 4.5: Schema of calibration of a compliant target with an active (pushing) transfer artefact of similar stiffness.

relative to, the body of the target instrument and somehow generate a strain (deflection) in the artefact, and hence in the target instrument platen (see figure 4.5). The task would then be to characterise, via set offline experiments or indenter operation of the LFB, the relationship between the stiffness of the target instrument and the degree to which the generated strain for a given input force (within the actuator) is 'blocked' (by the reaction force from the target).

The net force applied by the transfer artefact on the target instrument is then derived from this prior artefact characterisation, and the transfer artefact (and hence target) deflection derived from knowledge of the transfer artefact displacement sensitivity. The challenge in this scenario comes from the need to generate strain repeatably, which is non-trivial, as will be shown.

4.4 Calibration of stiff artefacts on LFB

In the case of calibration of compliant targets it was noted that the calibration of a stiff artefact on the LFB would be challenging. The LFB struggles to maintain a zero deflection state in contact with a stiff artefact due to the significant change in required control loop gain parameters compared to 'unladen' LFB operation. It is time consuming and impractical to retune the gains of the balance control system for use with each new artefact. Even if new gain parameters can be found, it is not possible, with the current LFB hardware and a stiff artefact, to transition between gain parameters correctly to maintain appropriate null deflection during make (or break) of LFB-artefact contact .

A work-around solution requires the operation of the LFB in a non-standard mode: indentation mode. In this approach, the balance stiffness is calibrated prior to artefact interaction by progressively increasing the internal electrostatic force and noting the resultant platen deflection interferometrically. Typically the balance control set-point is varied under displacement feedback control (superficially identical operation to null-deflection) to minimise uncertainties relating to noise. The force applied to achieve the setpoint is used to calculate the stiffness of the balance flexure.

Stiff artefacts can then, in principle, be calibrated by pushing them into the LFB platen with the LFB electrostatic drive disabled (or saturated to create a constant force). The LFB stiffness and interferometer data would be used to determine the reaction force from the LFB. According to Newton's laws, once again, the force applied to the transfer artefact would be equal to the reaction force in the balance. The spring constant of the artefact could be estimated from the calculated force and the discrepancy between the (calibrated) artefact holder displacement and the interferometric readout from the LFB. This spring constant would then be used to calculate the stiffness ratio and associated uncertainty in the interaction of the artefact with the balance and later targets. A key limitation to this approach, however, originates in the balance itself. The LFB flexures have been shown to exhibit a reasonably large amount of hysteresis, which results in a balance stiffness that is dependent on the position in the loop cycle (see section 3.7). This immediately imposes a best-case uncertainty limit on the performance of the artefact of about 0.6 %, which is certainly less than ideal.

An alternative approach that may permit normal operation of the LFB would be to place the artefact series with a third, compliant component (figure 4.6) and push the combined arrangement against the LFB platen. The secondary flexure would assist the LFB to maintain servo control and provided the resonant characteristics of the LFB and transfer artefacts do not overlap, force would equilibrate as required. The main source of uncertainty in this approach would be in the mechanics of the secondary flexure, such as parasitic com-

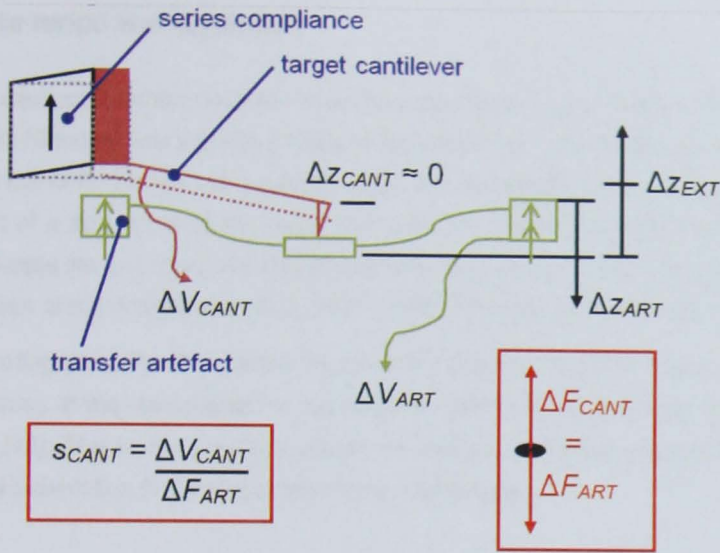


Figure 4.6: Schematic of stiff artefact calibration on LFB using secondary flexure

pliance in other axes. Furthermore, this approach would preclude the in-situ calibration of spring constant, which would have to be estimated by some other means.

4.5 Other general constraints

The remaining constraints determine the range of target instruments with which the artefacts can be used, and the ability of the artefact to maintain a calibration/repeatable behaviour over a range of external inputs. These remaining constraints will be discussed in turn.

4.5.1 Force vector

The successful artefact must be uniaxial. That is, the artefact must only accept (or generate) a force along a single, well-defined, constant vector. Practically this implies infinite stiffness in all but one of the six degrees of freedom of the artefact platen.

Successful use of the artefact sets the requirement for easy orientation to the working axis. Therefore, the artefact must have a suitable datum surface enable optimisation of orientation. Poor orientation between the working axis of the artefact and that of the LFB or the target instrument not only introduces a cosine error, but also implies parasitic lateral motion at the interface and hence friction related issues [34, 134].

4.5.2 Force range and resolution

Common to each case is the need to cover the entire force range of the LFB, that is, from 10 μN to 1 nN. Since no one artefact is likely to have the force input range and measurement resolution of the LFB, though this would be ideal, it is expected that the successful artefact will form part of a suite of artefacts, each optimised for different decades of the LFB force range. In principle the use of several complementary techniques across the suite of artefacts would introduce some comparison mechanism, whilst driving up the development cost.

A starting point for NPL efforts could reflect the current NIST target of an artefact to transfer forces at the nanonewton to micronewton level with an accuracy of a few tenths of a percent [73]. This is the accuracy sought for related draft measurement standards for instrumented indentation [135] and atomic force microscopy.

4.5.3 Artefact orientation

The artefact is likely to require inversion with respect to gravity without losing calibration. Most target instruments probe downwards onto a sample holder; in comparison the LFB is accessible only from above. The installation of a mechanism to invert the probing direction of the LFB would invalidate most of the unique design advantages of the LFB, significantly increasing working uncertainties.

If the artefact calibration is embodied in the value of some linear property, such as stiffness or force sensitivity, then provided the artefact is held steady in the required orientation, then measured *changes* in applied force should be independent of orientation. The absolute measured force value will of course vary according to the component of the moving mass weight acting along the working axis.

4.5.4 Tip design

The artefact will be required to make contact with the LFB in a well-defined manner. The base platen of the balance is currently the millimetre diameter circular top face of the glass rod, protruding from the balance body. Thus either the artefact must incorporate a tip, or one must be installed on the balance platen and characterised for the inevitable compliance at the interface (see section 3.10 for an example). A complication arises because most target instruments interact via their own tip, and tip-tip interactions are fraught with difficulties associated with achieving and maintaining alignment. A small radius sphere could form a compromise between a tip and a flat; the curvature of the sphere facilitates a certain amount

of fine adjustment of alignment by 'feel', that is, by monitoring the artefact sensor output rather than by optical inspection. The chosen tip must accommodate, by replacement or addition, a flat-pan platen for mass comparison experiments.

4.5.5 Size

The working volume of the target instrument will set the upper limits for the dimensions of the successful artefact. Instruments designed to probe objects or processes on the micro- to nanoscale typically have a short z range and clearance (throat) and the lateral range is typically minimised for metrology loop optimisation reasons.

As stated by Pratt *et al.* [136], a successful transfer artefact would be a device with a well defined loading point, responsive to loads only along a well-defined axis, and possessing its own sensor for converting the load into a useable readout. It should be noted, however, that any guidance system would represent an alternative force path. Pratt *et al.* [136] further suggest that for the transfer artefact to be capable of use in either transfer approach, it must be compatible with both commercial AFM sensor and specimen holders, limiting the artefact volume to the typical $3.6 \text{ mm} \times 1.6 \text{ mm} \times 0.1 \text{ mm}$.

The exception will be the case where the target instrument component to be calibrated, such as an AFM probe, can be removed and calibrated with the artefact more flexibly. Nevertheless, the remaining relative bulk of the probe chip and holder, to continue with the AFM example, will limit accessibility to the probe tip by the artefact (see figure 3.14).

It is expected that the working part of the artefact will need to occupy a volume of less than about $20 \text{ mm} \times 20 \text{ mm} \times 10 \text{ mm}$, and that the chip holder will be modified per application at a reduced cost.

4.5.6 Environmental stability

Though the environmental conditions achievable in the vicinity of the LFB are quite stable², considerably wider variation in operating environmental conditions can be expected at the various target instrument laboratories. The expected range during transport is wider still.

The ideal artefact would be expected to return to its calibrated state after excursions in temperature of say $0 \text{ }^\circ\text{C}$ to $50 \text{ }^\circ\text{C}$ and humidity excursions of say 0 \% RH to 100 \% RH . The artefact's behaviour would have well defined (ideally insignificant) dependencies on variation in atmospheric pressure, humidity and temperature.

²Temperature stability specification $20.00 \text{ m} \pm 0.01 \text{ m}$; humidity specification $40 \text{ \%} \pm 5 \text{ \% RH}$; pressure as ambient

Given the strong temperature dependence of most bulk material properties and dimensions, it is expected that temperature variation will have the more significant influence on artefact performance.

4.5.7 Ruggedness to environmental input and operator error

The ideal artefact must withstand the rigours of its operation and transport. In the ideal case, the LFB and target instrument would be placed a few metres apart, under controlled laboratory conditions. It is more likely, however, that transfer of calibration would involve kilometres of couriered transport, with the associated levels of mechanical and thermal stress. Further, the risks associated with manual mis-handling and target instrument mis-configuration, even by an experienced operator, should not be underestimated.

The ideal artefact would therefore have some form of over-force tolerance or mechanical blocking, a small moving inertial mass to minimise vibration sensitivity, and a tolerance of thermal cycling. A MEMS or other microfabricated device would be suitable, for example. In the event that the artefact does finally fail, it would be ideal to incorporate some indicator to alert the user to non-ideal operation.

Finally, the artefact should be insensitive to the levels of electromagnetic interference expected in the vicinity of the target instruments, including mains and RF noise, and stray electrostatic or magnetic fields. For example, the artefact must not be affected by the internal drive of the LFB.

4.5.8 Cost

It goes without saying that the cheaper the artefact to produce and calibrate, the more accessible it is to potential users. The strictness of this requirement depends on the architecture of the low force traceability dissemination infrastructure. More 'primary' artefacts will require higher performance and versatility but will be handled more carefully and can, within reason, be more expensive to make, calibrate and use. Artefacts to be sold to the general end user would need to be much more robust, simple and cheap to use, and semi-disposable.

The policy adopted for the described work has been to optimise performance and utility as the first priority, followed by fabrication cost. Minimisation of calibration and usage costs (typically time) were given a lower priority in line with its use at an NMI. The artefacts were to be used by an experienced operator in per-target case studies.

In any case, the logistics of the NMO project funding the reported work imposed upper limits on prototype development cost and risk.

4.6 Summary

This chapter sets out the function and features of the 'ideal' low force artefact, noting that the requirements for different applications conflict. In particular, the calibration and use of artefacts will differ depending on whether the artefact is intended for use with stiff or compliant targets.

The most significant requirement identified is the need to 'push' the target, or self-generate strain, in order to remove the deflection ambiguity in the interaction between artefact and target with similar compliance values.

Other key requirements include inversion tolerance, ruggedness, size, tip design, environmental stability and cost.

Given the above requirements, the task was now to achieve these with currently available technology, as is discussed in chapter 5.

Chapter 5

Review of the state-of-the-art in transfer artefact design

In the preceding chapters, the motivation and requirements for a traceable low force artefact have been discussed. A key component of this thesis was to develop working prototype artefacts to complete the NPL low force facility, bringing traceability to nanotechnology applications in research and industry.

It is therefore important to consider the current state of the art in low force transfer artefact technologies, and any fundamental limitations, by way of a representative review of the literature. Such a review is presented in this chapter, and aims to consider options beyond limitations imposed by operation of the NPL LFB.

There is a significant body of published work concerning techniques to measure or produce force on the desired scale. Some of these were considered in the context of balance design (section 2.4). The extent to which those techniques suit the requirements set out in chapter 4 vary significantly, however. In particular, traceable operation is rarely considered, and in many cases, concepts have not developed beyond the proof-of-concept stage, for good reason.

This chapter will update, condense and present components of a review of transfer artefact technologies previously published by the author [31]. Particular preference is given to prototypes developed by other NMIs. These prototypes have been considered separately by other authors in the context of reviews of global low force metrology facilities (for example [17]), but must be included here for completeness. Noting that any successful transfer artefact is likely to incorporate some sort of elastic working element, this chapter will consider flexure design, instrumentation and fabrication techniques. This chapter will not consider deadweight mass artefacts, which is evaluated in section 2.4.1.3.

5.1 Flexure design

5.1.1 The motivation for flexures

In order to measure the size of a force, it is necessary to observe the effect of that force when applied to a well-understood system. When a force is applied to a rigidly supported object, the object and its supports will deform by a finite amount dependent on the material properties involved.

This fact can be exploited to measure force accurately, forming a force transducer. The general form of a force transducer is a rigid platform, constrained to move along a single axis without rotation, with motion on the single axis restricted by a spring of known stiffness. The system is equipped with some means of detecting the position of the rigid platform. When a force is applied to the platform, the platform deflects until the restoring force in the spring equates to the component of the applied force along the axis of platform motion. Typically, then, the resultant displacement is detected by an electronic displacement transducer, or 'sensor', and a voltage is generated that has a fixed relationship to the displacement and therefore the applied force. A prior calibration of the relationship between force applied and distance moved, or voltage generated, can be used to turn later distance or voltage values into force values.

When using a force transducer, it is important that all desired components of the input force are measured. It is therefore important to have a well-defined single, constant axis of sensitivity (motion) in the transducer and to align the input force correctly to it.

The requirement for a well-defined axis of sensitivity has led to the development of various examples of uniaxial flexures, or approximations to these. The LFB mechanism itself is a very repeatable, compliant quasi-uniaxial flexure and the LFB can be made to operate as a displacement transducer. It is, however, large along the axis of motion. Other much thinner, planar devices make use of the fact that, over their intended deflection range, their behaviour approximates to the general transducer model above.

5.1.2 The cantilever

The rectangular cantilever is the simplest and most well-used force transducer used in nanometrology, in particular in the guise of SPM. Considering the transducer model above, the free end of the cantilever is the rigid contact platform; the root of the cantilever, in which stress is concentrated, is the compliant flexure. For small deflections the arcuate motion of the cantilever is approximately linear; and if the beam thickness is much less than its width and length, motion may be considered to be uniaxial.

The simplicity of the geometry and regular use for SPM applications means that cantilevers are well characterised, straightforward to model and readily available in a number of formats and materials. For this reason, as will be shown, most low force transducers produced to date have been based upon modified cantilevers.

5.1.2.1 Cantilever spring constant determination

To determine the spring constant as a function of axial position along a cantilever, a well known force must be applied at well defined positions along the cantilever and the resultant displacement accurately measured. The spring constant is strongly dependent on the position along the cantilever, with standard beam theory predicting an L^{-3} dependence, where L is the position along the cantilever from the fixed root. The cantilever would need to be brought accurately and repeatably into contact with a tip on the LFB platen and held during subsequent deflections. The same would be required when interfacing the cantilever with the target instrument. This need for accurate positioning implies that the requirement for high-magnification microscopy and high-precision initial cantilever positioning during all stages of the calibration transfer process.

The spring constants of seemingly similar elastic elements are often very different due to manufacturing imperfections and impurities in the material. Calculated estimates of spring constants based on geometry are generally inaccurate due to the combination of uncertainties. For rectangular cantilever geometry, the spring constant k is given by the following equation

$$k = \frac{Et^3w}{4L^3} \quad (5.1)$$

where E is Young's modulus, t the thickness, w the width and L the length of the cantilever [102]. The power dependence on the length and thickness dimensions and the direct contribution of the generally not accurately known Young's modulus result in relative uncertainties as high as 25 % [1]. Dimensional uncertainties are compounded when a coating is applied to the cantilever, for example to enhance reflectivity [133]. For these reasons it is not currently possible to manufacture a spring with a particularly accurately predefined spring constant. Hence a great deal of effort has been applied to methods of determining the spring constant; the methods are summarised in tables 5.1, 5.2 and 5.3, which were adapted from [2]. Verification of the thermal method of spring constant determination has since been carried out. The precision and accuracy of the thermal method were found to be 5 % and 10 % respectively [2].

The minimum force detectable by a cantilever is discussed in [152, 10]. This minimum force relates to the cantilever dimensions; thermodynamic and Johnson noise form the

Table 5.1: Summary of methods for determining a cantilever spring constant: dimensional methods (adapted from [1, 2])

Approach	Method, main source of uncertainty in parentheses	Risk of damage to tip	User friendliness	Advantages	Disadvantages
DIMENSIONAL					
Butt [137]	25 %; 50 % in paper (equation and t).	Low	High	Simple equation. Measures cantilever stiffness directly.	Not a good model, t and E needed. Requires calibration of pendulum.
Modified Neumeister and Ducker	11 % (t and E).	Low	High	Simple and accurate.	t and E needed.
FEA of statically loaded triangular cantilevers [138]	10 %; no attempt made at comparing with any other technique (t and E).	Low	Medium	Accuracy; computation allows both normal and lateral spring constants to be determined.	FEA programs expensive, complex, t and E needed.
FEA of oscillating composite V-shaped cantilevers [2]	6 % and 25 % compared with two different parallel beam approximations.	N/A	Medium	'Real' V-shaped cantilever geometry used.	Accuracy depends on uncertainty in material properties and type of parallel beam approximation used.
FEA of oscillating composite V-shaped cantilevers [139]	10 % for full FEA solution.	N/A	Medium	Simple formula suggested relating the cube of the resonant frequency to the spring constant.	Applies to limited resonant frequency range. Gold coating thickness dependent.
FEA of oscillating composite V-shaped cantilevers [140]	Up to 40 % for simple formula. Full FEA solution regarded as correct.	N/A	Medium	Real V-shaped geometry used.	Gold coating thickness significantly affects outcome of FEA.

Table 5.2: Summary of methods for determining a cantilever spring constant: static experimental methods (adapted from [1, 2])

Approach	Method, main source of uncertainty in parentheses	Risk of damage to tip	User friendliness	Advantages	Disadvantages
STATIC EXPERIMENTAL					
Static mass hanging [141] by inverting loaded cantilever	15 %–25 % (mass attached).	High	Poor	No geometry and E data needed. Just one particle required to be added to the tip.	Accurate placement of spheres, calibrated spheres and calibrated deflection needed
Cantilever on reference cantilever [142]	10 % (ref. cantilever).	Medium	Medium	Simple idea, geometry and coating independent.	Difficult to set one cantilever on other accurately. Need $k_{\text{ref}} \approx k_{\text{working}}$
Cantilever on reference spring [7, 143]	5 % (contact mechanics of working lever on ref spring).	Medium	High	Simple, potentially traceable to SI.	Contact method.
Static loading using two probes [144]	10 %–30 % (ratio of two probe stiffnesses).	Medium	Medium	Once one of the probes is calibrated it can be used to calibrate many different probes accurately.	Best for two probes of similar stiffness. Requires accurate probe positioning.
Nano-indenter [145]	8 % (nano-indenter calibration).	Low	Medium	Simple, quick.	Difficult to place indenter tip in correct position. Only for $k_c > 1 \text{ N m}^{-1}$.

Table 5.3: Summary of methods for determining a cantilever spring constant: dynamic experimental methods (adapted from [1, 2])

Approach	Method, main source of uncertainty in parentheses	Risk of damage to tip	User friendliness	Advantages	Disadvantages
DYNAMIC EXPERIMENTAL					
Forced oscillation/FEA [146]	5 %–20 %; 10 % compared with [147] for V-shaped levers (unloaded resonant frequency; Young's modulus).	Low	Medium	No masses need to be added, therefore, non-destructive. Just depends on unloaded resonant frequency.	Technique relies on accurate values of cantilever density and thickness.
Dynamic mass attachment [147]	15 %–25 % (mass attached).	High	Poor	No geometry data needed.	Need accurate placement of masses. Calibrated spheres needed.
Thermal noise analysis [148]	15 %–20 %. 20 % as obtained by [149] comparing with a static loading technique. 5 % as determined by [148]. Precision and accuracy of 5 % and 10 % respectively on a NIST-calibrated artefact [150]. (Interference from other noise sources).	Low	High once set up	Only frequency and T data needed.	Model validity unknown. Requires cantilever to be pressed against hard surface for calibration. Ignores damping effects – only for low k_z cantilevers.
Resonant frequency in air [151]	15 %–20 % (Reynolds no. for the fluid-cantilever system).	Low	Medium	Simple	Only for rectangular cantilevers.

fundamental limits.

The effects of temperature variation on the physical properties of an elastic element are generally significant and should not be ignored. From the ratio of stress to strain a material's Young's modulus varies as the inverse of the bulk material's relative expansion due to temperature. Use of well-known materials would facilitate calculations to compensate for expansion due to temperature variation, which at any rate should be well controlled. The temperature dependence of the resonant frequency of the first eigenmode of a microfabricated silicon cantilever, for example, is dominated by the variation of the Young's modulus, whereas the temperature dependence of geometrical dimensions due to thermal expansion, especially the thickness, can be neglected [153]. For piezoresistive elements, the temperature dependence of the piezoresistive coefficient and of the resistance itself will affect the force sensitivity [154, 155, 156]; a suitable method for compensation is to incorporate a parallel resistor as a thermal sensor [16].

5.1.2.2 Cantilever arrays

In order to provide suitable force transducer performance across a working range of forces, usually one device with a single spring constant is insufficient. It is common to design devices containing elements with a range of spring constants. This may be achieved in two ways with cantilever arrangements. Either an array of cantilevers with attached probes or single defined probing points is used, or one cantilever with multiple defined probing points is used. An example of the former, called an 'array of reference cantilevers', has been developed by Gates and Pratt at NIST [12] and is shown in figure 5.1. The arrays, microfabricated from single crystal silicon, contain cantilevers with estimated nominal spring constants in the range 0.02 Nm^{-1} to 0.2 Nm^{-1} . Variations in resonant frequency of less than 1 % are reported for the same cantilevers across manufactured batches, as an indication of uniformity. The spring constants were verified on the NIST electrostatic force balance. These cantilever arrays are relatively cheap to produce in bulk and may lead to a disposable transfer artefact with the level of uncertainty required for AFM calibration (parts in 10^2 to 10^3) [157].

Cantilever arrays are already commercially available for AFM non-traceable calibration, such as an example by Veeco Probes [13], with cantilevers of width $30 \mu\text{m}$ and length $100 \mu\text{m}$ to $400 \mu\text{m}$ (see figure 5.2). However, their route to traceability puts a much lower ceiling on their accuracy and the uncertainties specified.

As the simple devices described in this section are passive, they would require pushing into the LFB by an actuator system and some external means of measuring deflection. This second requirement is significant since it relies upon the displacement metrology of the

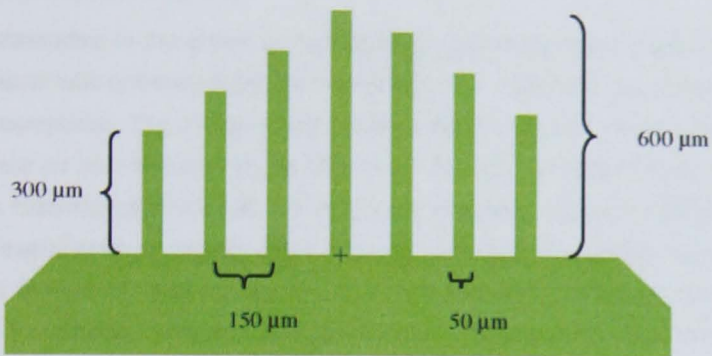


Figure 5.1: Experimental prototype reference cantilever array - plan view (from [12])

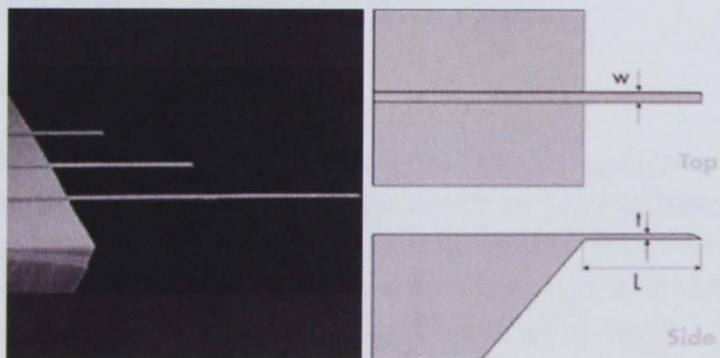


Figure 5.2: Commercially available AFM 'calibration' cantilevers from Bruker, formerly Veeco Probes: photograph of the three cantilevers, with quoted nominal spring constants of 0.157 Nm^{-1} , 1.3 Nm^{-1} and 10.4 Nm^{-1} (left) and a side view of one cantilever (right) (from [13]).

target instrument, as discussed previously. The working uncertainty of these devices is higher than with self-sensing cantilevers, to be discussed below, and may be better calibrated by such a self-sensing artefact. For a primary transfer artefact, however, direct use of these examples is probably not suitable.

The alternative to the arrays of high-quality passive cantilevers discussed above is a single cantilever with onboard deflection metrology. This metrology would add significantly to the device complexity. The device would not be a mass-produced, disposable tool; rather, it would operate as an extension of the LFB or as the second highest level of traceability for calibration laboratories in the UK – a secondary standard. These would be used to calibrate target instruments or indeed cheaper, lower accuracy, disposable transfer artefacts. Cantilevers of this active type usually are manufactured with multistage micro-fabrication [14]. Methods for sensing – and perhaps generating – displacement will be discussed in the following sections.

5.1.3 Other planar structures

Cantilevers are, however, not the only format of planar flexure, and alternative formats have additional benefits. It was noted in the previous section that the stiffness, and hence force sensitivity, of the standard cantilever is highly dependent on the axial position of the point of contact of the interfacing device. If the force transducer can be designed to have rotational symmetry, then it follows that this high dependency must be removed, with the clear practical benefit of relaxed lateral contact alignment requirements.

5.1.3.1 Triskelion flexure

Previous research at NPL led to the selection of the 'triskelion' geometry as the basis for MEMS devices for micro-coordinate metrology [158, 159]. As discussed previously, this 'Isle of Man' design (shown in figure 5.3) has three bent legs, the outer halves of which are thinner to allow flexure and so movement of the inner parts. With the ends shown free in figure 5.3 all rigidly supported, the relative stiffnesses provide an approximation to a 3DOF motion. The rotationally symmetric form can be tuned to generate isotropic stiffness behaviour at the tip of a suitably-long stem attached at the centre of the triskelion and aligned normal to the plane of the triskelion. With the beams (outer leg portions) instrumented with sensors and actuators, a flexure fabricated with this form becomes a device that can sense and generate translational and rotational motion at its centre, or at the end of an attached tip or stem.

If a stemless small tip (length on the order of the flexure thicknesses) is selected, the out-of-plane compliance dominates, creating an effectively uni-axial device ideal for low force

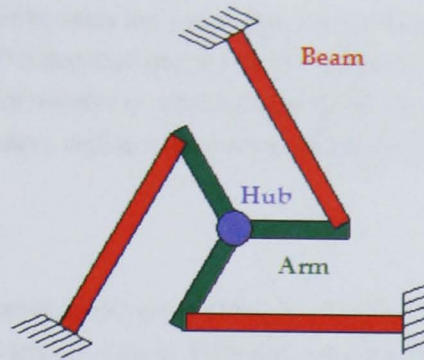


Figure 5.3: The NPL triskelion form, with nomenclature used in this and related documents. The hub and arms are nominally non-compliant (achieved through extra thickness on these portions) concentrating deflection in the outer beams.

measurement. The residual compliance in the other axes is useful for the coarse detection of tip-surface alignment and unwanted lateral forces. The relative compliances are tuned through the selection of beam dimensions.

The use of triskelia and tetraskelia in micro-coordinate metrology is now common and they have been incorporated into commercial instruments [65, 160, 161] for the purposes of dimensional metrology. However, the use of such forms for low-force artefacts is a novel approach.

Several features of the triskelion flexure design would be advantageous in this quasi-static low force application. Firstly, it is simple to model the first-order vertical behaviour of the flexure. The triskelion simplifies to three parallel sets of two simple cantilever springs in series. The total stiffness is 1.5 times that of one half of one beam. The simple geometry assists scalability of the concept into another operating force regime.

Secondly, the rotationally symmetric design intuitively contains a zone of near-constant spring constant, compared to the standard cantilever. This will be confirmed mathematically in section 6.2.3. The rotational symmetry also means it should be possible to detect significant lateral contact misalignment by way of signal differences between legs.

Microprobe work completed at NPL at the same time as the early stages of this project demonstrated the resilience of the nickel flexures to over-force, in addition to their intended isotropic properties. This rugged property has been confirmed in this project. The ability to tolerate reasonable excursions from the intended operating force range has practical benefits for use.

There are also some drawbacks to the triskelion design. The rotational symmetry demands that the chip body must surround the contact zone. For applications where a slender

final probe form is required to reach the active region of the target instrument, the triskelion is likely to be unsuitable. The triskelion device would calibrate a further, specialised sensor in this situation. To realise the benefits of rotational symmetry, the three beams would need to be well-matched in dimension, setting a limit on the uniformity of fabrication of the devices.

5.1.3.2 Helical springs

A different sort of elastic artefact, designed at NPL for AFM cantilever calibration, takes the form of a Microfabricated Array of (helical) Reference Springs (MARS) [7]. Twelve reflective discs are held supported above a substrate by a spring, each with a different spring constant in the range 0.16 Nm^{-1} to 11 Nm^{-1} , the standard range for most contact mode AFMs (see figure 5.4). The low inertia springs are usefully vibration and shock resistant and in their latest form can be directly calibrated via their resonant frequencies and Doppler vibrometry off the mirrored discs. The authors state that the position of an interacting tip on the $160 \mu\text{m}$ discs is much less critical than with cantilevers, with the entire disc having nominally the same spring constant. This would lead to an immediate operational advantage when used in a force transfer artefact interacting with a variety of instruments. However, the design may be susceptible to parasitic deflection; this would need to be quantified. An array of tipped cantilevers of varying spring constants could offer a suitable compromise. The other challenge in the use of this device in a transfer artefact is the lack of onboard deflection metrology. An independent capacitance-based system might represent a solution.

The current spring constant based methods seem to offer the most direct route forward for a viable transfer artefact. A suitable version of a current technology could be housed in a suitable unit complete with a three axis translation mechanism and an independent deflection measurement system. This unit could then be kinematically mounted onto the LFB, calibrated, inverted, and installed in the target instrument. A compact fibre-fed laser interferometer could provide the deflection metrology if not achieved through MEMS technology, provided it could be made resistant to physical inversion.

5.2 Force (or strain) detection and actuation mechanisms

5.2.1 Piezoresistors

5.2.1.1 Basic principle

A number of techniques exist to measure the strain of an object by a resultant change in bulk resistance of that object, or a sensor laminated onto it. One of the earliest examples of

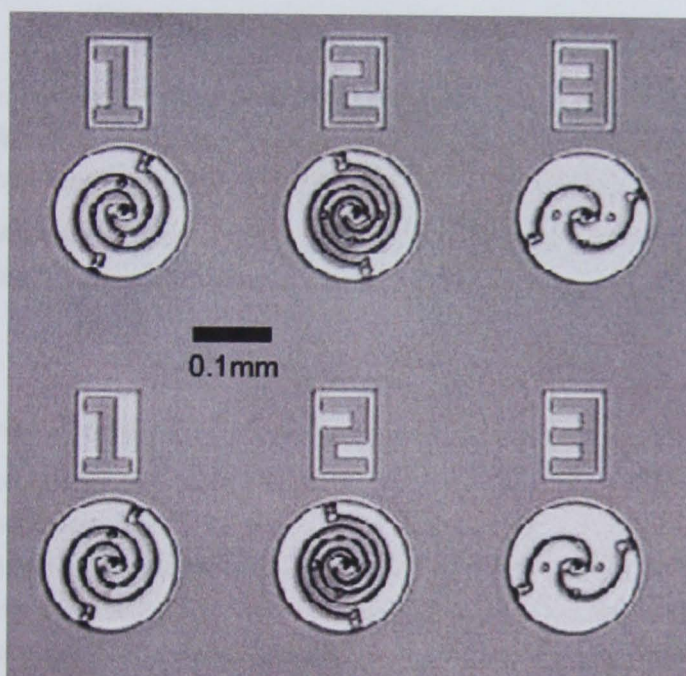


Figure 5.4: A MARS. Above the spiral spring is the more massive poly-crystalline silicon platform, suitable for AFM contact. A scale bar of 100 μm has been overlaid on this optical micrograph (from [7]).

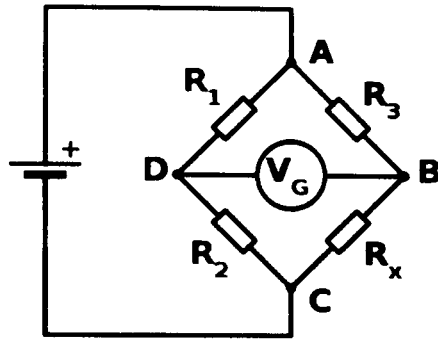


Figure 5.5: General form of the Wheatstone bridge.

such a sensor, invented in 1938, consists of a folded conductive foil pattern that stretches when the surface it is attached to deforms. The resultant dimensional change leads to a proportional increase in resistance, which is detected via a Wheatstone bridge.

The Wheatstone bridge circuit, shown in figure 5.5, detects small changes in a resistance, outputting a voltage analogue V_G of the variable resistance R_x according to equation 5.2

$$V_G = \left(\frac{R_x}{R_3 + R_x} - \frac{R_2}{R_1 + R_2} \right) V_s \quad (5.2)$$

where R_1 , R_2 and R_3 are the other bridge resistors and V_s is the supply voltage.

The class of semiconductor materials known as piezoresistors experience a change in resistance with strain several orders of magnitude larger than attributable to conduction path length changes [162]. These materials, formed by selectively doping regions of a semiconductor, are suitable for high-resolution force sensing. Bulk strain induces lattice deformations and a resultant change in resistance. In common with the simpler foil sensors, piezoresistive sensors are sensitive to temperature fluctuations and are interrogated using a Wheatstone bridge.

5.2.1.2 Precedent

One of the first examples of an AFM probe with on-board piezoresistive deflection sensing was developed by Tortonese *et al.* [163, 14]. The device, shown in figure 5.6, was fabricated as a single piezoresistive strain element with pointed-tip cantilever geometry. The researchers claim a 0.01 nm RMS vertical resolution, which is equivalent to 1 nN with a spring constant of 10 N m^{-1} for this proof of concept device.

To reduce the uncertainty of interaction position on the cantilever, and to allow operation at a range of spring constants, fiducial markings may be printed down its length. Since

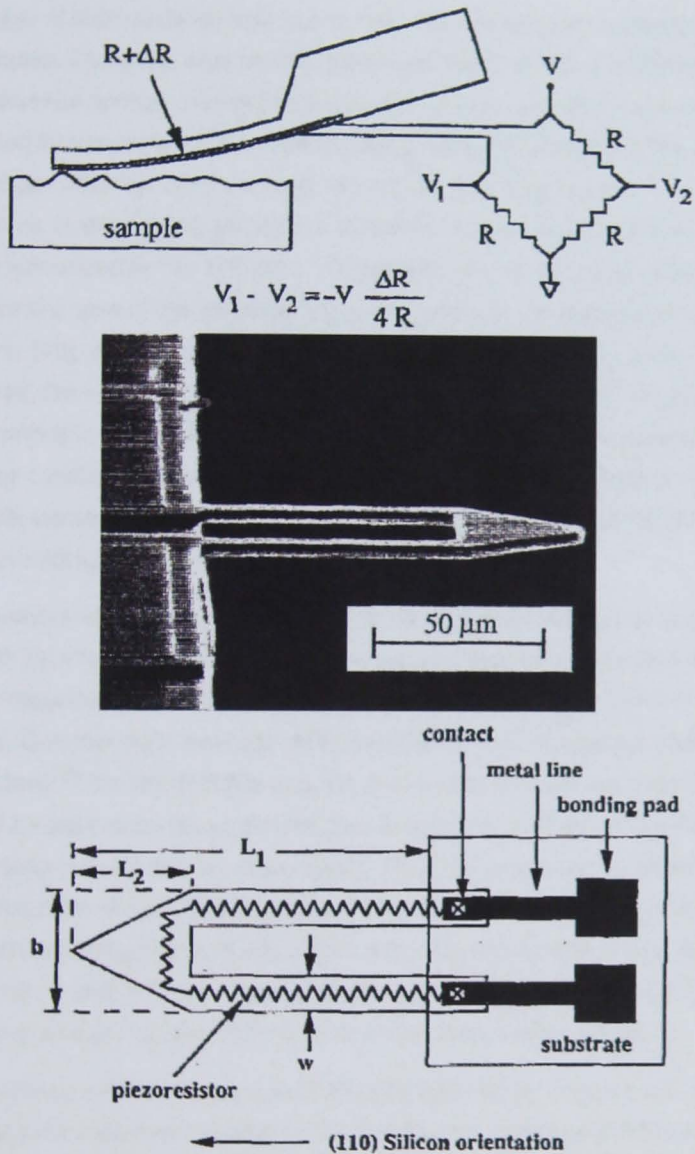


Figure 5.6: Tortonese et al.'s early piezoresistive AFM cantilever: schematic diagram of piezoresistive detection scheme (top); SEM photograph (centre) and plane view drawing (bottom). Images from [14].

interactions often permanently mark the cantilever (an indentation), the interaction position may in some cases be determined by the appropriate choice of microscope after the interaction.

A number of piezoresistive cantilevers have been developed by several national measurement institutes. Cumpson *et al.* at NPL developed the C-MARS (cantilever microfabricated array of reference springs) device [15] as part of a set of microfabricated elastic-element devices intended for traceable AFM cantilever spring constant calibration. The relatively large cantilever (150 μm wide by 1 600 μm long) is marked with fiducials that in principle allows precise alignment of the contact point for a cantilever-on-cantilever calibration. The size of the fiducials is influenced by the 100 $\mu\text{m} \times 100 \mu\text{m}$ field of view of typical AFMs. Surface piezoresistors near the base of the cantilever allow the monitoring of displacement and vibration of the cantilever [16], as required. Detail of the device is shown in figure 5.7. As for many similar examples, the small mass of the cantilever renders it relatively immune to mechanical shock, and in principle could withstand transport by mail. The authors present the determination of spring constant values at the cantilever tip using Sader's method, Euler-Bernoulli theory and finite element analysis (FEA). Spring constants are also quoted for interaction at each fiducial, providing a range of 0.03 N m^{-1} to 25 N m^{-1} .

Researchers at PTB have created a slightly larger piezoresistive cantilever, of one millimetre width by a few millimetres length, for use in nanoindentation and surface texture work [16]. An integrated temperature sensor may be used for direct sensor signal thermal drift correction. Commercially available AFM cantilevers with integrated strain gauges (for example PiezoleverTM by ThermoMicroscopes, Sunnyvale, CA) are reported to have dimensions too small for easy accurate alignment; their length and width are in the range of several hundreds and tens of micrometres, respectively. The PTB group has created both a two-leg sphere-probe example and a single-leg tip-probe example, as shown in figure 5.8. The prototypes, manufactured using standard silicon bulk micromachining technology, have a stiffness range of 0.66 N m^{-1} and 7.7 N m^{-1} . The authors report a highly linear relationship between the gauge output voltage and the probing force in the micronewton range.

Most recently NIST have developed the example shown in figure 5.9, which has thin legs at the root to concentrate bending in this root region. Numbered fiducial markings assist in the location of balance-artefact or artefact-target interaction via an optical microscope [18]. In continuous scanning mode, the probing tip of a piezoresistive cantilever, such as the NIST device, may be moved slowly down the cantilever beam, with beam deflection and external force values regularly recorded. Notches with well-defined positions show up as discontinuities in the recorded force-displacement curve, and act as a scale for accurate probe tip position determination from the data [164]. The result is a function that describes the

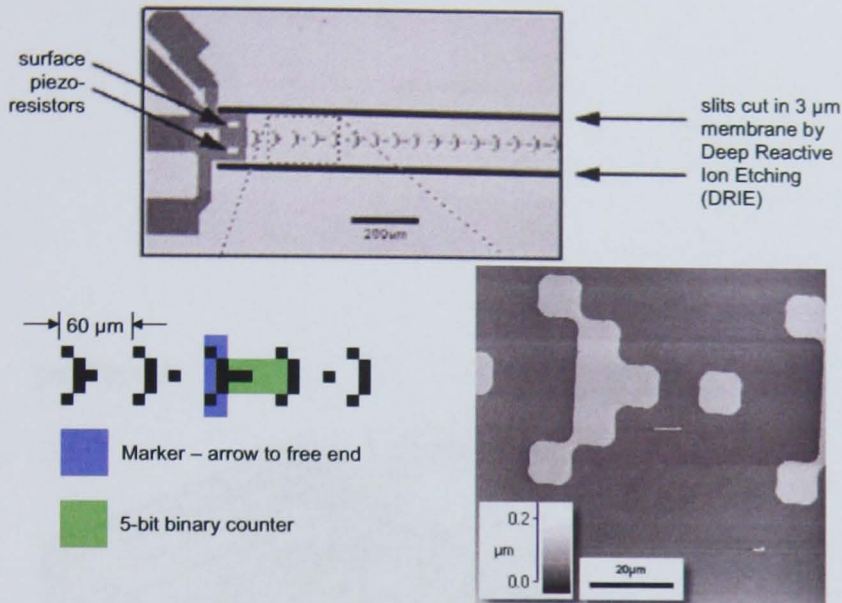


Figure 5.7: Images of the NPL C-MARS device, with detail of its fiducial markings; the 10 μm oxide squares form a binary numbering system along the axis of symmetry (adapted from [15]).

spring constant of the transfer artefact, after probing with a low force balance. For interaction with an electrostatic force balance operating in position-nulled mode, such a device would need to be pushed into the balance tip, creating a requirement for a metrologically stable precision multi-axis stage, preferably with near-continuous positioning capability compared to the resolution of the transfer device.

The choice of deflection metrology depends on the working range of the transfer artefact. For the higher end of the nanonewton force range a piezoresistive element can detect displacement via strain. At the lower end, where displacements are smaller, capacitance methods may be used. Such on-board MEMS systems are more suited to operation in vacuum or controlled environmental conditions, as well as occupying a significantly smaller amount of valuable space. It is now possible to manufacture piezoresistive elements that require only low voltages, offer a low failure rate and onboard electronics to make the electronic output signal more user-friendly in the field. In one such example developed at Spain's Centro Nacional de Microelectrónica, very small, sensitive micro-cantilevers with integral signal-processing have been constructed on CMOS polysilicon with spring constants in the range 1.5 mN m^{-1} to 12 mN m^{-1} [19] (see figure 5.10). In another example, the development of a piezoresistive pressure sensor has been reported incorporating a MOSFET differential amplifier to improve the output signal [165].

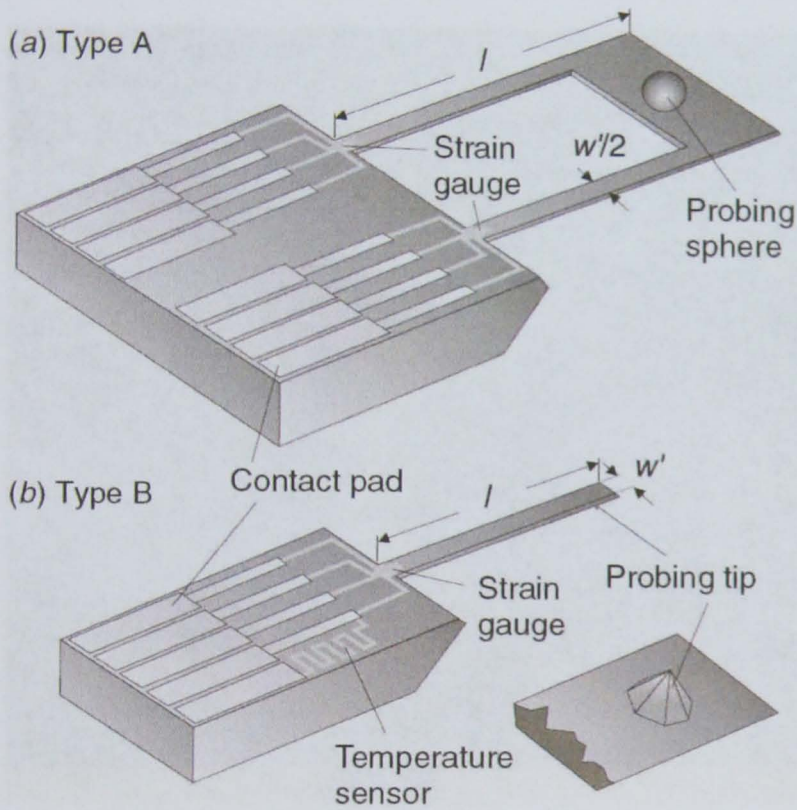


Figure 5.8: Types of piezoresistive silicon sensors developed at PTB: (a) two-leg cantilever with a glass sphere as probing tip; (b) single cantilever with integrated silicon tip (from [16]).

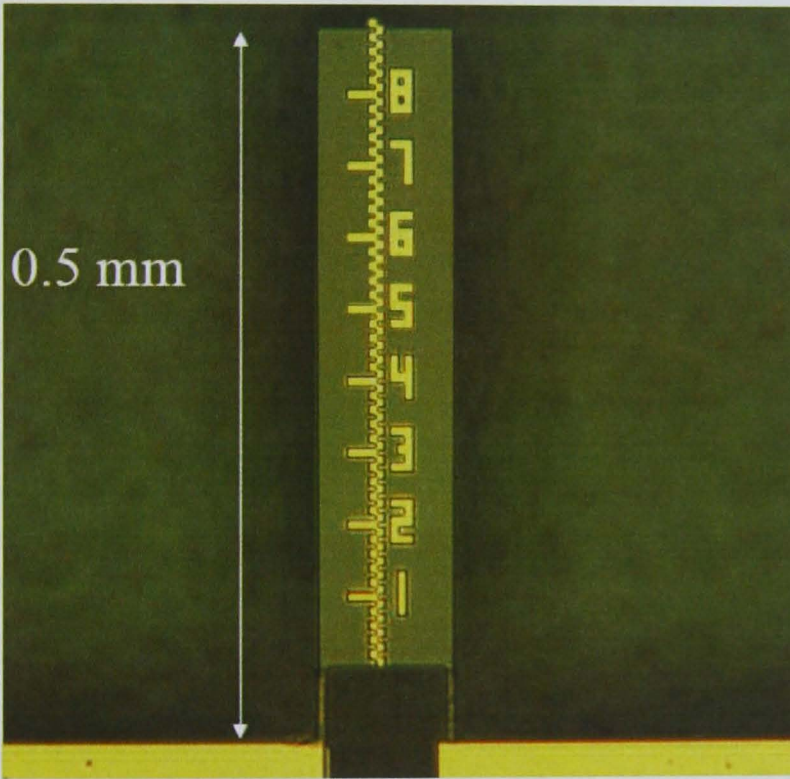


Figure 5.9: The NIST piezoresistive cantilever (from [17]; see also [18]).

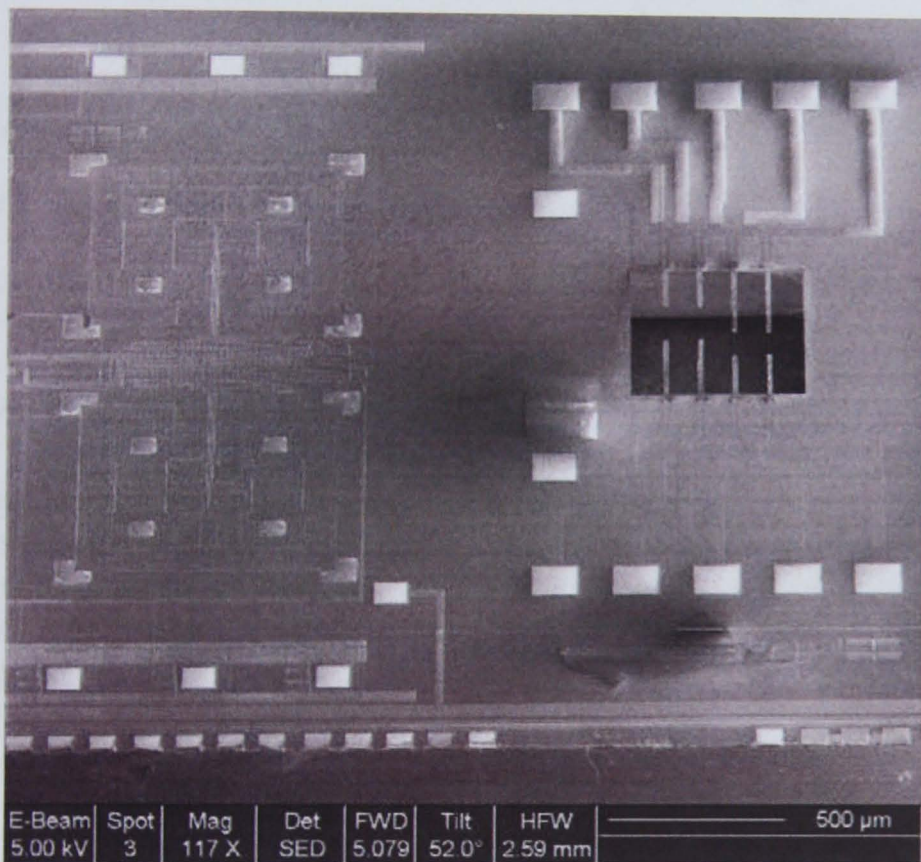


Figure 5.10: SEM micrograph of integrated cantilevers and CMOS circuits in an intermolecular force detection device developed at CNM-IMB, Spain (from [19]).

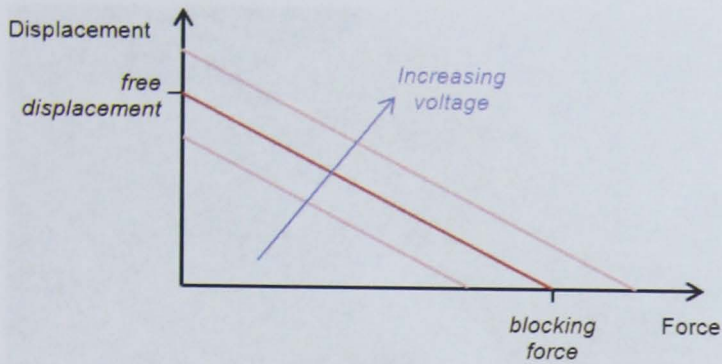


Figure 5.11: The 'blocking force' concept: Piezoelectric element free end displacement as a function of applied force and voltage.

5.2.2 Piezoelectric sensing and actuation

A particular class of materials, such as quartz, have intrinsic properties that allow them to reversibly convert a mechanical strain (and hence stress) into an electrical signal. This process, known as the piezoelectric effect, is based upon the creation of dipoles in a crystal lattice when it is deformed as part of bulk strain [166].

The reversible strain-charge relationship makes piezoelectric materials ideal for a variety of sensing and motion-generation applications, from cheaper buzzers in doorbells to cutting-edge dynamic MEMS pressure sensors. In principle a device based on the piezoelectric effect would also make an excellent low force transfer artefact: the ability to generate strain would have distinct metrological advantages, as discussed previously (see section 4.3).

The piezoelectric effect will be discussed in greater detail in chapter 7, but at the highest level, the function of a piezoelectric element can be described as follows.

In strain generation mode, a potential difference is applied across the element in a particular orientation, and the element deforms and holds its new shape. Under zero external load, the element achieves a repeatable final strain. In the one-dimensional case, this is known as the free displacement. An externally applied load shortens the achieved displacement, as shown in figure 5.11; such that at a maximum force, the blocking force, strain is just prevented.

In strain sensing mode, an applied strain causes a transient flow of charge; a constant strain rate creates a constant current from the piezoelectric element. If the piezoelectric element is placed in parallel with a flexure system, the flexure's deflection can be deduced. However, the development of an accurate strain sensor requires complete collection and summation of all charge emitted from the element, without loss to other sinks or addition of

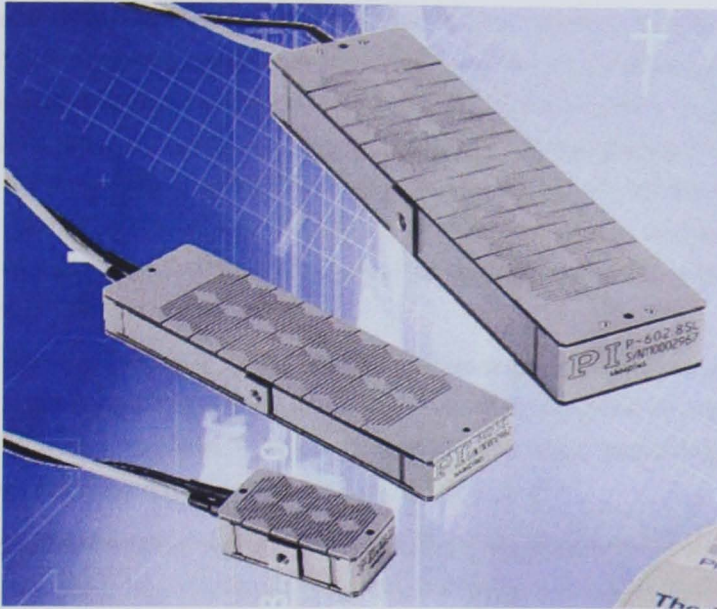


Figure 5.12: A commercially available stacked piezoelectric force actuator [20].

spurious charge from the environment. For practical reasons it is challenging to eliminate either sinks or sources, and such sensors must be operated in a frequency range where the peak sensor current dominates such leakage currents.

For high precision instrumentation for MEMS, however, it may be possible to isolate the electrical system to reduce losses to a tolerable level for quasistatic applications. This is achieved by appropriately isolating the sensor and electronics from the environment using shielding methods [167].

The type or format of piezoelectric element used depends on the application. For macroscopic devices, bulk crystal is used. For example, in the commercial piezoelectric stack actuator in figure 5.12, an applied voltage of 120 V generates a motion in the order 1 mm with a blocking force of 400 N. For microfabricated devices, machining practicalities set a lower limit on piezoelectric layer thickness and necessitate alternative approaches. For thick films below 10 μm , the sol-gel process was devised, based on the lead zirconate titanate (PZT) piezoelectric material. Further information on the process variant devised by Cranfield can be found in [168].

For sol-gel based PZT films the upper thickness limit is set by an increased tendency to crack [169]; the lower limit is set by the ability to spin-down the sol-gel. Both strain generating ability [170] and mechanical stiffness under sensing mode increase with film thickness, the former proportionally; thickness is therefore a key design factor for a pie-

zoelectric device. The piezoelectric properties of films differ significantly from those of well-characterised bulk materials; Duval et al [170] report the use of a piezoresistive cantilever to directly measure the blocking force of sol-gel film PZT microactuators as part of a wider material property evaluation. The authors note that film properties are highly dependent on processing conditions. The examined micro-actuators had a PZT thickness of 2.5 μm laid on a 10 μm \times 200 μm \times 900 μm silicon cantilever; the resonant frequency was on the order 20 kHz. A free displacement of around 0.5 μm and blocking force on the order 100 μN was reported for a 5 V, 100 Hz driving signal.

In section 2.2.7 the NPL microprobe was introduced; this device concept also uses a selectively poled sol-gel PZT layer as oscillation generating actuators and motion sensors. The phase difference between the actuator drive signal and sensor output signal indicates a change in resonant condition heralding surface contact.

The piezoelectric effect has formed the basis of devices to both generate and sense strain across a range of frequencies, as demonstrated by the following examples. Mohamed *et al.* present an example of a high-frequency voltage-to-motion transducer for scanning microscopy [171]. Ledermann *et al.* detect acoustic signatures, operating the principle in reverse [172]. Moallem *et al.* employ piezoelectric actuators to translate a flexure-based positioning system across a bandwidth ranging from quasistatic to moderate frequencies (or rather, transient accelerations) [173].

More recently Ivan *et al.* demonstrated a system capable of quasistatic ($\sim 10^3$ s) displacement metrology based on piezoelectric sensors [174]. To do so, known dissipative effects were intensively characterised and corrected online whilst maintaining the same conditions. No external mechanical interactions with the cantilever were demonstrated.

Known practical limitations associated with piezoelectric materials are creep, hysteresis and an inherent upper temperature limit to operation defined by the Curie temperature. In the latter item, as the device is brought close to the Curie temperature of its piezoelectric component, that component will progressively depole in line with the Boltzmann distribution.

It is evident that piezoelectric instrumentation may provide the additional, novel functionality desirable for a traceable low force artefact, but that there are significant challenges to repeatable sensor operation centred on the collection and handling of charge. Generated forces appear to be on the correct order of magnitude for the present application.

5.2.3 Capacitive sensors, electrostatic actuators

These techniques are grouped, being the passive and active application, respectively, of the electric field between charged surfaces.

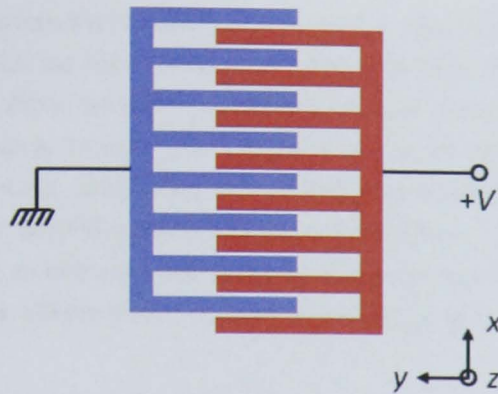


Figure 5.13: The capacitor comb for linear sensing and actuation.

A voltage applied across a pair of charged plates generates a force on those plates, acting to change the separation of the plates. This force is highly non-linear in separation, as noted in the context of the LFB. Similarly, when attempting to measure displacement, the capacitance of the two-plate is non-linear with separation, and therefore requires more sophisticated control circuitry to support a wider force range. Commercial capacitance-based displacement sensors are readily available, and so the challenge would be to adapt the associated electronics. Further, it is reasonably straightforward to arrange for adjacent plate regions of a multilayer planar structure to form a capacitor, particularly with MEMS fabrication techniques that allow well-defined lateral geometry.

The capacitance or generated force can be linearised by arranging for the plate overlap area, rather than the separation, to vary with artefact deflection along the working axis. Consider the comb arrangement in figure 5.13. Applying standard classical capacitance calculations, it can be shown that relative motion of one comb in $\{yz\}$ gives a linear ΔC (or linear ΔF with V); x sensitivity is small and nonlinear.

This comb arrangement is a standard component in MEMS design. Indeed, MEMS devices are good candidates for low force artefacts because their moving elements would have very small masses. Gravitational forces would be small improving possibilities of invertibility. Low inertia in MEMS devices lead to surprising resilience to mechanical shock.

Section 2.4.1.4 introduced the Electrical Nanobalance and Lateral Electrical Nanobalance (LEN) devices introduced by Cumpson *et al.* [8, 143]. In the first, a vertical asymmetry in the fields generated in a pair of comb drives levitates a landing stage against an internal elastic element. Measurements of the driving electrical signal and resultant deflection lead to a spring constant value potentially traceable to SI. At end-use, the device becomes a passive, calibrated, elastic device requiring no electrical connections and producing no

interacting fields. To convert the Nanobalance to an active device it may be possible to recalculate displacement from the capacitance across the comb-drive. The device is susceptible to stiction in the drives and to the well-known MEMS 'snap-on' effect where the moving stage catastrophically adheres to the base plate on contact due to van der Waals forces. The authors report a landing stage centre-point spring constant of $0.195 \text{ N m}^{-1} \pm 0.010 \text{ N m}^{-1}$ and suitability for calibration of AFM cantilevers in the range 0.03 N m^{-1} to 1 N m^{-1} . The device, calibrated dynamically, must be operated in vacuum to avoid dust contamination of the key working elements. The LEN is similar in concept, but designed to measure lateral spring constants.

Sun *et al.* [21] have demonstrated the use of a capacitively-instrumented cantilever to monitor the flight of a fruit fly (see figure 5.14). It is notable that this sensor operates satisfactorily in ambient conditions, even with the fly attached. A high sensitivity of $1.35 \text{ mV } \mu\text{N}^{-1}$ is reported along the single sensitive axis; the device was able to measure an average lift force of $9.3 \mu\text{N} \pm 2.3 \mu\text{N}$, which was confirmed by prior scale comparison with a commercial mass balance. Beyler *et al.* [175] employed a similar device to characterise a magnetic microrobot in three dimensions.

Similar force sensors are now available commercially in practical packaging; the example in figure 5.15 has a capacity of $160 \mu\text{N}$ and a resolution of 50 nN , though at the \$3 500 price level.

5.2.4 Electromagnetic actuator (voice coil)

The use of a voice coil or other electromagnetic actuator system was discussed previously in the context of precise force generation in macroscopic instruments such as the Watt balance and the instrumented indenter. It is less clear how such a technique could be successfully employed on a scale compatible with the previously discussed transfer artefact dimension requirements. The issues associated with miniaturising a voice-coil suspension system, such that the internal friction is reduced to an insignificant level would most likely prove to be insurmountable. Furthermore, reliable use of an artefact with a magnetic component with the LFB, which is constructed from paramagnetic titanium, is likely to prove impossible. A similar interaction between a fine motion stage and the flexures of the NIST balance led to a systematic uncertainty only identified by comparison with another route of traceability [33]. In any case there is absence of established precedent for the use of this technique in MEMS sensors, excluding the quantised flux experiment of Choi *et al.* [106].

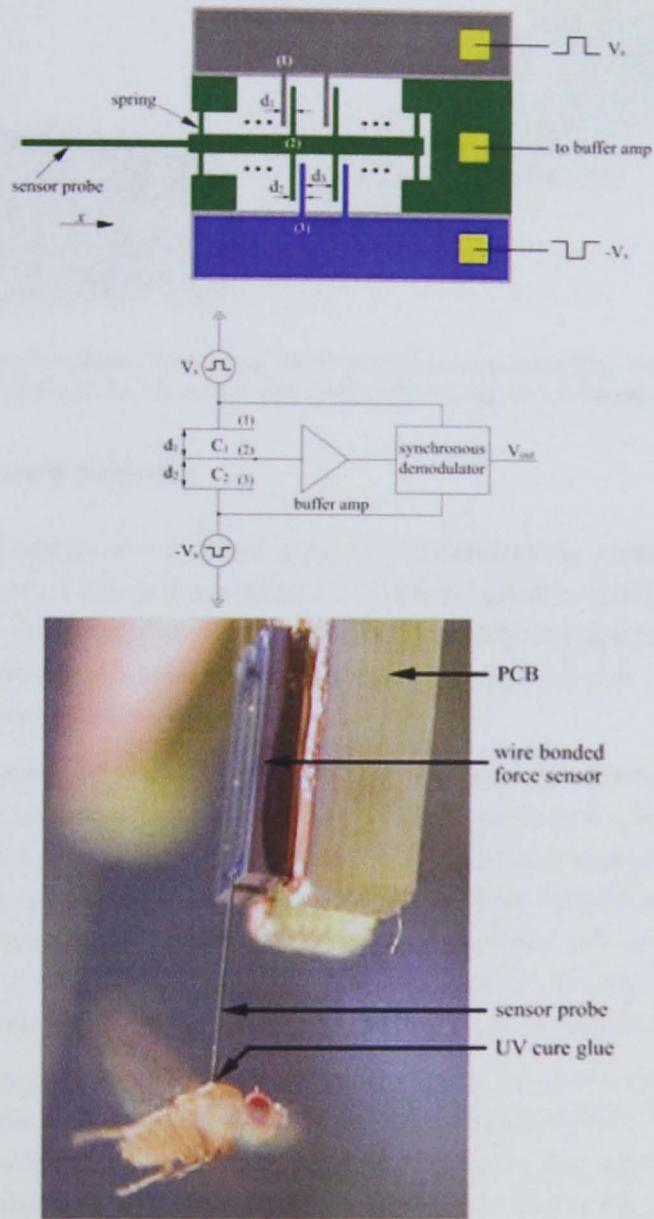


Figure 5.14: Capacitive force sensor and the study of fruit flies: (top) schematic diagram of probe showing axial force direction; (centre) block diagram of associated control circuitry; and (c) the sensor in action. From electronic version of [21].

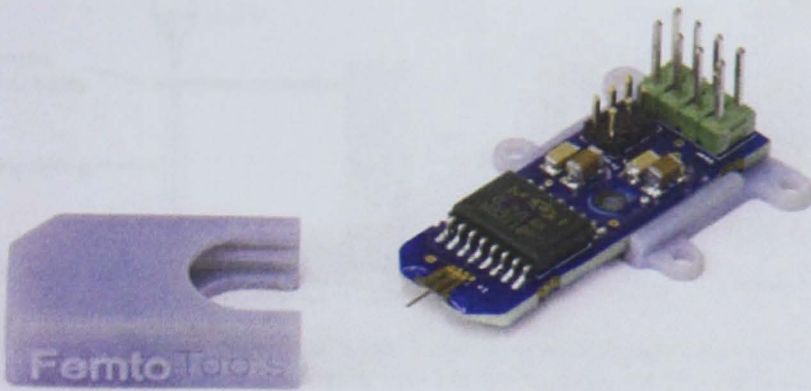


Figure 5.15: A commercially available capacitor-based force sensor (from [22]). The device is accompanied by a controller unit, the cable from which connects to the green pin headers shown.

5.2.5 Resonance methods

Changes in the tension of a stretched string can be detected via related changes in its resonant frequency. If a force is exerted on one of the string anchor points along the string axis, the tension in the string will decrease. For a well-characterised string the force exerted can be calculated from an accurate determination of the frequency shift. In this way a low force measurement device is created.

Force measurement via resonant frequency changes is an attractive approach due to the possibility for bandwidth selection. With a careful choice of working frequency through device design, the effect of noise on the measurement signal can be dramatically reduced in comparison to other methods. Operation at or near resonant modes of oscillation lowers energy requirements, in turn permitting lower power consumption and reduction of related heating effects. A lower limit to energy requirements is set by damping effects at device component boundaries, highlighted in examples below, and by intrinsic dissipation [176].

There are drawbacks with current examples, however. The first is the need for optical interrogation of the resonant frequency by laser Doppler vibrometry [177]. This significantly adds to the complexity of the device. Furthermore, the published designs are highly non-linear in force response (much like the NPL microprobe) such that they are better suited to contact detection rather than traceable force measurement or generation.

One apparently successful resonance force sensor is Stalder and Dürig's 'nanoguitar' [23] (see figure 5.16). Operating in vacuum, an SPM tip is pressed against the sample cantilever, changing the tension in the oscillating string. The beam is required to be soft compared to the string to transmit the interaction force, improving sensitivity. The setup allows

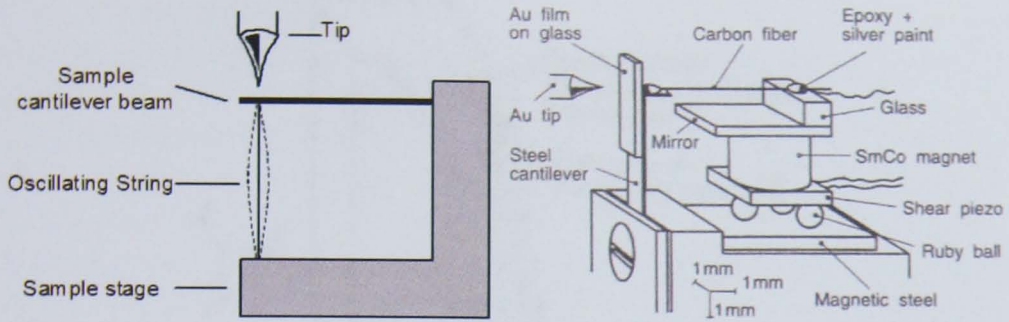


Figure 5.16: (left) schematic diagram of a resonance string sensor; (right) example of actual experimental set-up showing shear piezo for tension adjustment and magnet for actuation of Lorentz oscillations (from [23])

micrometres of string oscillation amplitude without significant amplitude of parasitic oscillations in the connected cantilever beam. The selection of a cantilever with a lower resonant frequency than the string helped prevent such parasitic oscillations. The prototype used a carbon fibre with a diameter of $5\ \mu\text{m}$ and a length of $4\ \text{mm}$, oscillating at $4\ \text{kHz}$. As string tension is decreased, force sensitivity rises but the response time drops. The force resolution is limited by thermal noise in the string oscillation. The authors report a force resolution of $2.5\ \text{nN}$, achieved in vacuum for a response time of $1\ \text{ms}$ and a sensor stiffness of $160\ \text{Nm}^{-1}$. The sensor performance was limited by a low Q-factor and required precise fibre tension adjustments. Vibration damping was significant because the string was glued to the cantilever. Initial tension was set by sliding one anchor relative to the other using a stick-slip mechanism. Oscillations were generated using the Lorentz force, an approach probably inappropriate for a suitable transfer artefact due to the likely interaction with the Low Force Balance. Even small ferromagnetic elements found in sample stage drives can contribute systematic force offsets on the order of a nanonewton [33].

Assuming the behaviour of the cantilever beam and string can be adequately modelled and designed to allow inversion, the remaining challenge would be to suitably mount an optical detector system to record the resonant frequency, for example with a fibre laser feed. Advances in MEMS technology mean that onboard diode lasers, light guides, focusing optics and photodetectors are possible. Thus, it may well be possible to build a complete onboard vibrometer, using the Stalder and Dürig method of detecting light bypassing the oscillator. A further level of sophistication could be the use of a small Fabry-Pérot interferometer using reflected light, although returning light intensity levels from the oscillator might prove insufficient. In any case, the cost of successfully prototyping a device of such complexity may prove prohibitive for commercial exploitation.

The double-ended tuning fork concept forms an alternative high-sensitivity force sen-

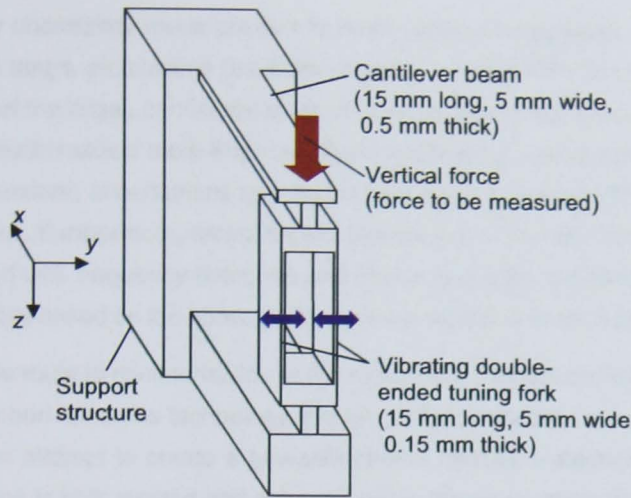


Figure 5.17: Schematic diagram of a double-ended tuning fork resonance force sensor (from [24]).

sensor, and has been studied by various groups. In an example presented by Fukuzawa *et al.* [24] a vertical force acting on the sample cantilever beam changes the resonant frequency of the fork 'prong' beams (see figure 5.17). The beams are vibrated by an external electromagnet and the amplitude measured with a laser Doppler vibrometer. The monolithically manufactured system has an experimentally determined minimum detection force limit of $19 \mu\text{N}$, with a theoretical value as low as $0.45 \mu\text{N}$, which is too high for use with the LFB.

Finite element simulation of a further double-ended tuning fork example is presented in [178]. This sensor was designed to be applied as a vibratory gyro-sensor, detecting acceleration in automotive applications for example. The sensor is not directly adaptable into a transfer artefact but the presented discussion provides an insight into noise reduction (through signal subtraction), device manufacture and oscillation driving methods.

A further example resonator was constructed to allow force measurements in the presence of large force gradients (see figure 5.18) [25]. Such force gradients are produced, for example, by sudden conformational changes when stretching proteins with an AFM. The presented AFM sensor probe employs a piezoresistively detected, electrostatically driven resonant beam sensor oriented perpendicularly to the sample surface. The authors report a force resolution of 9 nN in a 1 kHz bandwidth in air with an oscillation amplitude of 36 nm and a resonance quality of twenty. In a 1 mtorr (133 mPa) vacuum the force resolution in the same bandwidth improves to 200 pN with a resonance quality of 450 and oscillation amplitude of 53 nm . The resolution of the detector is limited by the white noise of the piezoresistor. The piezoresistor was chosen due to the difficulties in directing light onto the oscillator in an AFM for optical vibrometry.

Currently uncertainty levels are two to three orders of magnitude too large for use in a nanonewton range, piconewton resolution transfer artefact. This level of uncertainty is perhaps a result of the larger, centimetre scale of previous examples. Since many properties scale with size, mathematical modelling may determine that by scaling down the system by a factor of one hundred, uncertainties may be brought down to a level permitting transfer of nanonewton forces. Furthermore, recent MEMS research may provide the solutions to challenges associated with frequency detection and device inversion can be overcome. Hence resonance methods based on the above prototypes are worthy of some further investigation.

A possible route to miniaturisation of the nanoguitar concept could exploit recent developments in carbon nanotube technology, though further innovation is required. Sazonova *et al.* describe an attempt to create a tuneable carbon nanotube electromechanical oscillator whose motion is both excited and detected using the electrostatic interaction with the gate electrode underneath the tube [179]. They highlight the advantages of the nanotube: they are made of the stiffest material known, have low densities, ultra-small cross-sections and can be defect-free. The group report that despite great promise they have as yet failed to realise a room-temperature, self-detecting nanotube oscillator due to practical difficulties. For example, the adhesion of the nanotube to the electrodes inevitably reduces the device's quality factor by several orders of magnitude. Any successful implementation is likely to require a vacuum environment, reducing its usefulness.

5.2.6 Note on placement of electronics

In the higher-performance devices shown in this section, much of the required signal processing is located on the substrate of the sensor chip, adjacent to the sensing element. This is not undertaken merely for aesthetic reasons; short connections between sensor head and processing electronics minimise the input of unwanted spurious signals. This is particularly valid given that, for a given experiment, environmental conditions may only be optimised in the vicinity of the sensor (for example, in vacuum applications). However, the drawback is the inevitable cost of such devices; on-board integration of drive circuitry drives up the cost and duration of development, even relying upon proven components, such that the final cost per device is prohibitive. The examples shown here were developed as one-offs to support ground-breaking research programmes, in part to demonstrate the limits of micro- and nano-fabrication techniques. It is more likely that a successful artefact would be accompanied by a macro-scale dedicated controller/driver unit, as demonstrated by the Kleindiek force sensor equipment (see section 3.10) and the device in figure 5.15. As will be shown, development for the purpose of this thesis proceeded on that basis.

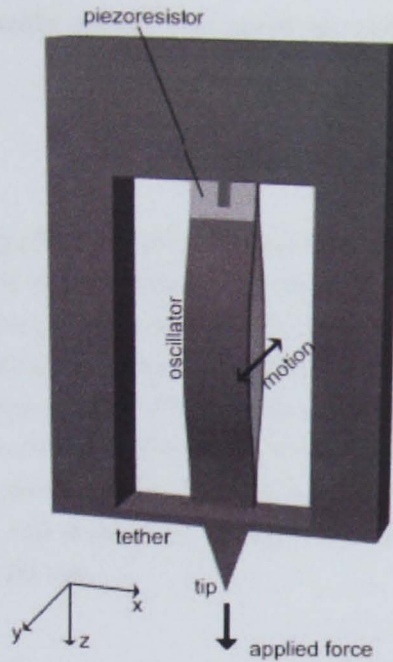


Figure 5.18: Illustration of resonance force sensing AFM tip presented by Harley *et al.* (from [25])

5.3 Summary of useful artefact fabrication techniques

Recent advances in microfabrication techniques open opportunities for novel designs for devices such as the low force transfer artefacts. Such techniques are, however, not as mature and can fundamentally limit the performance of the final design. For example, new additive processes allow for the creation of 'hidden' device features, but often introduce highly anisotropic mechanical properties. The advantages and disadvantages of the most relevant techniques are considered briefly below.

5.3.1 Layered microfabrication

In this approach, devices are constructed in a layer-by-layer approach, typically using well-established methods and pre-prepared masks. Each layer either has a structural, electromechanical or protective function. Additional steps remove material to achieve the desired device behaviour. This fabrication approach can yield extremely small features, below 100 nm, such as required for NEMS devices. All devices are essentially planar in form, though in many cases this is not a specific disadvantage. The production of the required masks and establishment of mask alignment jigs is a costly process, such that prototyping is expensive, but volume manufacture can be very cheap. The breadth of published experience is,

however, such that for specialist applications layered microfabrication is the only suitable method.

5.3.2 EDM

Electro-discharge machining (EDM) is a method of precision engineering in which an arcing needle etches away material to form features as small as 10 μm in size. Using CNC-type control a design prototype can be produced with three-dimensional structure. EDM was used to machine the monolithic structure of the LFB flexures and could perhaps be adapted to produce millimetre-sized flexures for a low force artefact. The author has prescribed the use of this technique to produce a concept model for the triskelion artefact; the NPL Engineering Workshop used a plate-foil-plate sandwich method to machine a sub-millimetre thick flexure without significant warping. The technique is limited by the thickness of the input material and the lateral resolution of the tool.

5.3.3 Stereolithography

Stereolithography, also known in some applications as rapid prototyping or 3D-printing, is an additive fabrication method in which a three-dimensional model is built up in layers by selective use of adhesive or curing agent. The technique allows the production of devices and models with hidden features and various aesthetic features.

In the context of microfabrication, several institutes have developed so-called micro-stereolithography facilities, in which specialist polymers are selectively cured by a highly-focused UV laser beam. These devices can produce items up to 10 mm \times 20 mm in terms of lateral dimensions; vertical range is theoretically unlimited, but in practice constrained by the slow writing time at the highest resolutions.

The produced polymer models may be selectively metallised or impregnated to enable a specific device function, or simply used for demonstration purposes (see figure 9.1 for an example). The mechanical properties of the layered structures are highly anisotropic, limiting functional application. Further, care must be taken when designing any model to avoid sudden increases in lateral dimensions during the fabrication process, or, to add supporting structures that are later machined away.

Table 5.4: Summary of findings of review.

Technology	Advantages	Disadvantages
Deadweight forces	Straightforward use. Need only a reliable lifting mechanism and correct material choice. No development.	Handling uncertainties; used as low force balance verification route.
Elastic element methods	Simple, well-established technology. Focus on ensuring traceability in a proven technology. Robust.	Integration of onboard deflection metrology. Dependence on position of interaction.
Electrostatics, and electromagnetism	MEMS watt and volt balances currently available and hence development relatively cheap and quick.	Integration of onboard deflection metrology without compromising primary mechanism. Crosstalk with balance.
Resonance methods	Promises lower relative uncertainties. Development of poorly represented technology would offer market an alternative.	Practical issues: bandwidth selection, low Q s, miniaturisation and absolute uncertainties. Risky development. Prototype iterations could prove costly.
Van der Waals and Casimir effect	Harnessing ubiquitous forces.	Extreme short-range interaction, implying less robust artefact. Dependence on interaction geometry. Hamaker constant determination.
Biochemical and protein manipulation	Possibility of intrinsic and hence highly repeatable force calibration.	Collaboration required due to new skills. Better for smaller forces (future work).
Fluid flow and capillary forces	Capillary forces always present and must be understood anyway.	Fluid flow totally unsatisfactory. High uncertainties in capillary methods due to, e.g. humidity dependence. Required level of traceability highly unlikely.
Radiation pressure	Simple experimental setup in principle.	High-power laser (heating, safety), used as low force balance verification route.

5.4 Conclusions

In this chapter a number of candidate technologies for transfer artefacts have been reviewed against the specific requirements of both target instruments and the NPL LFB. In chapter 2 additional candidate technologies were reviewed in the context of the Low Force facility as a whole, and dismissed. Constraints such as possible uncertainties, ease of development, risk and prior experience of other groups have been considered. The findings are summarised in table 5.4.

It is clear that to obtain the desired transfer artefact performance in terms of size, robustness and portability, the artefact system should take the form of a MEMS device. NPL has considerable prior experience in MEMS device production and can outsource the final device design and manufacture. Recently reported examples of devices with onboard electronics suggest an advantage in a complete self-contained design with a simple voltage

analogue signal output. This would remove the dependence of the artefact performance on the connected hardware and the possible need to ship that hardware with the artefact. However, the initial cost of prototyping such a design and the manufacturing cost (and hence a non-disposable nature) should not be underestimated.

In summary the following are key requirements for a successful transfer artefact. The artefact must interface with the NPL LFB platen, with the help of a metrologically stable adjustable mounting and viewing system if necessary. Such a system would probably be based on a low-specification AFM for simplicity. The artefact should also interface with other electrostatic force balances worldwide, in particular the NIST EFB, to facilitate comparison. The current iteration of the NIST EFB is configured with stable translation stages and an optical microscope viewing system compatible with AFM cantilever format devices. As the NIST EFB operates in an evacuated chamber, vacuum compatibility is desirable. This places a limit on the choice of materials. It should be noted that for most applications, satisfactory operation in standard atmosphere would be required.

The device must maintain calibration after inversion with respect to gravity due to the different approach directions of the LFB and targets such as AFMs. This points again to micro-scale devices where gravitational effects are very small.

This review has shown that a number of apparently successful calibration transfer systems exist performing at the higher end of the LFB force range. A successful artefact would cover the operating range of the LFB but would focus on the lower end of its performance. Uncertainties of less than 1 nN are essential, and less than 100 pN desirable, to make best use of the force range of the LFB.

To ensure the calibration transfer ability it is essential that the artefact is self-contained. If external metrology is required, this must form part of the artefact system, and would need to be present when calibrating a target instrument. In the case of artefacts based on elastic elements, this points strongly to the use of a MEMS-based displacement sensor, such as the piezoresistive elements or capacitor arrangements used on a number of examples presented in this report.

Several candidate technologies can be immediately dismissed on closer inspection. The extreme short ranges and non-linear effects, combined with exacting geometrical tolerances and poorly known material constants, mean that atomic and quantum effects will not yield a traceable transfer artefact. The uncertainties associated with fluid flow methods are simply too high. Surface tension methods introduce the complications of surface contamination, place a high dependency on atmospheric contamination and humidity and disallow the option of vacuum operation, required for international comparison and some target applications.

Radiation pressure is to be used in the low-range performance verification of the balance and could be used as an independent method for calibration transfer. Furthermore the high-power laser set-up and associated safety mechanisms are not particularly portable.

Biochemical methods, such as protein unfolding, will become the focus of future work as the calibrated force scale is reduced further. This field will hopefully lead to intrinsic force standards: repeatable conformation changes with fixed force input requirements that need only be characterised traceable to SI. However, for a force transfer artefact in the 10 μ N to 1 nN range, biochemical methods are not the best choice.

The remaining methods are based on elastic elements, with added piezoresistive, resonance or electrostatic-based metrology. These are all well represented in reported research, although the focus has remained mostly on proof of operating principle and optimisation of micro-fabrication techniques and not on the demonstration of traceability. Furthermore, the key will be to make a design as simple as possible, to reduce costs and increase confidence in the underlying metrology.

Previous research has often emphasised the transfer of a spring constant calibration, not a force calibration; whilst of use to the AFM field this approach is of little use in other applications. To ensure wider usefulness of the transfer artefact design, deflection metrology of the chosen transfer artefact should be self-contained, so for simple deflected springs an on-board sensor for deflection measurement would be required. A piezoresistive element would be a good choice, but as this has been the choice of most other groups it may be preferable to develop a transfer artefact based on a semi-independent technology for increased end-user confidence following inter-lab comparisons. The quickest route to force traceability would be to design an interface support to hold the piezoresistive cantilevers from NPL, NIST or PTB against the LFB platen. The support would incorporate a micrometer-scale $\{xyz\}$ positioning system that is metrologically stable when at rest. The LFB platen would require an attached tip to interface with the cantilevers.

An alternative option is some form of MEMS electrostatic balance, building on work already carried out at NPL. A comb-drive would not only provide an approximately linear displacement-dependent output, but also a feedback force, depending on the mode of operation. Assuming the output fields of the full-size electrostatic primary instrument do not affect such a MEMS balance, this technology remains a valid option.

The final area for possible further development is in utilising the change in resonance with tension of a resonating elastic element. Previously one major drawback for this method was the requirement for external optical interrogation of oscillation frequency, such as a laser Doppler vibrometry system, reducing the system portability. With the advances in MEMS technology, however, it may be possible to implement an onboard frequency detection sys-

tem with a simple voltage analogue output. With considerable further design work to reduce the scale, and uncertainties, of the technology, and in-depth consideration of external force interface, the technology may become suitable for use in a novel transfer artefact. However, the cost of this work may become prohibitive.

Following the discussions herein, development of a transfer artefact system based on incremental modifications of existing triskelion elastic element designs was recommended. Onboard electronic transducers should convert displacement into a suitably ranged, repeatable voltage analogue for ease of use in the field. The primary candidate for strain sensing was the piezoresistive effect, given the breadth of reported experience. However, noting that no precedent had been found for installation of piezoresistive strain sensors on a rotationally symmetric flexure of the intended force range, alternatives suggested for future consideration were the piezoelectric effect, capacitive and electrostatic technologies.

Chapter 6

Optimisation of transfer artefact flexure design by modelling

This chapter describes the design and optimisation of a flexure geometry for the transfer artefacts based on the triskelion concept. Analytical and finite element models were developed in order to predict the stiffness of prototype and future artefacts. This section describes the development and evaluation of a set of test flexures of known geometry designed to verify the models and inform future designs.

The developed devices are effectively multi-axis strain gauges, optimised for parallel sensing of near-vertical force input. The performance and operating regime of such devices will be dictated by geometry and device mechanical properties. The deformation must be measured, and the presence of the sensing technology has an effect on the device performance, but to a large extent the two design components, mechanical and electrical, can be considered separately.

6.1 Overview of chapter

6.1.1 Chosen flexure design: the triskelion

Any optimisation effort must be supplied with an initial estimate. In line with the discussion presented in previous chapters, in particular in section 5.1.3.1, the triskelion flexure design appeared to be a strong initial candidate for a low force artefact. On balance, it was decided to proceed with the triskelion concept, to determine its suitability. The anatomy of the triskelion is noted in figure 6.1.

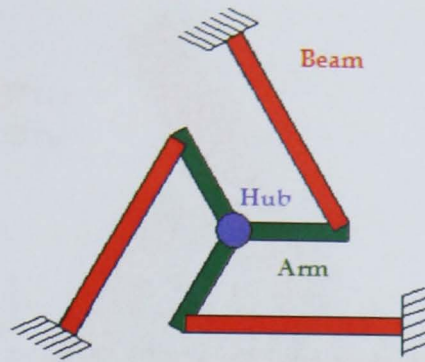


Figure 6.1: The NPL triskelion form, with nomenclature used in this and related documents. The hub and arms are nominally non-compliant, that is, much stiffer than the beams. This stiffness difference is achieved through extra thickness on the arms and hub, and results in concentration of deflection in the outer beams.

6.1.2 Geometrical parameters to investigate

The optimisation of the triskelion flexure can be isolated to a number of key dimensional parameters to be varied, as shown in figure 6.2 and listed as follows.

- L Flexure/beam length
- A Arm radius. That is, the distance from the centre of the hub to the knee where the beam attaches (indicated by a dashed line in figure 6.2)
- T_{beam} Total thickness of the beams
- T_{arm} Total thickness of the arms and hub, to ensure 'rigidity'

It follows from the assumption that the inner arms and hub are rigid that they can have any rotationally symmetric shape to suit the activities at the device centre, provided the mass distribution is known. From a modelling perspective, it is advantageous to place the centre of the inner ends of the beams at a known radius from the hub centre. Prior experience at NPL supports the rotation of the outer beams by 120° from these radial connection points. This results in the arm shape shown in figure 6.2. The hub and arms will of course have some finite compliance, which will translate to an effective additional un-sensed compliance in the outer beams. However, this parasitic contribution should remain small and repeatable. The key requirement, then, is for the arm/hub design to be consistent across any fabricated artefacts.

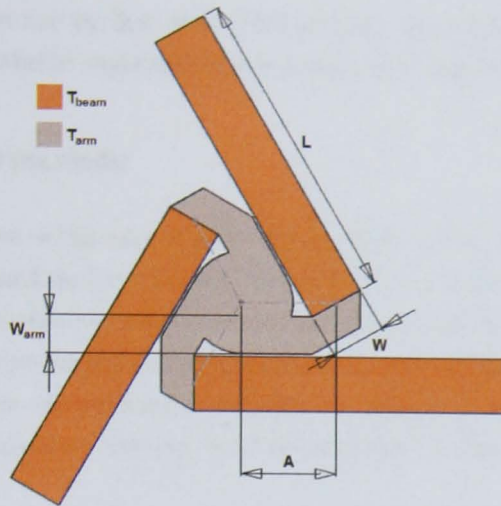


Figure 6.2: Schematic of general model, showing the five key geometry variables for the artefact concept. The shape of the inner arm and hub section is fairly flexible to suit fabrication constraints; the key is that it be much stiffer than the outer beams. Dashed lines show the effective radius of each beam end from the hub centre. The beams are rotated 120° from these lines.

6.2 Development of models for the triskelion

To ensure that the proposed artefacts will operate within the desired range, it is necessary to mathematically model the triskelion flexure's spring constant for a given set of geometry parameter values. To this end, analytical and finite element models of the triskelion were developed and compared. The discussion also presents other property estimations arising from the the modelling work. Simplifying approximations were necessary to permit comparison between models; the implications of these are discussed. Actual comparisons are discussed later in the chapter with reference to prototype artefacts.

6.2.1 Analytical model

If a device can be modelled with a combination of standard beam theory and a set of direct coordinate transformations, then analysis of behaviour and optimisation of geometry is simplified, at least to first order. Initial inspection suggested that the the proposed triskelion geometry was a suitable candidate for a simple model. Such a model is not strictly necessary for this test artefact production, since the small number of devices with deliberately constrained parameter values can be efficiently studied using FEA. However, analytical analysis will be much more useful for the fine-tuning of later 'functioning' prototypes and for this reason it was decided to take the opportunity to develop and test a suitable model. This

model is adapted from that by Sun *et al.* [180] and adopts, in this author's view, a more intuitive notation. The Matlab implementation is presented in appendix B.

6.2.1.1 Basic aim of the model

The simplest aim of the model was to allow the calculation of the vertical spring constant of the artefact for artefact design purposes. The vertical axis forms the major working axis for each of the devices. However, the remaining five stiffness values and estimates of stress and strain also result from the completed model. Of these five stiffness values, the two plane tilt rotational stiffnesses are expected to be finite. An attempt to estimate the first natural frequencies of the the devices, however, was less succesful, as discussed below.

6.2.1.2 Geometry

In the following analysis, the basic microprobe geometry (shown in figure 6.3) is placed in the xy plane so that the centre of the hub's top face is at the origin. The analytical model follows the design discussion above but for clarity of understanding the reader should follow variable definitions as given in this section. The model assumes that the hub and inner arms are rigid, and that all deformation occurs in the outer beams, whose outer ends are constrained in 6DOF. Calculation of the beam stiffness requires knowledge of their dimensions; these are shown in figure 6.4.

A displacement is imposed at this top face centre. This results in deformation in the outer beams. As the beams have finite stiffness, a force is required. As the system is in equilibrium, the forces in the beams sum to equal a force at the top face centre. The force and displacement can be used to calculate the stiffness in the system.

Displacements are given, as required for the stiffness mathematics to follow, as the 6-vector

$$X = \begin{pmatrix} x \\ \theta \end{pmatrix} = \begin{pmatrix} x \\ y \\ z \\ \theta_x \\ \theta_y \\ \theta_z \end{pmatrix}$$

where θ_x , θ_y and θ_z are angles but for small deflections are approximately equal to $\tan(\theta_x)$, $\tan(\theta_y)$ and $\tan(\theta_z)$ respectively.

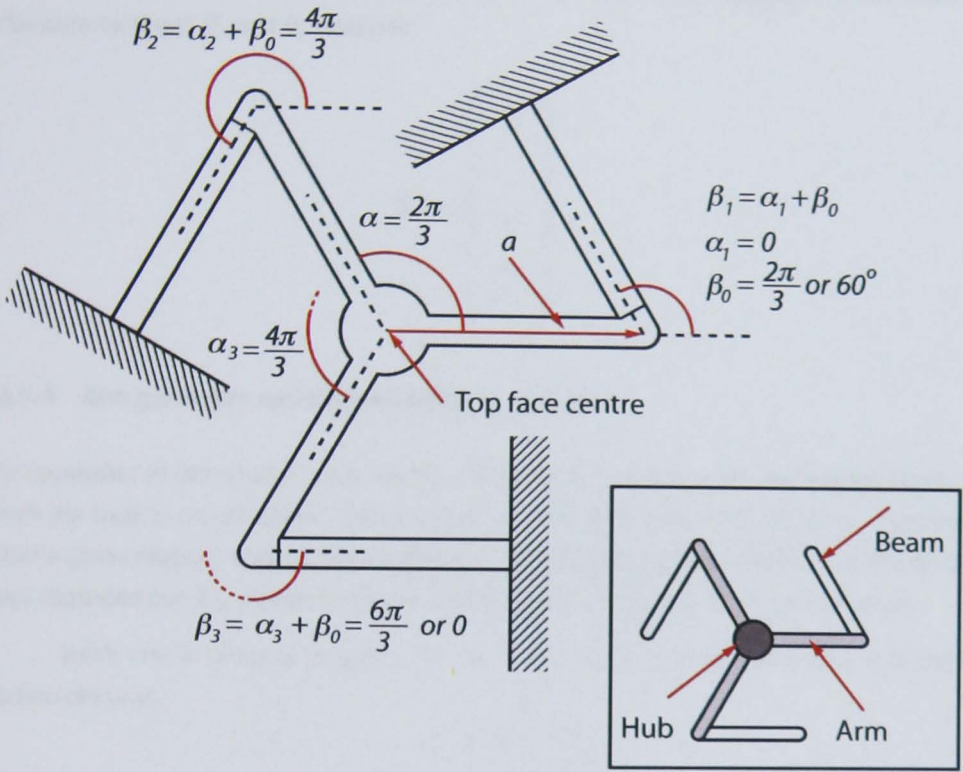


Figure 6.3: Microprobe geometry used in this discussion

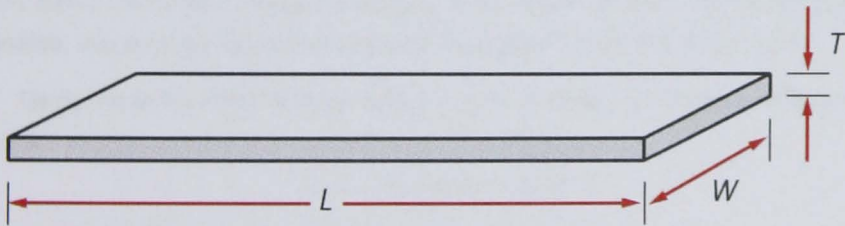


Figure 6.4: Dimensions of the rectangular outer beams

6.2.1.3 Input displacement

The input displacement X_0 that generates the reaction force to be calculated is restricted to z displacement and θ_x and θ_y rotations

$$X_0 = \begin{pmatrix} 0 \\ 0 \\ z \\ \theta_x \\ \theta_y \\ 0 \end{pmatrix}.$$

6.2.1.4 Arm geometry and displacement of arm tips

It is necessary to calculate a transformation from the hub centre to the ends of the arms, to which the beams are attached. The locations of these arm ends are, therefore, calculated under a given rotation, and the result used to form a transformation matrix to operate on the input displacement X_0 , giving the effect of the centre's displacement on the arm ends.

Each arm is of equal length a . For each arm $i = 1, 2, 3$ the arm end a_i is found in the hub plane at

$$a_i = \begin{pmatrix} a \cos(\alpha_i) \\ a \sin(\alpha_i) \\ 0 \end{pmatrix}$$

where $\alpha_i = (i - 1) \frac{2\pi}{3} = 0, \frac{2\pi}{3}, \frac{4\pi}{3}$. Note that a_i derives from a z rotation in α_i of $(a \ 0 \ 0)^T$, an arm lying along the x axis.

Consider a small rotation of the hub-arm system about the x axis, as shown in figure 6.5. Two of the arm ends will be deflected a short way from the $\{xy\}$ plane, resulting in a non-zero z coordinate. There will also be a small cosine-effect shortening of the (x, y) coordinates; this shortening may be assumed negligible for this first-order model.

Using the small angle approximation $\tan \theta \approx \theta$ it follows that the z deflection from x rotation is

$$a_{i,z,x} = a_{iy} \tan \theta_x \approx a_{iy} \theta_x$$

and similarly the z deflection from y rotation is

$$a_{i,z,y} = a_{ix} \tan \theta_y \approx a_{ix} \theta_y.$$

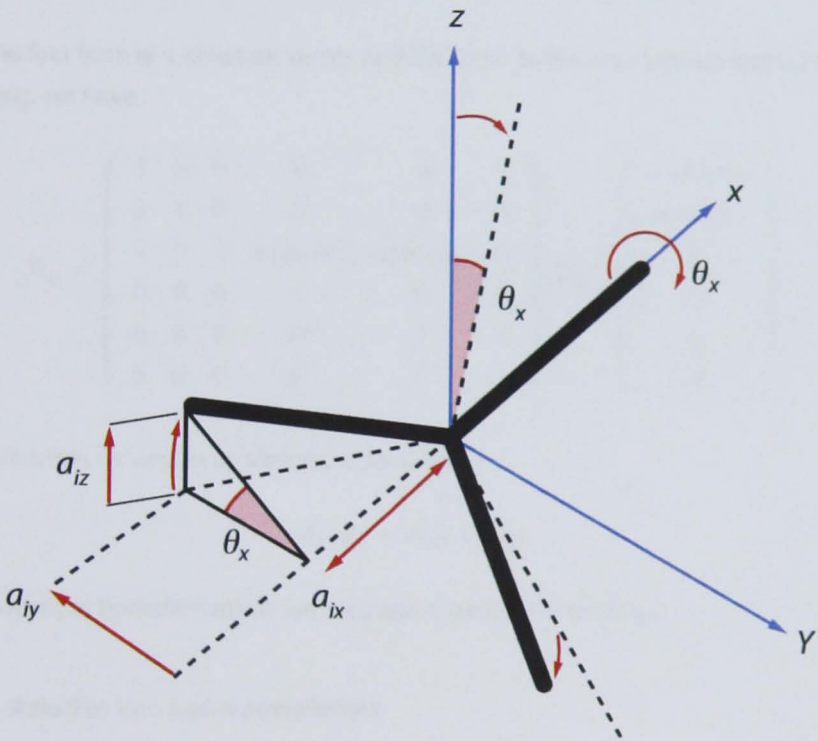


Figure 6.5: Effect of a small rotation about x on the vertical position of the arm ends

This gives a total z deflection of

$$a_{iz} = a \sin(\alpha_i) \cdot \theta_x + a \cos(\alpha_i) \cdot \theta_y.$$

The total displacement X_a of each arm end from the origin consists of three parts:

$$\begin{aligned} X_a &= \text{[displacement of hub centre from origin]} \\ &+ \text{[displacement of arm ends in hub plane]} \\ &+ \text{[vertical arm end displacement due to tilt]} \end{aligned}$$

where the first term is a constant vector and the other terms are matrices operating on X_0 . Combining, we have

$$X_{ai} = \begin{pmatrix} 1 & 0 & 0 & 0 & 0 & 0 \\ 0 & 1 & 0 & 0 & 0 & 0 \\ 0 & 0 & 1 & a \sin(\alpha_i) & a \cos(\alpha_i) & 0 \\ 0 & 0 & 0 & 1 & 0 & 0 \\ 0 & 0 & 0 & 0 & 1 & 0 \\ 0 & 0 & 0 & 0 & 0 & 1 \end{pmatrix} X_0 + \begin{pmatrix} a \cos(\alpha_i) \\ a \sin(\alpha_i) \\ 0 \\ 0 \\ 0 \\ 0 \end{pmatrix}.$$

This can be written as shorthand for later:

$$A_i(X) = A_{Ii}X + A_{Ili}$$

that is, a rotation (transformation) term A_{Ii} and a translation term A_{Ili} .

6.2.1.5 Rotation into beam coordinates

To calculate the mechanics in the outer beams, the use of a beam-aligned coordinate system is required. Specifically, the total displacement of the arm ends must be rotated in z by β_i , the angle in the 'global' coordinate system of each beam to the x -axis. If $\beta_0 = \frac{2}{3}\pi$ is the angle between each arm and beam, then

$$\beta_i = \alpha_i + \beta_0 = \begin{cases} 0 + \frac{2}{3}\pi = \frac{2}{3}\pi & (i = 1) \\ \frac{2}{3}\pi + \frac{2}{3}\pi = \frac{4}{3}\pi & (i = 2) \\ \frac{4}{3}\pi + \frac{2}{3}\pi = \frac{6}{3}\pi = 0 & (i = 3). \end{cases}$$

Define a generalised rotation in z of β , based on standard rotation operation

$$B_i = \begin{pmatrix} \cos(\beta_i) & -\sin(\beta_i) & 0 & 0 & 0 & 0 \\ \sin(\beta_i) & \cos(\beta_i) & 0 & 0 & 0 & 0 \\ 0 & 0 & 1 & 0 & 0 & 0 \\ 0 & 0 & 0 & \cos(\beta_i) & -\sin(\beta_i) & 0 \\ 0 & 0 & 0 & \sin(\beta_i) & \cos(\beta_i) & 0 \\ 0 & 0 & 0 & 0 & 0 & 1 \end{pmatrix}.$$

This can also be written as shorthand for later:

$$B_i(X) = B_i X$$

and the displacement of the 'free' ends of the beams given as $X_{bi} = B_i(A_i(X_0))$.

Displacement in this sense refers to the fixed geometry of the artefact: the displacement of one part of the geometry from another, or from the origin, as here. Under a finite input force, the free beam ends move to a new total displacement from the origin, and it is this relative vector move that is required when considering the compliance of the beams, as in the following sections. This relative displacement is calculable as $X_{bi} - X_{bi0}$ where $X_{bi0} = X_{bi}$ when $X_0 = X_{00} \equiv (0 \ 0 \ 0 \ 0 \ 0 \ 0)^T$.

6.2.1.6 Forces in the beams

All elastic deformation is assumed to occur in the outer beams, rectangular cantilevers of dimensions shown in 6.4. Each deformed beam is subject at equilibrium to a vector force F_i^* and moment M_i^* , where the asterisks refer to the beam coordinate system

$$P_i^* = \begin{pmatrix} F_i^* \\ M_i^* \end{pmatrix} = \begin{pmatrix} F_{xi}^* \\ F_{yi}^* \\ F_{zi}^* \\ M_{xi}^* \\ M_{yi}^* \\ M_{zi}^* \end{pmatrix}.$$

The total 'force' P_i^* is obtained as the product of the stiffness matrix k and the beam end displacement from its initial position

$$P_i^* = k(X_{bi} - X_{bi0})$$

where k simplifies for a simple cantilever from the classic suspension beam element stiffness matrix to

$$k = \frac{Etw}{l} \begin{pmatrix} \frac{w^2}{l^2} & 0 & 0 & 0 & 0 & -\frac{w^2}{2l} \\ 0 & 1 & 0 & 0 & 0 & 0 \\ 0 & 0 & \frac{t^2}{l^2} & \frac{t^2}{2l} & 0 & 0 \\ 0 & 0 & \frac{t^2}{2l} & \frac{t^2}{3} & 0 & 0 \\ 0 & 0 & 0 & 0 & k_{55} & 0 \\ -\frac{w}{2l} & 0 & 0 & 0 & 0 & \frac{w^2}{3} \end{pmatrix} \quad \text{where } k_{55} = \frac{G}{E} t^2 \left[\frac{1}{3} - 0.21 \frac{t}{w} \left(1 - \frac{t^4}{12w} \right) \right]$$

where E is the Young's modulus and G the shear modulus (see any standard elasticity textbook for the individual elements of this matrix).

6.2.1.7 Propagation of force back to hub centre

According to Newton's third law, the forces and moments on the end of each beam will equal those on the connected arm end. Further, the force at the hub centre (i.e. that exerted to generate the initial displacement X_0) will equal the vector sum of the forces on each arm end. It is, therefore, necessary to transform each force P_i^* into hub centre coordinates as P_i and sum to give the total input force P_0

$$P_i^* \mapsto P_i \mapsto P_{0i} \mapsto P_0,$$

each transition of which will be discussed briefly below.

Propagation $P_i^* \mapsto P_i$: This step is the reverse transformation of $B_i(X)$ and therefore given by

$$P_i = B_i^{-1}(P_i^*) = B_i^{-1} P_i^*.$$

Propagation $P_i \mapsto P_{0i}$: This step is the reverse transformation and translation of $A_i(X)$ and therefore given by

$$P_{0i} = A_i^{-1}(P_i) = A_i^{-1}(P_i - A_{Hi}).$$

Propagation $P_{0i} \mapsto P_0$: Finally, the input force P_0 is simply the sum of those from each leg, i.e. $\sum P_i$.

6.2.1.8 Stiffness

All of the steps described above can be summarised into one line, giving P_0 as a function of X_0 :

$$P_0 = K(X_0) = \sum A_i^{-1} B_i^{-1} k (B_i A_i X_0 - B_i A_i X_{00}).$$

It would be reasonable to expect that, for any given X_0 , for this first-order model, $K(X_0)$ would reduce to a diagonal matrix K , containing the effective spring constants for each degree of freedom:

$$K = \begin{pmatrix} k_x & 0 & 0 & 0 & 0 & 0 \\ 0 & k_y & 0 & 0 & 0 & 0 \\ 0 & 0 & k_z & 0 & 0 & 0 \\ 0 & 0 & 0 & \lambda_x & 0 & 0 \\ 0 & 0 & 0 & 0 & \lambda_y & 0 \\ 0 & 0 & 0 & 0 & 0 & \lambda_z \end{pmatrix}$$

which may be used to evaluate design specifications for the prototype artefacts.

6.2.2 Finite element model

In order to verify results obtained from the analytical model, a parameterised CAD model of the triskelion concept was developed, from which finite element analysis (FEA) load-displacement studies could be undertaken.

Solidworks Premium 2009 was used to generate the required generalised three-dimensional geometry shown in figure 6.2 above. A convenient feature of Solidworks is the ability to parameterise the CAD layout, provided suitable constraints and relationships are set up, so that the model can be quickly resized by changing variable values. The variables programmed were W , L , T_1 , T_2 and A , corresponding to the analytical model's variables, and a dependent variable $W-2$ equal to half of W . Figure 6.6 shows a working view in Solidworks highlighting the use of most of these variables. T_1 and T_2 correspond to T_{beam} and T_{arm} respectively. As mentioned previously, the design of the hub and arms is similar but not identical to that of the previously fabricated microprobe prototypes; the new design has been adjusted to set the 'knee' angles to exactly 120° .

The built-in mechanical FEA tool in Solidworks (SimulationXpress) was used to simulate the application of a known ($10 \mu\text{N}$) load in the z direction with the free beam ends held

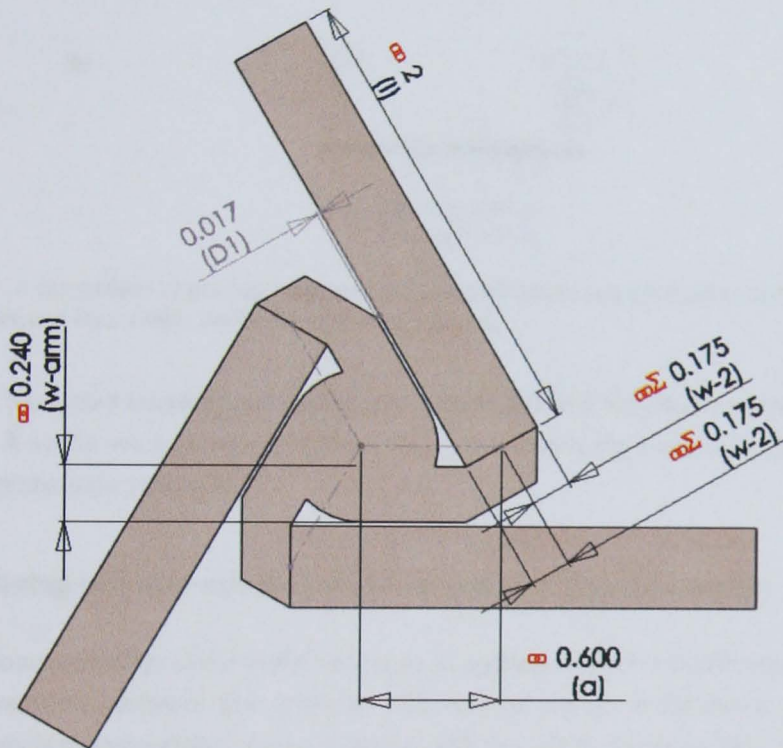


Figure 6.6: Schema of FEA model corresponding to simplest analytical model. This has been chosen as the basis for the shape of the prototype transfer artefact set. Shown are the in-plane geometry variables with their working values at the time this figure was created. The 'chain' and 'sum' signs indicate links to constant and derived parameters respectively. The quantity $w-2$ is a derived parameter equal to $w/2$. The measured gap $D1$ is shown at its smallest value of $17\ \mu\text{m}$, corresponding to the smallest value of A in the artefact set, $0.6\ \text{mm}$.

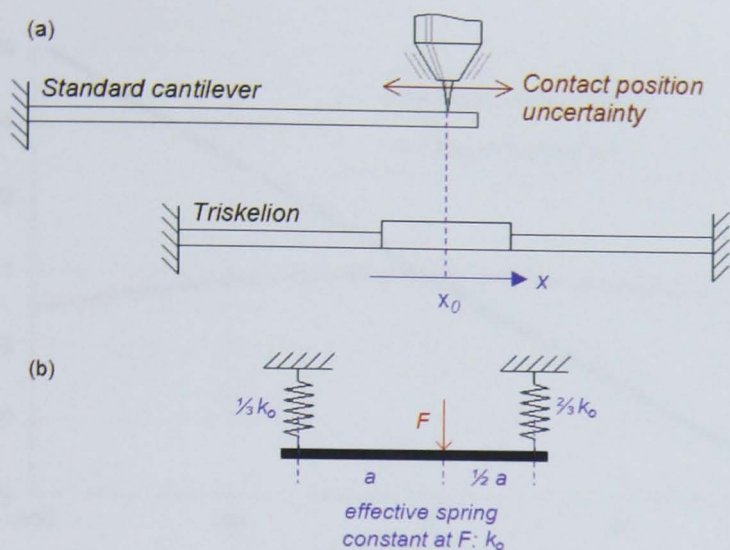


Figure 6.7: A comparison of the alignment sensitivity of a cantilever and a triskelion: (a) the physical comparison; and (b) a simple model of the triskelion flexure.

in 6DOF; the output displacement vector was used to estimate the effective vertical device stiffness. A similar analysis was completed applying a load in the x direction, to obtain an estimate of the lateral stiffness.

6.2.3 Spring constant sensitivity advantages of a triskelion design

The rotational symmetry of the triskelion flexure arrangement offers a significant advantage over conventional cantilever type artefacts. With nominal contact at the device centre, the device vertical spring constant shows a plateau with respect to lateral position, making alignment less critical. In contrast, the spring constant for a simple cantilever is always highly position-dependent. This result is best explained by reference to an example of each device (see figure 6.7). The triskelion may be modelled in two dimensions in the vertical plane as a bar on two springs. Assuming a suitably sized hub and a nominal spring constant of k_0 at perfect alignment, the vertical spring constant of the device will equal $\frac{2}{3}k_0$ at one extreme and $\frac{1}{3}k_0$ at the other, passing through a maximum of k_0 in the centre in a second-order alignment dependence. A similar derivation for a cantilever shows an approximately linear dependence on alignment for small misalignments.

The relative change in vertical spring constant as a function of misalignment is plotted in figure 6.8 for similarly dimensioned triskelion and cantilever of equal nominal spring constant. The benefit of the rotationally symmetric triskelion in this manner is clear.

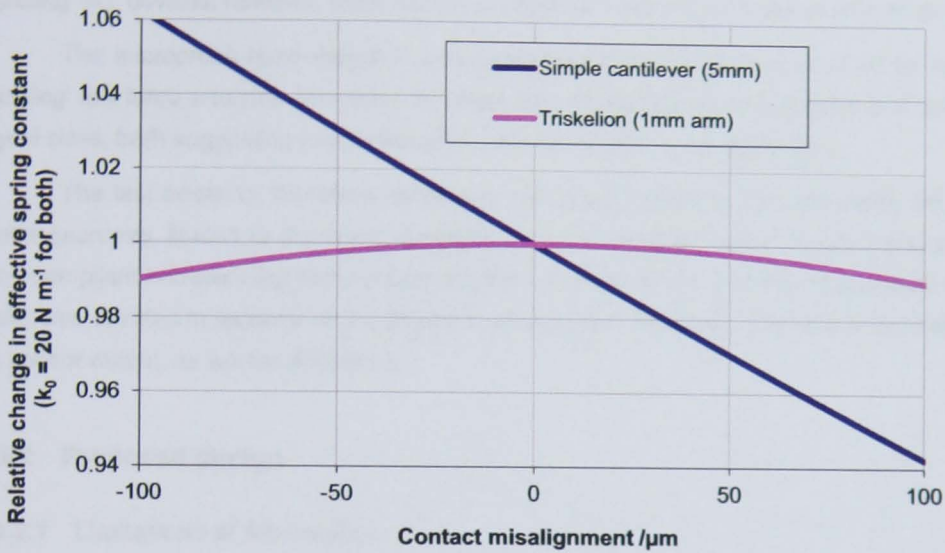


Figure 6.8: Representative results for comparative alignment sensitivity of triskelion and simple cantilever, with common nominal spring constant of 20 N m^{-1} . Modelled triskelion arm length: 1 mm. Modelled cantilever nominal axial contact point: 5 mm.

6.3 Prototype artefact development

In order to develop the low force transfer artefact concept and to verify the performance of the related mathematical models described above, a suite of prototype artefacts were designed and made. This section describes this process.

6.3.1 Specification for test artefact

The primary purpose of the prototype artefacts was not to function as an ideal transfer artefacts *per se*. Rather, they should allow the investigation of the geometry dependence of device performance and the present understanding of their behaviour as represented by the current software and mathematical models, by being optimised for easily available evaluation tools.

Advantages could be seen in making use of existing effort carried out, and planned, for the microprobe project, with the aim of reducing costs for these prototype artefacts. In particular, significant time had already been spent developing electronic and mechanical interfaces to the piezoelectric sensors on the microprobe prototypes. Whilst the prototype low force artefacts were intended to operate in a quasistatic, 'DC' mode, the microprobes are

vibrating 'AC' devices; however, there remained significant overlap to be taken advantage of.

The microprobe base design is somewhat larger than what may be used for later 'working' low force artefacts. However, its larger size implies greater robustness and larger signal sizes, both suggesting lower risks and costs for experimental evaluation.

The test artefacts, therefore, consist of calculated variations from the basic microprobe geometry, limited to the beam (compliant, sensor-equipped outer leg part) and arm (non-compliant hub-ward leg part) lengths, widths and thicknesses. Remaining space on the wafer was devoted to reduced-size artefacts to explore the dependency of sensor geometry on sensor output, as will be discussed.

6.3.2 Proposed design

6.3.2.1 Limitations of fabrication

The cost and complexity of device fabrication limit the variation of parameter values. The set of test artefacts must be contained within a finite-sized substrate wafer, limiting the artefact count. Certain variables, such as PZT film thickness, must be set at a constant value shared across the wafer and set of test artefacts. Whilst there are few constraints on the planar shape of the flexures, each additional region with a unique thickness adds significantly to the cost of fabrication, which must be minimised. Finally, the significant risk of some artefacts failing to operate implies the need for redundancy in the artefact set, further reducing the possible unique artefact count (and hence parameter variation). These limitations will be accounted for in the following sections.

Detailed information on the fabrication processes used to create the most recent batch of microprobe prototypes, on which the proposed artefacts are based, is beyond the scope of this document. However, it is important to note that the number and complexity of masks required defines a major variable cost in fabrication. Although some masks are reused for several fabrication steps, at least eight distinct masks will be required for the proposed work. The mask requirements are summarised below for ease of reference:

- Mask 1: preparation of silicon substrate
- Mask 2: deposition of titanium/platinum electrode network
- Masks 3-5: nickel flexure structure, layers 1-3
- Mask 6: PZT preparation; electrode preparation
- Mask 7: alignment aid removal

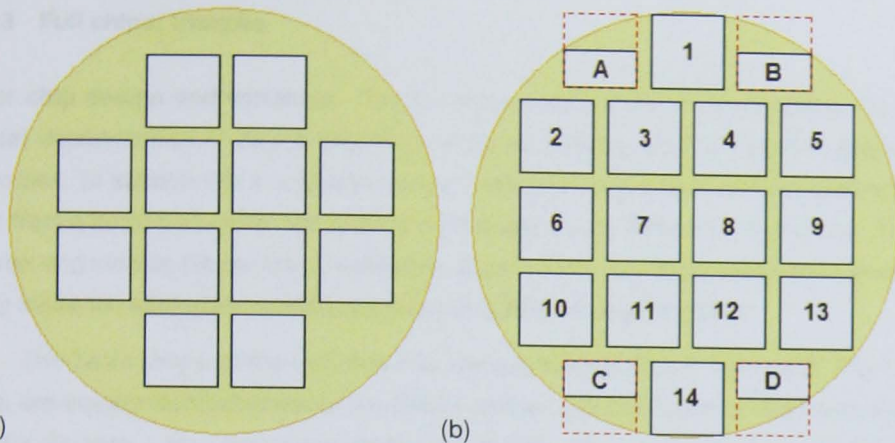


Figure 6.9: Wafer layout options: (a) existing layout with twelve 13 mm × 13 mm chips, as used successfully in microprobe project; (b) proposed higher density layout using 12 mm × 12 mm chips to maximise prototype population. Half-die, shown within the red dotted squares, were not present on the microprobe wafers but are to be added to further increase functionality; see 'partial chip' discussion below.

- Mask 8: wafer preparation for plating

The masks are sourced by Cranfield University from a commercial partner based on CAD drawings.

6.3.2.2 Wafer layout

The equipment used at Cranfield uses four inch (102 mm) silicon wafers, of which three inches (76 mm) of diameter is available for devices. For the microprobe project, the device die were arranged in a 2-4-4-2 cross grid with a 3 mm separation (figure 6.9a). The die are nominally half-inch (13 mm) squares containing the devices, and pads for electrical connections. Twelve square chips therefore resulted from this wafer design. A reduction in chip side to 12 mm, as shown in figure 6.9b, increased the possible die count to fourteen, permitting a greater variation of parameters.

Introduction of partial chips The spare wafer capacity around the full-size chips was used for 'partial' chips containing smaller devices with fewer connection requirements. To simplify both design and testing of the various chips, it was decided that the 'full' chips would contain full instrumented triskelia primarily for the study of mechanical behaviour, whilst the partial chips would contain simple cantilevers to focus on sensor/actuator performance dependencies.

6.3.2.3 Full chips: triskelia

Master chip design and variables The full chips were intended to demonstrate the mechanical dependencies of device properties such as stiffness on the triskelion geometry dimensions. To achieve this in a straight-forward way, the chips would vary by small adjustments from a basic parameter set optimised for experimental behaviour verification. To reduce risk and simplify the design of verification experiments, this basic parameter set would closely follow the microprobe prototypes previously fabricated at Cranfield.

The basic shape of the triskelion has already been shown in figure 6.2. The three beams are equally distributed about the device centre, and the centre of the beam end is held at a distance A from the device centre by the arms. The beams are rotated 120° from these radial connection lines. The arms and beams have widths W_{arm} and W respectively, which in the proposed artefact set would not be varied. The hub radius is defined by the above and is equal to $W_{\text{arm}} + \frac{1}{4}W$. The beams of a single device share a common thickness T_{beam} , and the arms and hub a common thickness T_{arm} .

Sensor design Constant force actuation is achieved in principle by maintaining a constant potential difference across the relevant actuator. The existing sensor and actuator design implemented on the microprobe flexures fabricated at Cranfield, upon which these test artefacts are based, was hoped to suffice for an initial proof of concept of quasistatic sensor function. Further, the reuse of the same design, and hence the same fabrication steps, was intended to significantly reduce the risk, and hence cost, associated with fabrication.

The in-plane shape of the sensor and actuators is defined by the geometry of the platinum electrodes that form the signal connections. Portions of the PZT film between the electrodes and the grounded nickel flexures are activated during the poling process to form the required active regions.

For simplicity the electrode design, would follow that from the microprobe prototypes, as shown schematically in figure 6.10a. To achieve the changes in beam length required between test artefacts, the entire beam layout design should be scaled lengthways. This would maintain the size ratio between sensor and actuator and maintain the same placement of sensors with respect to the regions of maximum strain. Maximised strain in the sensors maximises signal output and hence device sensitivity.

The fabrication process defines the minimum practical width and separation of the signal tracks running from the hub-ward electrodes onto the body of the chip. That is, a fixed minimum absolute width portion of the beams must be allocated to these tracks. It is important to maximise sensor/actuator area both to maximise basic function and to minimise the

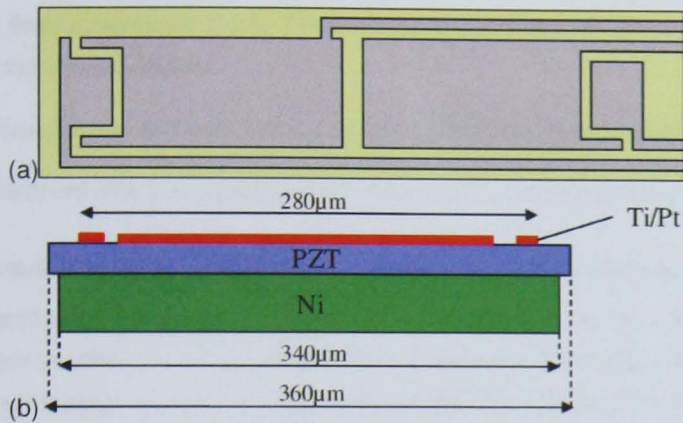


Figure 6.10: Schematic diagrams of the proposed sensor/actuator design adapted from previous drawings by Cranfield, not to scale: (a) top-down (from substrate side) view of sensor/actuator electrode layout over PZT and nickel layers; (b) expected cross-section of proposed beam showing PZT layer somewhat wider than the nickel flexure.

relative contribution of parasitic signals from the tracks themselves. Due to limitations of the fabrication process, the tracks also become activated, increasing the area of the connected sensor/actuator in an undesirable region.

Cranfield suggest a minimum nickel flexure (beam) width of $350\ \mu\text{m}$, which would permit a total electrode width of around $290\ \mu\text{m}$ and an active sensor/actuator width of around $250\ \mu\text{m}$. A typical cross-section given schematically in figure 6.10b highlights the fact that the PZT extends past the nickel layer due to the nature of the fabrication process.

The outer edges of the sensor regions should coincide with the effective ends of the beams, that is the ends of the regions of beam thickness. The sensors and actuators should be separated by the minimum recommended gap.

Wafer layer thicknesses Device stiffness is highly dependent on flexure thickness; beam theory has cantilever out-of-plane stiffness proportional to the cube of the thickness. The latest microprobe prototypes are assembled from a constant $4\ \mu\text{m}$ to $5\ \mu\text{m}$ layer of sol-gel PZT and two $9\ \mu\text{m}$ electroplated layers of nickel. Explicitly:

Hub and arms:	$9\ \mu\text{m (Ni)} + 4.5\ \mu\text{m (PZT)} = 13.5\ \mu\text{m}$ approximately
Beams:	$18\ \mu\text{m (Ni)} + 4.5\ \mu\text{m (PZT)} = 22.5\ \mu\text{m}$ approximately

The proposed design was to retain these thicknesses and add a third, to allow multiple beam thicknesses. Following consultation with Cranfield, it was proposed that the nickel structures on the wafer be constructed using three electroplating sessions (that is, one extra mask), using the following procedure:

1. Plate all flexure regions to 5 μm . This creates a stable base for all flexures and forms by itself the thinnest beams.
2. Plate thicker beams and hubs/arms with 4 μm , completing the thicker beams.
3. Finally plate only the hubs/arms with a further 9 μm , completing these inner regions.

The total thicknesses of these regions would, therefore, be approximately as follows:

Hub and arms (common):	$5 \mu\text{m (Ni)} + 4 \mu\text{m (Ni)} + 9 \mu\text{m (Ni)} + 4.5 \mu\text{m (PZT)} = 22.5 \mu\text{m}$
Thinner beams:	$5 \mu\text{m (Ni)} + 0 \mu\text{m (Ni)} + 0 \mu\text{m (Ni)} + 4.5 \mu\text{m (PZT)} = 9.5 \mu\text{m}$
Thicker beams:	$5 \mu\text{m (Ni)} + 4 \mu\text{m (Ni)} + 0 \mu\text{m (Ni)} + 4.5 \mu\text{m (PZT)} = 13.5 \mu\text{m}$

This approach maintains a relatively large arm to leg stiffness ratio whilst keeping the absolute stiffnesses small, as appropriate for testing.

As discussed, the PZT film layer, which is deposited via spin-coating, must be constant for the whole wafer. This, therefore, precludes any variation in sensor/actuator thickness, despite the value such variation might bring.

Chosen parameter values With the above discussion in mind, a set of parameter values were chosen for the test artefacts; these are given, with justifications, in table 6.1. The existing microprobe prototype has a central hub and arm set such that the arm radius is about 1 mm. The outer beams have length, width and thickness of 2 mm, 350 μm and 14 μm respectively. The second full chip device ('B') would be equivalent to this, with a modified hub shape as shown in figure 6.2. The vertical stiffnesses of the chosen devices have been calculated using analytical and finite element models, as described in section 6.3.3.

It was assumed that fourteen full chips would be possible. If closer inspection of the fabrication process had indicated that only twelve could be accommodated, the two variations labelled with an asterisk in table 6.1 would have been reduced by one. It was likely that some of the fabricated devices would fail to operate as designed due to failures in the fabrication process. Therefore, many of the variations were represented on two die which would be physically separated on the wafer to increase the chances of at least one surviving fabrication. However, the desire to try as many parameter combinations as possible had ruled out further duplication. See section 6.3.2.5 for the physical assignment of chips across the wafer.

Chip body design The devices were to be built on a silicon wafer substrate that forms the 12 mm \times 12 mm chip body. The chip body provides a rigid support for the nickel triskelion and a location for solder pads. The chip layout used on the latest microprobe prototypes

ID	#	A/mm	ΔA	L/mm	ΔL	W/mm	$T_{\text{beam}}/\mu\text{m}$	$\Delta T_{\text{beam}}/\mu\text{m}$	$T_{\text{arm}}/\mu\text{m}$	$\Delta T_{\text{arm}}/\mu\text{m}$
A	1	1.0		2.0		0.35	5.0 + 4.5		18.0 + 4.5	
'Master' artefact, similar to original microprobe dimensions with thinner beams; basis for comparisons										
B	2	1.0		2.0		0.35	9.0 + 4.5	+ 5	18.0 + 4.5	
Original microprobe in-plane dimensions; equivalent beam/arm thicknesses. For run to run comparison check.										
C*	3, 4	1.0		1.5	$\times 0.75$	0.35	5.0 + 4.5		18.0 + 4.5	
Shorter beams. For comparison with artefact D.										
D	5, 6	1.0		3.0	$\times 1.5$	0.35	5.0 + 4.5		18.0 + 4.5	
As C, with beams twice as long. Thus, should be a factor of eight more compliant.										
E	7, 8	1.0		3.0	$\times 1.5$	0.35	9.0 + 4.5	+ 5	18.0 + 4.5	
As D, with beams thicker as in B; should be around three times stiffer than D, but three times more compliant than B.										
F*	9, 10	0.5	$\times 0.5$	2.0		0.35	5.0 + 4.5		18.0 + 4.5	
The shorted beams in these artefacts should increase the rotational stiffness of the hub centre compared to A.										
G	11, 12	0.5	$\times 0.5$	3.0	$\times 1.5$	0.35	5.0 + 4.5		18.0 + 4.5	
As F, with longer beams, further increasing the arm:beam ratio and hence the rotational stiffness at the hub.										
H	13	1.5	$\times 1.5$	3.0	$\times 1.5$	0.35	5.0 + 4.5		18.0 + 4.5	
Beam theory predicts that this artefact should be as stiff as artefact A and will highlight deviations from the theory.										
I	14	10		2.0		0.35	5.0 + 4.5		5.0 + 4.5	- 13
This special case artefact has a hub/arm thickness equal to that of its beams. The behaviour of this artefact will deviate from what is predicted by the analytical model, and such deviations will inform the development of future analytical models.										

Table 6.1: List of proposed test artefacts and their parameter variation from the original microprobe prototype.

had proved successful, and was to be retained. Suitable interfacing hardware for the solder pads had been designed and sourced, and was not to be altered. As will be discussed, the pad locations on the partial chips should, if possible, use the same relative locations. A chip holder for the previous 13 mm × 13 mm chip can be altered to accommodate the proposed smaller chips.

It was not necessary for the void in the silicon to form a full triangle - this could be clipped to suit, particularly for the larger proposed triskelion. However, the microprobe ground-plane border from the nickel plating was to be retained in equivalent form.

6.3.2.4 Partial chips: cantilevers

Overview The function of the partial chips was to enable optimisation of sensor and actuator design. To do this, the devices on the partial chips were designed to allow comparative evaluation of different sensor/actuator geometries. The test sensors/actuators were placed on rectangular cantilevers that not only offer a simpler geometry, and hence analysis, but also required less room, as necessitated by the partial chip sizes. The four chips were grouped in two pairs. The first pair contained simple cantilevers with different sensor sizes; the second pair contained an advanced arrangement designed to further localise strain and hence attempt to increase sensitivity.

Simple cantilever: chips A, B To optimise the design of future triskelion low force artefacts, a good understanding of the relationship between sensor/actuator dimensions and performance was required. To achieve this effectively, it appeared useful to have simple physical test artefacts similar to the triskelion beams in which the sensor dimensions are varied. The first two partial chips would, therefore, take the form shown in figure 6.11.

The chips would contain three adjacent cantilevers, numbered C1 to C3 for ease of reference. Each cantilever would be instrumented with two sensor/actuator pads of equal length and unequal width. The width ratio would allow better understanding of width dependency by comparison of output under beam deflection. Cantilevers C1 and C2 were of equal length but carried sensors of unequal length. The comparison of these would confirm the sensitivity increase achieved by extending the sensor pads only over the region of maximum strain, and, conversely, the benefit of actuating all the available beam area. Cantilevers C2 and C3 had a 2/3 length ratio but the sensor coverage fraction was to be equal on both. Thus one cantilever should be around a factor of 3.4 stiffer yet the sensitivity should be approximately equal.

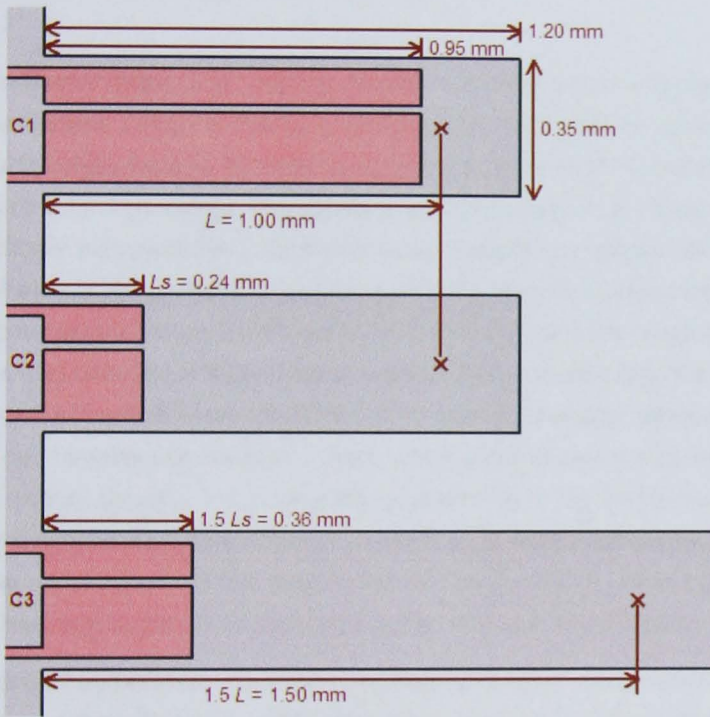


Figure 6.11: Simple cantilevers C1 to C3 equivalent to portions of beams on full artefacts A and D; these cantilevers allow investigation of sensor dimensional requirements in a simplified system. The cantilevers have common thickness nickel thickness $5 \mu\text{m}$ (circa $9.5 \mu\text{m}$ with PZT) equal to the beam thicknesses on full artefacts A, D.

Allowing for a 350 μm to 500 μm separation between adjacent cantilevers, the entire active area, from which the silicon substrate has been removed, should need to be no larger than 3 mm square; this would allow for some flexibility in placement on the chip.

The common cantilever thickness will be 9.5 μm , that is, formed only from the first 5 μm nickel plating mask. However, the later nickel plating layers were to be used to form locator fiducials at a well-defined point close to the cantilever ends, as shown in figures 6.11 and 6.12. The exact form of the fiducials was subject to discussion, not least regarding the lateral plating resolution achievable from the standard masks.

Modified cantilever: chips C, D Having devised test structures to help optimise the triskelion sensor/actuator design in the form of the simple cantilevers in section 6.3.2.4, the remaining partial chips were to be used to consider a non-standard cantilever design, as shown in figure 6.12. This design incorporated two narrow legs at the base of the cantilever that drastically increased the compliance (and hence strain concentration) in the root area. Beam theory suggests that this would not only dramatically increase the device sensitivity, but also somewhat reduce the dependence of detected stiffness on contact point along the cantilever. The latter result implied lower measurement uncertainties; this fact motivated the development of the NIST piezoresistively instrumented cantilever, discussed in section 5.2.1.2. The fact remains that cantilevers were less than ideal due to inherent asymmetries and arcuate motion concerns, motivating the development of the triskelion-based sensor. However, there may be situations in which a cantilever is more appropriate, and these devices were expected to help in that regard. Further, the cantilevers shall usefully simulate typical cantilever-type targets to be calibrated by the NPL Low Force Facility.

Figure 6.12 shows three cantilevers, labelled C4 to C6 for convenience; the key difference between the three being the width of the small symmetrical legs at the root. C4 has a continuous root region; C5 and C6 have 80 μm and 120 μm width legs respectively. The root legs have length 200 μm , and thickness 9.5 μm formed from the 5 μm initial nickel plating session. The remainder of the cantilevers, 1 000 μm \times 350 μm , have thickness 22.5 μm based on the full 18 μm nickel plating. Electrode size would be maximised but the exact shape was to be finalised as appropriate for fabrication at the mask design stage. The form of the fiducial marks would also be finalised at mask design stage.

Chip body design The wafer layout sketches shown earlier in figure 6.9 suggested that three-quarters of the full chip shape would be available; the removed section forms a rough triangle from one corner to the middle of an opposing side, as shown in figure 6.13. The sketch appears to support the four to six contact pads required by the proposed designs

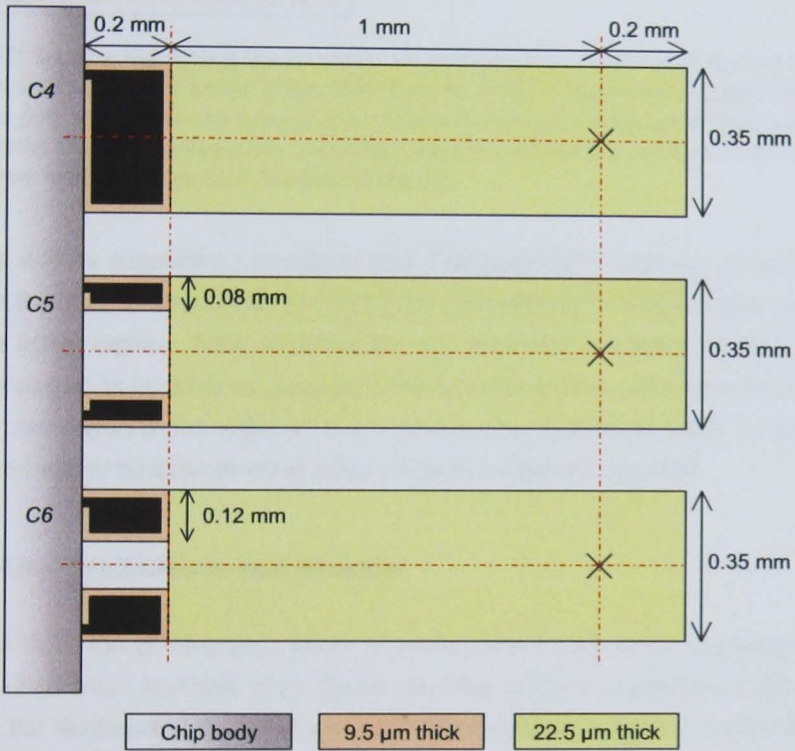


Figure 6.12: Multiple-legged cantilever variants with a less critical stiffness dependence on length. The cantilevers C4 to C6 are identical except for base leg width. These are based on a previous concept developed at NIST [18].

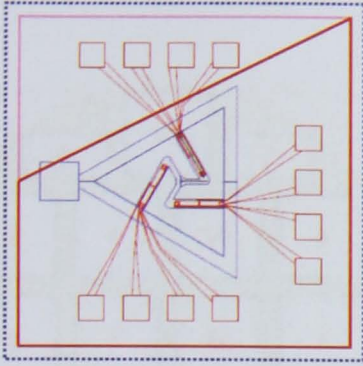


Figure 6.13: Schema highlighting the possibility for reuse of at least four, if not eight of the full chip solder contact pads on the partial chips. Note that the current ground pad position also remains viable. The pink square and red quadrilateral indicate the expected edge locations of the proposed full and partial chips respectively; the blue dotted square indicates the previous 13 mm chip edge. Adapted from mask drawings from Cranfield University.

above, as well as supporting the ground pad. The proposed cantilevers should require a fraction of the area of the triskelia, permitting the maintenance of a thick border of substrate about the active regions. Note, however, that the substrate-free active region of the chip should be placed as centrally as possible in the full-chip outline, certainly within the central 7 mm × 7 mm region of the larger 12 mm × 12 mm chip. Subject to these constraints, the exact layout was to be determined at mask production stage at Cranfield.

6.3.2.5 Chip distribution across the wafer

Due to the finite risk of fabrication failure for some chips on the wafer, duplicate chips had been specified when numbers allow. Given also that physical separation of the chips will decrease the likelihood of them being negatively affected by a given localised defect, the chips were to be distributed across the wafer. The mapping of the chip IDs (column '#') from table 6.1 onto the layout sketch in figure 6.9b is shown in figure 6.14.

6.3.3 Modelled stiffnesses

Table 6.2 summarises the results of applying the previously described finite element and analytical models to the parameter sets in table 6.1. The results show good correlation (< 15 %) between the vertical spring constants k_z obtained from the two methods, but significant discrepancies between the respective lateral stiffness estimates.

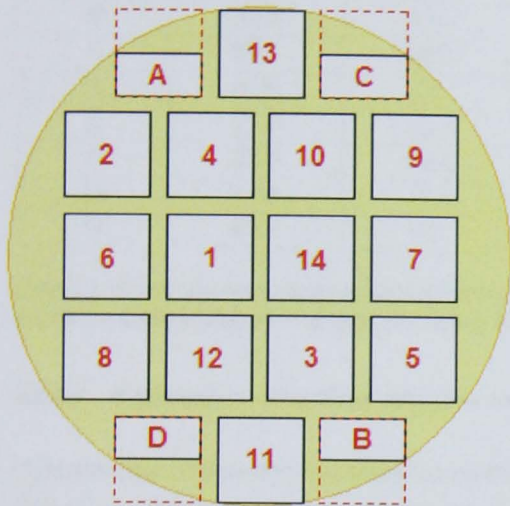


Figure 6.14: Placement of proposed chips on the wafer such that duplicate chips are spatially separated. The numbers refer to the chip ID (#) column in table 6.1. Letters refer to the partial chips; A, B are the simple cantilever; C, D are the two-legged cantilevers.

Chip ID	Dimensions relative to chip ID "A", as multiple or absolute change in μm				Modelled stiffnesses /Nperm			
					FEA		Analytical	
	ΔA	ΔL	ΔT_{beam}	ΔT_{arm}	k_z	k_x	k_z	k_x
A	$\times 1.0$	$\times 1.0$	0	0	22.3	63k	23.6	540k
B	$\times 1.0$	$\times 1.0$	+ 5 μm	0	52.6	84k	67.8	767k
C	$\times 1.0$	$\times 0.75$	0	0	50.3	84k	56.0	736k
D	$\times 1.0$	$\times 1.5$	0	0	6.75	63.3k	7.0	354k
E	$\times 1.0$	$\times 1.5$	+ 5 μm	0	17.0	68.9k	20.1	503k
F	$\times 0.6$	$\times 1.0$	0	0	22.9	182k	23.6	540k
G	$\times 0.6$	$\times 1.5$	0	0	7.09	146k	7.0	354k
H	$\times 1.5$	$\times 1.5$	0	0	6.88	22.7k	7.0	354k
I	$\times 1.0$	$\times 1.0$	0	- 13 μm	11.8	43.5k	N/A	N/A

Table 6.2: Summary of result of application of the previously described finite element and analytical models to the parameter sets in table 6.1. Note that the analytical model would produce meaningless values for model "I" identical to those for model "A", due to the identical beam geometry. As the arms are no longer rigid for this structure, the analytical model would clearly break down.

Artefact ID	$k_{z,FEA}/Nm^{-1}$	$k_{z,Anal}/Nm^{-1}$	$k_{z,Anal}/k_{z,FEA}$	% increase	s_A	s_L	s_T
A	22.3	23.6	1.058	5.8	1.0	1.0	1.0
B	52.6	67.3	1.279	27.9	1.0	1.0	1.26
C	50.3	56.0	1.113	11.3	1.0	0.75	1.0
D	6.75	7.0	1.037	3.7	1.0	1.5	1.0
E	17.0	20.1	1.182	18.2	1.0	1.5	1.26
F	22.9	23.6	1.031	3.1	0.6	1.0	1.0
G	7.09	7.0	0.987	-1.3	0.6	1.5	1.0
H	6.88	7.0	1.017	1.7	1.5	1.5	1.0

Table 6.3: Comparative analysis of vertical stiffnesses from the two models, and corresponding relative dimensional values as multiples of Artefact A's A , L and T values (s_A , s_L and s_T respectively).

6.3.3.1 Discussion of vertical stiffness estimates

The estimates obtained for the triskelion vertical stiffnesses show a good correlation between the two modelling approaches. Table 6.3 presents the percentage increase of the analytical results over the FE results. Adjacent are the dimensional scale factors relative to Artefact A's dimensions.

If, for the present purposes, it can be assumed that the FE models represent well the short-range behaviour of the model flexure described by the underlying CAD model, then for vertical stiffnesses the analytical model appears to be a satisfactory approximation and therefore the ideal candidate for automatic numerical parameter optimisation. The simple bending modes associated with vertical motion conform well to the assumptions made in simple beam theory, which underlies the analytical model.

The discrepancy between models is particularly large for those artefacts (B, E) with thicker beams, because the arm-to-beam thickness ratio reduces and the hub/arm infinite stiffness approximation breaks down. Similarly, decreasing the length of the beams drives up their relative stiffness, contributing to a lesser extent to the hub/arm rigidity assumption breakdown. The $1.3 Nm^{-1}$ negative increase observed for Artefact G may be a consequence of the finite FE mesh size, and therefore a good estimate of the internal uncertainty on the FE-derived results.

It must be noted that the CAD model behind the FE results is itself a simplification. In particular, the CAD model assumes beams and flexures constructed uniformly of nickel, rather than the proposed nickel-PZT bilayer. In order to estimate the significance of this, the vertical stiffness calculated for a flexure system consisting entirely of PZT can be considered as the worst case. Representative values for Young's modulus, Poisson's ratio and shear modulus are 65 GPa, 0.28 and 20 GPa respectively. Using PZT, Artefact A's vertical stiffness drops to $6.9 Nm^{-1}$, that is, a factor of 3.3 reduction. Thus typical (reduction) discrepancies

between modelled and physical artefact, considering material choice only, could be expected on this order.

Further, fabrication uncertainties introduce thickness discrepancies between modelled and actual beam thickness; for example, a half-micrometre fabrication error in beam thickness equates to around 3 Nm^{-1} stiffness error in the same direction.

A key benefit of typical FEA is the ability to quickly visualise the stress and displacement across a structure, and to identify where strain is concentrated. This latter ability can be used to evaluate the applicability of assumptions such as those made in the analytical model. Figures 6.15, 6.16, and 6.17 show such plots for artefacts A, I and F respectively. In Artefacts A and F, stress is concentrated in the beams, which show a mostly symmetric stress distribution consistent with the classic s-shaped double-ended cantilever. In Artefact I, however, stress is concentrated on the knee rather than the beam, and there is a strong stress peak in the inside corners. For high-load applications this peak would be designed out. Clearly the lack of a standard s-shape dictates that beam theory cannot be applied. Displacement itself is still concentrated in the beams, in line with the constant second derivative of vertical displacement, moving away from the centre of symmetry (the hub centre), predicted by basic beam theory.

6.3.3.2 Discussion of lateral stiffness estimates

The likely explanation for the lateral stiffness inconsistencies between the models reflects a common error produced by over-simplified mechanical models. The analytical model as devised does not allow for the parasitic hub rotation observed in the FE results. This rotation occurs about the axis in the plane perpendicular to the direction of the applied force, passing through the point of force application (see figure 6.18). The origin of the out of plane rotation is the vertical asymmetry of the device cross-section and an effective buckling at the knees; once this motion is initiated, further force amplifies the rotation. The effective fixing of these rotational degrees of freedom in the current analytical model derives from the basic assumption that the beams do not twist, and results in an effective stiffening of the structure, as reflected in the k_x values.

Each degree of freedom of the hub centre in the model has a stiffness associated with it - whether translational or rotational. The stiffnesses combine in series according to the general formula for springs $k_1, \dots, k_i, \dots, k_n$ in series

$$k_{\text{tot}} = \frac{\prod_i k_i}{\sum_{i \neq j} k_i k_j}.$$

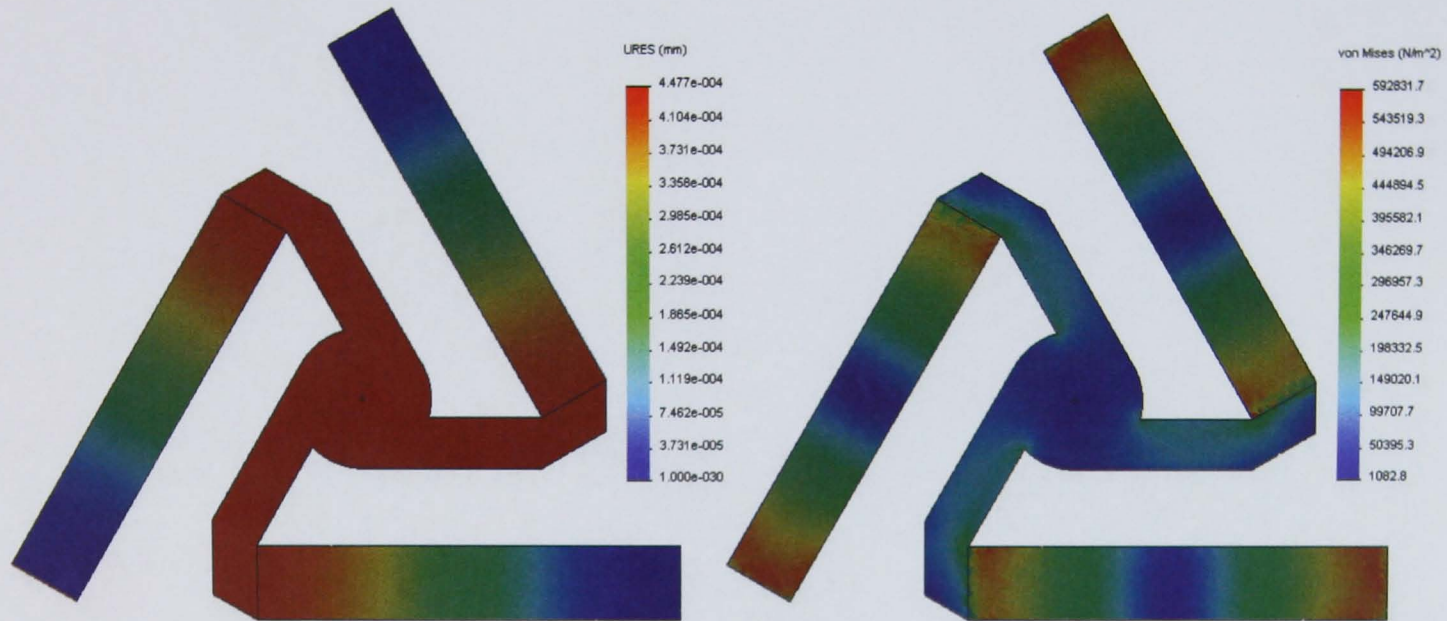


Figure 6.15: Total displacement (left) and strain (right) plots of artefact A under a ten micronewton vertical (z) load at the hub centre. View is in the $-z$ direction. Other views clarify that the total displacement is effectively entirely vertical in the hub centre.

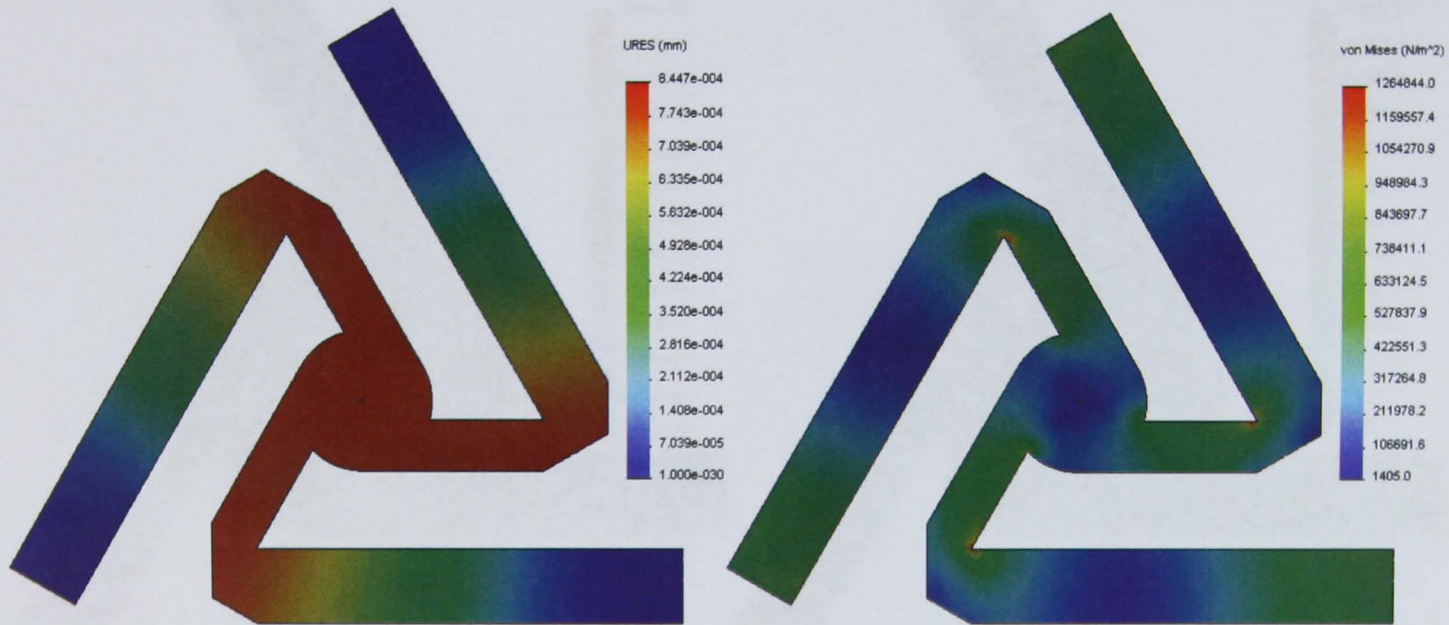


Figure 6.16: Total displacement (left) and strain (right) plots of artefact I under a ten micronewton vertical (z) load at the hub centre. View is in the $-z$ direction.

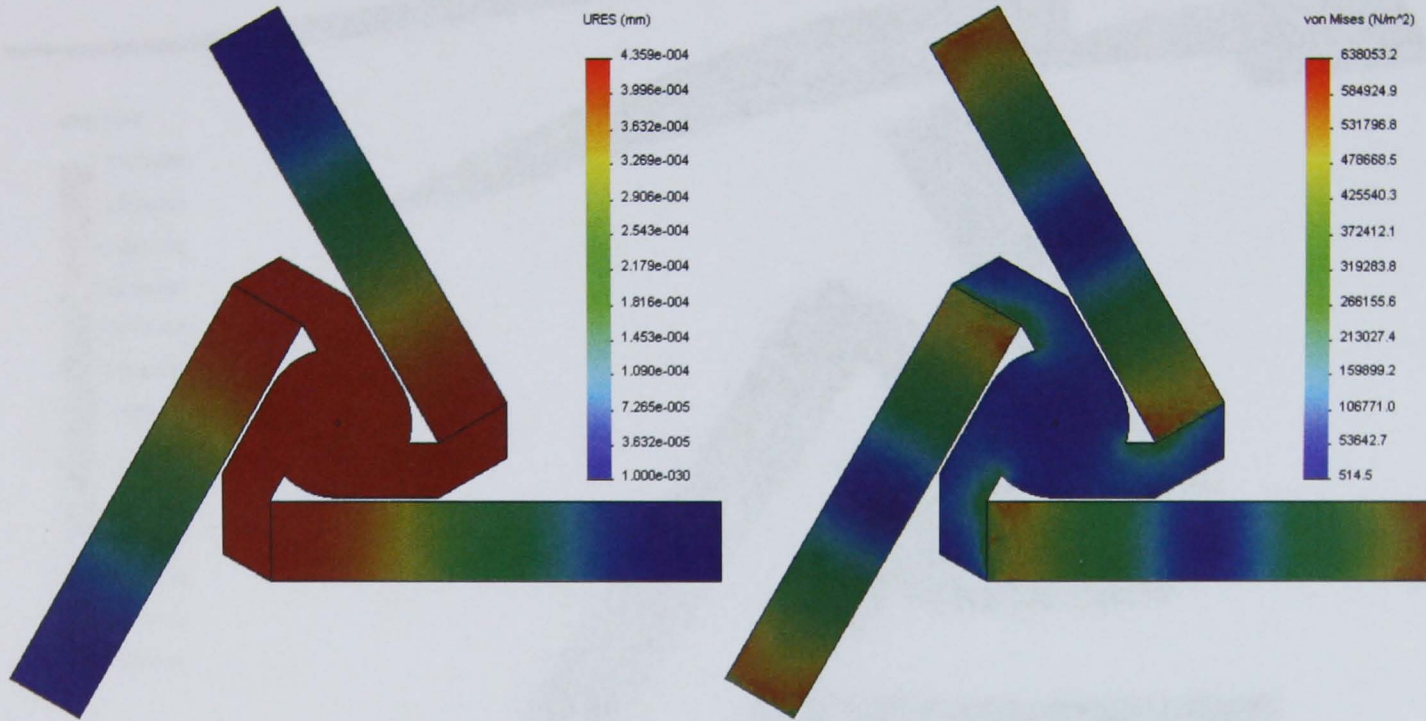


Figure 6.17: Total displacement (left) and strain (right) plots of artefact F under a ten micronewton vertical (z) load at the hub centre. View is in the $-z$ direction.

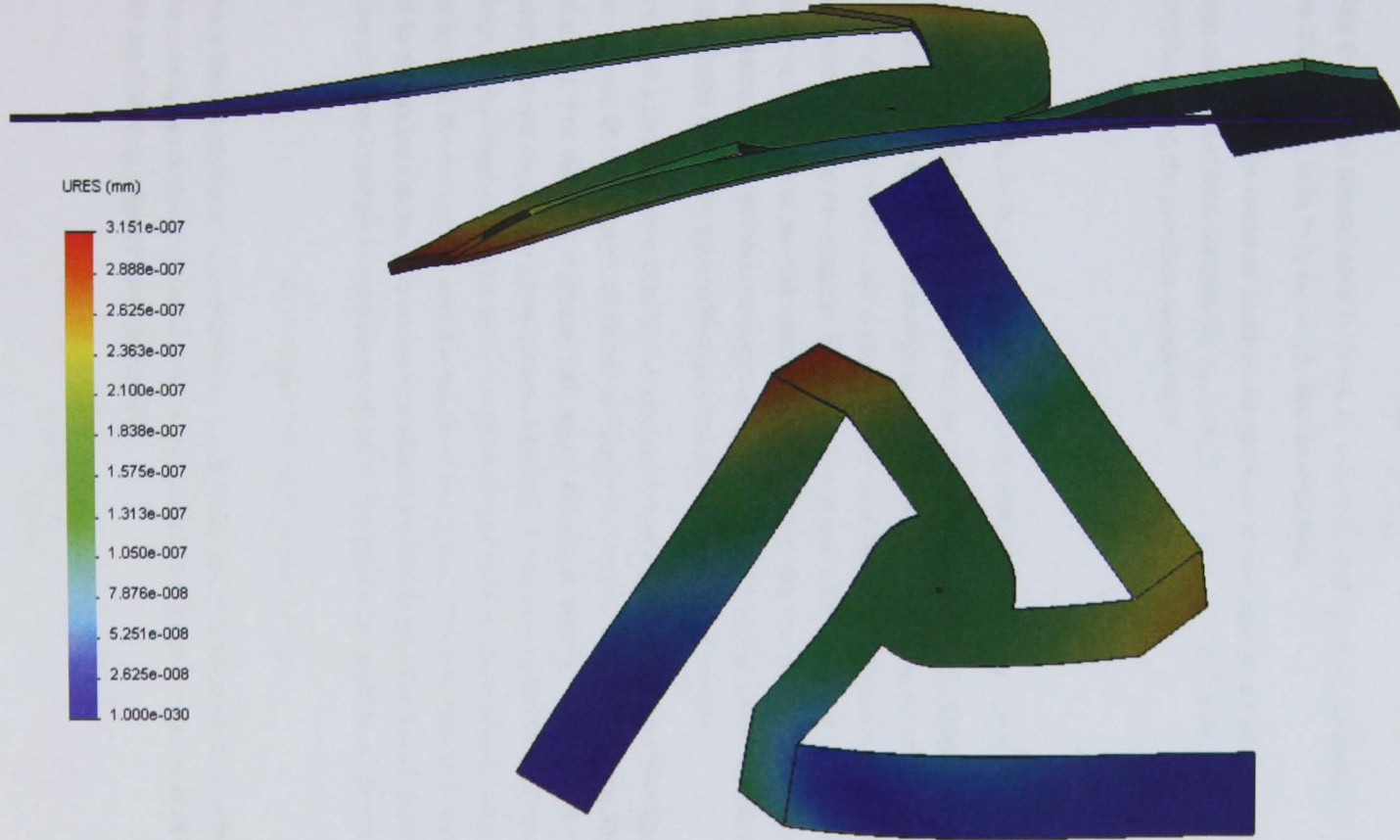


Figure 6.18: Total deflection of chip A under lateral (+x) force: (top) view along +x-axis; (bottom) view along -z-axis with +x direction towards this caption. Deflection at the hub centre is entirely along the +x-axis. The deflections in each axis are to scale but greatly magnified. Lateral deflections dominate.

For two springs k_1 and k_2 , this simplifies to

$$k_{\text{tot}} = \frac{k_1 k_2}{k_1 + k_2}.$$

Note that for the special case $k_1 \gg k_2$, $k_1 + k_2 \approx k_1$ and $k_{\text{tot}} \approx k_2$, as expected. Similarly, in the case that $k_1 = k_2 = k$, $k_{\text{tot}} = \frac{1}{2}k$, also as expected.

Viewed in terms of compliance (defined as the inverse of stiffness) the picture is even clearer. Let total compliance $c_{\text{tot}} = k_{\text{tot}}^{-1}$, $c_1 = k_1^{-1}$, $c_2 = k_2^{-1}$; then the total compliance simplifies using the previous equations to

$$c_{\text{tot}} = c_1 + c_2.$$

When $k_1 \gg k_2$, $c_1 \ll c_2$ and $c_{\text{tot}} \approx c_2$; also when $k_1 = k_2 = k = \frac{1}{c}$, $c_{\text{tot}} = 2c$.

The FEA model suggests that the triskelion moves in two degrees of freedom under an x -axis lateral force: x translation and y rotation. The analytical result shows only x translation of the bulk model, and a much higher total lateral stiffness (lower total compliance) than shown in the FE analysis. Based on the above relationships it is suggested that the total x compliance of the hub centre is dominated by the rotational compliance of the twisting beams. The x -stiffnesses reported by the analytical model would therefore be largely suppressed within the total stiffnesses that the FE analysis generates..

The device geometry is critical to its behaviour under applied load. Note from figure 6.18 that the majority of the artefact distortion occurs in the beams, though the arms are somewhat deformed. For different artefacts with equal-dimension beams, the same moment at the beam end will create the same beam distortion. A moment applied about the beam end, which would result in a beam twist, would be proportional to the relevant component of the net force at the hub centre and the length of the arm A . The arm acts as a lever to reduce the force required at the hub centre to create the same beam twist deformation, translating to an effective increase in compliance about y . The total x compliance c_x can be written as

$$c_x = c_{x, \text{pure}} + c_{x, \text{rot}} = c_{x, \text{pure}} + k_{x, \text{rot}}^{-1}$$

where the translational x compliance $c_{x, \text{pure}}$ is small and, it is suggested, may be neglected. The x compliance due to beam distortion, $c_{x, \text{rot}}$, relates to the beam torsional stiffness λ_{beam} with the following approximate relationship:

$$c_{x, \text{rot}} \approx \frac{\alpha A}{\lambda_{\text{beam}}}$$

where α is some constant. λ_{beam} has the form

$$\lambda_{\text{beam}} = \frac{KG}{L}$$

where G is the beam material modulus of rigidity, and K the polar 'moment of inertia'. For a general beam with rectangular cross section $a \times b$, $a \geq b$, K is given approximately by [181]

$$K \approx ab^3 \left[\frac{16}{3} - 3.36 \frac{b}{a} \left(1 - \frac{b^4}{12a^4} \right) \right] \approx \frac{16}{3} ab^3 .$$

The latter approximation applies when $a \gg b$, as here. Substituting the current beam dimension variables and collating the constants into the representative constant β , λ_{beam} is given by

$$\lambda_{\text{beam}} = \beta \frac{WT^3}{L}$$

and $c_{x, \text{rot}}$ is given by

$$c_{x, \text{rot}} \approx \frac{\alpha}{\beta W} \cdot \frac{AL}{T^3} .$$

The compliance due to beam distortion is of course dependent on the beam dimensions, which vary across the artefact set. Note that, for the artefact designs considered in this document, the beam width is constant, and hence has been grouped as such.

Numerical analysis in pursuit of this line of enquiry is summarised in table 6.4. The lateral stiffness values from the FEA method are reasonably spread, reflecting the range of dimensional parameters in play. The compliance dependencies derived above suggest that the ratio of the FEA lateral stiffness results $k_{x, \text{FEA}}$ to the geometry factor T^3/AL should be constant for all artefacts. The argument should remain valid if the absolute geometry factor T^3/AL is replaced by a relative geometry factor $s_T^3/s_A s_L$ where s_T , s_A and s_L are multiples of artefact A's dimensions for a given artefact. These unitless multiples derive directly from table 6.2 and are of the order of unity. The descaled stiffnesses, that is the ratio $k_{x, \text{FEA}} / [s_T^3/s_A s_L]$ should be constant and of the same order as the raw FEA lateral stiffnesses.

The calculated descaled stiffnesses, given in table 6.4 and in figure 6.19, in fact show no clear reduction in spread or an obvious common constant value. Clearly the simplistic analysis above fails to account for all the components of the relationship between the hub lateral stiffness and the twisting of the outer beams.

Despite the failure of the above analysis, it is interesting to note the apparent linear relationship between the descaled FEA stiffnesses and the ratio of the FEA and analytical stiffnesses shown in figure 6.19. Cancelling the FEA stiffnesses from those quantities, figure 6.20 shows and highlights the underlying apparent linear relationship between the relative

Table 6.4: Comparative analysis of lateral stiffness derived from FE and analytical modelling techniques.

Artefact ID	$k_{x,FEA}/\text{kNm}^{-1}$	$k_{x,Anal.}/\text{kNm}^{-1}$	$k_{x,FEA}/k_{x,Anal.}$	s_A	s_L	s_T	s_T^3/s_{ASL}	$[k_{x,FEA}/(s_T^3/s_{ASL})]/\text{kNm}^{-1}$
A	63.0	540	0.117	1.0	1.0	1.0	1.00	63.0
B	84.0	767	0.110	1.0	1.0	1.26	1.60	52.6
C	84.0	736	0.114	1.0	0.75	1.0	1.33	63.0
D	63.3	354	0.179	1.0	1.5	1.0	0.67	95.0
E	68.9	503	0.137	1.0	1.5	1.26	1.06	64.8
F	182	540	0.337	0.6	1.0	1.0	1.67	109
G	146	354	0.412	0.6	1.5	1.0	1.11	131
H	22.7	354	0.064	1.5	1.5	1.0	0.44	51.1

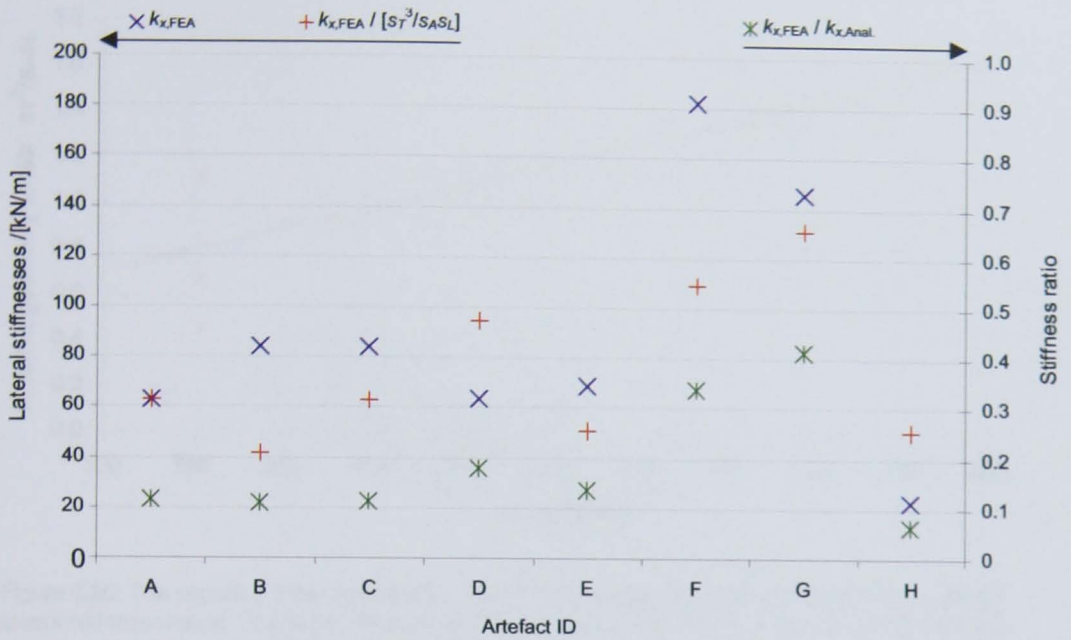


Figure 6.19: Comparative analysis of results from FEA and Analytical models of the eight comparable artefact types. The stiffness ratio $k_{x,FEA}/k_{x,Anal.}$ maps to the right-hand secondary axis; the other raw and descaled FE stiffness plots map to the left-hand axis.

geometry factor s_T^3/s_{ASL} and the analytical stiffness values $k_{x, Anal.}$, which as yet have not been linked by the analysis.

This apparent correspondence would require further study beyond the scope of this document, but any explanation would likely shore up the failed analysis earlier in this section.

6.3.3.3 Partial-chip artefacts: stiffness estimates

The partial-chip artefacts take the form of simple cantilevers (A, B) and pairs of cantilevers with a further pseudo-rigid extension. An analytical derivation of their stiffnesses would be a relatively trivial exercise in Euler-Bernoulli beam theory. However, as their dimensions are determined purely by the adjacent full artefacts to allow comparison as discussed above, FEA has been used exclusively in the interest of efficiency.

Simple cantilever: partial chips A, B A master cantilever was created in Solidworks 2009 to model the cantilevers in figure 6.11. As in the case of the full triskelia, the single nickel layer simplification was used. Each cantilever in turn was created, and subjected to a $5 \mu\text{N}$ vertical test force at its platen. Figure 6.21 shown one of these cantilevers with the resultant

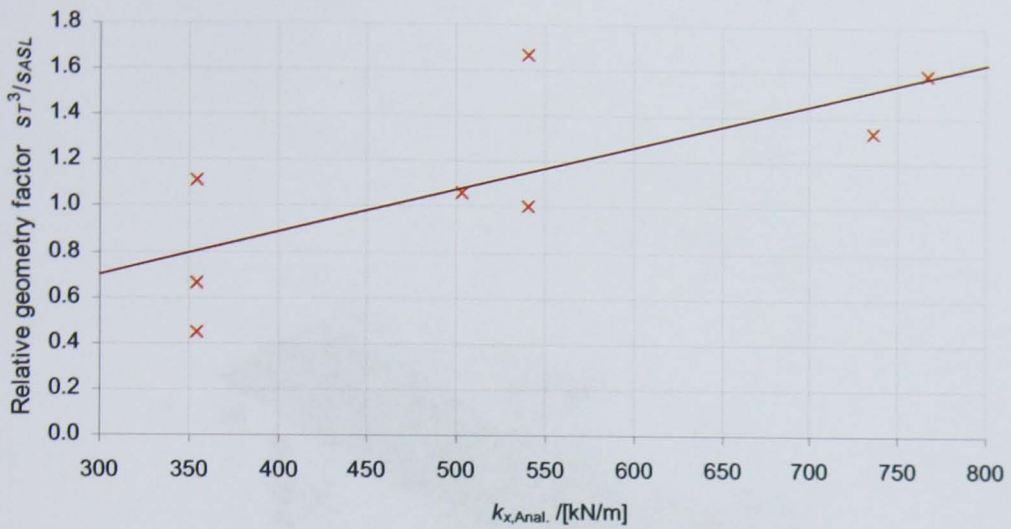


Figure 6.20: The apparent linear relationship between the relative geometry factor and the analytical lateral stiffness results. The trend line is a linear least-squares fit to the data. The horizontally groups points share common L and T values but different A values.

displacement and stress distributions. Note that cantilevers C1 and C2 are intended to have the same stiffness, and under the simplifications made for the FEA, are identical. Cantilever C3 is 50 % longer than its neighbours, or more precisely its platen is 50 % further from the cantilever root; consequently the modelled stiffness for C3 should be scaled by a factor of $(\frac{2}{3})^3 \approx 3.38$.

The modelled vertical stiffness of 'identical' cantilevers C1, C2 was 16.7 Nm^{-1} ; the stiffness estimate for C3 was 4.95 Nm^{-1} . The ratio of these stiffnesses corresponds to the above scale factor.

In addition, beam theory predicts that cantilevers C1/C2 should have a vertical stiffness 0.67 of that of artefact A; the actual ratio is 0.71. Finally, cantilever C3 should have 0.67 times the vertical stiffness of artefact D; the actual ratio is 0.74. These are reasonable given the approximations made in beam theory not reflected in the FEA, and the limited interpretation of point stiffnesses in FEA.

Modified cantilever: partial artefacts C, D Solidworks was also used to model the modified cantilevers introduced in figure 6.12; again the nickel-only simplification was employed. Cantilever C4 is shown subjected to the $5 \mu\text{N}$ test force in figure 6.22. Beam theory predicts a linear relationship between the leg width and the total cantilever stiffness, provided the leg compliance dominates that of the whole cantilever. The modelled vertical stiffnesses of the

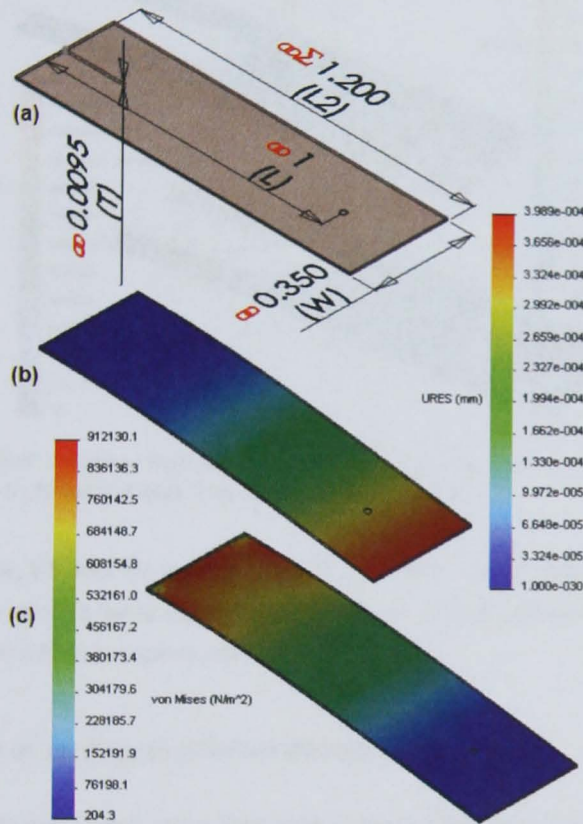


Figure 6.21: A 'simple' cantilever from partial chips A, B (a) and its displacement (b) and stress (c) distributions under a $5 \mu\text{N}$ vertical load. The cantilever shown is C1.

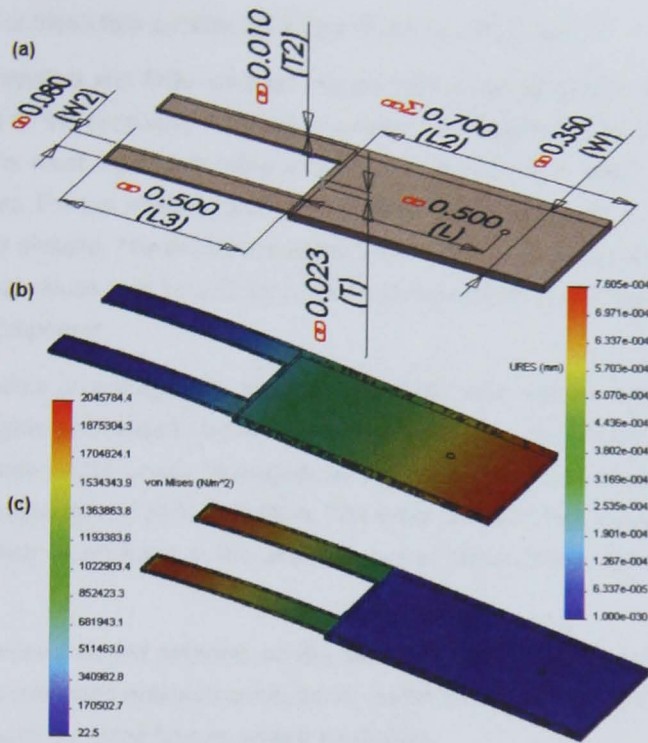


Figure 6.22: A 'modified' cantilever from partial chips C, D (a) and its displacement (b) and stress (c) distributions under a 5 μN vertical load. The cantilever shown is C4.

three cantilevers C4, C5 and C6 were 7.8 N m^{-1} , 11.9 N m^{-1} and 17.9 N m^{-1} respectively. These appear to support a linear dependency model of vertical stiffness on base leg width (80 μm , 120 μm and 175 μm respectively).

6.3.4 Summary of prototype artefact development

The objective of the work described in this section was to design a set of test artefacts to bridge the gap between current NPL knowledge and experience, particularly with micro-probes, and the knowledge required for successful future prototype low force transfer artefacts.

A suite of test artefacts have been designed and made that employ the fabrication processes from the recent microprobe prototypes manufactured by Cranfield University. The proposed test artefacts cover a range of geometrical parameter values to facilitate the optimisation of those parameters for the first working prototype artefacts.

The set of test artefacts contain both full triskelia, to study the relationships between stiffness and geometry, and simple cantilevers, to assist with sensor design optimisation,

though the use of these falls outside the scope of the reported work.

Both analytical and finite element models have been developed to estimate the likely stiffnesses of the proposed triskelion artefacts. The models make several simplifying assumptions, the most significant being a nickel-only construction; these have associated systematic errors. For the triskelia, both models show good agreement for vertical stiffness across the set of triskelia. The estimated range of stiffnesses is around 7 Nm^{-1} to 70 Nm^{-1} , though the actual values may be a factor of two to three smaller due to the neglected lower-stiffness PZT component.

The models do not agree in terms of lateral stiffness, with the analytical model reporting much higher estimates than the finite element analysis. The lateral estimates are, for both models, three to five orders of magnitude larger than the vertical stiffness estimates, suggesting effective uniaxial (1DOF) motion. The exact cause of the discrepancy is unclear; however, it is likely to originate in the different mathematical approximations employed in each model.

The cantilever-based artefacts on the partial chips were also modelled using FEA; vertical stiffness estimates obtained correspond, via the expected ratio, to those from the full triskelia with equivalent sized beams, where applicable.

The partial chip artefacts stiffnesses were in the range 5 Nm^{-1} to 18 Nm^{-1} and will also be somewhat smaller in practice.

These devices were not intended to work in practice as low force transfer artefacts; in particular they were not expected to have the desired force resolution to be more useful than currently available alternative artefacts. Instead, the devices were intended to operate in a similar way on a force scale more accessible to characterising instruments at NPL and the University of Warwick. An example of such an instrument is the Taylor-Hobson Talysurf-derived bespoke instrumented indenter system at Warwick [182], a candidate characterisation tool. The modelled vertical stiffnesses (approximately 10 Nm^{-1}) of the various proposed artefacts, as well as their dimensions and high force capacity, are well suited to this instrument.

The artefacts were specifically designed to assist in the optimisation of future artefacts' sensor performance and supporting electronics were to be developed as a parallel exercise, as described in the following chapter.

The output from the design process presented in this section informed the fabrication of the artefacts at Cranfield, and indeed Shaw *et al.* at Cranfield [183] were consulted throughout an iterative design process flattened into the discussion above.

6.4 Prototype artefact evaluation

6.4.1 Inspection and measurement

6.4.1.1 Overview

The chosen micro-fabrication route for the prototype artefacts was selected based on the prior experience of NPL and the fabrication partner, Cranfield University, in the context of microprobe development. The motivation for reusing the same fabrication technique with modified geometrical parameters was purely one of risk minimisation.

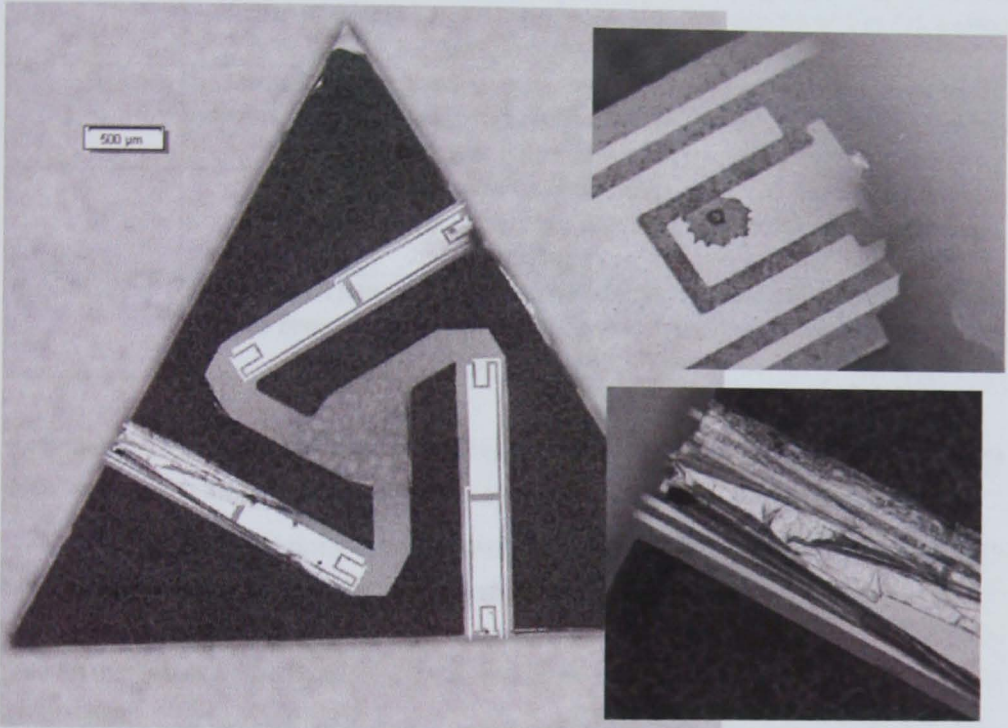
However, Cranfield's technique is nevertheless experimental and, as with all micro-fabrication techniques, there were discrepancies between design and end product. These fall into two main categories: localised defects and thickness variation. In addition, a failure of a key piece of fabrication equipment at Cranfield severely delayed final delivery of the prototype artefacts and subsequent work.

6.4.1.2 Localised defects

Defects to the produced devices included over-etched regions and holes, incompletely removed silicon substrate and mottled nickel plating. Examples for artefact A, representative of the set, are shown in figure 6.23. Clearly the nature and placement of such defects affect the mechanical and electrical behaviour of the devices. Descriptions of the artefacts to be considered in this chapter are given in table 6.5.

6.4.1.3 Dimensional measurement

The fabrication partner advised of variation in fabricated feature thickness compared to the dimensions specified. The device layer thicknesses are dependent on deposition and spin-off rates which are known to be highly environmentally sensitive and typically non-linear. Cranfield undertook measurements of the final thicknesses, for reference; these are presented in table 6.6 along with crude estimates of the impact on device spring constant. Such estimates should be treated with caution because of the bulk stiffness difference between layers. Further, the full extent of the uncertainties associated with the measured thicknesses is not clear. In exploratory experiments by Claverley *et al.* at NPL using a Zeiss F25 micro-CMM (not yet reported), it was not possible to define a suitable reference plane for the measurement; the artefacts proved too stiff for the CMM to push repeatably into an underlying hard surface. A fortuitous accident during later work deformed an artefact out of the plane



Underside, with detail



Top side

Figure 6.23: Fabrication defects on artefact A, obtained using a digital optical microscope.

Table 6.5: Summary of defects to artefacts considered in chapter 6

Artefact ID	Description of defects.
A	Incompletely removed silicon substrate on one flexure, suggesting localised stiffening. About 10 % missing from width of root of another flexure; reduced width at strain concentration zone suggests localised reduction in stiffness. Loss of sensor connectivity. Score-markings across one or more arms, compromising rigidity assumption.
B	Good condition, localised silicon flakes and small pits away from zones of maximum strain. Small pit in strain zone of one flexure. Localised flexure edge damage in another strain zone. Surface scoring on one flexure.
C	Good condition but with three significant pits; one each in two flexures' maximum strain zones; one where an arm meets the hub possibly compromising the rigidity assumption.
E	Significant pitting on one flexure, away from strain zone. Localised pitting in strain zone of another, affecting sensor connectivity. Residual silicon on final flexure, reinforcing strain zone. Poorly laid-down nickel layers.

such that the layers were visible from above; however, attempts to estimate the fractional thickness of each layer was confounded by poor contrast and lateral layer offsets.

The lateral dimensions of the delivered chips were not traceably measured, but a brief inspection using a digital optical microscope and its online measurement tools suggested that the fabricated feature lengths had ratios much more consistent with those specified than for the flexure thicknesses. In light of the above results no further measurements were undertaken.

6.4.2 Spring constant determination

6.4.2.1 Motivation

A knowledge of the vertical spring constant of the prototype artefacts would not only facilitate their immediate practical application but also permit the evaluation of the mechanical models developed previously. The experimental confirmation of modelled spring constants across a representative region of geometrical parameter space would add confidence to future simulations for alternative artefact sizes. This experimentation was undertaken by a student colleague under the direction of the author. Initial results were published in [35].

Table 6.6: Difference in thickness between specified and actually fabricated devices.

Artefact ID	Arm thickness/ μm			of which PZT thickness/ μm		and flexure (nickel plus PZT) thickness/ μm		
	Measured	Fraction of nominal	Spring constant modifier	Measured	Fraction of nominal	Measured	Specified	Fraction of specified
nominal	22.5	-	-	4.5	-	-	-	-
A	21.7	0.96	0.90	4.7	1.04	6.2	9.5	0.65
B	21.5	0.96	0.87	4.6	1.02	11.6	13.5	0.86
C	21.4	0.95	0.86	5.2	1.16	5.7	9.5	0.60
D	22.7	1.01	1.03	5.3	1.18	6.4	9.5	0.67
E	21.5	0.96	0.87	4.7	1.04	10.4	13.5	0.77
F	22.1	0.98	0.95	5.4	1.20	6.2	9.5	0.65
G	21.7	0.96	0.90	5.1	1.13	6	9.5	0.63
H	19.9	0.88	0.69	4.7	1.04	5.6	9.5	0.59

6.4.2.2 Approach to experimentation

In principle, the spring constants of the artefacts would be directly measured using the LFB over its working range. A previously-calibrated secondary stage would lower the artefact holder onto the LFB such that the artefact deflects; from the variation in LFB force readout with artefact holder position, the artefact spring constant would be calibrated.

In practice, the prototype artefacts were too stiff to allow the correct operation of the LFB, and an intermediate reference cantilever in the range 1 Nm^{-1} to 10 Nm^{-1} was used to complete the measurements. It was previously noted (see section 3.10) that the LFB struggles to calibrate devices of stiffness much above 10 Nm^{-1} . Test experiments with artefact A (nominal spring constant about 20 Nm^{-1}) confirmed this incompatibility.

An alternative, two-step, measurement process was devised, and is summarised in figure 6.24. In the first step, the spring constant k_{CANT} of the reference cantilever is determined from the variation in LFB force readout with cantilever holder position, or rather, the external stage displacement. In the second step, the reference cantilever is used to deflect the (unpowered) LFB flexure and transfer artefact in parallel. From the displacement of the external stage, that of the LFB mechanism, the spring constant of the reference cantilever and that of the LFB mechanism, the spring constant of the artefact can be calibrated. This can be derived mathematically as follows, using the quantities as defined in figure 6.24. Neglecting measurement frame compliance, the displacement of the secondary stage is distributed between the reference cantilever and LFB-artefact system:

$$\Delta z_{\text{EXT}} = \Delta z_{\text{CANT}} + \Delta z_{\text{LFB}} . \quad (6.1)$$

And at force equilibrium the following holds, assuming equal deflection of LFB and artefact:

$$k_{\text{CANT}} \Delta z_{\text{CANT}} = (k_{\text{LFB}} + k_{\text{ART}}) \Delta z_{\text{LFB}} \quad (6.2)$$

Inserting 6.1 in 6.2 and rearranging with $\frac{\Delta z_{\text{EXT}}}{\Delta z_{\text{LFB}}} = \left(\frac{dz_{\text{EXT}}}{dz_{\text{LFB}}} \right)^{-1}$ yields the following expression for the artefact spring constant k_{ART} :

$$k_{\text{ART}} = k_{\text{CANT}} \left[\left(\frac{dz_{\text{EXT}}}{dz_{\text{LFB}}} \right)^{-1} - 1 \right] - k_{\text{LFB}} \quad (6.3)$$

The uncertainty derivation associated with the above will be discussed later, but it is noted that for stiffer artefacts the poorly defined LFB stiffness has a smaller contribution to the relative uncertainty in artefact spring constant determination.

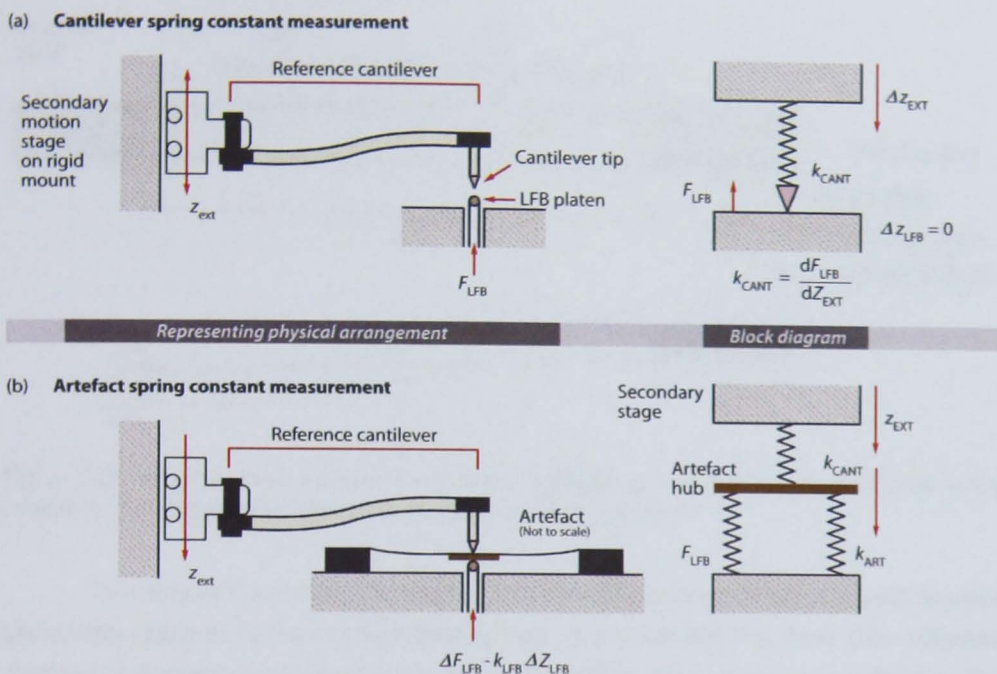


Figure 6.24: The workaround two-step prototype artefact spring constant measurement process.

6.4.2.3 Reference cantilever design

It was already noted that the required reference cantilever would have a spring constant in the range 1 Nm^{-1} to 10 Nm^{-1} . In addition, non-specialist manufacture and usage of the cantilever demanded macroscopic dimensions – that is, dimensions on the order ten millimetres. Finally, in order to access the artefact within its holder, a cantilever tip of several millimetres was essential. To reconcile these requirements and to minimise arcuate cantilever motion, and hence lateral tip motion, a parallel flexure design was implemented, as shown in figure 6.25.

Noting that for a parallel-beam cantilever the beam-theory spring constant equation for a simple cantilever modifies to

$$k = \frac{Ewt^3}{4(l/2)^3} = \frac{2Ewt^3}{l^3},$$

it was found that a practically-dimensioned cantilever could be constructed from $30 \mu\text{m}$ thick, 12.26 mm wide stainless steel slip gauges. Based on a Young's modulus for steel of 207 GPa , a 33 mm long cantilever would have a satisfactory nominal vertical spring constant of 3.8 Nm^{-1} .

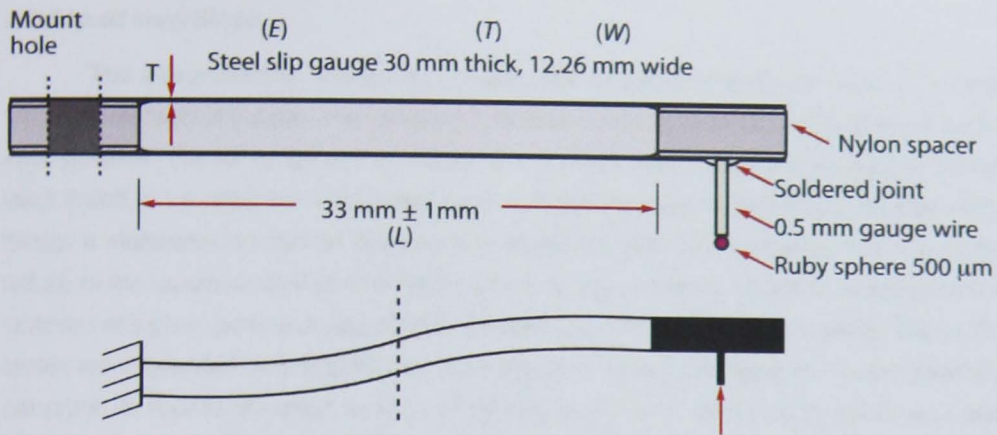


Figure 6.25: Parallel-flexure reference cantilever employed to measure prototype artefact spring constants: (top) schematic diagram; (bottom) actual implementation.

To minimise the unladen deflection of the double-cantilever, it was essential to use a low-density material for the spacers defining each end of the bending zone. One millimetre thick Nylon washers were machined to size and glued in place using epoxy adhesive. The length of the free-flexing region was then confirmed. The Nylon spacers, whilst light, were not particularly stiff, and in combination with the uneven boundaries of the adhesive were expected to contribute some non-linearities and hysteresis to the mechanical behaviour of the reference cantilever.

The cantilever tip consisted of a 4 mm length of 0.8 mm single-core steel electronics wire soldered to the underside of the cantilever. A 0.5 mm ruby sphere was glued to the tip of the wire to improve the definition of contact with the artefact and LFB platen and to reduce progressive tip shape change. Compliance in the tip stem was accounted for in the cantilever stiffness measurement, along with any compliance in the cantilever mount, an advantage of in-situ reference cantilever calibration.

6.4.2.4 Reference cantilever spring constant measurement

Generation and measurement of reference cantilever motion was achieved using the PI Nanocube nanopositioner system introduced previously (see section 3.10), where scale linearity at the 0.2 % level was determined. Measurement of force was provided by the LFB operating in indirect voltage measurement mode, thus contributing a further 2.5 % relative uncertainty. Basic alignment between LFB platen and cantilever tip was achieved by using the lateral axes of the nanopositioner to move one tip sphere over the other, finding the centre based on the LFB force readout. At 0.14 % for 3° misalignment, the cosine error was

considered insignificant.

The nanopositioner closed-loop target was cycled repeatedly between 0 μm and 10 μm in intervals of 0.2 μm . The resultant LFB force reading, once settled, was recorded for each position. The full range of the LFB force scale was used. Sixty-nine contiguous cycles were found to be valid; the associated force and displacement is presented in figure 6.26. Firstly, a significant amount of hysteresis is observed, perhaps consistent with the crude nature of the cantilever design and friction effects at the cantilever tip. Much of the apparent variation at a given point was assumed to be due to drift in the LFB force reading. The useful cycles were recorded over forty hours, with thirty-four minutes per cycle and twenty seconds per point. To reduce the effect of drift, an average force was calculated for each cycle and deducted from the member data of that cycle, in the manner of a zero-order drift correction. The result is plotted in figure 6.27 and shows residual variation due to short-term drift and repeatability in the mechanical motion of the reference cantilever.

From figure 6.27 two linear regions were identified for approach and retract operation respectively. A linear least-squares fit was calculated for these regions for each drift-corrected cycle, returning the gradient and the associated fitting uncertainty. Figure 6.28 summarises these results. The mean and standard deviation of these values were 4.48 N m^{-1} and 0.11 N m^{-1} respectively with no significant difference between approach and retract values. Since most of this variation is assumed to be due to the behaviour of the reference cantilever itself, rather than measurements of it, the standard deviation is taken as an estimate of repeatability. The uncertainty due to repeatability is reducible with repeated use of the cantilever; after ten repeats the total uncertainty is dominated by the known scaling error in the LFB (about 2.6 %) which persists. Given at least ten repeated uses of the cantilever, its spring constant was therefore estimated as $k_{\text{CANT}} = 4.48 \text{ N m}^{-1} \pm 0.11 \text{ N m}^{-1}$.

6.4.2.5 Prototype artefact spring constant measurement

The measurement of the spring constant of each artefact proceeded in the following manner. The artefact was inserted between reference cantilever and LFB platen to achieve the arrangement in figure 6.24. The nanopositioner target displacement (that is, k_{EXT}) was stepped incrementally over a range of 30 μm , in steps of up to 500 nm resulting in a total LFB-artefact displacement on the order of 5 μm . At least ten complete bi-directional cycles were completed for each artefact. In each case, hysteresis was observed consistent with that recorded above (see for example figure 6.29). The hysteresis cycle followed an anti-clockwise path with the lower portion describing the approach and the upper portion the retract motion.

The aim was to determine the ratio $\frac{d_{\text{LFB}}}{d_{\text{EXT}}}$ from linear regions of the plot of LFB (and

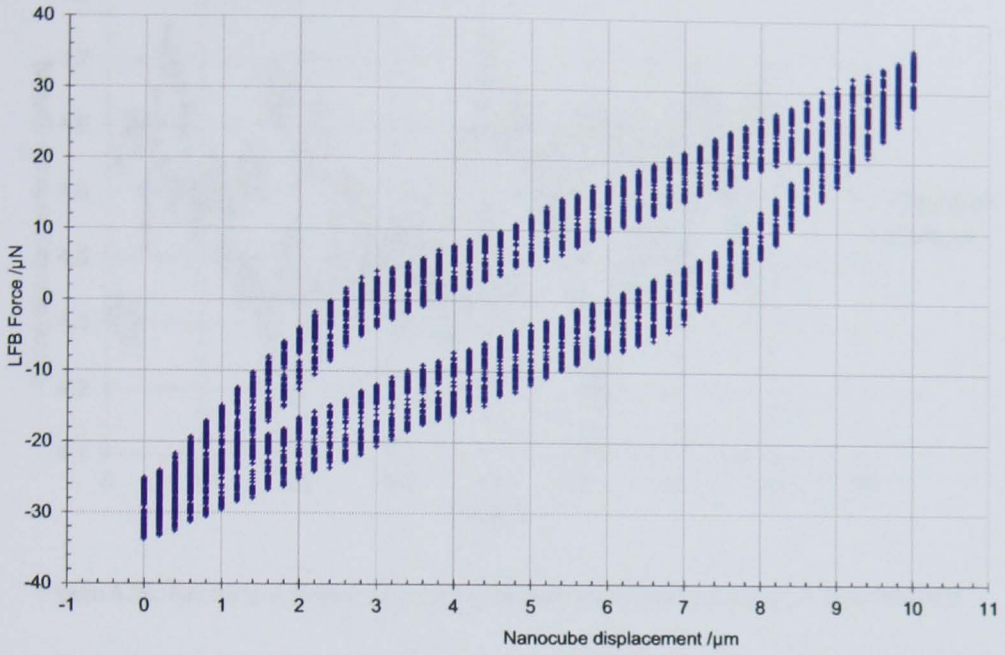


Figure 6.26: Raw data from the measurement of the reference cantilever spring constant.

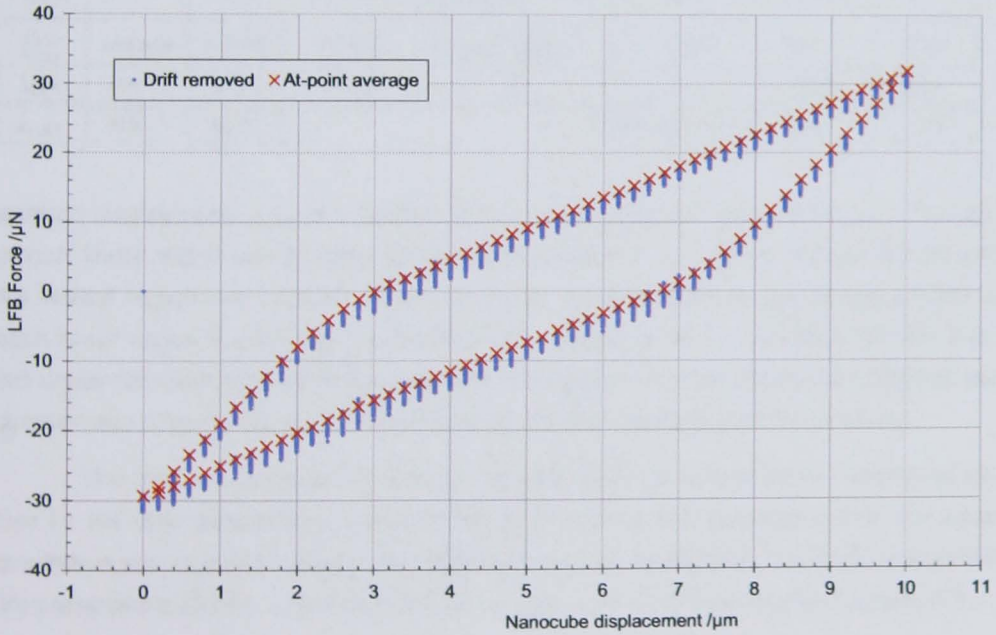


Figure 6.27: Processed data from the measurement of the reference cantilever spring constant.

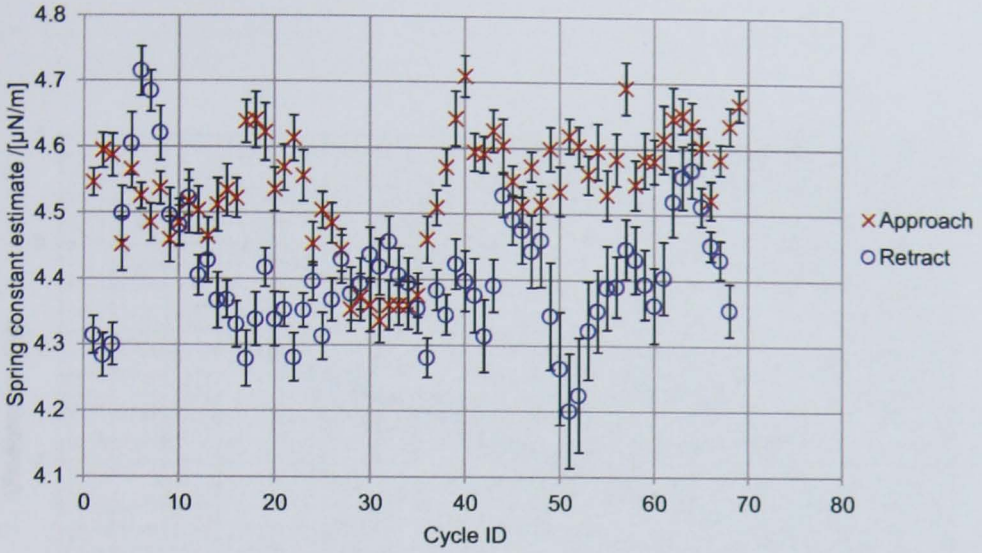


Figure 6.28: Per-cycle approach and retract stiffness estimates from least-squares linear fits.

Table 6.7: Exemplary calculation of uncertainty in measurement of artefact spring constant, for artefact B.

Term	Unit	Value	Uncertainty	Sensitivity coeff.	Coeff. value	Coeff. unit	Product
k_{CANT}	Nm^{-1}	4.48	0.11	$\left(\frac{dz_{\text{LFB}}}{dz_{\text{EXT}}}\right)^{-1} - 1$	10.8	unitless	1.19
$\frac{dz_{\text{LFB}}}{dz_{\text{EXT}}}$	unitless	0.0848	0.0006	$k_{\text{CANT}} \left(\frac{dz_{\text{LFB}}}{dz_{\text{EXT}}}\right)^{-2}$	623	Nm^{-1}	0.35
k_{LFB}	Nm^{-1}	1.615	0.009	1	1	unitless	0.01
k_{ART}	Nm^{-1}	46.72	<i>Quadrature sum</i>			Nm^{-1}	1.24

artefact) displacement z_{LFB} as a function of the nanopositioner target position z_{EXT} . The 'approach' linear region was typically defined as between the z_{EXT} values of 6 μm and 30 μm ; the 'retract' region was between 24 μm and 0 μm . A linear least-squared fit was applied to each linear region to estimate the required ratio. Based on the assumption that the artefact under test demonstrates better mechanical behaviour than the reference cantilever, the decision was taken to calculate a mean and associated standard error for all values.

The ratio was propagated through equation (6.3) using previously determined values for the other parameters. The associated uncertainty was calculated using the usual quadrature sum approach. Sensitivity coefficients and an exemplary uncertainty calculation are presented in table 6.7. The final results for each artefact are summarised in table 6.8.

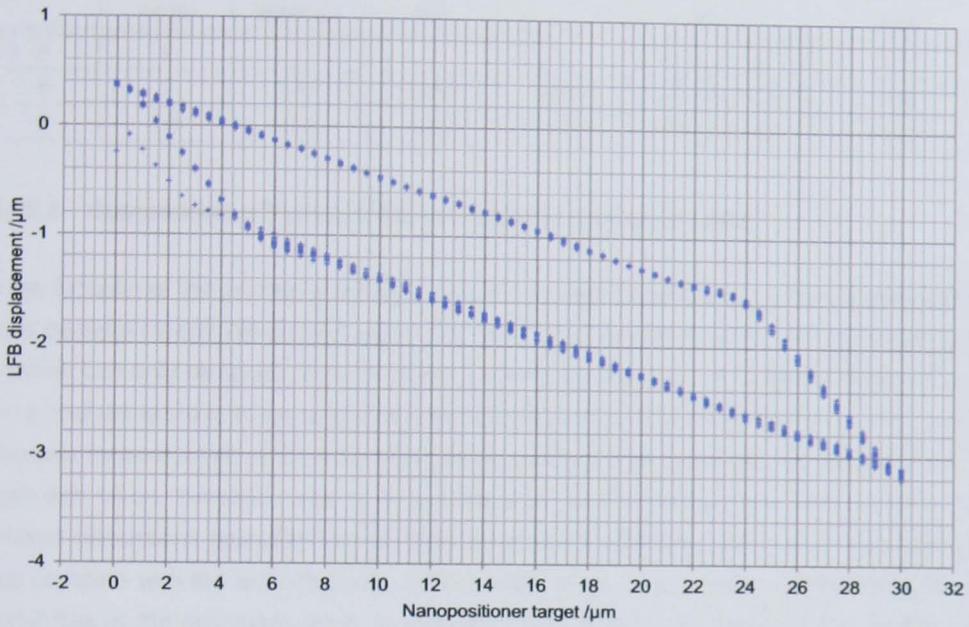


Figure 6.29: Displacement-displacement curve for the use of the reference cantilever to measure the spring constant of artefact B.

Table 6.8: Summary of spring constant estimates for all mechanically-tested artefacts

Artefact ID	Experiment ID	$k_{\text{ART}}/\text{Nm}^{-1}$	Uncertainty $/\text{Nm}^{-1}$	Weighting	Rel. uncertainty
A	4	15.15	0.42		2.8 %
B	1	46.72	1.24		2.7 %
C	5	31.86	0.95		3.0 %
E	2	15.53	0.43	37.5 %	2.8 %
	3	14.87	0.43	62.5 %	2.9 %
	combined	15.12	0.43		2.8 %

Table 6.9: Comparison of modelled and experimentally obtained spring constant estimates for three artefacts. Ratios are defined to simplify comparison.

Artefact	Beam length	Beam thickness	Analytical ratio	FEA ratio	Expt. stiffness /Nm ⁻¹	Experimental ratio
A	1	1	1	1	15.15 ± 0.42	0.76
B	1	1.42	2.87	2.36	46.72 ± 1.24	2.36
E	1.5	1.42	0.85	0.76	15.12 ± 0.43	0.76

6.4.2.6 Comparison with modelled estimates of spring constants

A key function of the prototype artefacts was to evaluate the suitability of the analytical and finite element models developed; such an evaluation is described here. The performance of a model can only be as good as the input parameters provided. As noted in section 6.4.1, the actual dimensions of the artefacts appear to differ somewhat from that specified, but the accurate measurement of those dimensions, in particular the thickness, is problematic. The approach taken, therefore, was to recalculate the model outputs using best estimates for artefact dimensions (specified lateral dimensions and Cranfield's thickness measurements) and compare with the experimentally determined values. Due to suspected correlated uncertainties in the estimates, such as incorrect material property inputs to the models, an additional step was taken to calculate stiffness *ratios* between the artefacts for each method. The results are presented in table 6.9; they are not particularly conclusive. Whilst the experimental ratio between B and E is in line with the FEA results, which might be assumed to be the accurate model, artefact A appears to be much more compliant in practice than justified by the circa 20 % narrowing of one leg due to damage.

6.5 Conclusions

Described in this chapter is the employment of a triskelion flexure design in a novel way to form the elastic element of the transfer artefact's transducer function, based on the earlier review of the precedent for low force transfer artefacts. The planar triskelion flexure shares the majority of the features and functionality of the popular cantilever artefact format, whilst its spring constant is comparatively insensitive to lateral contact misalignment. Significant misalignment may be detected as signal differences between sensors on the three legs.

In order to be able to predict the spring constant of an artefact with given dimensions, models of the triskelion flexure were developed. The spring constant is key to the function of the artefact, and most significantly determines the type of target instrument or process

the transfer artefact can interact with. Therefore, the ability to predict spring constant will inevitably shorten expensive design and fabrication iteration processes.

An analytical model of the triskelion flexure was developed for low force measurement based on similar reported models. The model incorporated several first-order approximations to limit the computational complexity for later artefact performance predictions. A complementary finite-element model was also developed, and parameterised to allow comparison with the analytical model.

A comparison of results from the two models supports the following conclusions. The analytical model satisfactorily predicts the vertical spring constant of the triskelion, that is, along the nominal single degree of freedom of the flexure design. The analytical model performed much more poorly when predicting the parasitic compliance of the remaining degrees of freedom of the artefact hub centre, due to mathematical over-constraints. The performance of the analytical model also decreases when the triskelion geometry is set such that the 'thin flexure' approximation no longer holds.

An extension of the analytical model to consider the response to lateral forces was undertaken. A linear combination of lateral and rotational compliance of the artefact hub top face centre did not conclusively account for the differences between predicted behaviour from the simple analytical and finite element models.

It can therefore be concluded that the analytical model is suitable for rapid initial geometry parameter value selection for a given target spring constant, but that verification of the chosen parameter values using finite element analysis should be undertaken where possible to better understand both linear and non-linear behaviour.

The key common weakness of both models as developed is the representation of the combined material properties of the laminated artefact structure. A suitable extension of the model to reflect the nickel-PZT layer structure should be incorporated in future. Nevertheless, the current analytical model can be used to rapidly establish bounds on the artefact spring constant based on all-nickel and all-PZT construction in turn.

A suite of prototype artefacts was developed to assist with the optimisation of the flexure and sensor design. The microfabricated artefacts consisted of a nickel flexure and piezoelectric instrumentation, with dimensions chosen to cover a volume of geometry parameter space and hence a range of spring constants. The fabricated artefacts were observed to have a number of fabrication defects that were likely to affect both the observed mechanical and electronic behaviour.

The vertical spring constants of a number of the fabricated devices were directly measured using the LFB and a secondary cantilever. The ratio of measured spring constants

broadly followed the expected ratio as modelled, but the level of agreement was low. It is suspected that, given the high sensitivity of spring constant to beam dimensions, fabrication defects were the primary cause of the poor agreement. Thus, the accuracy of the mathematical models remains unconfirmed and would benefit from further experimental confirmation, perhaps using a macroscopic equivalent or flexure-only microfabricated devices.

Chapter 7

Optimisation of instrumentation and control for the artefacts

7.1 Overview of chapter

In the previous chapter, the development of the triskelion flexure system for the low force artefact concept was presented. The process involved the production of a set of test artefacts, based on the production method used for the NPL microprobes, in order to minimise development risk. As such, the test artefacts were equipped with piezoelectric sensors and actuators.

This chapter describes efforts to develop and optimise interface circuitry for the prototype transfer artefact sensors, with the aim of exploiting the possibility for strain generation. From the previous comparison of sensor/actuator candidate technologies, the piezoelectric effect was identified as a possible transducer mechanism for a low force transfer artefact, but not necessarily the primary choice. Operational constraints on the project precluded the development of further prototypes, and so the test artefacts were considered in more detail.

This chapter is organised as follows. A brief summary of applicable background theory is provided, with an emphasis on practical aspects. The incremental development of a sensor circuit for quasistatic operation from the proven operating range of near-resonance is presented. Finally, the ability of a demonstration system to measure near-constant forces is evaluated.

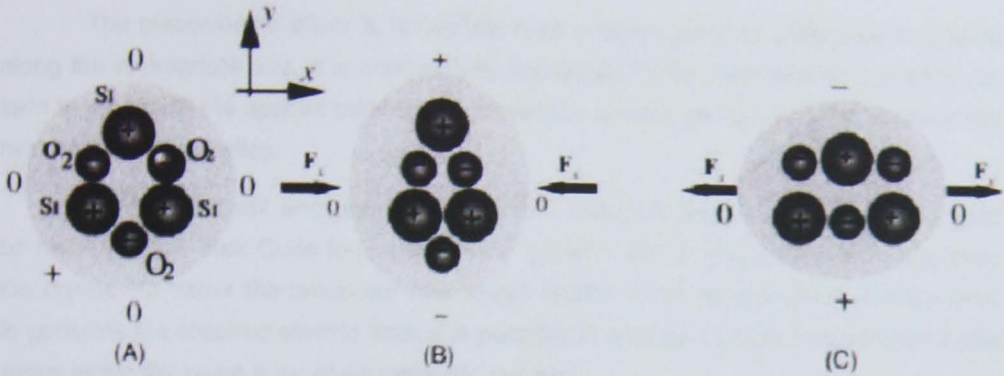


Figure 7.1: The piezoelectric effect in quartz: (A) unstressed unit cell; (B) unit cell under compression produces a dipole; (C) under tension, the sign of the dipole is reversed (from [26]).

7.2 Background theory

The discussion in this section builds upon the introduction in section 5.2.2.

7.2.1 The piezoelectric effect

Piezoelectricity is a bulk property of a crystalline material whose unit cell develops a charge dipole when subjected to a stress [26]. The piezoelectric effect can only occur along axes of asymmetry in the unit cell, and so, not all materials exhibit this property.

A common natural piezoelectric material is quartz. Figure 7.1 shows a simplistic ball model of the quartz unit cell. Stress applied along the x axis results in a displacement of charge in the y direction according to the magnitude and sign of the stress. This charge displacement equates to an induced potential difference across the bulk material, or a transient current. Due to the finite Poisson's ratio of quartz it follows that stresses in the y direction will also result in a y charge displacement. Further interactions can typically be identified in other crystal planes.

A full characterisation of the piezoelectric effect for a given material would consider the tensor equation for polarisation

$$P = \begin{pmatrix} P_{xx} \\ P_{yy} \\ P_{zz} \end{pmatrix} = \begin{pmatrix} d_{11} & d_{12} & d_{13} \\ d_{21} & d_{22} & d_{23} \\ d_{31} & d_{32} & d_{33} \end{pmatrix} \begin{pmatrix} \sigma_{xx} \\ \sigma_{yy} \\ \sigma_{zz} \end{pmatrix}$$

where σ_{ii} are axial stresses and d_{mn} are the piezoelectric coefficients, with units of coulombs per newton.

The piezoelectric effect is reversible; if an external potential difference is applied along the appropriate axis, it is energetically favourable for the piezoelectric crystal to deform to neutralise the applied potential. This process is lossy, giving piezoelectric materials hysteretic characteristics.

In practice most engineered piezoelectric materials are polycrystalline, and must be heated above their Curie temperature and 'poled' within a strong electric field to align the crystals to mirror the behaviour of a single crystal. If the sensor electrodes are used to generate the required electric field, it is possible to arrange multiple independent active zones within the same layer of piezoelectric material.

7.2.2 Generating motion

As discussed, the method of generating a force within a piezoelectric device would simply be to apply a suitable potential difference and constrain the device to prevent it from reaching its free displacement state. The act of constraining the device will subject the constrainer, the LFB or target instrument, to a force calculable based upon prior artefact calibration.

It had been expected at the planning stage of the project that the established triskelion concept would be able to generate quasistatic displacements on the order of 0.1 μm to 1 μm and exhibit related blocking forces on the order of 0.1 μN to 1 μN , such as later demonstrated elsewhere [170]. However, preliminary experiments with the microprobe triskelion using, in turn, a laser Doppler vibrometer and the LFB could not resolve any displacement. Voltages were applied up to, and slightly beyond the 8 $\text{V}\mu\text{m}^{-1}$ potential gradient limit recommended by the fabrication partner, with no success. The problem may have been compounded by the unavailability of a proportion of actuators on each artefact due to defects. Further diagnosis was not attempted under the scope of this thesis.

7.2.3 Sensing motion

There are two ways in principle to detect the electronic output of a piezoelectric sensor: using a voltage amplifier or a charge amplifier. The voltage amplifier presents the sensor with an infinite impedance, trapping the displaced charge within the sensor, and amplifying the potential difference induced across the sensor to a useful level. The charge amplifier presents the sensor with zero impedance, collects all the charge, and by means of a feedback capacitor, produces a practically scaled analogue of the sum of charge collected.

Implementations of either approach are subject to practical limitations. As the input impedance of the voltage amplifier is increased, the charge will find another route towards

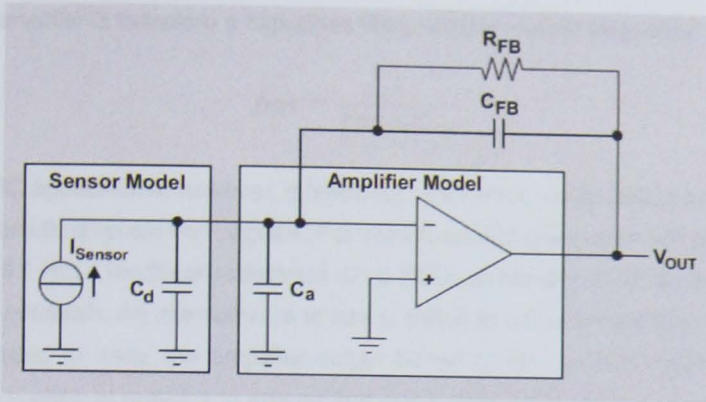


Figure 7.2: An electronic model of the sensor, charge amplifier system (from [27])

ground, such as via cable capacitance. In the case of the charge amplifier, charge may be lost to leakage currents into the amplifier. In either case, it is essential to properly shield the sensor and interfacing circuit from additional, external sources that would result in inaccuracy of strain analogue. The amount of charge generated by sensors of the size used in the prototype artefacts is estimated to be on the order of picocoulombs.

The charge amplifier is the established choice for piezoelectric sensors, and consequently is frequently discussed in the literature. Bartolome [27] gives a pragmatic description of the amplifier, of which the following is a summary.

The sensor charge amplifier system is shown schematically in figure 7.2. The sensor is modelled as a capacitor and a charge source in parallel, which reflects the behaviour of the PZT and also conforms to the standard form of a device with high output impedance.

The charge amplifier has a very low input impedance, presenting a virtual ground to the sensor output and hence accepting all charge input. Charge arriving at the sensor (C_d) or on the parasitic capacitance of the operational amplifier (op-amp) (C_a) will establish a potential at the non-inverting op-amp input. This potential will immediately be compensated by a current through the feedback network. Neglecting the feedback resistance R_{FB} for a moment, this current will lead to buildup of charge on the feedback capacitor in principle equal to the net sum of all charge from the sensor. The resultant potential difference across C_{FB} is the output voltage of the charge amplifier V_{out} , and hence the gain of the charge amplifier can be approximated as $gain = C_{FB}^{-1}$. The feedback resistance R_{FB} slowly allows charge past C_{FB} to bring the charge sum back to zero over time, counteracting unwanted drift and DC components in dynamic applications. This action aims to make saturation of the op-amp output more difficult, permitting a higher gain factor and hence higher sensitivity.

The charge amplifier is therefore a high-pass filter, with the cut-off frequency

$$f_{\text{HPF}} = \frac{1}{2\pi R_{\text{FB}} C_{\text{FB}}} .$$

For DC applications, however, a feedback resistance would distort or remove slow-moving, quasistatic displacement signals. For a feedback capacitance of 100 pF and a cut-off frequency of 0.1 Hz, a feedback resistance of 16 G Ω is necessary. Such a resistance would be difficult to establish. An alternative is to use a switch to only connect R_{FB} , with a smaller value, as needed to 'zero' the amplifier output based on an external monitoring system. However, the challenge remains to ensure that cross-trace PCB resistances do not provide an additional R_{FB} .

In order to achieve a successful charge amplifier implementation, the central op-amp must have the following characteristics:

- very high input impedance, to avoid direct interaction between signal wire and ground via the two inputs;
- very low input bias current, or at least very low input offset current, and an excellent common mode rejection ratio, so that signal is not lost to the workings of the amplifier;
- excellent thermal stability of output; and
- low noise.

7.3 Sensor circuit development

7.3.1 Overview and early attempts

Based on section 7.2, noting the challenges to DC operation and the fact that local disruptive influences were not fully understood, an incremental sensor circuit (charge amplifier) development approach was employed as summarised below.

1. Verification of sensor operation at the resonant frequency of the flexures.
2. Development and optimisation of circuit between 50 Hz barrier and resonant frequency.
3. Signal detection below 50 Hz barrier.
4. Optimisation for quasistatic operation.

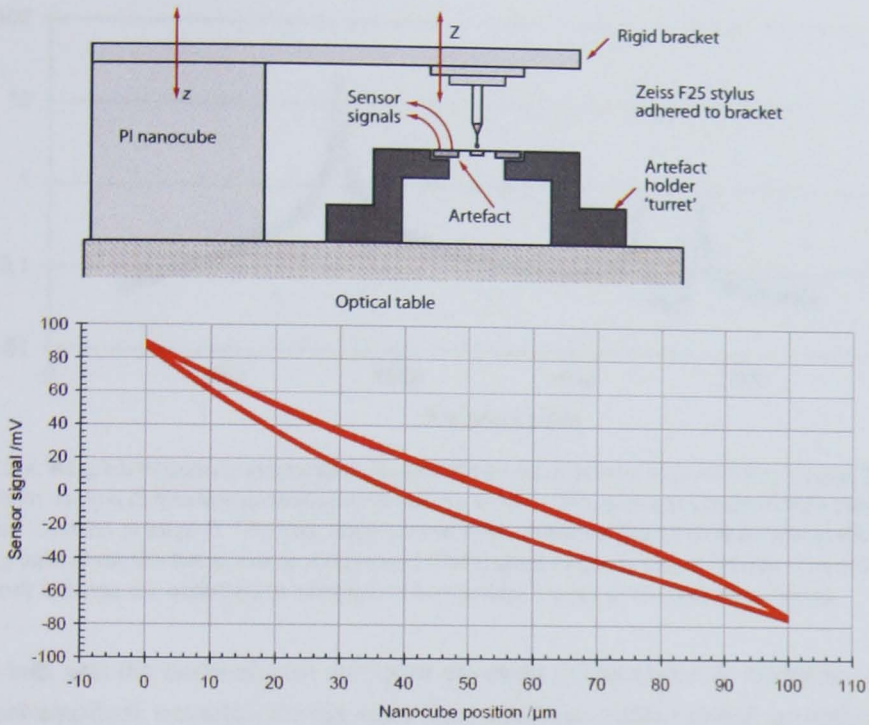


Figure 7.3: An unsuccessful early interaction experiment that produced a fictitious sensor signal, due to electric fields from the PI Nanocube nanopositioner system: (top) the physical arrangement; (bottom) example results.

A key challenge was the establishment of pure mechanical inputs to the triskelion device for testing, such that the external flexure actuator would not induce a parasitic charge mistaken for a signal from the sensor.

Previously, more optimistically planned experiments used the arrangement shown in figure 7.3 (top) to displace the artefact. The nanopositioner, itself piezoelectrically actuated, interacted with an early charge amplifier circuit to produce a false signal (figure 7.3 bottom) of the expected form. The problem was finally identified when the characteristic form was recreated with the pusher tip lifted away from the triskelion, having been previously masked by poor repeatability.

7.3.2 First stage: behaviour at resonance

The microprobe development process at NPL had previously established a vibrometer-based technique for evaluating the integrity of each sensor and actuator; this technique was applied to the prototype artefacts reported here. The chip was mounted beneath a Polytec CLV 2543 laser Doppler vibrometer such that the vibrometer's measurement beam struck the centre

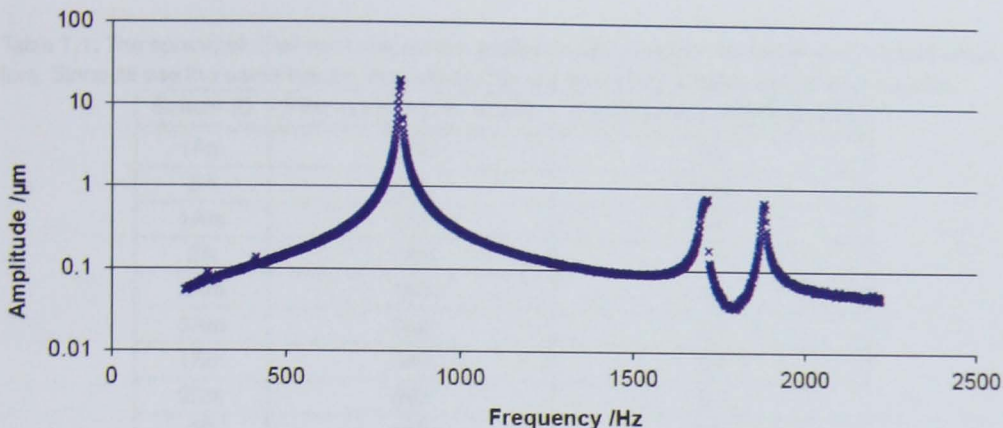


Figure 7.4: A typical frequency response characteristic for the triskelion obtained from a laser Doppler vibrometer using a software tool developed by others at NPL. This plot was obtained from energising actuator '3Am' on artefact D. The first mode corresponds to the vertical oscillation mode; the higher pair of peaks show the two plane-tilt modes and if fabricated perfectly would overlap. The small low-frequency notches are assumed to correspond to resonant modes of the metrology frame.

of the hub, with the beam aligned normal to the plane of the device. A moderate-voltage, constant-amplitude sinusoidal driving signal from a programmable function generator (AIM-TTi TG330) was connected to each sensor and actuator in turn and a frequency response spectrum acquired from the vibrometer over the range 200 Hz to 2250 Hz. The vibrometer used relies on the mechanical loop for displacement reference but this is acceptable for the described purpose. Figure 7.4 shows a typical response from an actuator on artefact D. Resonant peaks associated with the primary vertical and two plane rotational modes are evident.

In a separate activity relating to the microprobe development process, it was noted that the resonant peaks of the piezoelectric triskelia increase in frequency by a few percent after the device has been baked at around 80 °C for ten minutes. This is probably due to the resultant evaporation of absorbed humidity and either a lower moving mass or a change in piezoelectric properties (or some combination). Heating was required in order to fully cure the silver conductive paint used to implement connections from the artefact chip to the underlying printed circuit board.

The peak amplitude for each sensor and actuator at the first resonant frequency was recorded. Table 7.1 gives example results for artefact D. There is no conclusive difference in amplitude between actuator and sensor response; the variation in performance within each set is too great. The variation was attributed to fabrication defects and only those elements with highest response selected for future use.

Based on the assumption of reversibility of the piezoelectric effect, these results

Table 7.1: The spread of maximum resonance amplitudes achieved for the set of sensors and actuators. Since all use the same flexure, the results indicate the quality of each sensor and actuator.

Sensor ID	First mode maximum /Hz	Displacement amplitude / μm
1Am	845	1.2
3A	845	10.0
1Am	845	1.0
2A	845	1.0
2Am	844	1.0
3Am	843	8.0
1Sm	843	9.0
2Sm	843	2.6
2S	843	2.1
3S	843	5.0
1S	845	1.0
3Sm	843	3.2

appear to confirm that the devices would sense correctly at resonance, using an interface circuit of the form developed elsewhere for the NPL microprobes.

7.3.3 Second stage: AC operation below resonance

A pure mechanical input trivially implies the use of a mechanical resonator. The challenge lies in choosing a resonator with the correct amplitude and decay time constant, and further in generating a repeatable initial oscillation amplitude without a dangerous transient mechanical input. The test system developed, shown in figure 7.5, adapts a medical tuning fork to include a voice-coil actuator and a pusher stylus. The pusher stylus was a sharpened length of wire. The aluminium tuning fork, commonly used for hearing and peripheral sensory tests, had a nominal resonant frequency of 128 Hz and a mass of around 100 g. The voice coil drive was implemented as a 5 mm diameter neodymium magnet surrounded by a hand-wound coil. The coil, constructed to standard hobbyist instructions widely available, consisted of around 200 turns of 30 AWG (0.26 mm diameter) insulated copper wire, and had a DC resistance of around 8 Ω . Two paper or plastic film layers are secured around the circumference of the magnet and the coil wound on; after gluing the coil, the inner layer is removed to free the magnet, leaving the two elements to be mounted independently as required. The coil was attached to the fork to avoid the situation of a moving magnet over the nickel flexure.

The coil was attached to the TG330 function generator 50 Ω output and the resonant peak determined for a 5 V sinusoidal driving signal. The assymmetrically distributed additional

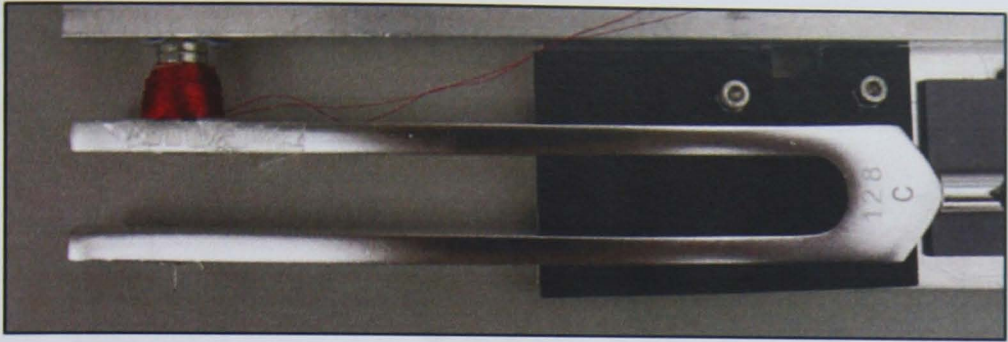


Figure 7.5: The tuning fork actuator system. The fork is placed across the centre of this image and secured with bolts through the handle out of shot. The coil is glued to the fork, and the magnet to the square-section rigid aluminium bar along the top of the image. On the opposite fork, approximately coaxial to the coil, a wire stylus is attached to contact the artefact. The system was rigidly mounted to a 5 mm high-resolution motion stage of the kind used elsewhere in this work.

mass raised the maximum-amplitude frequency to $230 \text{ Hz} \pm 1 \text{ Hz}$ with a slight response at around 120 Hz. Under normal operation the driving voltage was reduced at $230 \text{ Hz} \pm 1 \text{ Hz}$ until oscillation blurring was just visible, with the amplitude estimated at around $100 \mu\text{m}$.

7.3.4 Proof of pure mechanical input

To verify that any obtained sensor signal was purely due to the piezoelectric response to the mechanical input, the tuning fork was brought to a steady state oscillation, the coil power abruptly disconnected, and the decay of the coil voltage and sensor signal compared. An abrupt drop in sensor signal would indicate interaction with the electromagnetic drive; a clearly exponential decay, even if rapid, would suggest dependence only upon the mechanical motion of the tuning fork.

Artefact H, leg 3 outer sensor was used for this work. $6 \mu\text{m}$ of oscillation amplitude was observed for this sensor using the laser Doppler vibrometer in an earlier characterisation experiment, based on a 10 V peak-to-peak driving signal at the artefact H vertical mode frequency of $590 \text{ Hz} \pm 5 \text{ Hz}$. The feedback capacitance and resistance were 3.3 pF and $500 \text{ M}\Omega$ respectively, giving a cut-off frequency of 96 Hz. The charge amplifier was powered by standard 9 V batteries to minimise noise input from this source; however, a 7 V peak-to-peak 50 Hz notched sinusoid mains signal persisted throughout all experiments. The feedback capacitor was shorted manually to recentre the output voltage between the amplifier rails.

Figure 7.6 summarises the physical interactions and data flow in the experiment. A software tone measurement function measured the RMS amplitude of the 230 Hz component of the filtered sensor and coil driving signals. Figure 7.7 demonstrates a typical response to

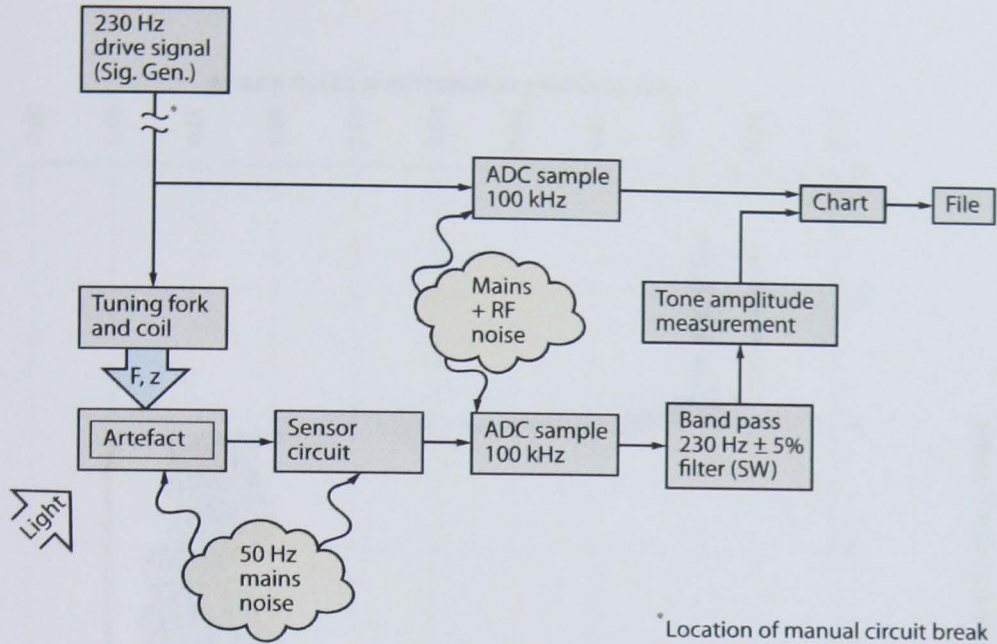


Figure 7.6: Summary of physical interactions, noise sources and data flow in the tuning fork experiment.

abruptly connecting and disconnecting the function generator from the coil. The 230 Hz sensor signal amplitude with the coil de-energised was about 7 mV, most likely due to limitations in the ADC unit. With the coil energised to 0.8 V at the 230 Hz coil resonant frequency, the 230 Hz sensor amplitude component amplitude increased to 70 mV. This latter amplitude appeared to oscillate over time, probably due to an interaction between motion signal and the 250 Hz harmonic of the mains noise.

On change of connection state of the function generator, there is a sharp discontinuity in the coil voltage indicating a switch between effective 'speaker' and 'microphone' modes, due to finite energy conversion efficiencies in each direction. There are no detectable equivalent discontinuities in the sensor data. On connection, there is a slight phase lag between amplitude variation in the driving and response signals consistent with the behaviour of a driven resonator. The phase lag may be explained by considering the finite rate of energy transfer to the resonator. On disconnection of the function generator, the coil voltage decays exponentially as the fork amplitude decays. The lack of discontinuity in only the sensor data is shown more clearly in figure 7.8.

Both lack of discontinuities in the sensor signal and the presence of phase lag from the driving signal for low-frequency amplitude variation clearly indicated that the charge amplifier circuit was detecting the mechanical motion of the artefact.

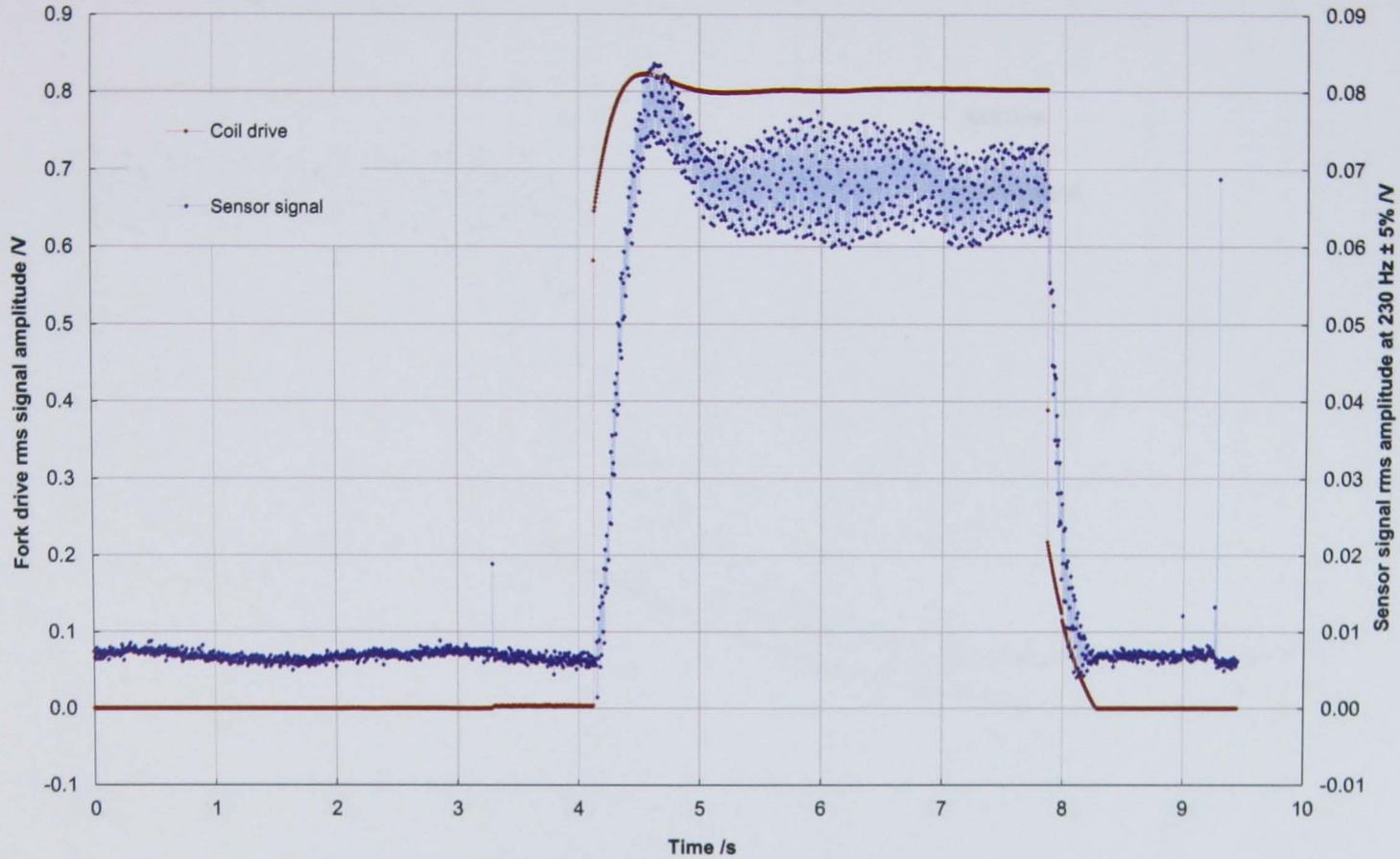


Figure 7.7: Sensor reponse to abrupt coil power connection state changes.

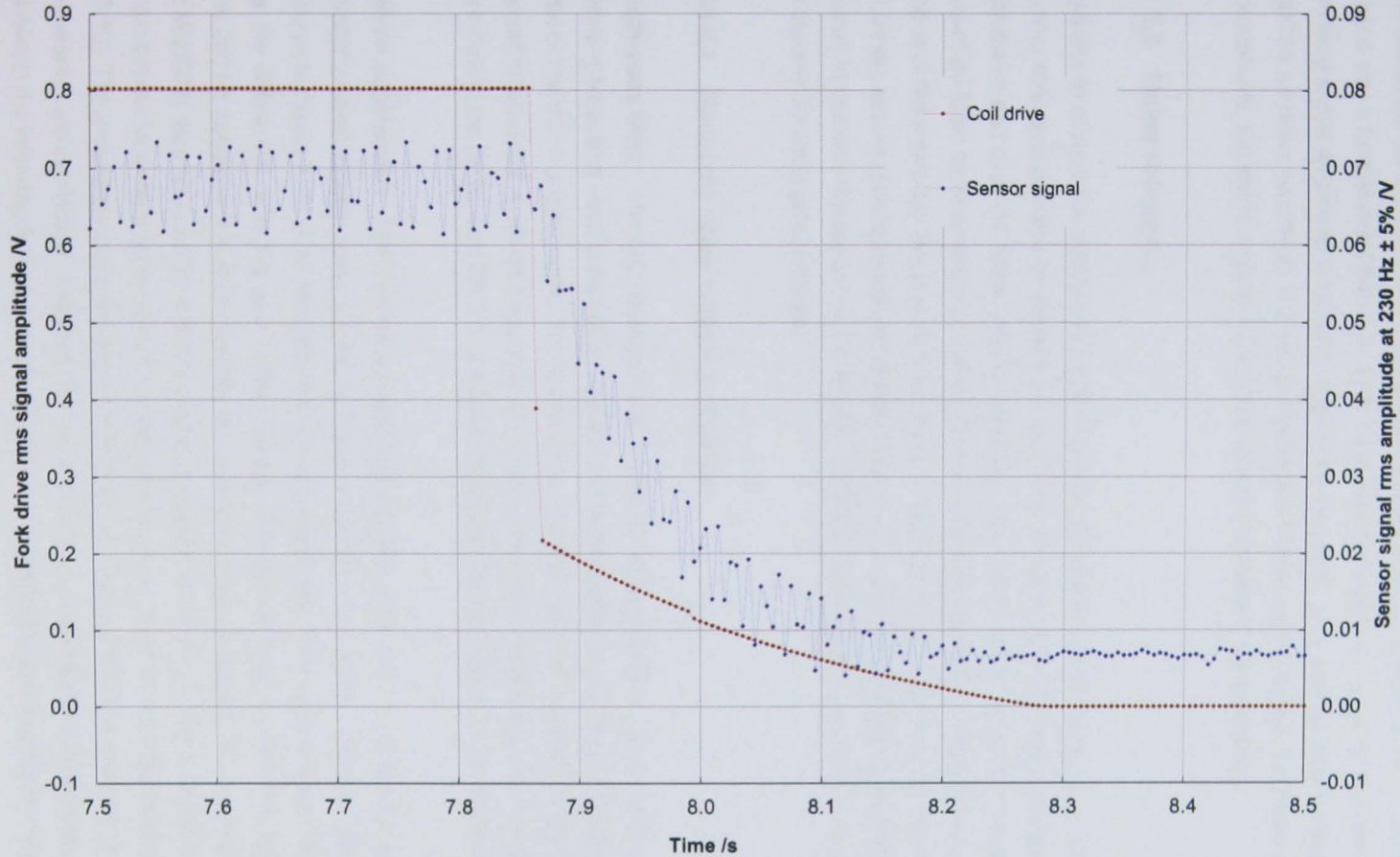


Figure 7.8: Sensor response to abrupt coil removal of driving signal from function generator.

However, the amplitude of the background mains noise remained much larger than the useful sensor signal itself. The main consequence for AC operation below artefact resonance was a fundamental barrier to gain selection, and hence an upper limit on the possible working signal amplitude. If the gain were to be increased such that the mains signal is 'clipped' by amplifier saturation, this would distort any filtered, useful signal. For lower operating frequencies, the mains supply noise could obscure the useful signal entirely.

7.3.5 Noise reduction

Options to reduce the influence of mains supply noise were considered, using the proven tuning fork arrangement to provide a consistent signal-to-noise contrast reference. Both electronic and physical filters were considered. Physical solutions (that is, shielding) were expected to be more successful, but would also introduce significant constraints on the operation of the artefacts. The experiments were undertaken in an RFI-shielded laboratory with, however, known problems with earth-connection noise. Shielded cables were used from the outset to connect the sensor to the charge amplifier, with shield foil connected to ground in a manner avoiding ground loops.

7.3.5.1 Electronic noise reduction: filtering

High-pass filter The first approach was to set the high-pass filter significantly above the working frequency, and to accept a reduction in working signal in exchange for further reduction of the mains supply noise. The feedback components (6.8 pF, 10 M Ω) on the LF412CN amplifier provided a cut-off frequency of 2.3 kHz. With the mechanical input as described previously, the 50 Hz and 230 Hz components had similar magnitudes (see figure 7.9)

Noise subtraction Next, an instrumentation amplifier was used to attempt to subtract a similarly-sized nearby noise reference signal from the noisy sensor signal. The circuit is shown in figure 7.10. A 10 k Ω gain resistor was used with the instrumentation amplifier to fix the differential gain; the gain value was six. The output result is shown in figure 7.11; the 230 Hz component now dominated, though mains noise remained. An improved op-amp (LMC6082) was sourced for the two charge amplifier sub-circuits. The LMC6082 benefits from a lower input bias current (4 pA compared to 4 nA, and half the total harmonic distortion (THD)). The improved results are shown in figure 7.12. Both the 50 Hz noise spike and higher harmonics are significantly reduced. The circa 470 Hz peak and wobble on the sensor signal shown in the following figures is due to excessive fork amplitude and consequential excitation of the fork's higher modes.

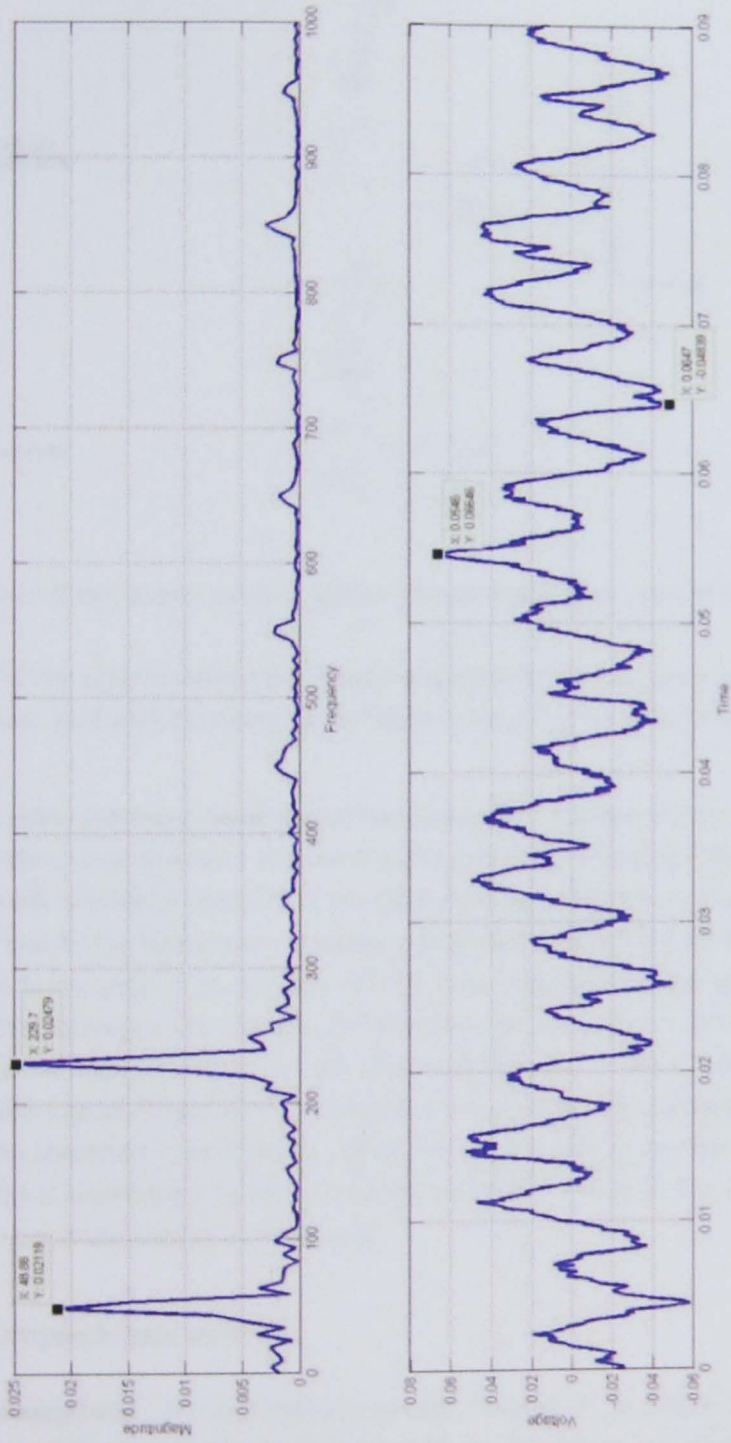


Figure 7.9: Sensor response using charge amplifier with high-pass filter of 2.3 kHz. Time and frequency are in units of seconds and hertz respectively.

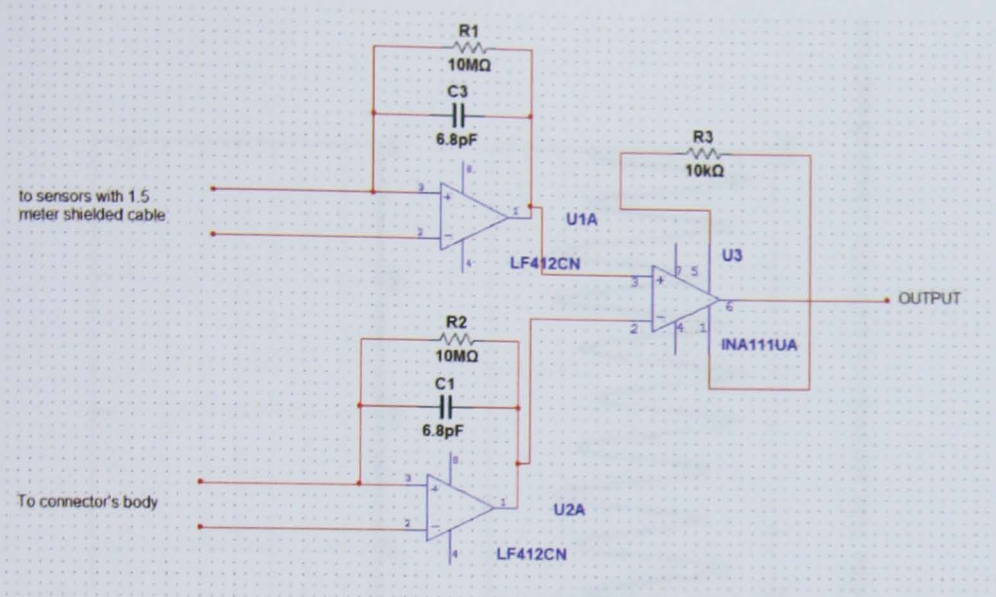


Figure 7.10: Circuit diagram for noise reduction through subtraction of a nearby noise reference.

Further experimentation permitted the optimisation of the instrumentation amplifier gain resistor; for $2.5\text{ k}\Omega$ the mains supply noise was significantly reduced (see figure 7.13).

Effect of cable and input capacitance: low pass filter It was mentioned previously that, provided the charge amplifier circuit input impedance is sufficiently low, the potential difference across, and hence influence of, the cable and input capacitance is negligible. This is certainly true for low frequencies. However, a finite input capacitance will contribute a low-pass filter to the circuit in combination with the output impedance of the sensor, defining a bandwidth of operation. For example, by increasing the value of a capacitor placed across the charge amplifier terminals from 500 pF to 5 nF the ratio between 230 Hz and 470 Hz components was increased from two to seven. However, since the definition of this filter relies on the properties of each sensor, which can be expected to vary somewhat, it is not appropriate to implement a block for a specific noise source using such a method, even for operation below 50 Hz as to be discussed.

7.3.5.2 Physical noise reduction

Cable management The importance of correct shielding of electronics and connections is clear. However, appropriate implementation without affecting sensor function was challenging.

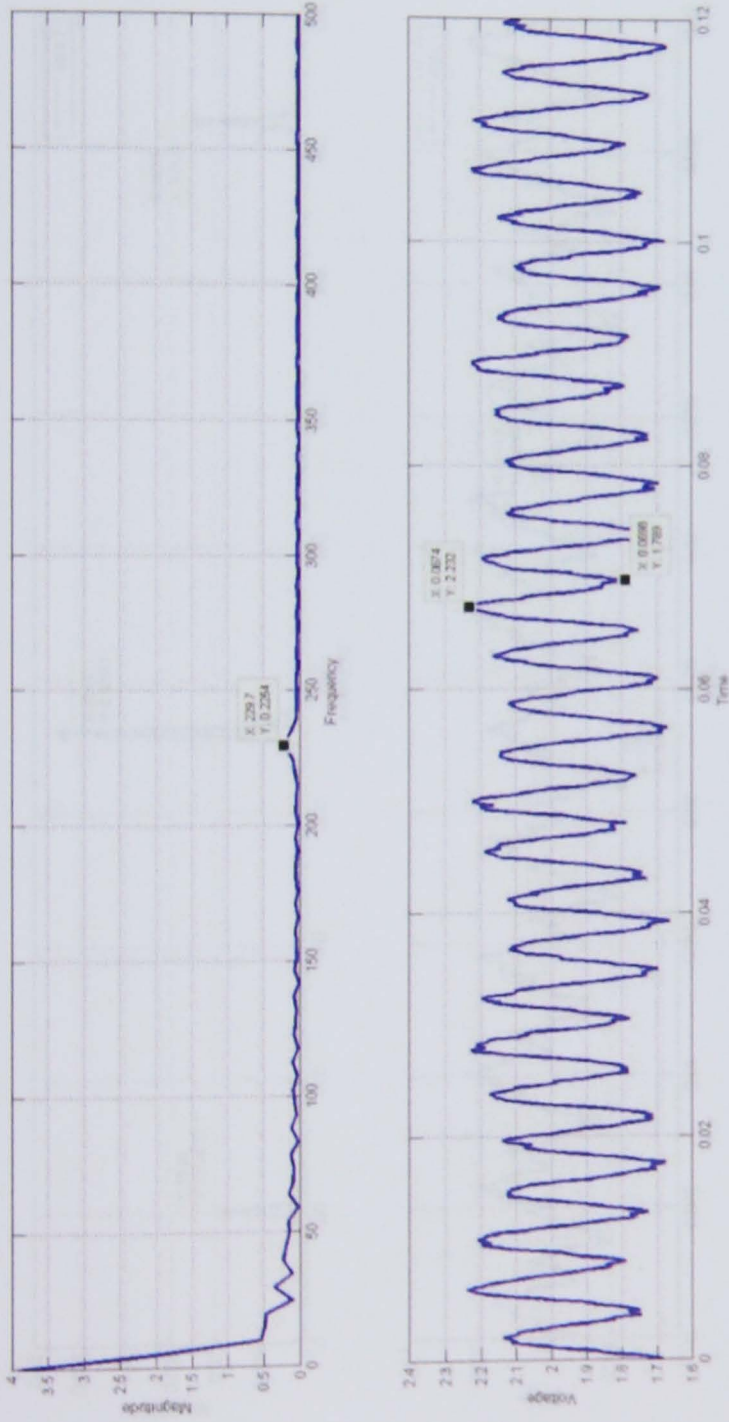


Figure 7.11: Sensor circuit output voltage using noise subtraction circuit, using the LF412CN amplifier. Time and frequency are in units of seconds and hertz respectively.

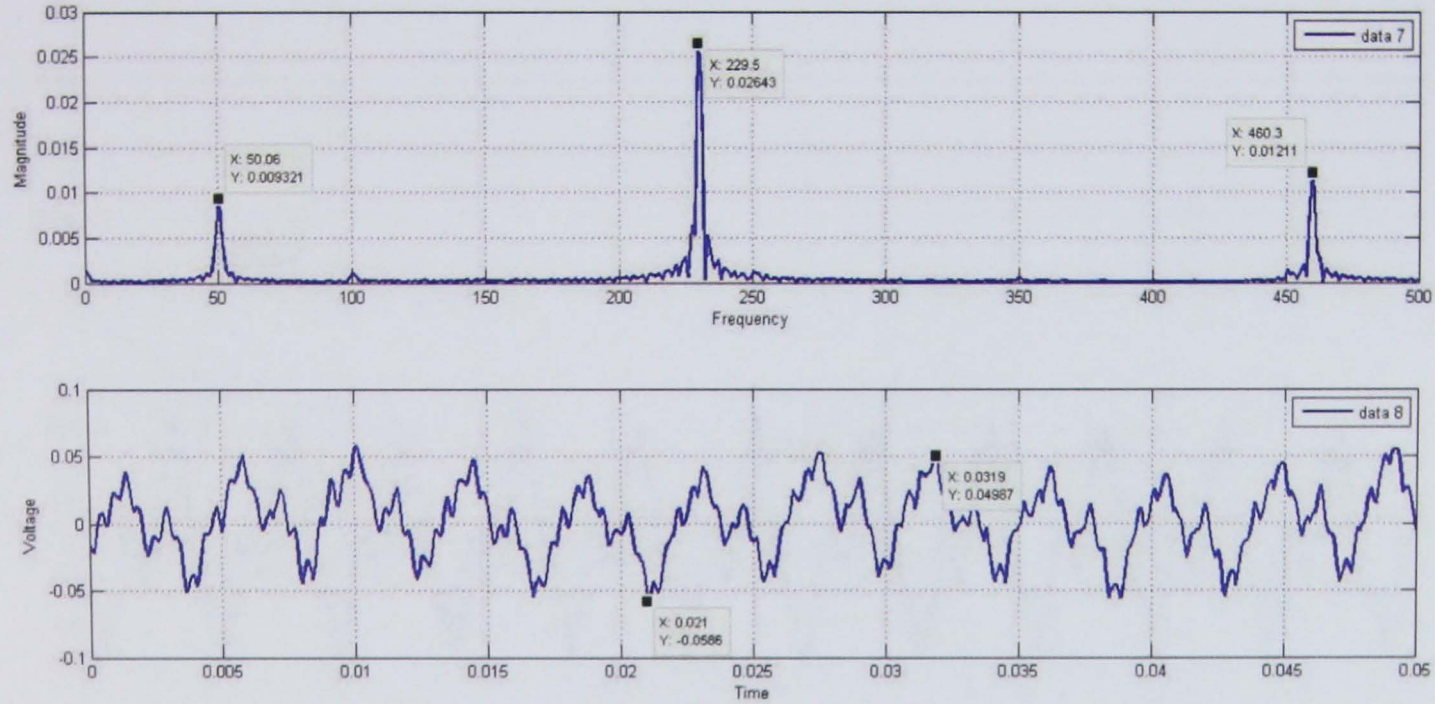


Figure 7.12: Sensor circuit output voltage using the noise subtraction circuit based on the LMC6082 amplifier. Time and frequency are in units of seconds and hertz respectively.

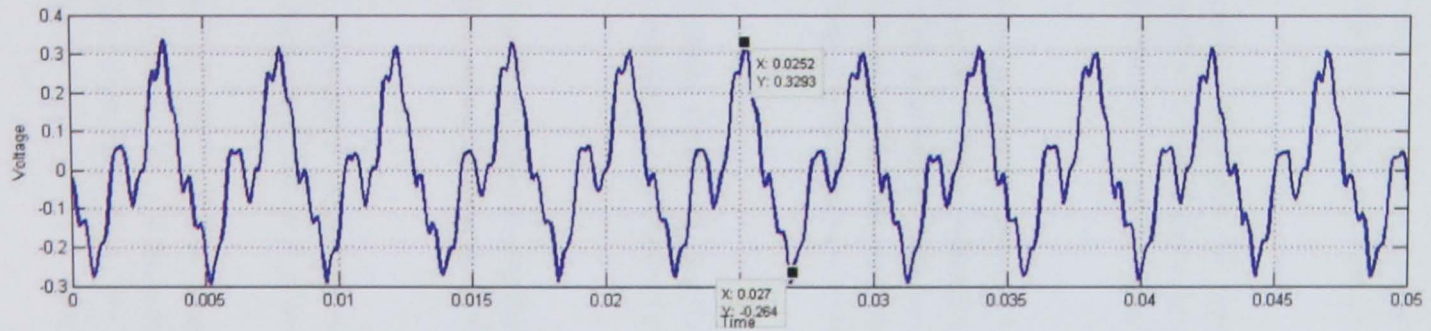
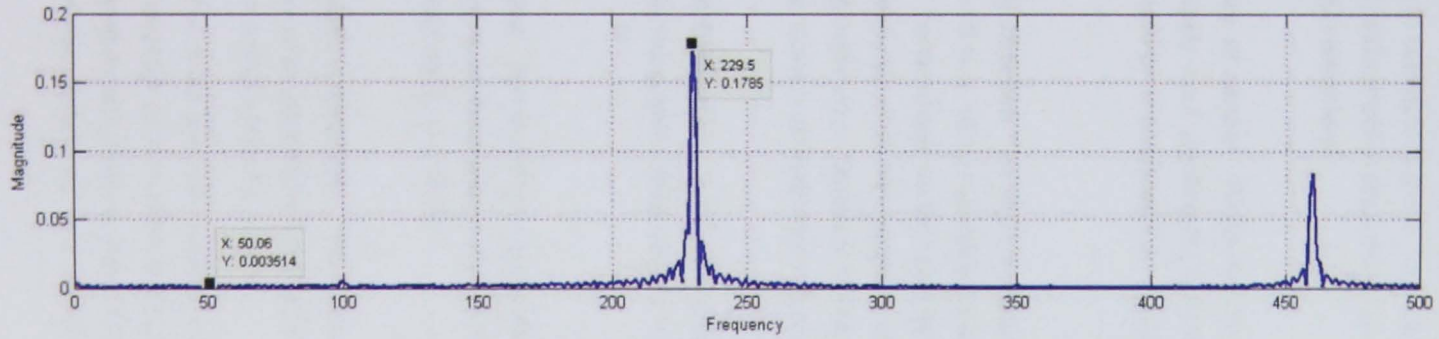


Figure 7.13: Observed reduction in noise in the sensor circuit output due to optimisation of feedback resistor. Time and frequency are in units of seconds and hertz respectively.

Care was taken to ensure the correct connection of shield lines such that ground loops were avoided. The ground connection of each artefact was isolated from the artefact holder (turret) and cable shielding and passed through the twisted pair cable to the charge amplifier to connections there. The cable from turret to amplifier was kept as short as practical and held immobile; even small cable motions were found to have a significant influence on the DC sensor level.

Enclosure of sensor Whilst the above cable management and circuit design reduced mains supply input significantly, both 50 Hz noise and other drift sources remained; such inputs would be unacceptable for quasistatic sensor operation and would need to be removed.

Humidity variation An unplanned humidity excursion in the laboratory to 65 % (usual specification $40 \% \pm 10 \%$) highlighted a large and almost linear relationship between humidity and PZT performance, as indicated by the change in resonant frequency and amplitude of a functionally identical microprobe. It was expected that humidity variation would also affect quasistatic operation. Transient humidity changes would be a feature of human interaction as well as many in-process applications.

Residual EMF input Inevitable proximity of the artefact and amplifier circuit to mains cables, trunking and similar results in the insertion of EMF noise of the form discussed above.

Light input Semiconductor devices such as the low force test artefacts function as good light sensors, as the artefacts demonstrated. A voltage analogue to a torch strobed over the artefact was easily identifiable.

Electrostatic interaction Finally, the artefact-amplifier system was found to have good remote sensing capabilities, being able to sense the proximity of a rubber-soled shoe to the floor from a distance of four metres.

The most practical solution to the above drift inputs was to entirely enclose the artefact-amplifier system within a grounded aluminium box, stabilising the humidity as well as temperature and blocking light, electrostatic fields and EMF. An enclosure of sufficient thickness (two millimetres) was chosen to approximate the ideal Faraday cage [184]. Ports

of maximum diameter 10 mm were cut to allow connections and mechanical input for future experiments, as are to be shortly described.

It was apparent that drift would remain an issue and warrant some sort of low-frequency cyclical artefact usage to isolate longer-term drift. Such operation would limit application of the artefacts but would be acceptable for the calibration of other secondary artefacts.

7.3.6 Third stage: proof of sensor signal below 50 Hz

To continue the optimisation of the sensor circuits, it was first necessary to detect, isolate and improve a sensor response to actual mechanical input below the mains noise threshold. A crude mechanical oscillator was assembled, as shown in figure 7.14. Since steady linear manual motion is much easier to provide, a simple low-AWG wire pull-cord was wound upon the cam axle such that oscillation frequencies between 2 Hz and 30 Hz were possible, with the cord failing preferentially in the event of over-force. The shape of the lever was compatible with the shielding enclosure. The vertical position of the lever pivot axle set the limits of artefact deflection.

To simplify this detection-only stage and avoid saturation, a feedback resistor was employed; 500 M Ω and 6.8 pF feedback components set the high-pass pole to 47 Hz. Figure 7.15 shows the result of driving the artefact in bursts at around 5 Hz within each burst.

The resultant periodic features have a frequency of around 35 Hz. Those cycles at the start of the highlighted trace (figure 7.15 bottom) have the form of a u-shaped tapping input subjected to a high-pass filter. In the remainder of that trace the tapping appears to settle to full oscillations in contact. The observations are, collectively, evidence of the oscillator bar vibrating at its resonant frequency of 35 Hz under the energy input of the cam system. This unwanted vibration was confirmed by change and removal with the addition of extra moving mass to the oscillator bar.

Figure 7.15 does not, however, show significant signs of the intended 5 Hz driving signal; this was a result of the high-pass filter. An increase of feedback resistance to 1 G Ω reduced the pole to 23 Hz but caused the charge amplifier circuit to become unstable. Instability only occurred when shielded from the mains supply noise within the enclosure. The cause of the problem was diagnosed as due to the limited extent to which the capacitor approximates the ideal capacitor.

Standard references (for example [184]) note that any real capacitor can be represented by an equivalent circuit containing additional elements such as dielectric loss equivalent resistance, isolation resistance, packaging series resistance, series inductance and so

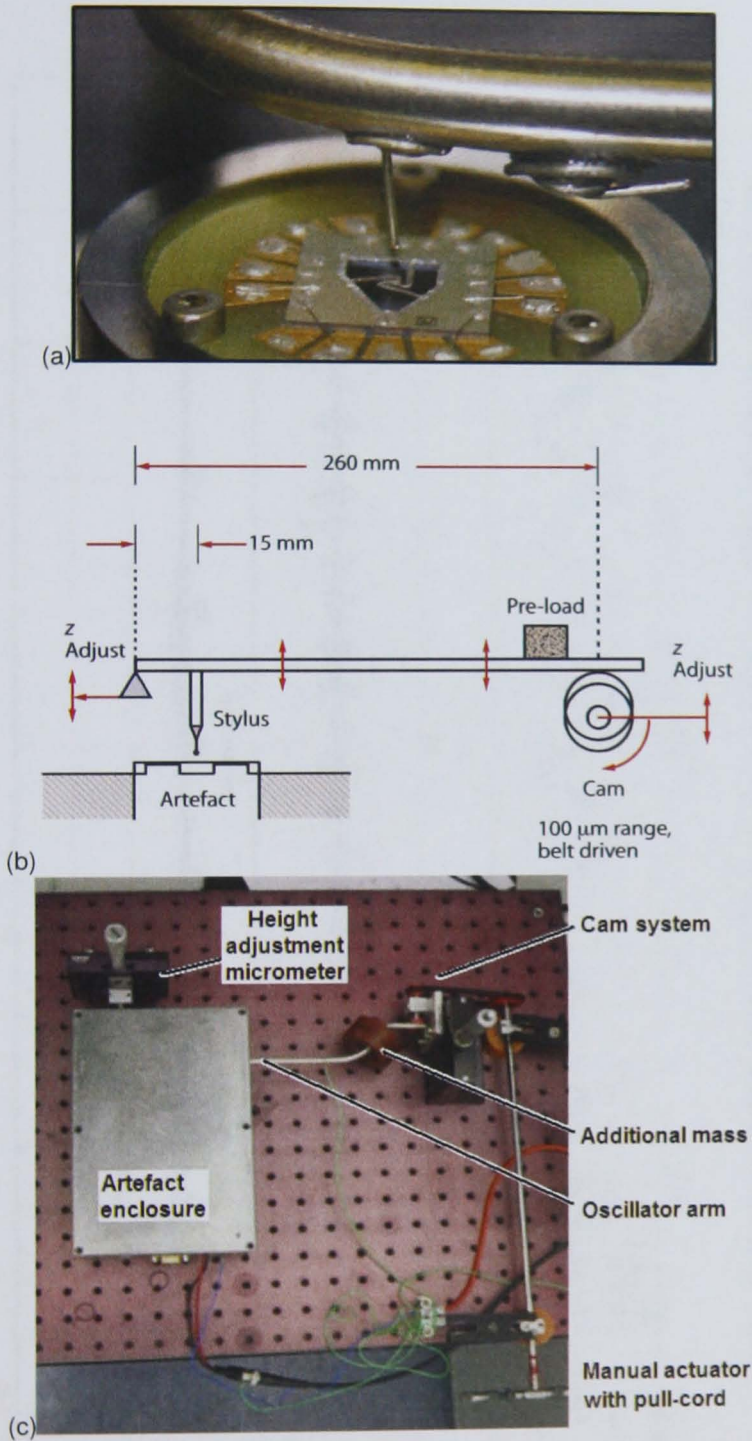


Figure 7.14: The manual mechanical oscillator system: (a) detail of artefact interaction; (b) schematic overview of physical arrangement of cam oscillator; (c) overview photograph showing noise enclosure and pull-cord system bottom-right.

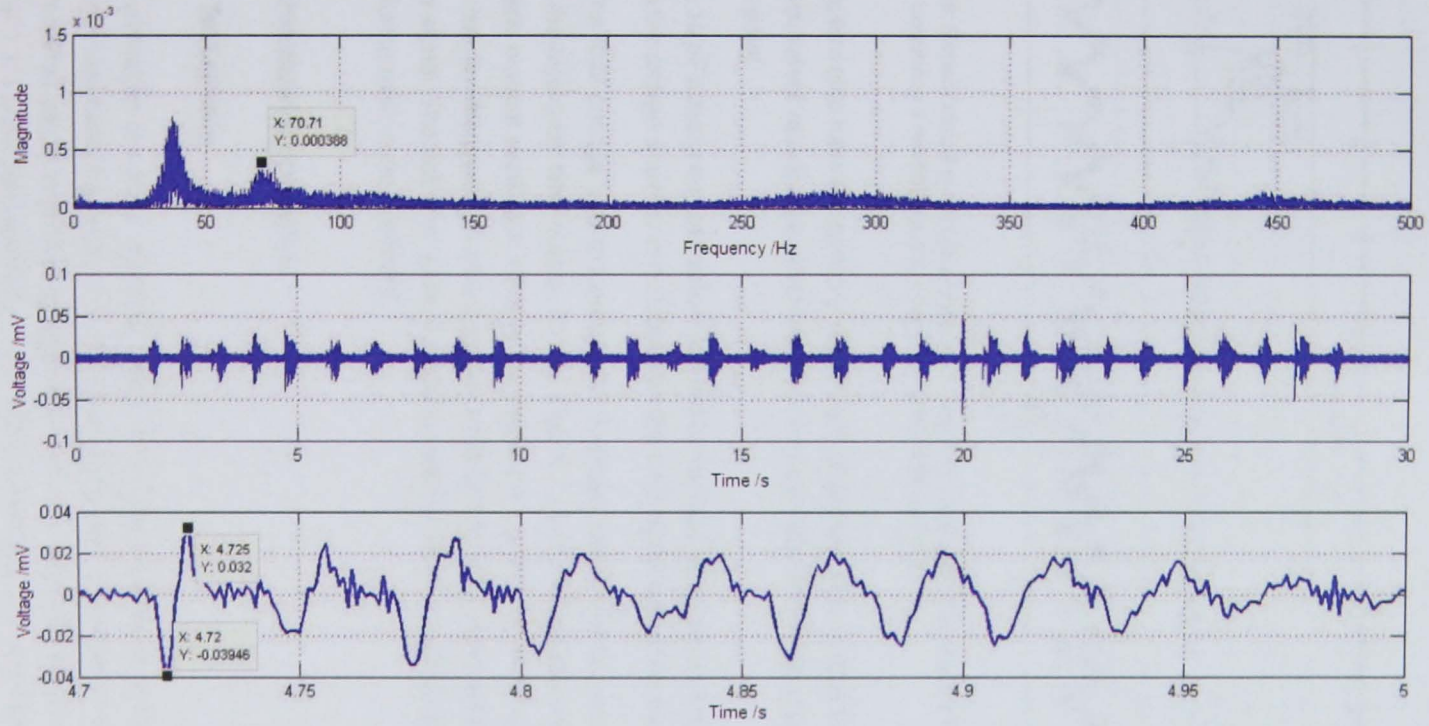


Figure 7.15: Sensor circuit output response to repeated bursts of excitation at around 5 Hz using the cam oscillator system.

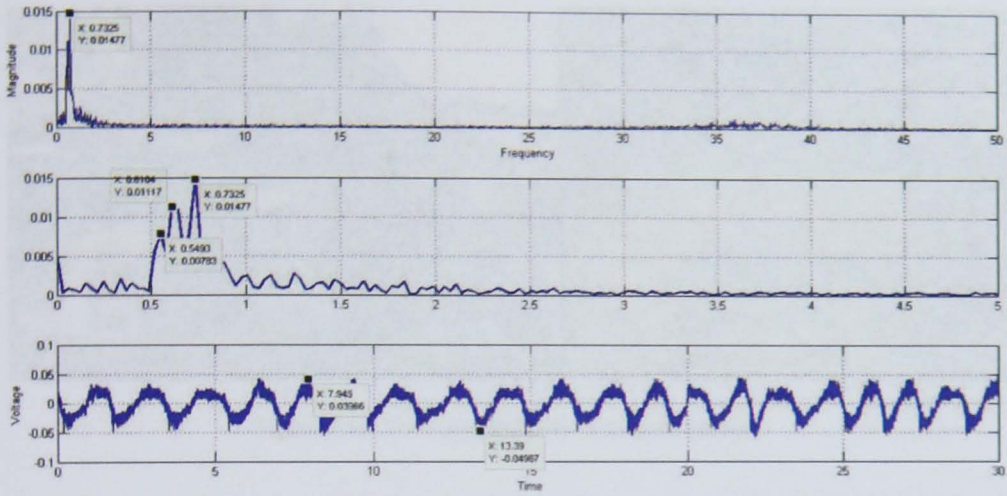


Figure 7.16: Sensor circuit output response for a steady manual oscillation input in the range 0.5 1Hz. Time and frequency axes have units of seconds and hertz respectively.

on. Capacitors also have temperature-dependent properties. Most critical for this application are the equivalent resistances which were particularly high for the ceramic capacitor used up to this point.

A 10 pF polystyrene capacitor intended for low loss replaced the 6.8 pF. This change stabilised the charge amplifier circuit, but with the 5 Hz signal remaining small.

The final change was to increase the feedback resistance to a nominal 5 G Ω , decreasing the high-pass filter pole to 3.2 Hz. Figure 7.16 shows the resultant sensor signal for a steady manual oscillation input in the range 0.5 Hz to 1 Hz. The frequency analysis shows a clear low-frequency cluster of peaks consistent with the slight variation in frequency of the raw signal. The half-sine trace of partial contact of the mechanical oscillator upon the artefact during each cycle is evident.

7.3.7 Quasistatic operation

7.3.7.1 Test system

The demonstration of sensor operation below 1 Hz prompted return to the Physik Instrumente Nanocube nanopositioner for further evaluation work. A simple arrangement consisting of a modified pair of metal forceps attached to the working surface of the nanopositioner (see figure 7.17) facilitated generation of artefact deflections in a way compatible with the noise enclosure. Indeed it appears that any useful application of the current artefacts will

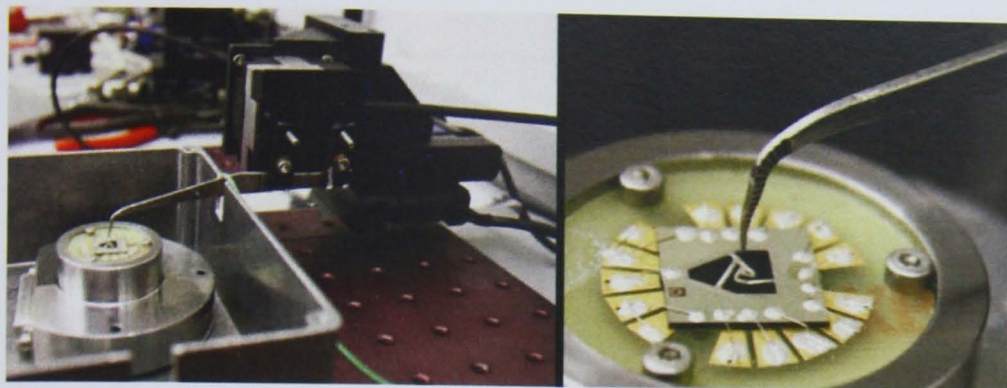


Figure 7.17: The nanopositioner actuation system.

involve this form of interface. The enclosure lid was replaced after initial alignment, for which the Physik Instrumente 5 mm-range coarse stage axes were used.

A National Instruments ADC/DAC interface device (NI USB-6009) permitted software generation of closed-loop displacement targets for the nanopositioner, to allow automation of motion. The NI interface limited the range of motion to $50\ \mu\text{m}$ and was found to ultimately limit the scope of the device evaluation, as will be discussed in section 7.3.7.4. Initial experiments were undertaken to confirm that the charge amplifier circuit could not 'see' the motion of the nanocube, but rather only the resultant mechanical input once in contact.

7.3.7.2 Initial square-wave tests

For the purposes of resolving a useful signal from a noisy background, a well-defined signature in frequency space is ideal. This fact motivated the use of reference mechanical resonators in the characterisation reported so far. To evaluate efforts to minimise charge leakage and resultant drift, however, a square or triangular waveform studied in the time domain is more useful.

Initial experiments with the final charge amplifier circuit from section 7.3.6 (feedback resistance $5\ \text{G}\Omega$) showed large peaks at the edges of a $0.5\ \text{Hz}$, $10\ \mu\text{m}$ square wave mechanical input, dissipating each time within $0.5\ \text{s}$ (figure 7.18). A further multistep experiment indicated a proportional relationship between mechanical and sensor step size (Figure 7.19). It might be possible to use such a circuit and appropriate analysis software to sum a series of such peaks to track incremental displacement, but it is likely that the result would be highly dependent on the exact abruptness used. Figure 7.20 compares the sensor response to similar-frequency, equal-amplitude square and triangle inputs. The latter is an order of magnitude smaller than the former.

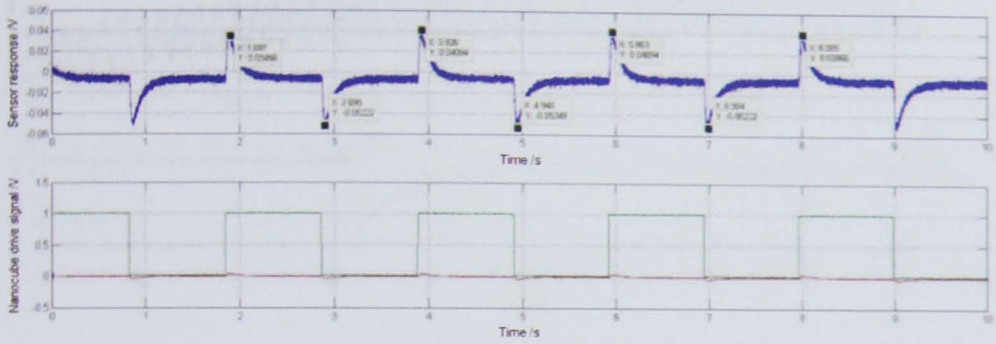


Figure 7.18: Sensor response using section 7.3.6 circuit under square wave input. One volt supplied to the nanopositioner will command a ten micrometre move in closed-loop operation.

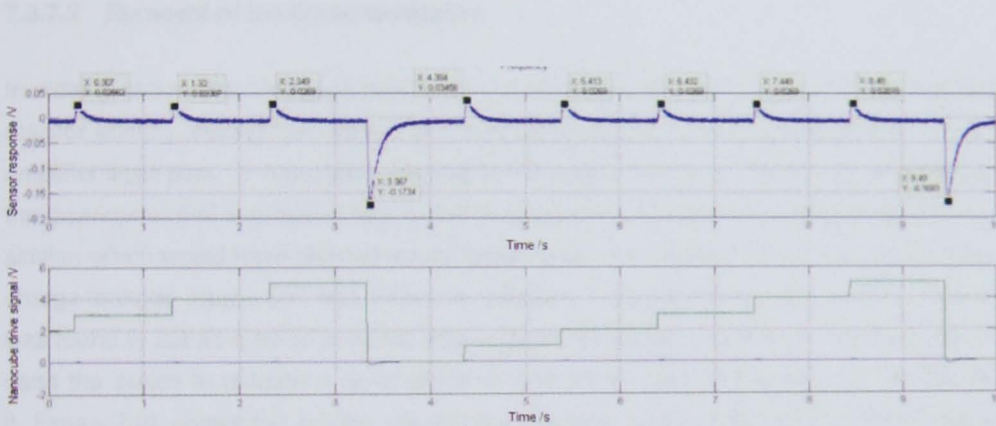


Figure 7.19: Sensor response using section 7.3.6 circuit under stepped input.

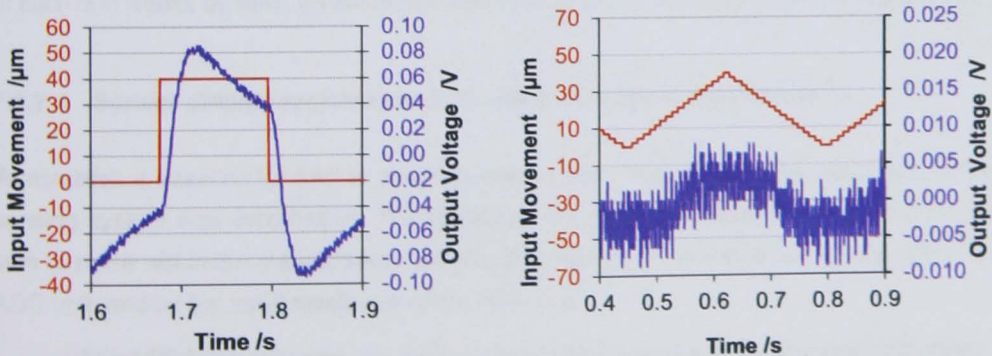


Figure 7.20: Response of initial circuit to square (left) and triangle (right) wave input displacements.

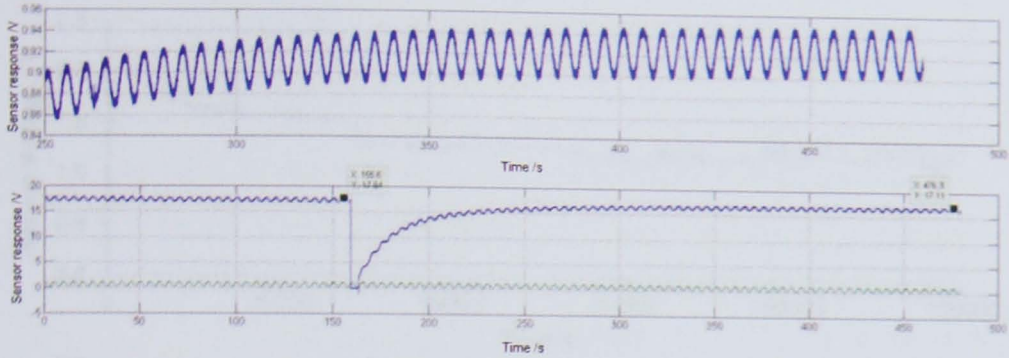


Figure 7.21: Sensor-charge amplifier response to a sinusoidal mechanical input, showing effect of use of the feedback capacitor reset button. The top plot shows detail of the lower plot.

7.3.7.3 Removal of feedback resistance

In order to reduce the high-pass pole further, the decision was taken to remove the feedback resistor entirely, setting the system to a limit defined by the PCB resistance between the amplifier input pins. To repeatably initialise the charge amplifier feedback loop necessitated the development of a suitable reset switch arrangement. Solutions involving transistors and similar, which would have allowed for automatic reset-on-saturation action, would introduce charge-leakage routes and was therefore rejected. A simple mechanical switch, however, was found to act as a noise antenna when placed for human interaction. The best solution used the switch to actuate a relay, which in turn briefly shorted the capacitor to initialise it. Figure 7.21 shows the system resuming a previous steady state around three minutes after use of the reset button. The response to a sinusoidal artefact actuation is overlaid for reference. Figure 7.22 demonstrates typical longer term behaviour: a rise to an apparent point of long-term stability followed by slow but significant drift and later instability. The level of such drift would, by itself, preclude the use of the artefacts for calibrated force comparison.

7.3.7.4 Sensor circuit resolution and vibration sensitivity determination

To establish a baseline for further characterisation work, the background noise level in the sensing system was established. The resolution of the sensor system was limited by the sum of noise within the measurement bandwidth, whether received by artefact, amplifier or ADC unit, and by the input resolution of the ADC unit.

The ADC/DAC unit used, the National Instruments USB-6009, incorporates fourteen-bit ADCs with a range of ± 10 V and hence a resolution of 1.2 mV; the ADC accuracy is about 1.4 %. The accompanying DAC channels produce a voltage in the range 0 V to 5 V with a

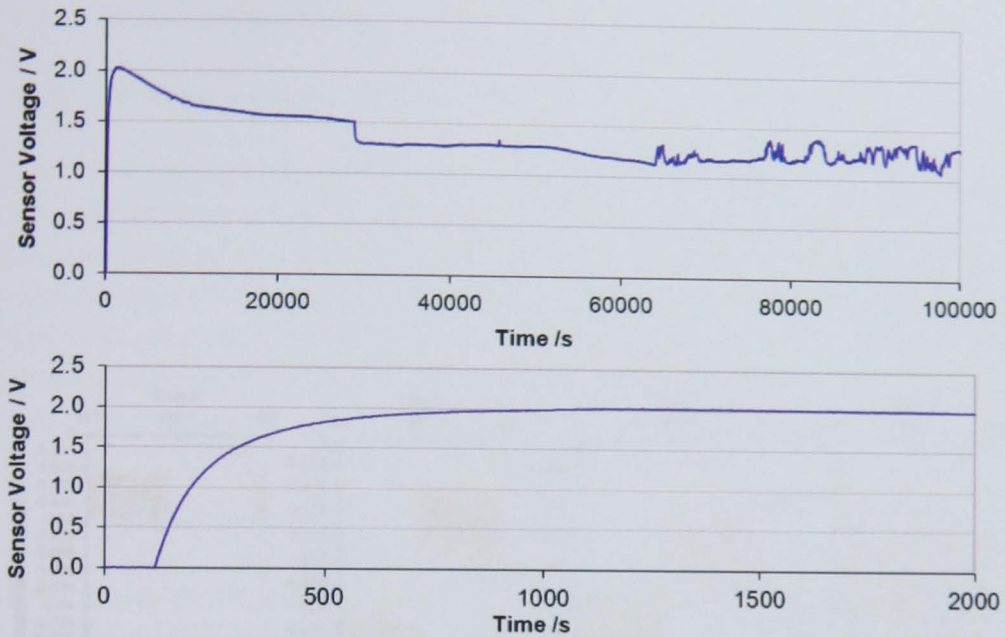


Figure 7.22: Evaluation of the long-term behaviour of the charge amplifier circuit. One day equates to about 82 ks. The simplicity of the lower plot, taken from the upper plot, emphasises the danger of assumptions about long-term behaviour.

twelve-bit resolution, giving a resolution of 1.2 mV also; the output accuracy is 7 mV or 0.1 % of full range.

Figure 7.23 summarises an attempt to define a resolution by progressively decreasing the mechanical input until no longer resolvable; a steady state statistical method would also have provided a measure of resolution. The upper plots show the drive signal from a DAC monitored by an ADC on the same device. The discrete bands have standard deviations on the order 3 mV; this would equate to a maximum nanopositioner position jitter of 30 nm, which is on the same order as the nanopositioner's repeatability. The standard deviation on the sensor input signal noise as shown was around 12 mV. The individual noise source contributions were not clear but from prior experience the ADC unit was expected to have a significant contribution. Figure 7.23 suggests that for small amplitudes the DAC output was non-linear and produced a smaller-than-expected target shift; the demonstration was limited by the ADC/DAC unit. For large amplitudes the driving signal was much cleaner than the sensed signal, implying that the amplifier circuit noise dominated. An independent confirmation of the nanopositioner motion would have added confidence to interpretation of this data.

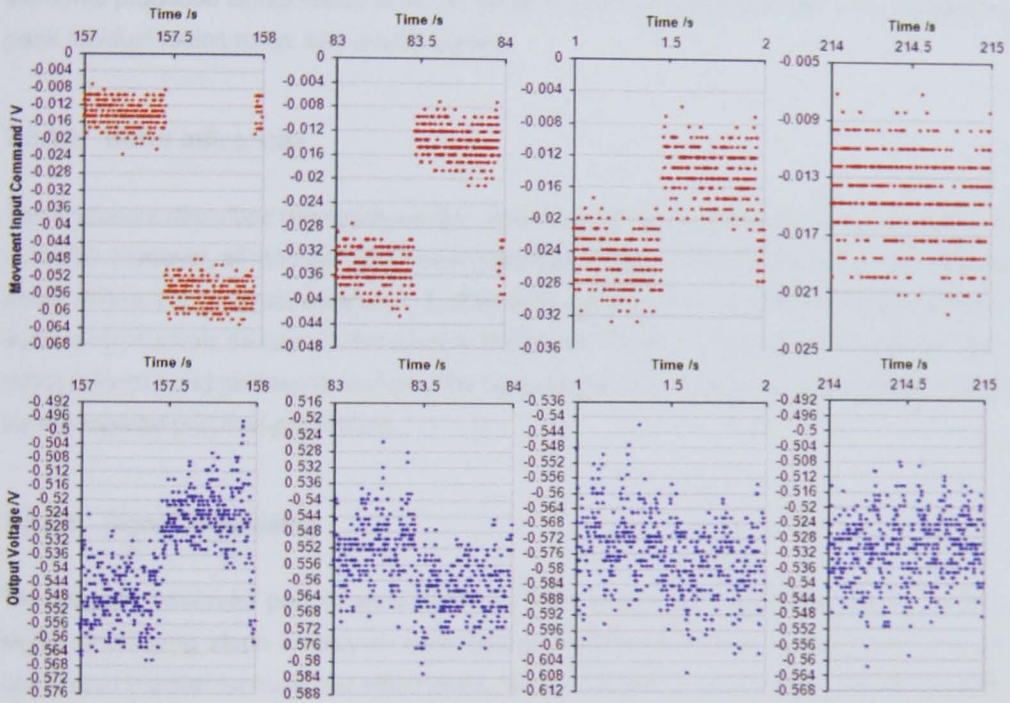


Figure 7.23: Driving signal and sensor response signals in response to 1 Hz motion commands with intended amplitudes 500 nm, 300 nm, 200 nm and 100 nm respectively from left to right.

7.3.8 General comments on influences upon the circuit

7.3.8.1 Variation between device sensors

Earlier work (section 7.3.2) highlighted significant variation and occasional gross discrepancies in performance across the array of actuators and sensors for a given artefact, most likely due to fabrication defects. The variation seen using each element to excite vibration was echoed by sensor response variation during the tuning fork experiments. In an experiment in which well-performing elements produced a sensor signal of around 3 V peak to peak, other elements produced signal levels of 50 mV peak to peak against which the 100 mV peak to peak residual mains noise was clearly visible.

7.3.8.2 Noise influences

The enclosure described previously significantly reduced the contributions of external electrical noise. However, all mechanical and electronic connections into the enclosure re-introduced noise. Whilst it is no doubt possible to further optimise the artefact's own circuitry to prevent such reintroduction, sensor performance is likely to be highly dependent on the nature, operating principle and packaging format of the target instrument, a dependency that is not ideal for widespread practical application.

7.3.8.3 Signal processing

The ultimate observed performance of the artefact sensor will be affected by the sensor signal processing steps employed. Both charge amplifier and final interface will have an associated transfer function, the effect of the former component dominating. Additional software steps also modify the signal. The evaluation work presented here has benefited from a well-defined input frequency, for which an equivalent-pole software band-pass filter or tone measurement could be applied. The broader bandwidth associated with a real application would reduce the effectiveness of noise rejection measures. This would support the use of the artefact at a low (0.1 Hz to 1 Hz) but well-defined frequency.

Brief attempts to implement a low-pass filter to smooth signal noise resulted in unacceptable phase shifts; a higher order filter might have had greater success. In any case, in the author's experience better results can be obtained from statistical analysis of key metrics obtained from unfiltered data.

7.3.8.4 Power supply limitations

To minimise the impact of mains noise upon the sensor circuit, batteries were used to power the circuit amplifier. Gradual reduction of battery supply voltage over time should not scale the output signal, which is dependent only upon the feedback capacitor, but will gradually reduce the saturation limits and working range of the circuit. For the brand of 9 V cells used, a 150 mV drop was observed in the first twenty-four hours from new with an exponential trend. Such behaviour is reasonable given the sink properties of the interface box but will be battery-specific.

7.4 Verification experiments

7.4.1 Expected behaviour

Based on preliminary results, the artefacts were not expected to perform in a manner appropriate for a low force artefact. For the purposes of the narrative and future comparison, however, the dependence of force sensitivity upon artefact deflection amplitude and rate was evaluated.

For the perfect artefact-circuit system, the change in output voltage should be proportional to the change in artefact deflection. The constant of proportionality, the displacement sensitivity, should be independent of amplitude or speed. In addition, the sensitivity should be repeatable under constant amplitude and velocity. It was expected that, in practice, there would be a finite repeatability due to drift, a speed dependence due to filtering and charge losses, and non-linear behaviour for small amplitudes due to hysteresis.

7.4.2 Initial overview

In the first instance, a set of seven experiments were undertaken varying combinations of either amplitude or velocity, using triangular waveforms to quickly iterate parameters. Table 7.2 summarises the experiments and figure 7.24 presents the related waveforms. The experiments were undertaken with artefact D. The collection of experiments are combined in the displacement-voltage plot figure 7.25. Overlying noise and drift are apparent; however, the consistency of gradient across the set was sufficient to warrant further evaluation.

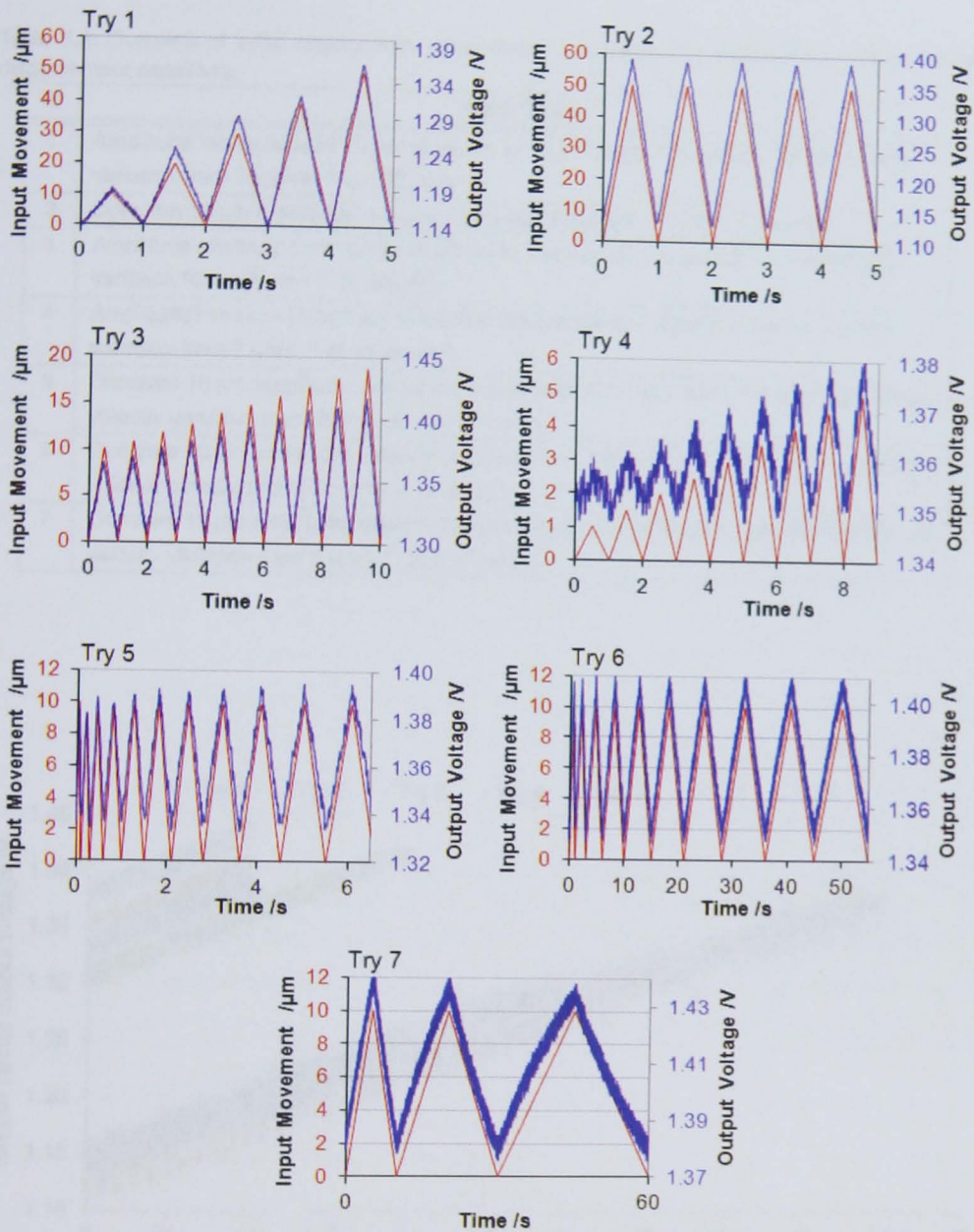


Figure 7.24: Results of initial experiments undertaken on artefact D to evaluate the stability of the displacement sensitivity. The input movement is the commanded nanopositioner displacement step calculated from the change in command voltage; it was not independently verified.

Table 7.2: Overview of initial experiments undertaken on artefact D to evaluate the stability of the displacement sensitivity.

ID	Description
1	Amplitude increase from 10 μm to 50 μm in 10 μm steps, 1 s period; hence, velocity variation from 20 $\mu\text{m s}^{-1}$ to 100 $\mu\text{m s}^{-1}$.
2	Constant 50 μm amplitude, 1 s period; hence, constant 100 $\mu\text{m s}^{-1}$ velocity.
3	Amplitude increase from 10 μm to 20 μm in 1 μm steps, 1 s period; hence, velocity variation from 20 $\mu\text{m s}^{-1}$ to 40 $\mu\text{m s}^{-1}$.
4	Amplitude increase from 1 μm to 5 μm in 0.5 μm steps, 1 s period; hence, velocity variation from 2 $\mu\text{m s}^{-1}$ to 10 $\mu\text{m s}^{-1}$.
5	Constant 10 μm amplitude, period increased from 0.1 s to 1 s in 0.1 s intervals; hence, velocity variation from 200 $\mu\text{m s}^{-1}$ to 20 $\mu\text{m s}^{-1}$.
6	Constant 10 μm amplitude, period increased from 1 s to 10 s in 11 s intervals; hence, velocity variation from 20 $\mu\text{m s}^{-1}$ to 2 $\mu\text{m s}^{-1}$.
7	Constant 10 μm amplitude, period increased from 10 s to 13 s in 10 s intervals; hence, velocity variation from 2 $\mu\text{m s}^{-1}$ to 0.67 $\mu\text{m s}^{-1}$.

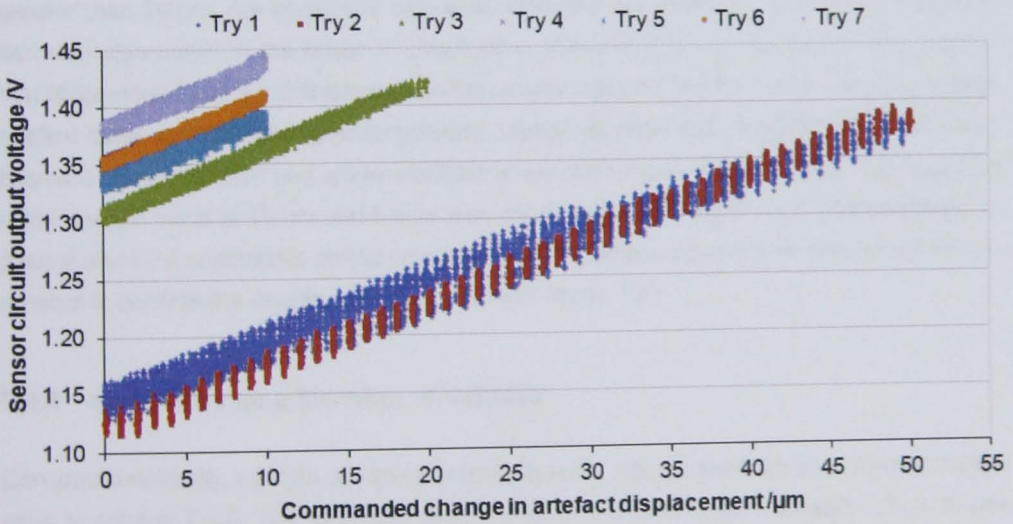


Figure 7.25: Displacement-sensor voltage plot for collection of initial experiments.

7.4.3 Sensitivity as a function of artefact displacement amplitude

To quantify the variation in sensitivity as a function of amplitude, a series of constant speed, constant amplitude experiments were undertaken, using triangle-wave target displacement waveforms as above. The constant velocity specified for all was $10 \mu\text{m s}^{-1}$, equivalent to the peak velocity of a $1.6 \mu\text{m}$ amplitude, 1 Hz sinusoidal displacement trajectory. The displacement amplitude specification was increased in $5 \mu\text{m}$ steps for each successive experiment, between $5 \mu\text{m}$ and $50 \mu\text{m}$. For each experiment, at least twenty-five repeats were completed.

Since direction-dependent effects such as hysteresis and one-way drift was expected in the experimental data, the data were separated by direction and a least-squares linear fit applied to the linear region of each traversal of the range. Figure 7.26 shows example fit parameter data for the $5 \mu\text{m}$ experiment. Error bars are based on the statistical errors associated with the mathematical fit. It was not clear what caused the event between the thirty-fifth and fortieth loops. The slight separation between offset curves indicated background drift occurring in each period.

Figure 7.27 summarises the results of the remainder of the experimentation. Error bars are the standard error in the mean of all gradient estimates for the direction of motion for a given amplitude and do not include the obvious systematic effects in the system. Despite consistently stable gradients within each experiment in line with figure 7.26, the data show a factor of two variation across the range of amplitudes. It is noticeable that for amplitudes greater than $20 \mu\text{m}$, the sensitivity estimates separate per direction. An increased separation was also noted in the linear fit offset value above the $20 \mu\text{m}$ threshold. It is possible that differences in beam stiffness across the artefact caused the hub to tilt under a centrally applied force, and that at higher amplitudes, lateral slippage both modified the relationship between nanopositioner and artefact deflection and introduced friction effects. The apparent initial upward trend at $20 \mu\text{m}$ and below was not thought to be significant. Unfortunately, logistical and time constraints on the project prevented repeat experiments with an alternative artefact to confirm the results, which conflict with figure 7.25.

7.4.4 Sensitivity as a function of velocity

Constant amplitude, variable speed experiments were also undertaken in a manner analogous to section 7.4.3. The experiments undertaken are summarised in table 7.3; a $20 \mu\text{m}$ amplitude was used for all experiments except for two low-speed instances in series two, in order to limit the duration of those two experiments. Series one through three were completed with artefact D; series four used artefact G. Artefact G, which was supplied to NPL

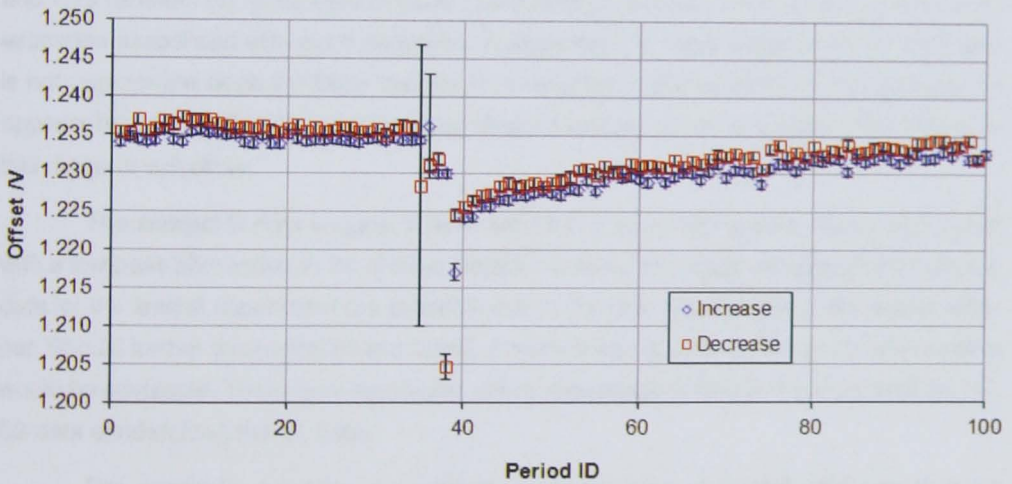
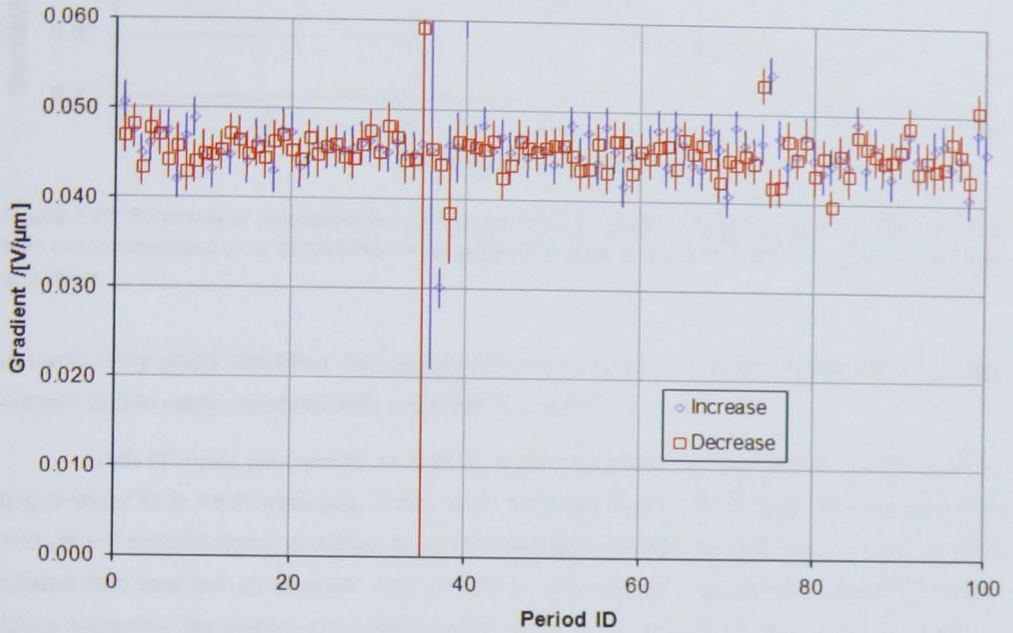


Figure 7.26: Example gradient linear fit data for $5 \mu\text{m}$ amplitude, $10 \mu\text{m s}^{-1}$ artefact deflection experiment, artefact D.

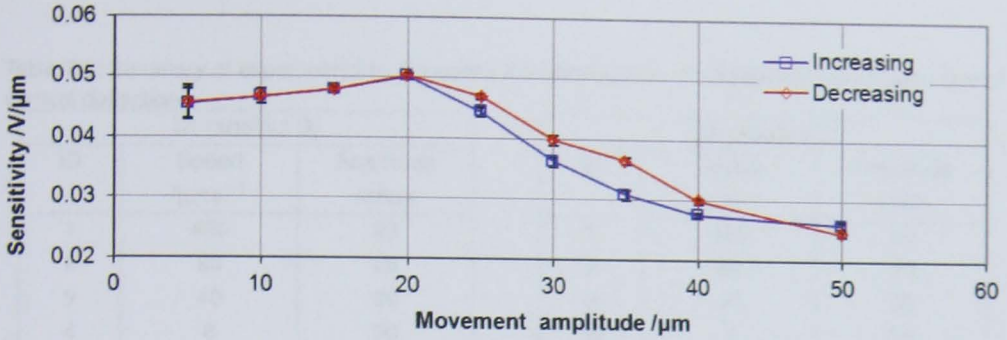


Figure 7.27: Summary of calculated sensitivity as a function of artefact displacement amplitude. Error bars are the standard error in the mean of all gradient estimates for the direction of motion for a given amplitude.

in particularly good condition, had previously been reserved for later application, but was chosen due to early concerns with the artefact D data.

Data analysis proceeded as before, separating data by direction of motion and fitting a linear fit to each traversal. It was clear from the hysteresis in data for speeds above $100 \mu\text{m s}^{-1}$ that the nanopositioner could not track the provided targetting command, and the related data was not considered. The sensitivity estimates and associated statistical uncertainty estimates derived from the fitting process are summarised in figures 7.28 (artefact D) and 7.29 (artefact G). Error bars indicate one standard deviation in the spread of sensitivity estimates associated with each datapoint. A calculation of the standard error of the mean is not appropriate since it is likely that the true variation of the sensitivity is being shown. It appears that, for artefact D, there is no significant dependence upon direction of motion over this range of velocities.

The artefact D data suggest a downward trend in sensitivity with velocity consistent with a low-pass filter action in the charge amplifier circuit. The increased spread of artefact D data for the fastest experiment are probably due to the finite capabilities of the nanopositioner. Should further evaluation be warranted, a more sophisticated motion generation system would be advisable. There is no resolvable effect of passage of time in the data, with the S2, S3 data sandwiching the S1 data.

The sensitivity estimates for artefact G are an order of magnitude larger than for artefact D, suggesting higher performance levels and a better-quality artefact. The data show a decrease in sensitivity with increased speed, consistent with the observations for artefact D. Whilst the sensitivity estimates for motion in the direction of decreasing deflection are consistently lower than those for the direction of increasing deflection, the offset is within one standard deviation of most datapoints.

Table 7.3: Summary of experiments to determine the dependence of artefact sensitivity upon rate of vertical deflection.

S1 (artefact D)		
ID	Speed / $\mu\text{m s}^{-1}$	Amplitude /micm
1	400	20
2	80	20
3	40	20
4	8	20
5	4	20
6	800	20
7	4000	20

S2 (artefact D)		
ID	Speed / $\mu\text{m s}^{-1}$	Amplitude /micm
1	400	20
2	80	20
3	40	20
4#	4	10
5#	2	10
6	800	20

NB. Series S2, S3 were undertaken

approximately three days after series S1.

S3 (artefact D) and S4 (artefact G)		
ID	Speed / $\mu\text{m s}^{-1}$	Amplitude /micm
0	800	20
1	400	20
2	80	20
3	40	20
4	4	20
5	2	20

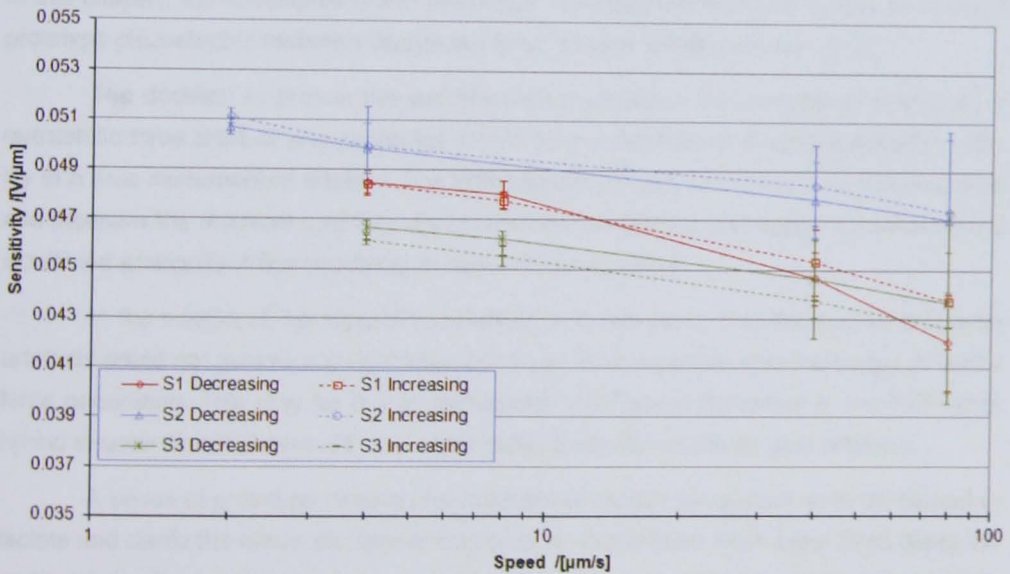


Figure 7.28: Summary of experiment series S1, S2 and S3 to determine the dependence of displacement sensitivity upon rate of artefact deflection. Data for increasing and decreasing artefact deflection are shown separately. Series are connected for readability and not necessarily to infer a trend.

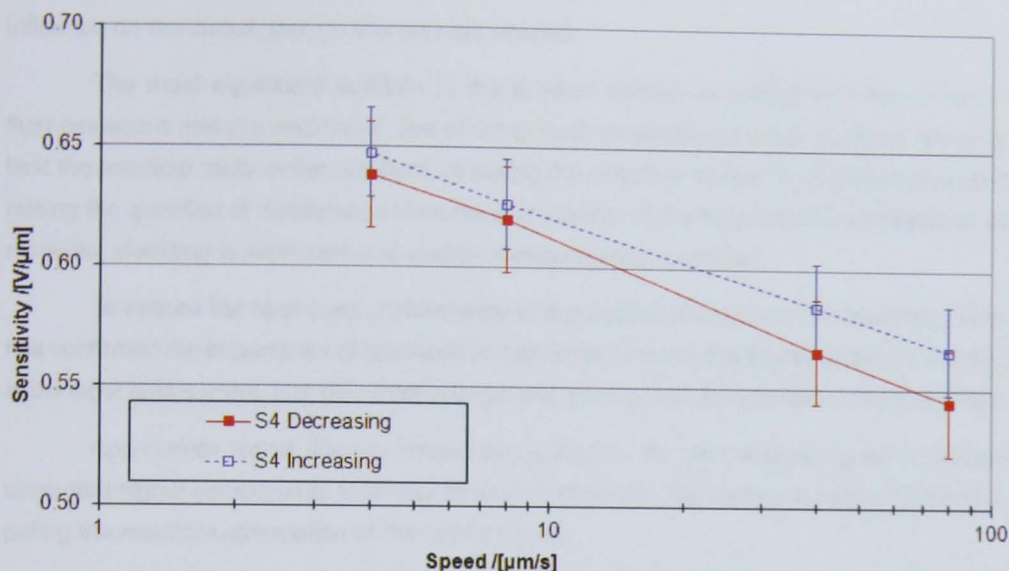


Figure 7.29: Summary of experiment series S4 to determine the dependence of displacement sensitivity upon rate of artefact G deflection. Data for increasing and decreasing artefact deflection are shown separately. Series are connected for readability and not necessarily to infer a trend.

7.5 Conclusions

In this chapter, the development and evaluation of instrumentation and control for a set of prototype piezoelectric triskelion flexure low force transfer artefacts is described.

The decision to pursue the unconventional choice of the piezoelectric effect for a quasistatic force artefact was motivated in part by the promise of direct self-deflection ability in a thus-instrumented artefact. The ability to self-deflect, to internally generate a force and measure the resultant collinear, equal deflection of artefact and target, would remove a significant ambiguity in the operation of current force artefacts.

In the course of the reported investigation it was found that the current prototype artefacts could not generate a significant deflection and were therefore incapable of useful force generation. This may be due to unforeseen mechanical behaviour in the PZT-nickel hybrid structure inconsistent with that of similarly dimensioned silicon-type artefacts.

A series of prototype circuits and mechanical motion generators were developed to isolate and clarify the electronic sensor response to well-defined mechanical input along the vertical axis of the artefact. In doing so, key influences upon the circuit have been identified and, where possible, their effects minimised. These influences include, in approximate order of significance: 50 Hz mains supply interference; nearby charge sources; external illumination; humidity variation; and RF noise. Temperature was also expected to have some

influence on the circuit, though this was not verified.

The most significant addition to the artefact system to control external noise influences was a metallic enclosure. The effect of such an enclosure does, however, severely limit the practical utility of the artefacts, breaking the effective artefact size requirement and raising the question of interference from the end effector of the target instrument itself. In all respects, shielding is important and worthy of investment to optimise.

To ensure the best-case performance of a piezoelectric sensor, the described work has confirmed the importance of appropriate component choice. For the amplifier, for example, a low input bias current, low DC offset voltage and good noise characteristics are important.

Appropriate signal filtering should be applied to the raw charge signal to remove unwanted signal components that may otherwise dominate the sensor signal, whilst anticipating the resultant attenuation of the useful signal.

Final performance verification experiments indicate that, whilst the developed sensor-circuit system is capable of producing an approximate analogue of the vertical deflection of the artefact, accuracy and repeatability fall well below that which might reasonably be expected from, for example, piezoresistive strain gauges. It can reasonably be concluded based on the findings of this chapter that even in the best case, the current artefact concept is unlikely to be made reliable and cost-effective under the constraints of the present application.

The observation of fabrication defects on the chips would support non-linear behaviour and the observed inconsistent performance between sensors on an artefact. Further, trends such as the decrease in sensor displacement sensitivity with device speed may be solvable with further circuit optimisation. However, the observed variation and noise in the sensitivity data alone ensures that the technology does not meet the stability demands of the ideal low force transfer artefact.

It is, therefore, recommended that an alternative technology be selected to instrument the triskelion flexure in any future artefact design.

Chapter 8

Conclusions

The general aim of the work described in this thesis was to complete the NPL Low Force Facility in order to create an accessible route to traceability for the measurement of small forces in the UK. The facility was to benefit, in particular, nanometrologists and users of nanotechnology in UK industry and academia.

To conclude on the degree to which this general aim has been achieved, it is necessary to consider the individual objectives defined in section 1.2.

The first key strand of the described work was to upgrade, commission and verify the performance of the LFB, to act as the primary source of traceability for 10 nN to 30 μ N forces.

8.1 Achievement of objectives

Objective 1.1 It was hypothesised that initial force measurement drifts of up to 60 % were caused by surface charging effects on the dielectric vane of the LFB mechanism. The LFB feedback controller was successfully rewritten to modulate a DC controller output with a high-frequency carrier, whilst maintaining phase between plate voltages to effect a constant DC force. The controller hardware was extensively redesigned and built to amplify propagate the AC signal from controller to LFB plates. This objective was therefore successfully achieved.

Objective 1.2 A high-speed FPGA lissajoux phase counter was incorporated into the LFB controller to enable full, continuous fringe counting operation for the LFB z interferometer. This objective was therefore successfully met. A direct comparison with another traceable displacement interferometer is recommended.

Objective 1.3 A vibration isolation table and acoustic enclosure were procured and installed, and significantly reduced unwanted medium-to-high frequency inputs to the LFB system. However, the resultant need to site the displacement interferometer laser on a cantilevered platform outside the enclosure may have affected the low-frequency stability of the LFB. A fibre laser feed to the interferometer is the only realistic solution to be applied in the future. This objective was therefore partially achieved.

Objective 1.4 A procedure for measurement of the capacitance gradients of the LFB was established. In doing so, a better understanding of the non-linearities in the nominally constant capacitance gradients was established. An appreciation of position-dependent non-linearities is essential for specifying the required capability of an absolute displacement reference for the LFB displacement interferometer.

The possibility of indirect measurement of the plate voltages, that is, traceability of the generated plate voltages via pre-calibration, was investigated and rejected. Direct, calibrated, synchronised measurement of the three AC voltages supplied to the plates must form the basis of a successful voltage measurement procedure. Objective 1.4 was successfully achieved.

Objective 1.5 Measurement of the weight of small masses on the LFB were compared to independent mass-traceable calibrations and were used to quantify the systematic uncertainty associated with indirect measurement of voltage (see above). This work was analogous to a comparison carried out at NIST that also led to the correction of a key systematic uncertainty. Objective 1.5 was therefore met.

Objective 1.6 The performance of the LFB was compared to the equivalent facilities at laboratories worldwide. To do this, the force sensitivity and spring constant of a commercial cantilever were measured at each facility in turn, and the results compared. The LFB measurements agreed with the results from the other facilities within quoted uncertainties. Further experimentation would have yielded more useful information on uncertainty in the operation on the LFB. Nevertheless, this objective was broadly met.

Strand two was to develop an improved transfer artefact flexure design based on the triskelion concept.

Objective 2.1 A targeted review was undertaken of the state-of-the-art in flexure design, as well as relevant fabrication techniques. Particular attention was paid to precedent arte-

facts at other NMIs. The strengths and weaknesses of the common rectangular-cantilever artefact format were considered. Objective 2.1 was successfully achieved.

Objective 2.2 Based on the flexure design and fabrication review, the triskelion flexure concept was selected as the basis for a novel flexure design, achieving objective 2.2.

Objectives 2.3, 2.4 An analytical model of the triskelion flexure was developed for low force measurement based on similar reported models. The model incorporated several first-order approximations to limit the computational complexity for later artefact performance predictions. A complementary finite-element model was also developed, and parameterised to allow comparison with the analytical model.

A comparison of results from the two models supports the following conclusions. The analytical model satisfactorily predicts the vertical spring constant of the triskelion, that is, along the nominal single degree of freedom of the flexure design. The analytical model performed much more poorly when predicting the parasitic compliance of the remaining degrees of freedom of the artefact hub centre, due to mathematical over-constraints. The performance of the analytical model also decreases when the triskelion geometry is set such that the 'thin flexure' approximation no longer holds.

An extension of the analytical model to consider the response to lateral forces was undertaken. A linear combination of lateral and rotational compliance of the artefact hub top face centre did not conclusively account for the differences between predicted behaviour from the simple analytical and finite element models.

It can therefore be concluded that the analytical model is suitable for rapid initial geometry parameter value selection for a given target spring constant, but that verification of the chosen parameter values using finite element analysis should be undertaken where possible to better understand both linear and non-linear behaviour.

The key common weakness of both models is the representation of the combined material properties of the laminated artefact structure. A suitable extension of the model to reflect the nickel-PZT layer structure should be incorporated in future. Nevertheless, the current analytical model can be used to rapidly establish bounds on the artefact spring constant based on all-nickel and all-PZT construction in turn. Objectives 2.3 and 2.4 were therefore achieved, though there is plenty of scope for additional model functionality.

Objective 2.5 A suite of prototype triskelion artefacts was fabricated in collaboration with Cranfield University. The known fabrication method from the NPL microprobe device was

deliberately employed to reduce the fabrication risk and to produce artefacts suitable sized for in-depth performance evaluation. A range of triskelion dimensions were specified to produce a range of spring constants and to verify the models. The analytical model was used to predict the spring constants of the devices.

The delivered suite of artefacts contained a large number of defects and a very low yield rate. This influenced the results of the below experimental objectives. Objective 2.5 was therefore only partially achieved.

Objective 2.6 The performance of selected members of the suite of prototype artefacts was evaluated and compared with modelled behaviour. A low-cost parallel flexure cantilever was successfully developed to extrapolate the force measurement range of the LFB to that of the prototype artefacts.

The ratios of experimentally measured spring constants of three representative artefacts broadly agreed with ratios from the finite element and analytical models. Discrepancies were attributed to the fabrication defects and variation in flexure thickness across each artefact. It is difficult to draw conclusions on the comparison of modelled and measured spring constants for these artefacts. Objective 2.6 was achieved.

The third strand of the project was to evaluate the suitability of the piezoelectric effect for traceably calibratable quasistatic force sensors for low forces. If suitable, the sensors could be used with the triskelion flexure to form a complete artefact to complete the traceability chain.

Objective 3.1 A review of the state-of-the-art in on-board strain sensing in microfabricated flexures was undertaken with the aim of identifying promising candidates for use in a low force artefact. The piezoresistive effect was identified as the most suitable sense-only technique, having been exploited by other NMIs with low force measurement capabilities.

Nevertheless, the piezoelectric effect was identified as a candidate for strain generation, required to avoid a key displacement ambiguity in the use of the artefacts. Objective 3.1 was successfully achieved.

Objective 3.2 A sensor circuit was developed capable of detecting the electronic response of the piezoelectric elements on the prototype artefacts to quasistatic flexure deflection. The circuit was developed iteratively, demonstrating operation at flexure resonance, at 230 Hz, at around 30 Hz, and under quasistatic motion equivalent to 0.1 Hz to 1 Hz. Based on

the correspondence between features of the recorded sensor signal and generated pure-mechanical input to the flexures, it can be concluded that the circuit could detect the strain of the flexure via the piezoelectric film. That is, it can be concluded that parasitic electronics interactions related specifically to motion generation were not responsible for the detected signals. Objective 3.2 was therefore met.

Objectives 3.3, 3.4 Initial experiments clearly indicated that the prototype artefacts were incapable of useful quasistatic strain generation, and this intended functionality was not pursued further.

Experimental comparisons of sensor output to known quasistatic mechanical strain inputs were undertaken. The developed sensor-circuit system is capable of producing an approximate analogue of quasistatic deflection of the prototype artefact flexure. However, the accuracy and repeatability fall well below the requirements for a calibratable transfer artefact. It can reasonably be concluded based on the experimental findings that even in the best case the current artefact concept is unlikely to be made reliable and cost-effective under the constraints of the present applications.

It is noted that further improvements could be implemented to reduce the effect of spurious noise sources and systematic effects such as performance variation across a set of nominally identical sensors.

Nevertheless, it can be reasonably concluded that the piezoelectric effect should not be considered further for use in low force transfer artefacts. It is therefore recommended that an alternative technology be selected to instrument the triskelion flexure in any future design. Objectives 3.3 and 3.4 have been achieved.

8.2 Overall conclusions

Based on the above analysis it is evident that the majority of the objectives for this thesis have been achieved. The LFB has been upgraded, commissioned and independently verified. A flexure design concept for a transfer artefact for use with the LFB has been proposed and modelled, with the models experimentally confirmed. The piezoelectric effect has been successfully evaluated for use for traceable quasistatic force measurement, and conclusively rejected in favour of established techniques. In summary, it can be concluded that, whilst the NPL Low Force Facility is not yet complete, the reported work has placed NPL in a strong position to do so in the near future.

8.3 Recommendations

Since the motivation for low force metrology remains clear and increasing, it is highly recommended that efforts continue to complete the traceable low force facility at NPL. The following chapter will present the recommendations for the transfer artefact in the form of a proposed design. The priority with the LFB is to fully understand all sources of uncertainty in operation, including quantification of those in the interaction of an artefact or other sensor with the balance. A key component of this work will be in the form of future comparisons with other laboratories. Further iterations of low force transfer artefacts should form the medium of such comparisons.

Chapter 9

Recommendations for a future working low force transfer artefact

The conclusions to the investigative chapters of this thesis presented in chapter 8 may be applied to the design of an improved low force transfer artefact suitable for end use. Presented in this chapter are the recommendations of the author for such an artefact.

9.1 Overview of recommended design

The proposed modified low-force transfer artefact system would have the following key features. It would retain the triskelion flexure design of the earlier prototypes in light of the symmetry benefits presented earlier. The triskelion flexure design would be instrumented with piezoresistive deflection sensors, choosing a more reliable strain sensing technology at the cost of the possibility of direct strain generation. To achieve strain generation, the artefact will be supplied with a precision nanopositioner stage of suitable specification. Provided the nanopositioner can be appropriately calibrated, the artefact metrology system is then closed and independent of user equipment. However, optional compatibility with user-supplied nanopositioners, particularly at other NMIs, will be maintained. The following sections explain how this summary function might be achieved.

9.2 Flexure fabrication

The central zone of stiffness insensitivity to contact misalignment, due to the symmetry of the triskelion, is very attractive, and it is expected that any future devices would use the same

flexure geometry.

To maintain the isotropic stiffness required for symmetry, nickel would continue to be used, or a suitable replacement found. The nickel beam flexures have also shown resilience to over-loading, in situations where a silicon flexure would have shattered. This would likely increase the working life of each artefact, provided that over-loading did not change the mechanical properties of the artefact significantly. One point to clarify would be the consequence of material choice to beam flexure thickness uncertainty and uniformity due to fabrication constraints at the chosen fabrication partner.

The author understands from communications with the current fabrication partner that it can be challenging to attach films correctly to the nickel plating, representing a risk to development.

It is also necessary to find a suitable piezoresistive film with the correct gauge factor and isotropic behaviour. One option might be to use selectively-doped polycrystalline silicon deposited on the nickel flexures. Suitably-prepared polycrystalline silicon should be isotropic in bulk, though the validity of this bulk approximation for small film thicknesses should be considered. It is not clear what thickness would be required or what resultant displacement sensitivity would be achievable.

If it is not possible to design an isotropic piezoresistively-instrumented triskelion flexure, an alternative four-legged geometry could be specified. Beam flexures and lines of symmetry would be aligned with crystal planes of a (non-isotropic) silicon wafer to maintain symmetry of mechanical response. Beam flexure lengths would then be scaled with effective material properties for that direction of alignment. Piezoresistive sensors would then be added using standard doping methods also used for the NIST and PTB piezoresistive cantilevers discussed in section 5.2.1.2.

9.3 Flexure dimensions and related performance

The required artefact and flexure dimensions are dictated by the intended range of operation of the artefact. It was noted previously that uncertainties associated with the calibration of current low force sensors is at the 0.1 % level. In order to at least meet this uncertainty level, the use of at least two artefact force ranges is suggested to cover the range of the LFB. The upper range would have a maximum force of 50 μN , repeatability and linearity at the 50 nN level, and a resolution of around 5 nN; the lower range would have a maximum force of 1 μN , repeatability and linearity at the 1 nN level, and a resolution of around 1 pN. This latter device would also enable future intercomparisons between NMIs.

In addition to the subdivision of the LFB force range above, it is necessary to support a range of target instrument spring constants. Further user consultation would be advisable, but in the first instance, artefacts for each decade of stiffness from 0.1 Nm^{-1} to 100 Nm^{-1} should cover the majority of applications.

Without knowledge of the replacement device layer required to implement piezoresistive sensing, it is not yet possible to use the models developed earlier to define exact artefact dimensions for a given force range. Any optimisation effort would, however, follow the same route.

Total effective vertical artefact stiffness will be defined predominantly by the length of the beam flexures and the thickness of the nickel layer of the beam flexures. Because the uncertainties and variation in final fabricated dimensions are typically absolute and independent of dimension, longer, thicker beam flexures could be specified to achieve the same total stiffness with lower relative uncertainties. Since beam flexure length is constrained by packaging size limits, it would be best to maximise beam length and adjust beam thickness to suit.

The theoretical force range is defined by the stiffness of the artefact flexures and by the maximum permissible vertical deflection for the given flexure length. The maximum deflection would be set by the sensor range or linear region, itself tuned to cover some fraction of the flexure elastic zone.

To ensure a linear force-displacement characteristic and a constant stiffness within the required range-resolution window, second order bending effects would need to be minimised. From inspection of the triskelion design informed by standard texts (e.g. [123]) two non-linear effects become apparent, each of which is dependent upon the elbow angle, labelled as β_0 in section 6.2.1 (see figure 6.3). When β_0 equals 0° (straight legs) or 180° (folded legs), the beam flexures must stretch laterally to accommodate an out-of-plane deflection. When β_0 is in the region of 90° , the hub centre rotates to allow the lateral projection of the flexure to shorten as it is deflected out of plane. This minimises the beam flexure stretching effect but introduces a lateral bending stiffness at the hub that is highly dependent upon beam width. The author understands that the current choice of β_0 aimed to optimise the contribution of these two non-linear effects, though this was not confirmed. In any case, such non-linear effects should be modelled using a finite-element approach and optimised to bring stiffness non-linearities below the specified threshold.

9.4 Piezoresistive sensors and control electronics

The current prototype artefacts have sensors at both inner and outer ends of the beam flexures. This was intended to offer redundancy and has helped to circumvent fabrication flaws. However, the connection along the beam to the inner pad is itself particularly vulnerable to flaws, and occupied valuable beam width once minimum track separations were set. If fabrication yield rate can be improved then redundancy would only be required for noise reduction, and omission may be simpler.

It is expected that, due to fabrication limitations, each beam flexure will have a different deflection sensitivity, and, in combination with beam stiffness inequalities, a different force sensitivity. Each sensor would be connected to an independent Wheatstone bridge, voltage amplifier and ADC circuit. Standard sixteen-bit ADCs give a resolution of less than 0.003 % of full sensor force range which is likely to be significantly better than other measures of device performance such as linearity and repeatability. Repeatability is typically the ultimate limiting factor on the calibration of a self-sensing transfer artefact such as the one proposed.

Thermal variation is a significant source of uncertainty for piezoresistive sensors. The artefact chip would incorporate an additional resistive element to function as a temperature reference probe, of the form used by the PTB artefacts shown in section 5.2.1.2. An independent circuit would monitor the temperature analogue and automatically correct the sensor signals.

9.5 Interpretation of signals

In principle, the triskelion is a platform suspended on three independent, parallel linear springs. For a single, vertical force applied to the hub centre, three independent analogues of the applied force are created. If the contact location is misaligned, the three independent force measures will adjust accordingly, indicating the additional moment. If the displacement sensitivities of the three legs are known, under this approximation of independence, three heights are known and the plane of the artefact hub can be deduced.

In practice, the three legs are not independent. Even if only one elbow is displaced vertically whilst the other two are constrained in the vertical direction, the effective stiffness of the deflected beam will be influenced by the torsional stiffness of the other beams. However, the correlation between sensor responses should be repeatable and, therefore, characterisable.

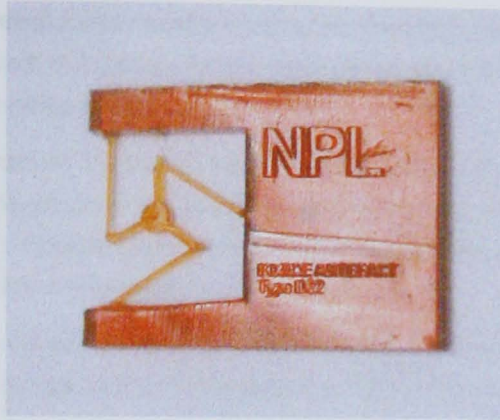


Figure 9.1: A rapid-prototyped artefact demonstrator designed by the author and produced by the University of Nottingham showing a likely packaging format for the low force artefact. The dimensions are 10 mm × 7 mm × 1 mm.

One experiment to be included in the commissioning of each artefact would, therefore, be to build a sensor response map as a function of contact point over the area of the hub centre, using the LFB as the force reference. If displacement measurement is also required, it should be possible to use a fast optical imaging system to map the displacement and tilt of the hub centre as a function of alignment. This data would then be used automatically by the artefact software to calculate misalignment and effective applied force in application. If the final artefact stage is used for this work, it should be possible to absorb certain repeatable systematic errors into the correction maps. The final stage should be suitable also for this experiment.

9.6 Packaging

In view of the work reviewed and reported in this document, including discussions with experts in the low force metrology community, the following artefact packaging requirements will be important to enable practical use of the artefacts.

The chip forming the substrate for the artefact must have a shape compatible with interfacing devices. A chip width no more than 10 mm is recommended, with electronics placed together to one side of the artefact. Figure 9.1 demonstrates the general shape to be considered.

The contact surface at the hub centre should be aligned co-planar with the surface of the chip to allow close approach to target instruments and minimal tilt for interface. This is likely to mean that the sensors and their connections will be in the same plane as contact.

Consequently the electrical contact pads should be removed from the vicinity of the triskelion and any connections kept to minimum height. The limit on connection track length may be defined by increases in noise sensitivity.

In some applications it is useful to measure the stiffness of the measurement loop. This is done by applying a force to a rigid part of the chip close to the same axial position as the force sensor platen. Fiducial marks will be located on the supporting arms of the chip to improve alignment for this measurement.

Finally, to keep the sensors clean and safe until installed and ready to use, the sensor would incorporate a dust-cap, in the manner demonstrated in figure 5.15.

9.7 External motion stage requirements

The external motion stage must satisfy three criteria, summarised in the following paragraphs.

The stage must move the artefact over the required range with the required resolution and repeatability. The stage positioning specifications translate to force specifications via the artefact stiffness (or that combined with any series compliance, as discussed below). If stage motion is only required to generate an artefact deflection and hence a reaction force, then stability in position is essential and good repeatability and resolution convenient for operation. If spring constant is to be calibrated then stage sensor accuracy and sensor resolution becomes essential, in addition to stability.

Single-axis stages with suitable performance characteristics are readily available from commercial suppliers. For example, the P-772 from Physik Instrumente [185] has a quoted range of 10 μm with a sub-100 pm resolution; its resonant frequency should be sufficiently high to average out jitter in position. The question remains whether the cost associated with such a stage allows the total artefact package to remain affordable.

The stage must incorporate an optional vertical series compliance to facilitate interaction with the LFB. This additional compliance would also have the effect of increasing the effective stage resolution by dividing the displacement. Should it be necessary to know the series stiffness of the metrology loop, for example to allow spring constant calibration, then it should be possible to isolate and measure that stiffness. If the motion stage and all fixtures are provided with the sensor, then to some extent metrology loop compliance can be incorporated into automatic software corrections through prior calibration. In section 9.6 the inclusion of fiducial marks for this purpose was discussed.

The stage must not exhibit significant compliance in any other axis, and should assist with angular alignment. The primary purpose of this is to minimise and fix the cosine error term in the uncertainty budget associated with the use of the artefacts.

Aspects of the preceding sections are summarised in the concept drawing figure 9.2. The key labelled features are as follows. Supported on a rigid immovable surface or equivalent coarse positioning system (A) is a modular low force artefact system consisting of a precision vertical motion stage (B), an optional series flexure (C), the artefact chip holder (F) and the replaceable artefact chip (H). Electrical connections (D) would need to be very compliant in order not to affect the behaviour of (C). However, (C) could be replaced with a rigid connector as required. Low profile clips (G) achieve mechanical and electrical connections between (F) and (H). (I) is an optional dust and safety jacket for the artefact flexure (M). (J) represents an interfacing instrument such as the LFB. Clustered away from the working part of the artefact chip are the electrical connections; the number shown would be for a half-bridge arrangement plus connections for the temperature sensor (L). The restraining contact clips would need to have a total stiffness (N) several orders of magnitude higher than that of the artefact flexure. It is suggested that tipless instruments (represented by cantilever (P)) would approach from above, where a small tip or sphere could be installed, whereas instruments with styli or tips (represented by (Q), such as the LFB, would contact the artefact from either vertical direction.

9.8 Uncertainty in operation

In most respects, the uncertainty analysis for the proposed low force artefact is similar to that presented for the Kleindiek commercial force sensor in section 3.10. Without experimental data to derive estimates from, it is not possible to complete an uncertainty budget for an artefact concept. However, key differences from the Kleindiek example can be discussed as follows. The most significant change is the introduction of temperature correction and multiple parallel sensors in the form of the three legs.

In the Kleindiek calculation, relating to measurements undertaken at an NMI, temperature was assumed to vary within tight environmental control tolerances, and uncertainties estimated accordingly. With the provision of a temperature sensor and the likelihood of operation in more general environments, the measured temperature can be used to apply a known correction or indicate an uncertainty contribution for live user feedback. A temperature correction would be ideal, since most research and industrial users would be able to achieve a stable if uncalibrated temperature. However, such a correction factor would have an associated uncertainty.

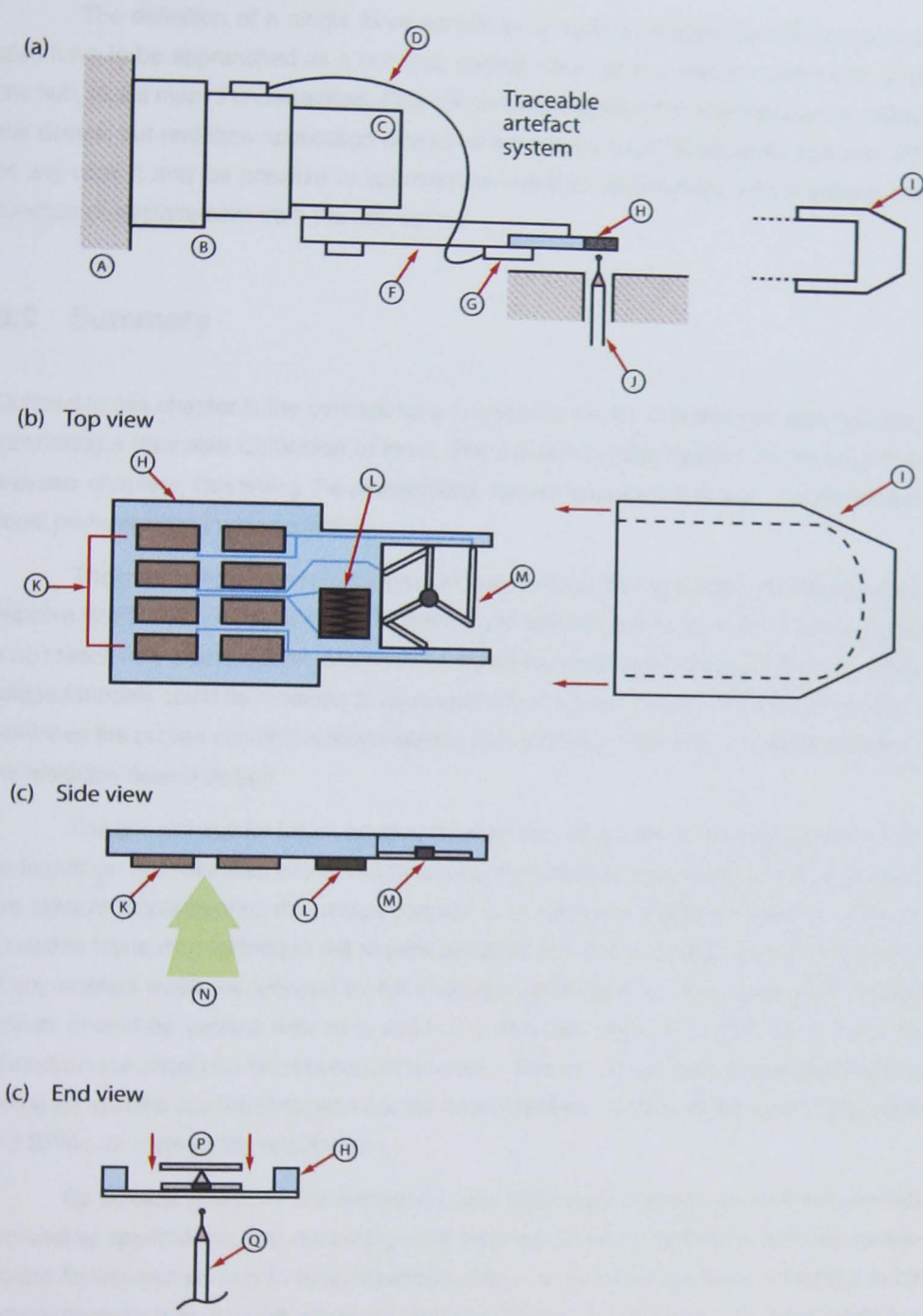


Figure 9.2: A concept sketch for a better traceable low force artefact: (a) overview of artefact system including artefact module and external positioning stage; (b) top view of artefact chip showing location of electronic contacts and artefact; (c) side view of the same; and (d) cross-sectional end view through the hub centre with suggested instrument contact modes. The labelled items are explained in the text.

The definition of a single force sensitivity or spring constant for the device would also have to be approached as a nominal, central value, plus a map of corrections across the hub, plus a map of uncertainties. This will certainly increase the time required to calibrate the device, but real-time application of such error maps should be trivial for standard PCs. In any case it may be possible to approximate variation satisfactorily with a second-order function of displacement from the hub centre.

9.9 Summary

Outlined in this chapter is the concept for a functioning low force artefact system capable of transferring a traceable calibration of force. The concept brings together the findings of the previous chapters, discarding the piezoelectric sensor approach in favour of more conventional piezoresistive instrumentation.

The most critical barrier to success is likely to be in finding a nickel-compatible piezoresistive film that is suitably isotropic in mechanical and electrical properties. However, there is no reason why a pure-silicon design could not be implemented to mitigate this risk; the developed models could be modified to represent a four-legged design. The presented design combines the proven concept of strain-sensor plus external stage with a novel application of the triskelion flexure design.

The general aim for future artefact development should be to devise a suitable, high-performance, cost-effective way of instrumenting the triskelion flexure design with piezoresistive sensors, implementing the design concept outlined in this chapter. The development of a suitable fabrication technique will require collaboration with a suitable partner. Fabrication of any artefact would be followed by full characterisation at NPL. The developed triskelion models should be verified with early artefact prototypes, and the models used to set the fabrication specifications for subsequent artefacts. This would facilitate artefact performance tuning for specific applications, whether for nanoindenters, surface topography instruments and SPMs, or more exotic applications.

As suitable artefacts are developed, and third-party alternatives identified for less demanding applications, the remaining core task would be to develop a suitable measurement facility and service to bring traceable micro- to nanonewton force metrology to UK nanotechnology industry and academia. Suitable licence agreements with appropriate instrument manufacturers would accelerate this process significantly.

Appendix A

Summary of surface interaction forces

A full derivation of the surface interaction forces significant at the MEMS scale is beyond the scope of this document, and indeed has been presented by various groups previously. Nevertheless the basic force separation dependencies are worthy of consideration by the reader and a selection are presented in table A.1. Equations obtained from referenced works have, where necessary, been adapted to use common nomenclature. To simplify comparison, the interaction of a sphere and flat plate is considered where possible. Since the tips of most probes can be adequately modelled as a (hemi-) sphere, this is a suitable approach. The sphere-plate separation is assumed to be much less than the sphere radius. Figure A.1 is a comparative plot using typical values for the given parameters.

Table A.1: Summary of surface interaction force equations. In these equations F is a force component, U the work function difference between the materials, D the sphere-flat separation, γ the free surface energies at state boundaries, and H the Hamaker constant. In the capillary force the step function $u(\cdot)$ describes the breaking separation; e is the liquid layer thickness and r the radius of meniscus curvature in the gap. θ , the contact angle of in-interface liquid on the opposing solid surfaces, is assumed to be approximately zero (wet).

Interaction	Equation
Electrostatic (based on [186])	$F = -\epsilon_0 U^2 \pi \frac{R^2}{D^2}$
Capillary [186, 187]	$F = 4\pi\gamma R \left(1 - \frac{h-2e}{2r}\right) \cdot u(-h+L)$
Van der Waals, for non-retarded, attractive forces [188]	$F = -\frac{HR}{6D^2}$
Casimir effect [117]	$F = -\frac{R\pi^3 h c}{360D^3}$

Appendix B

Analytical model of triboelectric contact mechanics: MATLAB code

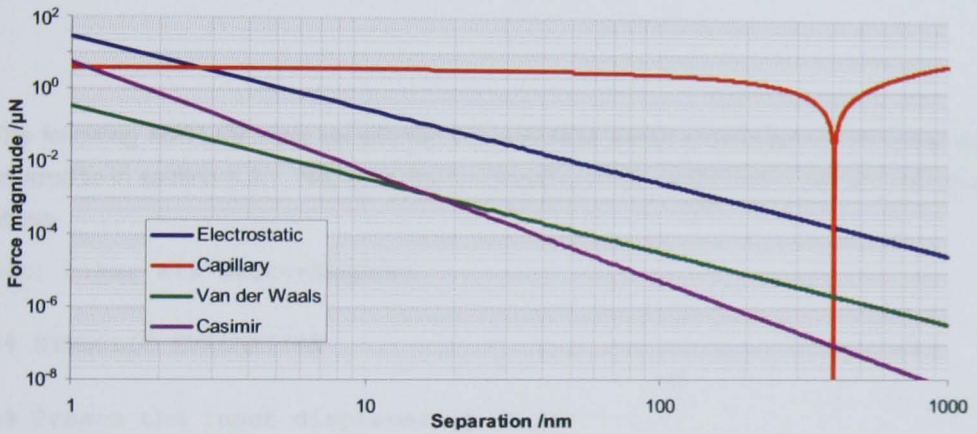


Figure A.1: Comparative plot of described surface interaction forces, based on the following values: $R = 2 \mu\text{m}$; $U = 0.5 \text{ V}$; $\gamma = 72 \text{ mJ m}^{-2}$; $H = 10^{-18} \text{ J}$; $e = r = 100 \text{ nm}$. Physical constants take their standard values: $\epsilon_0 = 8.854 \times 10^{-12} \text{ C}^2 \text{ N}^{-1} \text{ m}^{-1}$; $\hbar = 1.055 \times 10^{-34} \text{ m}^2 \text{ kg s}^{-1}$ and $c = 3 \times 10^8 \text{ m s}^{-1}$.

Appendix B

Analytical model of triskelion flexure mechanics: MATLAB code

The following MATLAB code constitutes the analytical model developed for the work and referred to in section 6.2.1. Not all of the functionality in the model code has been reported above.

```
clc; clear all %#ok<SAGROW>

%% SYMBOLIC EVALUATION

%% Create the input displacement $X_0$
display('### Create input displacement X_0')

syms x0 y0 z0 thx0 thy0 thz0

X0 = [x0; y0; z0; thx0; thy0; thz0];
X00= [0; 0; 0; 0; 0; 0];
% we will later set x0 y0 thz0 to zero when values are provided

%% Derive tilt $A_{\{Ii\}}$ and translation $A_{\{IIIi\}}$ to arm ends
display(...
    '### Derive tilt A_{Ii} and translation A_{IIIi} to arm ends')

syms a ap1 ap2 ap3 % define arm length and alphas
ap = [ap1 ap2 ap3];

for i = 1:3
    AI{i} = [ 1      0      0      0      0      0; ...
```



```

0      1      0      0      0      0; ...
0      0      1  a*sin(ap(i)) a*cos(ap(i)) 0; ...
0      0      0      1      0      0; ...
0      0      0      0      1      0; ...
0      0      0      0      0      1]; ...

AII{i}= [ a*cos(ap(i)); ...
a*sin(ap(i)); ...
0; ...
0; ...
0; ...
0];

end

%% Derive rotation into beam coords $B_{i}$
display('### Derive rotation into beam coords B_{i}')

syms be1 be2 be3 % define arm length and alphas
be = [be1 be2 be3];

for i = 1:3
    B{i} = [ cos(be(i))  sin(be(i))  0      0      0      0; ...
-sin(be(i))  cos(be(i))  0      0      0      0; ...
0      0      1      0      0      0; ...
0      0      0  cos(be(i))  sin(be(i))  0; ...
0      0      0 -sin(be(i))  cos(be(i))  0; ...
0      0      0      0      0      1]; ...
end

%% Derive stiffness matrix $k$
display('### Derive stiffness matrix k')

syms E G l w t
%G = double(50e+9); E = double(120e+9);

k55 = (G*(t^2)/E)*(1/3 - (((0.21*t)/w)*(1 - (t^4)/(12*w^4))));

kmat = [ (w/l)^2      0      0      0      0  -(w^2)/(2*1); ...
0      1      0      0      0      0 ; ...
0      0      (t/l)^2      (t^2)/(2*1)  0      0 ; ...

```

```

          0          0 (t^2)/(2*1)    (t^2)/3    0          0          ;...
          0          0          0          0          k55        0          ;...
    -(w^2)/(2*1)  0          0          0          0          0          ((w^2)/3) ];

k = ((E*t*w)/1) * kmat;

%% Apply $A_{Ii}$, $A_{III}$, $B_i$ and $k$ to $X_0$
display('### Apply AI, AII, B and k to X_0')

for i = 1:3
    Xa{i} = AI{i}*X0 + AII{i};
    Xa0{i} = AI{i}*X00 + AII{i};
    Xb{i} = B{i}*Xa{i};
    Xb0{i} = B{i}*Xa0{i};
    Pb{i} = k*(Xb{i}-Xb0{i});

                                % Use A\b instead of inv(A)*b ?
    Pa{i} = inv(B{i}) * Pb{i};
    %Pa2{i} = Pb{i} \ B{i}; % matrix divide, equiv. to B^-1 * Pb

    P0i{i} = inv(AI{i}) * (Pa{i}-AII{i});
    %P0i2{i} = (Pa{i}-AII{i}) \ AI{i};
end

P0 = P0i{1} + P0i{2} + P0i{3};

%% Substitute in actual values for symbolic variables
% Note that the displacement input X_0 is not specified until later.
display(...)
    ['### Substitute in actual values for symbolic variables (not X_0)']

% Device properties
    % material
    E = 210e+9;
    G = 76e+9;

    %arm info
    a = 21e-6;

    %angles
    ap1 = 0; ap2 = (2/3)*pi; ap3 = (4/3)*pi;
    be0 = (2/3)*pi;
    be1 = ap1+be0; be2 = ap2+be0; be3 = ap3+be0;

```

```

        %beam dimensions
l = 200e-6;
w = 10e-6;
t = 1e-6;
Ltip = 20e-6; % stylus length

%% Evaluate $P_0$

display('### Evaluate P_0 in terms of X_0')
P0eval = eval(P0); %evaluate P_0 as a function of X_0 (messy exact output)

% display('--- P_0, evaluated to 12 s.f.:')
% P0ev12 = vpa(P0eval,12) % evaluate new P0eval to 6 sig. fig. and display
% pretty(P0ev12) % redraw P0ev6 in 'pretty' format
% display(' ')

display('--- P_0, evaluated to 3 s.f.:')
P0ev3 = vpa(P0eval,3) % evaluate new P0eval to 2 sig. fig. and display
pretty(P0ev3) % redraw P0ev6 in 'pretty' format
display(' ')

display(['L= ' num2str(l)])
display(['A= ' num2str(a)])
display(['W= ' num2str(w)])
display(['T= ' num2str(t)])

%% Derive stresses, strains
display('### Derive stresses, strains')

for i = 1:3
    % sigma
    sig(i) = 6*(P0i{i}(3)-P0i{i}(6))/(w*t^2); % i.e. 6*(F_zi-M_zi)/wt^2
    % epsilon
    sig(i+3) = sig(i)/E;
end
%sig(:)

%pretty(vpa(eval(sig')))
%display(' ')

```

```

%% Derive stiffness summary
display('### Calculate stiffness summary ###')

coeff=coeffs(P0ev3(1),x0); kx = coeff(1); % FIX THESE MANUAL
coeff=coeffs(P0ev3(2),y0); ky = coeff(1); % ASSIGNMENTS
coeff=coeffs(P0ev3(3),z0); kz = coeff(2);
coeff=coeffs(P0ev3(4),thx0); lamxx = coeff(2);
coeff=coeffs(P0ev3(4),thy0); lamxy = coeff(2);
coeff=coeffs(P0ev3(5),thx0); lamyx = coeff(2);
coeff=coeffs(P0ev3(5),thy0); lamyy = coeff(2);
coeff=coeffs(P0ev3(6),thz0); lamz = coeff(1);

kxrot = lamxy/(Ltip^2);
kyrot = lamyx/(Ltip^2);

ktip = [kxrot; kyrot; kz]; ktip=abs(eval(ktip))

%% NUMERICAL EVALUATION
% New code added 26JAN2010

%% Create trial input displacement(s) $X_0$

X0 = [1e-6, 1e-6, 1e-6, 0, 0, 0]';

%% Derive tilt $A_{Ii}$ and translation $A_{IIIi}$ to arm ends
display(...)
    '### Derive tilt $A_{Ii}$ and translation $A_{IIIi}$ to arm ends')

% redefine arm length and alphas numerically
ap = [ap1 ap2 ap3];

for i = 1:3
    AI{i} = [ 1      0      0      0      0      0; ...
             0      1      0      0      0      0; ...
             0      0      1  a*sin(ap(i)) a*cos(ap(i)) 0; ...
             0      0      0      1      0      0; ...
             0      0      0      0      1      0; ...
             0      0      0      0      0      1]; ...
    AII{i} = [ a*cos(ap(i)); ...
              a*sin(ap(i)); ...
              0; ...
              0; ...

```

```

        0; ...
        0];
end

%% Derive rotation into beam coords $B_{i}$
display('### Derive rotation into beam coords B_{i}')

% redefine beam angles numerically
be = [be1 be2 be3];

for i = 1:3
    B{i} = [ cos(be(i))  sin(be(i))  0      0      0      0; ...
            -sin(be(i))  cos(be(i))  0      0      0      0; ...
            0            0          1      0      0      0; ...
            0            0          0      cos(be(i))  sin(be(i))  0; ...
            0            0          0     -sin(be(i))  cos(be(i))  0; ...
            0            0          0      0          0      1]; ...
end

%% Derive stiffness matrix $k$
display('### Derive stiffness matrix k')

k55 = (G*(t^2)/E)*(1/3 - (((0.21*t)/w)*(1 - (t^4)/(12*w^4))));

kmat = [ (w/l)^2      0      0      0      0      -(w^2)/(2*l); ...
        0            1      0      0      0      0      ; ...
        0            0      (t/l)^2  (t^2)/(2*l)  0      0      ; ...
        0            0      (t^2)/(2*l)  (t^2)/3  0      0      ; ...
        0            0      0          0          0      k55      0      ; ...
        -(w^2)/(2*l)  0      0          0          0      0      ((w^2)/3) ];

k = ((E*t*w)/l) * kmat;

%% Apply $A_{Ii}$, $A_{IIIi}$, $B_i$ and $k$ to $X_0$
display('### Apply AI, AII, B and k to X_0')

for i = 1:3
    i;
    Xa{i} = AI{i}*X0 + AII{i}; Xa{i};
    Xa0{i} = AI{i}*X00 + AII{i}; Xa0{i};
    Xb{i} = B{i}*Xa{i}; Xb{i};
    Xb0{i} = B{i}*Xa0{i}; Xb0{i};
end

```

```

    Pb{i} = k*(Xb{i}-Xb0{i}); Pb{i};
    Pa{i} = inv(B{i}) * Pb{i}; Pa{i};
    P0i{i} = inv(AI{i}) * (Pa{i}-AII{i});
    %P0i2{i}= (Pa{i}-AII{i}) \ AI{i};
    P0i{i};
end

P0 = P0i{1} + P0i{2} + P0i{3}
K0 = P0./X0

display('### Run complete ')

```

Bibliography

- [1] Clifford C A and Seah M P 2005 The determination of atomic force microscope cantilever spring constants via dimensional methods for nanomechanical analysis *Nanotechnology* **16** 1666–1680 ISSN 0957-4484 URL <http://iopscience.iop.org/0957-4484/16/9/044/>
- [2] Burnham N a, Chen X, Hodges C S, Matei G a, Thoreson E J, Roberts C J, Davies M C and Tendler S J B 2003 Comparison of calibration methods for atomic-force microscopy cantilevers *Nanotechnology* **14** 1–6 ISSN 0957-4484 URL <http://iopscience.iop.org/0957-4484/14/1/301/>
- [3] NanoWorld AG Products catalogue for AFM tips URL www.nanosensors.com/products_catalog.html
- [4] Leach R K, Claverley J D, Giusca C L, Jones C W, Nimishakavi L, Sun W, Tedaldi M and Yacoot A 2012 Advances in engineering nanometrology at the National Physical Laboratory *Measurement Science and Technology to be publ*
- [5] Pratt J R, Kramar J, Newell D and Smith D T 2005 Review of SI traceable force metrology for instrumented indentation and atomic force microscopy *Measurement Science and Technology* **16** 2129 ISSN 0957-0233 URL <http://iopscience.iop.org/0957-0233/16/11/002>
- [6] Mettler Toledo AG 2010 Weighing Components Catalog 2010/11
- [7] Cumpson P J and Hedley J 2003 Accurate force measurement in the atomic force microscope: a microfabricated array of reference springs for easy cantilever calibration *Nanotechnology* **14** 918–924 ISSN 0957-4484 URL <http://iopscience.iop.org/0957-4484/14/8/314>
- [8] Cumpson P J, Hedley J and Clifford C A 2005 Microelectromechanical device for lateral force calibration in the atomic force microscope: Lateral electrical nanobalance

- Journal of Vacuum Science & Technology B: Microelectronics and Nanometer Structures* **23** 1992 ISSN 0734211X URL <http://link.aip.org/link/JVTBD9/v23/i5/p1992/s1&Agg=doi>
- [9] Rief M 1997 Reversible Unfolding of Individual Titin Immunoglobulin Domains by AFM *Science* **276** 1109–1112 ISSN 00368075 URL <http://www.sciencemag.org/cgi/doi/10.1126/science.276.5315.1109>
- [10] Viani M B, Schaeffer T E, Chand A, Rief M, Gaub H E and Hansma P K 1999 Small cantilevers for force spectroscopy of single molecules *Journal of Applied Physics* **86** 2258 ISSN 00218979 URL http://jap.aip.org/resource/1/japiau/v86/i4/p2258_s1
- [11] Kleindiek Nanotechnik GmbH Force measurement system URL <http://www.nanotechnik.com/fms-em.html>
- [12] Gates R S and Pratt J R 2006 Prototype cantilevers for SI-traceable nanonewton force calibration *Measurement Science and Technology* **17** 2852–2860 ISSN 0957-0233 URL <http://stacks.iop.org/0957-0233/17/i=10/a=041><http://stacks.iop.org/0957-0233/17/i=10/a=041?key=crossref.462ef42194fffc648c1f6e30d4fc147>
- [13] Veeco Probes 'CLFC - Force Calibration Cantilevers' product specification URL https://www.veecoprobes.com/probe_detail.asp?ClassID=9
- [14] Tortonese M, Barrett R C and Quate C F 1993 Atomic resolution with an atomic force microscope using piezoresistive detection *Applied Physics Letters* **62** 834 ISSN 00036951 URL <http://link.aip.org/link/APPLAB/v62/i8/p834/s1&Agg=doi>
- [15] Cumpson P J, Clifford C A and Hedley J 2004 Quantitative analytical atomic force microscopy: a cantilever reference device for easy and accurate AFM spring-constant calibration *Measurement Science and Technology* **15** 1337–1346 ISSN 0957-0233 URL <http://iopscience.iop.org/0957-0233/15/7/016/>
- [16] Behrens I, Doering L and Peiner E 2003 Piezoresistive cantilever as portable micro force calibration standard *Journal of Micromechanics and Microengineering* **13** S171–S177 ISSN 0960-1317 URL <http://stacks.iop.org/0960-1317/13/i=4/a=325?key=crossref.df4a2f39187dcf64b0c9bb4787617cd3>

- [17] Kim M S and Pratt J R 2010 SI traceability: Current status and future trends for forces below 10 microNewtons *Measurement* **43** 169–182 ISSN 02632241 URL <http://linkinghub.elsevier.com/retrieve/pii/S0263224109001961>
- [18] Pratt J R, Kramar J, Shaw G A, Gates R S and Rice P New reference standards and artifacts for nanoscale property characterization *nsti.org* URL <http://www.nsti.org/Nanotech2006/showabstract.html?absno=914>
- [19] Villanueva G, Perezmurano F, Zimmermann M, Lichtenberg J and Bausells J 2006 Piezoresistive cantilevers in a commercial CMOS technology for intermolecular force detection *Microelectronic Engineering* **83** 1302–1305 ISSN 01679317 URL <http://linkinghub.elsevier.com/retrieve/pii/S0167931706002796>
- [20] PI (Physik Instrumente) GmbH & Co KG P-602 PiezoMove Flexure Actuator with High Stiffness URL <http://www.physikinstrumente.com/en/products/prdetail.php?sortnr=202700>
- [21] Sun Y, Fry S N, Potasek D P, Bell D J and Nelson B J 2005 Characterizing Fruit Fly Flight Behavior Using a Microforce Sensor With a New Comb-Drive Configuration *Journal of Microelectromechanical Systems* **14** 4–11
- [22] Nanoscience Instruments Inc Nano manipulation and sensing URL <http://store.nanoscience.com/store/pc/viewCategories.asp?idCategory=187>
- [23] Stalder A and Dürig U 1995 Nanoguitar: oscillating string as force sensor *Review of scientific instruments* **66** 3576–3579 URL http://ieeexplore.ieee.org/xpls/abs_all.jsp?arnumber=4993194
- [24] Fukuzawa K, Ando T, Shibamoto M, Mitsuya Y and Zhang H 2006 Monolithically fabricated double-ended tuning-fork-based force sensor *Journal of Applied Physics* **99** 094901 ISSN 00218979 URL <http://link.aip.org/link/JAPIAU/v99/i9/p094901/s1&Agg=doi>
- [25] Harley J and Kenny T W 2001 A high-stiffness axial resonant probe for atomic force microscopy *Journal of Microelectromechanical Systems* **10** 434–441 ISSN 10577157 URL <http://ieeexplore.ieee.org/lpdocs/epic03/wrapper.htm?arnumber=946802>
- [26] Fraden J 2010 *Handbook of Modern Sensors: Physics, Designs, and Applications* 4th ed (London: Springer) ISBN 1441964657

- [27] Bartolome E 2010 Signal conditioning for piezoelectric sensors *Analog Applications Journal* **1Q** 24–31 URL <http://www.ti.com/lit/an/slyt369/slyt369.pdf>
- [28] Singh J 2011 *Testing of mechanical computational models for low force calibration transfer artefacts* Masters dissertation King's College London
- [29] Mashini H S M 2011 *Control circuitry for piezoelectric instrumentation for micro scale traceable metrology application* Msc dissertation Brunel University
- [30] Lestage L 2012 *Experimental optimisation of piezoelectric sensor for quasistatic force metrology (working title)* Masters dissertation (to be submitted) Arts et Métiers Paris-Tech (ENSAM)
- [31] Jones C W and Leach R K 2008 Review of Low Force Transfer Artefact Technologies *NPL Report* **ENG 5**
- [32] Jones C W and Leach R K 2008 Adding a dynamic aspect to amplitude-wavelength space *Measurement Science and Technology* **19** 055105 ISSN 0957-0233 URL <http://stacks.iop.org/0957-0233/19/i=5/a=055105?key=crossref.435efa089f9212ce94a023e8f2681030>
- [33] Jones C W, Kramar J A, Davidson S, Leach R K and Pratt J R 2008 Comparison of NIST SI force scale to NPL SI mass scale *Proceedings of ASPE Annual Meeting Portland Oregon* pp 1–4 URL http://www.mel.nist.gov/publications/get_pdf.cgi?pub_id=824727
- [34] Kim M S, Pratt J R, Brand U and Jones C W 2012 Report on the first international comparison of small force facilities: a pilot study at the micronewton level *Metrologia* **49** 70–81 ISSN 0026-1394 URL <http://stacks.iop.org/0026-1394/49/i=1/a=011>
- [35] Jones C W, Chetwynd D G, Singh J and Leach R K 2011 Concept and modelling of a novel active triskelion low force transfer artefact *Proc. 11th Int. Conf. of the Euspen (Como, Italy)* pp 191–194
- [36] Leach R K, Claverley J D, Giusca C, Jones C W, Nimishakavi L, Sun W, Tedaldi M and Yacoot A 2012 Advances in engineering nanometrology at the National Physical Laboratory *Measurement Science and Technology* **23** 074002 ISSN 0957-0233 URL <http://iopscience.iop.org/0957-0233/23/7/074002/>

- [37] Leach R K, Boyd R, Burke T, Danzebrink H U, Dirscherl K, Dziomba T, Gee M, Koenders L, Morazzani V, Pidduck A, Roy D, Unger W E S and Yacoot A 2011 The European nanometrology landscape. *Nanotechnology* **22** 062001 ISSN 1361-6528 URL <http://stacks.iop.org/0957-4484/22/i=6/a=062001><http://www.ncbi.nlm.nih.gov/pubmed/21212479>
- [38] Davis R S 2005 Possible new definitions of the kilogram *Philosophical Transactions of the Royal Society - Series A: Mathematical, Physical and Engineering Sciences* **363** 2249–2264 URL <http://www.ncbi.nlm.nih.gov/pubmed/16147508>
- [39] BIPM/DIN 1994 International Vocabulary of Basic and General Terms in Metrology Tech. rep. Beuth, Berlin
- [40] BIPM, IEC, IFCC, ISO, IUPAC, IUPAP and OIML 1995 *Guide to the Expression of Uncertainty in Measurement* (Geneva, Switzerland: International Organisation for Standardisation) ISBN 92-67-10188-9
- [41] BIPM, IEC, IFCC, ILAC, ISO, IUPAC, IUPAP and OIML 2008 *Evaluation of measurement data - Guide to the expression of uncertainty in measurement* (GUM 1995 with minor corrections. Joint Committee for Guides in Metrology, JCGM 100)
- [42] BIPM, IEC, IFCC, ILAC, ISO, IUPAC, IUPAP and OIML 2008 *Evaluation of Measurement Data - Supplement 1 to the 'Guide to the Expression of Uncertainty in Measurement' - Propagation of Distributions Using a Monte Carlo Method* (Joint Committee for Guides in Metrology, JCGM 101)
- [43] International Bureau of Weights and Measures 2006 *The International System of Units (SI)* 8th ed ISBN 92-822-2213-6
- [44] Poynting J H 1878 On a method of using the Balance with great delicacy, and on its employment to determine the Mean Density of the Earth *Proceedings of the Royal Society of London* **28** 2–35
- [45] Falconer I 1999 A purely local experiment-Poynting and the mean density of the Earth *Measurement Science and Technology* **10** 525 URL <http://iopscience.iop.org/0957-0233/10/6/318>
- [46] Lewis S L and Havard D C 1996 History of Kilogram 18 and Other Important UK Reference Mass Standards *NPL Report MOT1*
- [47] National Physical Laboratory Force measuring devices and systems URL <http://www.npl.co.uk/engineering-measurements/>

mass-force-pressure/force/products-and-services/
force-measuring-devices-and-systems

- [48] Jabbour Z J and Yaniv S L 2001 The kilogram and measurements of mass and force *Journal Of Research Of The National Institute Of Standards And Technology* **106** 25–46 URL <http://nvlpubs.nist.gov/nistpubs/jres/106/1/j61jab.pdf>
- [49] International Organisation of Legal Metrology 2004 R111-1 Weights of classes E1, E2, F1, F2, M1, M1-2, M2, M2-3 and M3 Part 1: Metrological and technical requirements Tech. rep. URL <http://www.oiml.org/publications/R/R111-1-e04.pdf>
- [50] Franks A, Luty M, Robbie C and Stedman M 1998 A design study of a micro-thrust balance for space applications *Nanotechnology* **9** 61–66 URL <http://iopscience.iop.org/0957-4484/9/2/004>
- [51] Hughes E B and Oldfield S 2003 Traceable, high accuracy thrust measurement for electric propulsion 3rd Int *3rd Int. Electric Propulsion Conf (Toulouse, France)*
- [52] Rocca S, Menon C and Nicolini D 2006 FEED micro-thrust balance characterization and testing *Measurement Science and Technology* **17** 711–718 ISSN 0957-0233 URL <http://stacks.iop.org/0957-0233/17/i=4/a=016?key=crossref.203f5f5aa1754004159553e18a2e7923>
- [53] Gee M and Jennett N 1996 High resolution characterisation of tribochemical films on alumina *Wear* **193** 133–145 ISSN 00431648 URL [http://dx.doi.org/10.1016/0043-1648\(95\)06612-8](http://dx.doi.org/10.1016/0043-1648(95)06612-8)
- [54] Herrmann K, Jennett N M, Kuypers S, Mcentegaart I, Ingelbrecht C, Hangen U, Chudoba T, Pohlenz F and Menelao F Investigation of the properties of candidate reference materials suited for the calibration of nanoindentation instruments *Zeitschrift für Metallkunde* **94** 802–806 ISSN 0044-3093 URL <http://cat.inist.fr/?aModele=afficheN&cpsidt=15044970>
- [55] Oliver W C and Pharr G M 2004 Measurement of hardness and elastic modulus by instrumented indentation: Advances in understanding and refinements to methodology *Journal of Materials Research* **19** 3–20 ISSN 08842914 URL <http://www.mrs.org/publications/jmr/jmra/2004/jan/0002.html>

- [56] Agilent Technologies Inc U9830A Agilent Nano Indenter G300 URL <http://www.home.agilent.com/agilent/product.jsp?nid=-34000.901861.00&cc=GB&lc=eng>
- [57] Asylum Research MFP Nanoindenter URL <http://www.asylumresearch.com/Products/NanoIndenter/NanoIndenter.shtml>
- [58] Bruker AXS CETR-Apex Indenter \& Scratch Tester URL <http://www.bruker-axs.com/cetr-apex-nano-micro-indenter-scratch-tester.html>
- [59] Hysitron Corporation TI 950 TriboIndenter URL <http://www.hysitron.com/products/ti-series/ti-950-triboindenter>
- [60] MTS Systems Corporation 1998 Nano Indenter XP URL <http://www.mts.com/downloads/Nano500008-23.pdf>
- [61] Binnig G, Quate C F and Gerber C 1986 Atomic Force Microscope *Physical Review Letters* **56** 930–933 ISSN 0031-9007 URL http://prl.aps.org/abstract/PRL/v56/i9/p930_1
- [62] Yacoot A and Koenders L 2011 Recent developments in dimensional nanometrology using AFMs *Measurement Science and Technology* **22** 122001 ISSN 0957-0233 URL <http://stacks.iop.org/0957-0233/22/i=12/a=122001>
- [63] Leach R, Haycocks J, Jackson K, Lewis A, Oldfield S and Yacoot A 2001 Advances in traceable nanometrology at the National Physical Laboratory *Nanotechnology* **12** R1–R6 ISSN 0957-4484 URL <http://stacks.iop.org/0957-4484/12/i=1/a=201>
- [64] Leach R K, Chetwynd D G, Blunt L, Haycocks J, Harris P M, Jackson K, Oldfield S and Reilly S 2006 Recent advances in traceable nanoscale dimension and force metrology in the UK *Measurement Science and Technology* **17** 467–476 ISSN 0957-0233 URL <http://stacks.iop.org/0957-0233/17/i=3/a=S02>
- [65] Carl Zeiss IMT GmbH Zeiss F25 URL <http://www.zeiss.de/f25>
- [66] Leach R K, Oldfield S and Georgakopoulos D 2006 Traceable nanonewton force measurement at the National Physical Laboratory, UK *UK Proc. Euspen* 2–5
- [67] Kibble B P, Robinson I A and Belliss J H 1990 A Realization of the SI Watt by the NPL Moving-coil Balance *Metrologia* **27** 173–192 ISSN 0026-1394 URL <http://stacks.iop.org/0026-1394/27/i=4/a=002>

- [68] Robinson I A and Kibble B P 2007 An initial measurement of Planck's constant using the NPL Mark II watt balance *Metrologia* **44** 427–440 ISSN 0026-1394 URL <http://stacks.iop.org/0026-1394/44/i=6/a=001>
- [69] Williams E, Steiner R L, Newell D and Olsen P 1998 Accurate Measurement of the Planck Constant *Physical Review Letters* **81** 2404–2407 ISSN 0031-9007 URL http://prl.aps.org/abstract/PRL/v81/i12/p2404_1
- [70] Sienknecht V and Funck T 1986 Realization of the SI Unit Volt by Means of a Voltage Balance *Metrologia* **22** 209–212 ISSN 0026-1394 URL <http://stacks.iop.org/0026-1394/22/i=3/a=018>
- [71] Gallop J 2005 The quantum electrical triangle. *Philosophical transactions. Series A, Mathematical, physical, and engineering sciences* **363** 2221–47 ISSN 1364-503X URL <http://rsta.royalsocietypublishing.org/cgi/content/abstract/363/1834/2221>
- [72] Newell D, Kramar J, Pratt J, Smith D T and Williams E 2003 The nist microforce realization and measurement project *IEEE Transactions on Instrumentation and Measurement* **52** 508–511 ISSN 0018-9456 URL http://ieeexplore.ieee.org/xpl/freeabs_all.jsp?arnumber=1202085
- [73] Pratt J R, Smith D T, Newell D, Kramar J A and Whitenon E 2004 Progress toward Systeme International d'Unites traceable force metrology for nanomechanics *Journal of Materials Research* **19** 366–379 ISSN 0884-2914
- [74] Pratt J, Newell D, Kramar J and Seugling R 2004 Realizing and disseminating the SI micronewton with the next generation NIST electrostatic force balance *Proc. ASPE 2004 Annual Meeting (Orlando, FL)* URL http://www.aspe.net/publications/Annual_2004/PAPERS/1METRO/1466.PDF
- [75] Pratt J R and Kramar J A 2006 SI realisation of small forces using an electrostatic force balance *Proceedings of the 18th IMEKO World Congress, 17th to 22nd September (Rio de Janeiro, Brazil)* pp 17 – 22 URL <http://www.imeko.org/publications/wc-2006/PWC-2006-TC3-046u.pdf>
- [76] Nesterov V, Pelyushenko A, Kart A and Brand U 2007 A novel test facility and methods for the measurement of micro- and nano-newton forces *Proceedings of the 7th euspen International Conference* May

- [77] Nesterov V 2007 Facility and methods for the measurement of micro and nano forces in the range below $\text{SI}\{e-5\}\{\text{newton}\}$ with a resolution of $\text{SI}\{e-12\}\{\text{newton}\}$ (development concept) *Measurement Science and Technology* **18** 360–366 ISSN 0957-0233 URL <http://stacks.iop.org/0957-0233/18/i=2/a=S06?key=crossref.989dae959f8d004c3dcbf4505af6b74d>
- [78] Nesterov V, Mueller M, Frumin L L and Brand U 2009 A new facility to realize a nanonewton force standard based on electrostatic methods *Metrologia* **46** 277–282 ISSN 0026-1394 URL <http://stacks.iop.org/0026-1394/46/i=3/a=016?key=crossref.79052571264aa75c8523e3dd95500dcbhttp://stacks.iop.org/0026-1394/46/i=3/a=016>
- [79] Nesterov V 2009 A nanonewton force facility and a novel method for measurements of the air and vacuum permittivity at zero frequencies *Measurement Science and Technology* **20** 084012 ISSN 0957-0233 URL <http://iopscience.iop.org/0957-0233/20/8/084012/>
- [80] Niehe S 2003 A new force measuring facility for the range of 10 mN to 10 N *Proc. of the XVII IMEKO World Congress, (Dubrovnik, Croatia)* pp 335–340
- [81] Illemann J and Kummel R 2006 Research for a national force standard machine in the range from micronewton to newton relying on force compensation *Proceedings of the 18th IMEKO World Congress, 17th to 22nd September (Rio de Janeiro, Brazil)* pp 17 – 22
- [82] Illemann J 2007 The achievable uncertainty for balance-based force standard machines in the range from micronewton to newton *IMEKO 20th TC3, 3rd TC16 and 1st TC22 Merida, Mexico, 27th-30th November* URL <http://www.imeko.org/publications/tc3-2007/IMEKO-TC3-2007-KL-023u.pdf>
- [83] Hoffmann W, Loheide S, Keine-Besten T, Brand U and Schlachetzki A 2000 Method of characterizing micro mechanical beams and its calibration for the application in micro force measurement systems *Proceedings of the MicroTec 2000, Hannover, Germany, 25th - 27th September*
- [84] Menelao F 2010 Micro and Nanoforce metrology at PTB URL <http://www.imeko.org/publications/tc3-2010/IMEKO-TC3-2010-WS-001.pdf>
- [85] Doering L and Brand U 2006 Calibration of V-shaped cantilever for micro force metrology in biomedical engineering *Proceedings of 6th euspen International Conference (Baden-bei-Wien, Austria)* pp 192–195

- [86] Kim M S, Choi J H, Kim J H and Park Y K 2007 SI-traceable determination of spring constants of various atomic force microscope cantilevers with a small uncertainty of 1% *Measurement Science and Technology* **18** 3351–3358 ISSN 0957-0233 URL <http://stacks.iop.org/0957-0233/18/i=11/a=014?key=crossref.9bb85ed224f45daf535427c044260e40>
- [87] Kim M S, Choi J H, Park Y K and Kim J H 2006 Atomic force microscope cantilever calibration device for quantified force metrology at micro- or nano-scale regime: the nano force calibrator (NFC) *Metrologia* **43** 389–395 ISSN 0026-1394 URL <http://stacks.iop.org/0026-1394/43/i=5/a=008?key=crossref.d8e3b08ff1e9b4379f557579813ded68>
- [88] Kim M S, Choi J H, Kim J H and Park Y K 2010 Accurate determination of spring constant of atomic force microscope cantilevers and comparison with other methods *Measurement* **43** 520–526 ISSN 02632241 URL <http://dx.doi.org/10.1016/j.measurement.2009.12.020>
- [89] Chen S J and Pan S S 2010 Introduction to research activities on traceable force measurements below 10 μN in center for measurement standards *SICE Annual Conference 2010, Proceedings of* pp 3169–3173 URL http://ieeexplore.ieee.org/xpl/freeabs_all.jsp?arnumber=5602898
- [90] Chen S J and Pan S S 2009 Nanonewton Force Generation and Detection Based on a Sensitive Torsion Pendulum *IEEE Transactions on Instrumentation and Measurement* **58** 897–901 ISSN 0018-9456 URL http://ieeexplore.ieee.org/xpl/freeabs_all.jsp?arnumber=4749299
- [91] Chen S J and Pan S S 2010 The activities of micro-force measurement below 10 μN in Center for Measurement Standards URL <http://www.imeko.org/publications/tc3-2010/IMEKO-TC3-2010-WS-004.pdf>
- [92] Chen S J 2010 Development of nanonewton force standard based on a torsion pendulum *CPEM 2010 (IEEE)* pp 508–509 ISBN 978-1-4244-6795-2 URL http://ieeexplore.ieee.org/xpls/abs_all.jsp?arnumber=5543636
- [93] Micro-g LaCoste 2011 Absolute Gravimeters URL <http://www.microglacoste.com/absolutemeters.php>
- [94] Ardalan A A and Grafarend E W 2001 Somigliana-Pizzetti gravity : the international gravity formula accurate to the sub-nanoGal level *Journal of Geodesy* **75** 424–437

- [95] Great Britain Ministry of Defence 1987 *Admiralty manual of navigation Volume 1, General navigation, coastal navigation and pilotage*. (London: The Stationery Office) ISBN 0117728802
- [96] Madec T, Mann G, Meury P A and Rabault T 2007 Micro-mass standards to calibrate the sensitivity of mass comparators *Metrologia* **44** 266–274 ISSN 0026-1394 URL <http://stacks.iop.org/0026-1394/44/i=5/a=002>
- [97] Stowe T, Yasumura K and Kenny T W 2009 Attonewton force detection using ultrathin silicon cantilevers *Applied Physics* **71** 288–290 URL http://ieeexplore.ieee.org/xpls/abs_all.jsp?arnumber=4892357
- [98] Chung K, Scholz S, Shaw G A, Kramar J and Pratt J R 2008 SI traceable calibration of an instrumented indentation sensor spring constant using electrostatic force *Review of Scientific Instruments* **79** 095105 ISSN 1089-7623 URL <http://link.aip.org/link/?RSINAK/79/095105/1>
- [99] Chung K H, Shaw G A and Pratt J R 2009 Accurate noncontact calibration of colloidal probe sensitivities in atomic force microscopy. *The Review of scientific instruments* **80** 065107 ISSN 1089-7623 URL <http://link.aip.org/link/?RSINAK/80/065107/1>
- [100] Nesterov V, Mueller M, Frumin L L and Brand U 2009 A new facility to realize a nanonewton force standard based on electrostatic methods *Metrologia* **46** 277–282 ISSN 0026-1394 URL <http://stacks.iop.org/0026-1394/46/i=3/a=016>
- [101] Feat M, Zhao C, Ju L and Blair D G 2005 Demonstration of low power radiation pressure actuation for control of test masses *Review of Scientific Instruments* **76** 036107 ISSN 00346748 URL <http://link.aip.org/link/RSINAK/v76/i3/p036107/s1&Agg=doi>
- [102] Young H D and Freedman R A 2001 *Sears and Zemansky's University Physics with Modern Physics* 10th ed (Addison Wesley; 10 edition) ISBN 0201603365 URL http://www.amazon.co.uk/Sears-Zemanskys-University-Physics-Addison-Wesley/dp/0201603365/ref=sr_1_3?ie=UTF8&qid=1323362799&sr=8-3
- [103] Kleckner D and Bouwmeester D 2006 Sub-kelvin optical cooling of a micromechanical resonator. *Nature* **444** 75–8 ISSN 1476-4687 URL <http://dx.doi.org/10.1038/nature05231>

- [104] Weld D M and Kapitulnik A 2006 Feedback control and characterization of a micro-cantilever using optical radiation pressure *Applied Physics Letters* **89** 164102 ISSN 00036951 URL <http://link.aip.org/link/?APPLAB/89/164102/1>
- [105] Choi J H, Kim M S, Park Y K and Choi M S 2007 Quantum-based mechanical force realization in piconewton range *Applied Physics Letters* **90** 073117 ISSN 00036951 URL <http://link.aip.org/link/APPLAB/v90/i17/p073117/s1&Agg=doi>
- [106] Choi J H 2010 Measurement, Backaction, and Future Standard in Ultra-small Force Metrology URL <http://www.imeko.org/publications/tc3-2010/IMEKO-TC3-2010-WS-005.pdf>
- [107] Carrion-Vazquez M, Oberhauser A F, Fowler S B, Marszalek P E, Broedel S E, Clarke J and Fernandez J M 1999 Mechanical and chemical unfolding of a single protein: a comparison. *Proceedings of the National Academy of Sciences of the United States of America* **96** 3694–9 ISSN 0027-8424 URL <http://www.pubmedcentral.nih.gov/articlerender.fcgi?artid=22356&tool=pmcentrez&rendertype=abstract>
- [108] Oberhauser A, Marszalek P, Erickson H, Fernandez J and Others 1998 The molecular elasticity of the extracellular matrix protein tenascin *Nature* **393** 181–184 URL <http://note.cellbio.duke.edu/Faculty/Erickson/pdf's/TNAFMFernandezErickson.pdf>
- [109] Oberhauser A F, Hansma P K, Carrion-Vazquez M and Fernandez J M 2001 Stepwise unfolding of titin under force-clamp atomic force microscopy. *Proceedings of the National Academy of Sciences of the United States of America* **98** 468–72 ISSN 0027-8424 URL <http://www.pubmedcentral.nih.gov/articlerender.fcgi?artid=14610&tool=pmcentrez&rendertype=abstract>
- [110] Fulton A B and Isaacs W B 1991 Titin, a huge, elastic sarcomeric protein with a probable role in morphogenesis. *BioEssays : news and reviews in molecular, cellular and developmental biology* **13** 157–61 ISSN 0265-9247 URL <http://www.ncbi.nlm.nih.gov/pubmed/1859393>
- [111] Gao M, Lu H and Schulten K 2001 Simulated refolding of stretched titin immunoglobulin domains. *Biophysical journal* **81** 2268–77 ISSN 0006-3495 URL [http://dx.doi.org/10.1016/S0006-3495\(01\)75874-2](http://dx.doi.org/10.1016/S0006-3495(01)75874-2)

- [112] Marszalek P E, Oberhauser A F, Pang Y P and Fernandez J M 1998 Polysaccharide elasticity governed by chair-boat transitions of the glucopyranose ring. *Nature* **396** 661–4 ISSN 0028-0836 URL <http://dx.doi.org/10.1038/25322>
- [113] Wright W M D and Chetwynd D G 1998 Can charge writing aid nanotechnological manipulation? *Nanotechnology* **9** 133–142 ISSN 0957-4484 URL <http://stacks.iop.org/0957-4484/9/i=2/a=016>
- [114] Autumn K, Sitti M, Liang Y a, Peattie A M, Hansen W R, Sponberg S, Kenny T W, Fearing R, Israelachvili J N and Full R J 2002 Evidence for van der Waals adhesion in gecko setae. *Proceedings of the National Academy of Sciences of the United States of America* **99** 12252–6 ISSN 0027-8424 URL <http://www.pubmedcentral.nih.gov/articlerender.fcgi?artid=129431&tool=pmcentrez&rendertype=abstract>
- [115] Argento C and French R H 1996 Parametric tip model and force-distance relation for Hamaker constant determination from atomic force microscopy *Journal of Applied Physics* **80** 6081 ISSN 00218979 URL <http://link.aip.org/link/JAPIAU/v80/i11/p6081/s1&Agg=doi>
- [116] Ackler H D, French R H and Chiang Y M 1996 Comparisons of Hamaker constants for ceramic systems with intervening vacuum or water: From force laws and physical properties *Journal of Colloid and Interface Science* **179** 460–469 ISSN 0021-9797 URL <http://www.lrsm.upenn.edu/~frenchrh/download/9509aqham1.pdf>
- [117] Lamoreaux S 1997 Demonstration of the Casimir force in the 0.6 to 6 μm range *Physical Review Letters* **78** 5–8 ISSN 1079-7114 URL <http://link.aps.org/doi/10.1103/PhysRevLett.78.5>
- [118] Mohideen U and Roy A 1998 Precision measurement of the Casimir force from 0.1 to 0.9 μm *Physical Review Letters* **81** 4549–4552 ISSN 1079-7114 URL <http://link.aps.org/doi/10.1103/PhysRevLett.81.4549>
- [119] Bulgac A, Magierski P and Wirzba A 2005 Scalar Casimir effect between Dirichlet spheres or a plate and a sphere 13 (*Preprint* 0511056) URL <http://arxiv.org/abs/hep-th/0511056>
- [120] Sparnaay M J 1958 Measurements of attractive forces between flat plates *Physica* **24** 751–764 ISSN 00318914 URL <http://linkinghub.elsevier.com/retrieve/pii/S0031891458800907>

- [121] Degertekin F L, Hadimioglu B, Sulchek T and Quate C F 2001 Actuation and characterization of atomic force microscope cantilevers in fluids by acoustic radiation pressure *Applied Physics Letters* **78** 1628 ISSN 00036951 URL <http://link.aip.org/link/APPLAB/v78/i11/p1628/s1&Agg=doi>
- [122] Dushkin C 1996 Direct Measurement of Nanonewton Capillary Forces *Journal of Colloid and Interface Science* **181** 657–660 ISSN 00219797 URL <http://linkinghub.elsevier.com/retrieve/pii/S0021979796904245>
- [123] Smith S T and Chetwynd D G 1994 *Developments in Nanotechnology, volume 2: Foundations of Ultra-Precision Mechanism Design* (London: CRC Press) ISBN 9782884490016
- [124] Leach R K, Oldfield S, Awan S, Blackburn J and Williams J 2004 Design of a bi-directional electrostatic actuator for realising nanonewton to micronewton forces *NPL Report DEPC-EM001*
- [125] Henselmans R, Rosielle N, Cacace L, Kappelhof P, Klinkhamer F and Spierdijk H 2004 Low-Force Measurement Facility: Mechanical Design Report Tech. rep.
- [126] Leach R K, Flack D, Hughes E and Jones C W 2009 Development of a new traceable areal surface texture measuring instrument *Wear* **266** 552–554 ISSN 00431648 URL <http://linkinghub.elsevier.com/retrieve/pii/S0043164808003074>
- [127] Reilly S and Leach R K 2006 Critical review of seismic vibration isolation techniques. *NPL Report DEPC-EM007*
- [128] Shi X and Polycarpou A A 2005 Measurement and Modeling of Normal Contact Stiffness and Contact Damping at the Meso Scale *Journal of Vibration and Acoustics* **127** 52 ISSN 07393717 URL <http://link.aip.org/link/JVACEK/v127/i1/p52/s1&Agg=doi>
- [129] Stone J A and Zimmermann J H Elastic compression of spheres and cylinders at point and line contact URL <http://emtoolbox.nist.gov/Elastic/Case2.asp>
- [130] Hess P 1996 Laser diagnostics of mechanical and elastic properties of silicon and carbon films *Applied Surface Science* **106** 429–437 ISSN 01694332 URL [http://dx.doi.org/10.1016/S0169-4332\(96\)00369-8](http://dx.doi.org/10.1016/S0169-4332(96)00369-8)

- [131] Dolbow J and Gosz M 1996 Effect of out-of-plane properties of a polyimide film on the stress fields in microelectronic structures *Mechanics of Materials* **23** 311–321 ISSN 01676636 URL [http://dx.doi.org/10.1016/0167-6636\(96\)00021-X](http://dx.doi.org/10.1016/0167-6636(96)00021-X)
- [132] Wolfram Research Inc Technical data for Nickel URL <http://www.periodictable.com/Elements/028/data.html>
- [133] Shaw G A, Kramar J A and Pratt J R 2007 SI-Traceable Spring Constant Calibration of Microfabricated Cantilevers for Small Force Measurement *Experimental Mechanics* **47** 143–151 ISSN 0014-4851 URL <http://www.springerlink.com/index/10.1007/s11340-006-9394-9>
- [134] Pratt J R, Shaw G A, Kumanchik L and Burnham N A 2010 Quantitative assessment of sample stiffness and sliding friction from force curves in atomic force microscopy *Journal of Applied Physics* **107** 044305 ISSN 00218979 URL <http://link.aip.org/link/JAPIAU/v107/i4/p044305/s1&Agg=doi>
- [135] ISO group TC 164/SC 3/WG 1 and ASTM E280611 2002 *Metallic Materials—Instrumented Indentation Test for Hardness and Materials Parameters*
- [136] Pratt J R, Smith D T, Kramar J A and Newell D B 2003 Microforce and Instrumented Indentation Research at the National Institute of Standards and Technology, Gaithersburg, MD *Proceedings of 4th International Symposium of MEMS and nanotechnology* (Charlotte, North Carolina) pp 299–306
- [137] J Butt H, Siedle P, Seifert K, Fendler K, Seeger T, Bamberg E, L Weisenhorn A, Goldie K and Engel A 1993 Scan speed limit in atomic force microscopy *Journal of Microscopy* **169** 75–84 ISSN 00222720 URL <http://www.mendeley.com/research/scan-speed-limit-in-atomic-force-microscopy/>
- [138] Neumeister J M and Ducker W A 1994 Lateral, normal, and longitudinal spring constants of atomic force microscopy cantilevers *Review of Scientific Instruments* **65** 2527 ISSN 00346748 URL http://ieeexplore.ieee.org/xpl/freeabs_all.jsp?arnumber=4991975
- [139] Hazel J L and Tsukruk V V 1998 Friction Force Microscopy Measurements: Normal and Torsional Spring Constants for V-Shaped Cantilevers *Journal of Tribology* **120** 814–819 URL <http://link.aip.org/link/?JTQ/120/814/1>

- [140] Hazel J L and Tsukruk V V 1999 Spring constants of composite ceramic/gold cantilevers for scanning probe microscopy *Thin Solid Films* **339** 249–257 ISSN 00406090 URL [http://dx.doi.org/10.1016/S0040-6090\(98\)00961-4](http://dx.doi.org/10.1016/S0040-6090(98)00961-4)
- [141] Senden T J and Ducker W A 1994 Experimental Determination of Spring Constants in Atomic Force Microscopy *Langmuir* **10** 1003–1004
- [142] Tortonese M and Kirk M 1997 Characterization of application specific probes for SPMs *Proceedings of SPIE* **3009** 53–60 ISSN 0277786X URL <http://link.aip.org/link/?PSI/3009/53/1&Agg=doi>
- [143] Cumpson P J, Hedley J and Zhdan P 2003 Accurate force measurement in the atomic force microscope: a microfabricated array of reference springs for easy cantilever calibration *Nanotechnology* **14** 918–924 ISSN 0957-4484 URL <http://stacks.iop.org/0957-4484/14/i=8/a=314?key=crossref.650d65cff40fe364b704364d5cfb238c>
- [144] Gibson C T, Watson G S and Myhra S 1996 Determination of the spring constants of probes for force microscopy/spectroscopy *Nanotechnology* **7** 259–262 ISSN 0957-4484 URL <http://stacks.iop.org/0957-4484/7/i=3/a=014>
- [145] Holbery J D, Eden V L, Sarikaya M and Fisher R M 2000 Experimental determination of scanning probe microscope cantilever spring constants utilizing a nanoindentation apparatus *Review of Scientific Instruments* **71** 3769 ISSN 00346748 URL <http://link.aip.org/link/?RSINAK/71/3769/1>
- [146] Sader J E, Larson I, Mulvaney P and White L R 1995 Method for the calibration of atomic force microscope cantilevers *Review of Scientific Instruments* **66** 3789–3798
- [147] Cleveland J P, Manne S, Bocek D and Hansma P K 1993 A nondestructive method for determining the spring constant of cantilevers for scanning force microscopy *Review of Scientific Instruments* **64** 403 ISSN 00346748 URL <http://link.aip.org/link/RSINAK/v64/i2/p403/s1&Agg=doi>
- [148] Hutter J L and Bechhoefer J 1993 Calibration of atomic-force microscope tips *Review of Scientific Instruments* **64** 1868 ISSN 00346748 URL <http://link.aip.org/link/RSINAK/v64/i7/p1868/s1&Agg=doi>
- [149] Svoboda K and Block S M 1994 Biological applications of optical forces. *Annual review of biophysics and biomolecular structure* **23** 247–85 ISSN 1056-8700 URL <http://www.ncbi.nlm.nih.gov/pubmed/7919782>

- [150] Matei G A, Thoreson E J, Pratt J R, Newell D B and Burnham N A 2006 Precision and accuracy of thermal calibration of atomic force microscopy cantilevers *Review of Scientific Instruments* **77** 083703 ISSN 00346748 URL <http://link.aip.org/link/?RSINAK/77/083703/1>
- [151] Sader J E, Chon J W M and Mulvaney P 1999 Calibration of rectangular atomic force microscope cantilevers *Review of Scientific Instruments* **70** 3967 ISSN 00346748 URL <http://link.aip.org/link/?RSINAK/70/3967/1>
- [152] Martin Y, Williams C C and Wickramasinghe H K 1987 Atomic force microscope-force mapping and profiling on a sub 100-Åscale *Journal of Applied Physics* **61** 4723–4729 URL http://ieeexplore.ieee.org/xpls/abs_all.jsp?arnumber=5079544
- [153] Gysin U, Rast S, Ruff P, Meyer E, Lee D, Vettiger P and Gerber C 2004 Temperature dependence of the force sensitivity of silicon cantilevers *Physical Review B* **69** 1–6 ISSN 1098-0121 URL <http://link.aps.org/doi/10.1103/PhysRevB.69.045403> <http://prb.aps.org/abstract/PRB/v69/i4/e045403>
- [154] Willemin M, Rossel C, Brugger J, Despont M H, Rothuizen H, Vettiger P, Hofer J and Keller H 1998 Piezoresistive cantilever designed for torque magnetometry *Journal of Applied Physics* **83** 1163 ISSN 00218979 URL <http://link.aip.org/link/?JAPIAU/83/1163/1>
- [155] Rossel C, Bauer P, Zech D, Hofer J, Willemin M and Keller H 2009 Active micro-levers as miniature torque magnetometers *Journal of Applied Physics* **79** 8166–8173 ISSN 0021-8979 URL http://ieeexplore.ieee.org/xpls/abs_all.jsp?arnumber=5013925
- [156] Kanda Y 1991 Piezoresistance effect of silicon *Sensors and Actuators A: Physical* **28** 83–91 ISSN 09244247 URL [http://dx.doi.org/10.1016/0924-4247\(91\)85017-I](http://dx.doi.org/10.1016/0924-4247(91)85017-I)
- [157] Pratt J R 2007 Private communication
- [158] Weckenmann a, Peggs G and Hoffmann J 2006 Probing systems for dimensional micro- and nano-metrology *Measurement Science and Technology* **17** 504–509 ISSN 0957-0233 URL <http://stacks.iop.org/0957-0233/17/i=3/a=S08?key=crossref.6793f6b3a8fa45322074db69ca2b57c4>

- [159] Claverley J D and Leach R K 2009 A vibrating micro-scale CMM probe for measuring high aspect ratio structures *Microsystem Technologies* **16** 1507–1512 ISSN 0946-7076 URL <http://www.springerlink.com/index/10.1007/s00542-009-0967-2>
- [160] IBS Precision Engineering BV Triskelion ultra-precision touch probe URL <http://www.ibspe.com/category/isara-400-3d-cmm/triskelion-touch-probe.htm>
- [161] XPRESS Precision Engineering BV Gannen-XP Ultra precision 3D tactile sensor URL <http://www.xpresspe.com/probe2.htm>
- [162] Bahreyni B 2008 *Fabrication and design of resonant microdevices* (Norwich, NY: William Andrew Inc) ISBN 9780815515777
- [163] Tortonese M, Yamada H, Barrett R and Quate C 1991 *Atomic force microscopy using a piezoresistive cantilever* (IEEE) ISBN 0-87942-585-7 URL <http://ieeexplore.ieee.org/lpdocs/epic03/wrapper.htm?arnumber=148908>
- [164] Doering L, Frühauf J and Brand U 2002 Micro force transfer standards *Proceedings of IMEKO (TC3/TC5/TC20): paper no. ID-006* URL <http://www.imeko.org/publications/tc3-2002/IMEKO-TC3-2002-003.pdf>
- [165] Kumar V V, Dasgupta A and Bhat K N 2006 Process Optimization for Monolithic Integration of Piezoresistive Pressure Sensor and MOSFET Amplifier with SOI Approach *Journal of Physics: Conference Series* **34** 210–215 ISSN 1742-6588 URL <http://iopscience.iop.org/1742-6596/34/1/035/>
- [166] Haertling G 1999 Ferroelectric ceramics: history and technology *Journal of the American Ceramic Society* **82** 797–818 URL <http://onlinelibrary.wiley.com/doi/10.1111/j.1151-2916.1999.tb01840.x/abstract>
- [167] Kibble B P and Rayner G H 1984 *Coaxial AC bridges* (Adam Hilger Ltd)
- [168] Duval F F C, Dorey R a, Wright R W, Huang Z and Whatmore R W 2004 Fabrication and modeling of high-frequency PZT composite thick film membrane resonators. *IEEE transactions on ultrasonics, ferroelectrics, and frequency control* **51** 1255–61 ISSN 0885-3010 URL <http://www.ncbi.nlm.nih.gov/pubmed/15553509>
- [169] Ledermann N, Muralt P, Baborowski J, Gentil S, Mukati K, Cantoni M, Seifert A and Setter N 2003 {1 0 0}-Textured, piezoelectric Pb (Zr_x, Ti_(1-x)) O₃ thin films

- for MEMS: integration, deposition and properties *Sensors and Actuators A: Physical* **105** 162–170 ISSN 09244247 URL <http://www.sciencedirect.com/science/article/pii/S0924424703000906>
- [170] Duval F, Wilson S, Ensell G, Evanno N, Cain M and Whatmore R 2007 Characterisation of PZT thin film micro-actuators using a silicon micro-force sensor *Sensors and Actuators A: Physical* **133** 35–44 ISSN 09244247 URL <http://linkinghub.elsevier.com/retrieve/pii/S0924424706002792>
- [171] Mohamed H, Polla D, Ebbini E and Zurn S 2001 Micromachined piezoelectric ultrasonic imaging transducer *Microelectromechanical Systems Conference, 2001* (IEEE) pp 95–98 ISBN 0780372247 URL http://ieeexplore.ieee.org/xpls/abs_all.jsp?arnumber=992751
- [172] Ledermann N, Muralt P, Baborowski J, Forster M and Pellaux J P 2004 Piezoelectric $\text{Pb}(\text{Zr}_x, \text{Ti}_{(1-x)})\text{O}_3$ thin film cantilever and bridge acoustic sensors for miniaturized photoacoustic gas detectors *Journal of Micromechanics and Microengineering* **14** 1650–1658 ISSN 0960-1317 URL <http://stacks.iop.org/0960-1317/14/i=12/a=008?key=crossref.4381152431a8f97385e0da3cab3330a3>
- [173] Moallem M, Kermani M and Patel R 2004 Flexure control of a positioning system using piezoelectric transducers *Control Systems* **12** 757–762 URL http://ieeexplore.ieee.org/xpls/abs_all.jsp?arnumber=1327615
- [174] Ivan I A, Rakotondrabe M, Lutz P and Chaillet N 2009 Quasistatic displacement self-sensing method for cantilevered piezoelectric actuators *Review of scientific instruments* **80** 065102 ISSN 1089-7623 URL <http://www.ncbi.nlm.nih.gov/pubmed/19566221>
- [175] Beyeler F, Muntwyler S, Nagy Z, Graetzel C, Moser M and Nelson B J 2008 Design and calibration of a MEMS sensor for measuring the force and torque acting on a magnetic microrobot *Journal of Micromechanics and Microengineering* **18** 025004 ISSN 0960-1317 URL <http://stacks.iop.org/0960-1317/18/i=2/a=025004?key=crossref.97a9aafb7c34e3d38292684be7e1aaef>
- [176] Mohanty P, Harrington D, Ekinci K, Yang Y, Murphy M and Roukes M 2002 Intrinsic dissipation in high-frequency micromechanical resonators *Physical Review B* **66** 1–15 ISSN 0163-1829 URL <http://link.aps.org/doi/10.1103/PhysRevB.66.085416>

- [177] Keely C A 1989 Solder joint inspection using laser Doppler vibrometry *Hewlett-Packard Journal* **40** 81–85
- [178] Sato K, Ono A and Tomikawa Y 2003 Finite Element Method Simulation of Double-Ended Tuning-Fork Quartz Resonator for Application to Vibratory Gyro-Sensor *Japanese Journal of Applied Physics* **42** 3115–3119 ISSN 0021-4922 URL <http://jjap.ipap.jp/link?JJAP/42/3115/>
- [179] Sazonova V, Yaish Y, Ustünel H, Roundy D, Arias T a and McEuen P L 2004 A tunable carbon nanotube electromechanical oscillator. *Nature* **431** 284–7 ISSN 1476-4687 URL <http://www.ncbi.nlm.nih.gov/pubmed/15372026>
- [180] Sun Y, Fowkes C R, Gindy N and Leach R K 2010 Variation risk analysis: MEMS fabrication tolerance for a micro CMM probe *The International Journal of Advanced Manufacturing Technology* **47** 1113–1120 ISSN 0268-3768 URL <http://www.springerlink.com/index/10.1007/s00170-009-2251-0>
- [181] Young W C 1989 *Roark's formulas for stress and strain* sixth ed. ed (New York: McGraw Hill)
- [182] Chetwynd D G, Liu X and Smith S T 1992 Signal fidelity and tracking force in stylus profilometry *International Journal of Machine Tools and Manufacture* **32** 239–245 ISSN 0890-6955 URL <http://linkinghub.elsevier.com/retrieve/pii/089069559290084T>
- [183] Shaw C 2009 private correspondence
- [184] Williams T 2005 *The Circuit Designer's Companion* 2nd ed (Oxford: Newnes) ISBN 0750663707
- [185] Physik Instrumente 2012 P-772: Ultra-Compact Piezo NanoAutomation(R) Stage with Direct Metrology URL <http://www.physikinstrumente.com/en/products/prspecs.php?sortnr=200500>
- [186] Sitti M and Hashimoto H 2000 Controlled pushing of nanoparticles: modeling and experiments *IEEE/ASME Transactions on Mechatronics* **5** 199–211 ISSN 10834435 URL <http://ieeexplore.ieee.org/lpdocs/epic03/wrapper.htm?arnumber=847093>
- [187] Burnham N A, Colton R and Pollock H 1993 Interpretation of force curves in force microscopy *Nanotechnology* **4** 64 URL <http://iopscience.iop.org/0957-4484/4/2/002>

[188] Tabor D 1991 *Gases, Liquids and Solids: And Other States of Matter* 3rd ed (Cambridge: Cambridge University Press; 3rd edition) ISBN 0521406676

Vita

<i>Name</i>	Christopher Weir Jones
<i>Contact</i>	christopher.jones@npl.co.uk
<i>Affiliation</i>	National Physical Laboratory Hampton Road, Teddington TW11 0LW, United Kingdom
<i>Education</i>	PhD, The University of Warwick, 2012 MSci ARCS, Imperial College London, 2005

Permanent Address: 23 Turnoak Avenue
Woking
Surrey GU22 0AJ

This thesis was typeset with $\LaTeX 2_{\epsilon}$ ¹ by the author.

¹ $\LaTeX 2_{\epsilon}$ is an extension of \LaTeX . \LaTeX is a collection of macros for \TeX . \TeX is a trademark of the American Mathematical Society. The style package *warwickthesis* was used.